Laser Diagnostics for Spatially Resolved Thermometry in Combustion and Flows

Christopher Willman

St Anne's College

DPhil, Trinity 2016

Laser Diagnostics for Spatially Resolved Thermometry in Combustion and Flows

Christopher Willman, St Anne's College. DPhil, Trinity 2016.

Abstract

The development of Laser-Induced Thermal Grating Spectroscopy (LITGS) for diagnostics of combusting and non-combusting flows is described. The first use of LITGS to provide in situ calibration of 2-Dimensional temperature distributions generated using Two-Colour Planar Laser-Induced Fluorescence (TC-PLIF) is reported. Time-resolved measurements of temperature distributions in a firing GDI optical engine obtained by TC-PLIF were made during the compression stroke and calibrated to the absolute temperature scale by simultaneous LITGS measurements. The accuracy and precision of the temperatures derived from LITGS data are evaluated using alternative methods of data analysis – Fast Fourier Transform and Fitting to theoretical models of the experimental data. The relative merits of the two methods are examined for analysis of weak LITGS signals obtained under engine conditions of low pressure and high temperature. The combined TC-PLIF and LITGS system was demonstrated by performing repeated single-shot measurements for 1 in every 10 four-stroke cycles showing excellent correlation of the temperatures derived from both techniques. Direct measurement of the effect of 'charge cooling', of order 5 K, for operation with direct injection is reported. Inhomogeneous temperature distributions were observed during the compression stroke for fired operation with Port Fuel Injection (PFI) and also with Gasoline Direct Injection (GDI). The effects of varying the relative concentrations of toluene and iso-octane in the two-component fuel were investigated.

Extension of the LITGS technique to multi-point measurements along a 1-D line is described. By recording signals from 4 points on separate detectors using a fibre-coupled photodiode array the limitations of Streak Cameras used previously for 1-D LITGS measurements were overcome. Demonstration of principle experiments are reported in which simultaneous 4-point measurements were made with 1 mm spatial resolution and a precision of 0.7 % in temperature gradients in gas flows and in boundary layers at surfaces.

Acknowledgements

This thesis would not have been possible without the support, advice and inspiration of a great many people, both within the Physics and Engineering Science departments of the University of Oxford and further afield, to whom I am forever thankful.

Firstly, I would like to thank Professor Paul Ewart whose interesting and challenging undergraduate Masters project first kindled my desire to work in the field of laser diagnostics, and whose excellent supervision and guidance over the last four years has been key to the success of my research.

I owe a great deal of my experimental skills to Dr Ben Williams, whose sunny disposition, willingness to discuss my work at length and seemingly limitless patience in teaching me the tricks of the trade serve as an aspiration for my future career.

Many thanks to Professor Richard Stone, not only for providing months of access to the optical engine and allowing me to fill every available space in the engine bay with lasers, but also for his welcoming manner and willingness to help and provide advice during my time in Engineering Science.

My thanks also to Dr Henry Northern, Andrew Luers, Shea O'Hagan, Dr Felix Förster and Dr Anna-Lena Sahlberg, who are wonderful people to bounce ideas off or trade stories with of the latest equipment breakdowns, and who make working in the Ewart group such an enjoyable experience.

Running the optical engine would not have been possible without the assistance of the students and post-docs of Richard Stone's group in Engineering Science, whether fixing breakdowns or answering my many engine-based questions. In particular, thanks to Dr Joe Camm and Blane Scott for their assistance in operating the engine and Dr Felix Leach whose finely-tuned ears were the diagnostic of choice for determining smooth optical engine operation.

Thanks to Professor Neville Harnew and Professor Patrick Irwin for their support during my undergraduate degree at St Anne's and for providing me with a series of teaching opportunities during my DPhil. Thanks also to Dr John Williams for providing an insight into industry throughout my research.

Much of the apparatus for the preliminary testing of the TC-PLIF and LITGS systems started out life in the Research Workshop of the Clarendon Laboratory, where I was fortunate enough to receive expert tuition in machining from Mathew Newport and advice from Simon Moulder. I would also like to thank Alan and Dan in Stores for cheerfully accepting my almost daily requests for odds and ends vital to my experiments, as well as Tom Hopkins for regularly helping me to navigate the uncharted waters of University finances.

My thanks to all my friends and family who provided welcome distractions and perspective during the writing of this thesis, and to my parents for their ever-present support, not to mention several hundred pages of proof-reading.

Finally to my wife Daniele, my inspiration, for her unwavering support and encouragement and her ability to make even the greatest challenges achievable.

Contributions to this research

All work presented in this thesis is my own, except where referenced or otherwise identified in the text. Consideration must also be given to those recognised in the acknowledgments and to the specific cases highlighted below which describe the sections of this thesis which build upon, or otherwise rely on, work done by others.

- LITGS theory. The derivation of the evolution of the grating density perturbation is a summary of the work of Paul et al. [1].

- LITGS fitting routine. The MATLAB implementation of the above LITGS model in this thesis was developed by Stevens [2] and previously applied by Williams [3].

- LITGS FFT routine. The initial MATLAB implementation of FFT LITGS analysis, discussed and improved upon in this work in chapter 4, was supplied by Williams [3].

- Point-LITGS equipment. The compact point-LITGS system used in this thesis was designed and built by Williams et al. [4].

- Toluene emission spectrum data. Data for a range of temperatures was provided by Faust et al. [5] for use in this work, enabling modelling of the TC-PLIF spectral filtering optics.

- LITGS 'fitted' FFT analysis. The appendix discussion of potential future improvements to LITGS analysis with FFT was inspired by discussion with the authors of [6], who also provided the 'fitted' FFT analysis implemented in MATLAB for discussion in this thesis.

Publications based on this research

P. Ewart, C. Willman, B. A. O. Williams, J. Williams, and C. R. Stone, "High precision in-cylinder thermometry using laser induced grating spectroscopy," I Mech E, 2015.

C. Willman and P. Ewart, "Multipoint temperature measurements in gas flows using 1-D Laser-Induced Grating Scattering", Experiments in Fluids, 2016.

Christopher Willman

Contents

List of Acronyms

1D-LITGS	1-Dimensional Laser Induced Thermal Grating Spectroscopy
ATDC	After Top-Dead-Centre
BBO	Beta-Phase Barium Borate
BTDC	Before Top-Dead-Centre
CAD	Crank Angle Degrees
CARS	Coherent Anti-Stokes Raman Spectroscopy
CCD	Charge-Coupled Device
CFD	Computational Fluid Dynamics
CFT	Continuous Fourier Transform
CI	Compression Ignition
CoV	Coefficient of Variation
CW	Continuous-Wave
DFT	Discrete Fourier Transform
DFWM	Degenerate Four Wave Mixing
DNI	Direct Numerical Integration
DPSS	Diode-Pumped Solid State
EGR	Exhaust Gas Residuals
EMCCD	Electron-Multiplying Charge-Coupled Device
ERE-CARS	Electronically Resonantly Enhanced Coherent Anti-Stokes Raman Spectroscopy
EVC	Exhaust Valve Closing
EVO	Exhaust Valve Opening
FARLIG	Fuel/Air Ratio by Laser-Induced Thermal Gratings
FFT	Fast Fourier Transform
FPDA	Fibre-Coupled Photodiode Array
FQY	Fluorescence Quantum Yield
FWHM	Full Width Half Maximum
FWM	Four Wave Mixing
GDI	Gasoline Direct Injection
IC	Internal Combustion
ICCD	Intensified Charge-Coupled Device

ISC	Inter-System Crossing
IVC	Inlet Valve Closing
IVO	Inlet Valve Opening
LIEF	Laser-Induced Exciplex Fluorescence
LIEGS	Laser-Induced Electrostrictive Grating Spectroscopy
LIF	Laser-Induced Fluorescence
LIGS	Laser Induced Grating Spectroscopy
LITA	Laser-Induced Thermal Acoustics
LITGS	Laser Induced Thermal Grating Spectroscopy
MUMAS	Multi-Mode Absorption Spectroscopy
NOx	Nitrogen Oxides
PAH	Polycyclic Aromatic Hydrocarbons
PFI	Port Fuel Injection
PIV	Particle Image Velocimetry
PLIF	Planar Laser-Induced Fluorescence
PM	Particulate Mass
PMT	Photomultiplier Tube
PN	Particulate Number
PS	Polarisation Spectroscopy
QPLIF	Quantitative Planar Laser-Induced Fluorescence
SI	Spark Ignition
SLIPI	Structured Laser Illumination Planar Imaging
S-PIV	Stereoscopic Particle Image Velocimetry
TC-PLIF	Two-Colour Planar Laser-Induced Fluorescence
TDC	Top-Dead-Centre
TDLAS	Tunable Diode Laser Absorption Spectroscopy
THC	Total Hydrocarbons
TLAF	Two-Line Atomic Fluorescence
TMB	Tri-Methylbenzene
UV	Ultra-Violet

1. Introduction

The aim of this thesis is to develop and demonstrate an optical diagnostic for in-situ calibrated 2-dimensional thermometry in a spark-ignition internal combustion engine.

1.1. Combustion

Combustion has a part to play in almost every aspect of modern life. From heating our homes, providing the power for our electronic devices, to transporting the goods and food we purchase from around the world, worldwide energy consumption has increased by 25 % to 12.3 TW over the past decade [7]. Of this energy demand, 80 % is generated by some form of combustion process [7].

Climate change is now widely accepted[1] to be a critical international issue. The 'Paris Agreement' on climate change was adopted on the 12th December 2015 and as of August 2016 has been signed by 180 countries [8]. One of the key aims of this agreement is limiting the global average temperature rise to less than 2 °C above pre-industrial levels by reducing the global emission of greenhouse gases. CO_2 emissions from combustion processes account for 60 % of the worldwide greenhouse gas emissions [9] and hence combustion efficiency is vital to the reduction in global emissions.

Recent changes in policy have led to a shift away from highly polluting forms of energy such as coal[2], towards 'green' renewable energy production[3]. Renewables currently provide just 3 % of world energy consumption [10], hence there will be a dependence on non-renewable forms of energy for many decades to come. Coupled with the finite nature of the world's fossil fuel reserves, improving the efficiency of combustion processes will have a key role to play in satisfying our increasing energy demands.

[1] at a governmental level

[2] The USA and China were largely responsible for a fall of 1.8 % in global coal consumption in 2015 [10].

[3] The share of world energy consumption provided by renewable sources has more than tripled in the past 10 years from 0.8 % to 2.8 % [10].

The chemical reactions that occur during combustion are dependent on not only the species and concentrations of the reactants, but also temperature and a wide variety of other environmental parameters including pressure and flow dynamics. Measurement of any of these parameters can offer an insight into the combustion process and inform the development of future fuels and engines for improvements in efficiency and emissions.

1.2. Thermometry

Temperature is a critical parameter in many aspects of the combustion process. For many applications the desired output is not heat but mechanical work, which can then be used to drive machinery or generate electricity. The relative temperatures of the input fluid, T_{hot}, and the environment, T_{cold}, define the maximum theoretical efficiency of any heat engine, the Carnot efficiency, η_{Carnot}, given by equation (1-1) [11].

$$\eta_{achievable} < \eta_{Carnot} = 1 - \frac{T_{cold}}{T_{hot}} \tag{1-1}$$

The desire to increase the 'hot' temperature of the working fluid to ever higher values in search of improving efficiencies can lead to extreme demands of the materials used in engine construction. Heat transfer to surfaces within an engine, such as the cooling requirements for gas turbine blades, is an active area of research [12].

Chemical reaction rates are often highly temperature dependent. Temperature typically affects both the frequency of collisions and, for reactions with an activation energy, the fraction of collisions which are 'successful' in overcoming the energy barrier to allow the reaction to proceed. This exponential temperature dependence is described by the Arrhenius equation,

$$k = Ae^{-\frac{E_a}{k_B T}} \tag{1-2}$$

where k is the rate constant for the reaction, E_a is the activation energy, k_B is Boltzmann's constant and T is temperature. The scaling factor 'A' is typically assumed to be independent of temperature, although for analysis of data over a wide range of temperatures it can be useful to include a temperature dependence of the form T^n as an additional multiplicative factor [13].

Knowledge of the temperatures within an engine is therefore an important factor in predicting the performance, efficiency and lifetime of the system.

1.3. Optical diagnostics

Thermometry techniques range from simple physical probes such as thermocouples to optical diagnostics involving multiple lasers and cameras. The motivation behind the development of complex and costly optical techniques is twofold.

Firstly, while highly suited to thermometry of solid, stationary engine components, physical probes are invasive and perturb the temperature of the working fluid. This limits the accuracy of such techniques [14]. Optical diagnostics can be entirely non-invasive by simply collecting light emitted by the combustion process itself [15]. Most are however minimally invasive and involve applying small perturbations to the medium, often in the form of laser pulses, to excite or scatter light from species within the flow. The resulting emitted or scattered light is collected and analysed to derive the parameters of interest.

Secondly, combustion occurs in 3 dimensions and so point measurement techniques provide a very limited view of the likely inhomogeneous temperature distribution throughout the engine. Optical diagnostics have the potential for performing linear, planar or even volumetric measurements.

1.4. Internal Combustion engines

There were 36 million vehicles on the road in the UK in 2014 [16], approximately one vehicle for every two people [17]. This is a trend reflected around the world as road transport accounts for 17 % of the global CO2 emissions from fossil fuel combustion [9]. The latest EU standard ‘Euro 6’ sets out stringent limits on harmful emissions from road vehicles [18] (CO, NOx, THC, PM, PN – carbon monoxide, nitrogen oxides, total hydrocarbons, particulate mass, and particulate number respectively). Meeting these standards requires careful engine design and optimisation.

In-cylinder temperatures have a significant effect on the combustion efficiency and the production of particulates i.e. soot [19]. Even small temperature changes can have significant effects on the overall combustion, as localised hot spots of just 5 % difference to the bulk temperature are correlated with knock [4] [20]. Accurate and precise diagnostic techniques for liquid fuel combustion, capable of performing spatially and temporally resolved measurements play a vital role in improving theoretical models of combustion and contribute to the design of future fuels and engines. Such improvements in understanding the fundamental physical and chemical processes involved and subsequent increases in efficiency and reduction of harmful emissions will help to minimise the environmental impact of hydrocarbon combustion.

1.5. Structure of thesis

This introductory chapter explores the motivation for improving the capability of thermometry in engines.

Chapter 2 presents a brief introduction to the operating principles of spark-ignition internal combustion engines, along with a summary of the terminology in common usage throughout the engines community and adopted in this thesis.

Chapter 3 summarises the main optical techniques of relevance to combustion engine diagnostics and reviews the relevant literature, focussing on techniques with potential for thermometry.

Chapter 4 describes the theory and application of the Laser-Induced Thermal Grating Spectroscopy (LITGS) technique for in-situ calibration measurements. The implications of potential analysis methods for the accuracy of in-cylinder thermometry are discussed.

[4] Undesirable auto-ignition of the fuel-air mixture before the intended ignition timing, leading to a reduction in power output and potentially engine damage.

The selection of Two-Colour detection Planar Laser-Induced Fluorescence (TC-PLIF) as the technique for 2-dimensional in-cylinder thermometry is discussed in chapter 5. The background theory, initial development, methods of analysis and results of validation tests are presented.

Chapter 6 presents the results of combining TC-PLIF and LITGS techniques for in-situ calibrated 2D thermometry. The effects of varying fuel composition and injection strategy on the in-cylinder temperature distributions are described and sources of inaccuracy investigated.

The development of an extension of the LITGS technique for 1-dimensional time-resolved thermometry is presented in Chapter 7 and compared to that of previous publications. The application of the technique to single-shot measurements of thermal boundary layers in flows near surfaces is reported.

Chapter 8 summarises the achievements of this work, while the potential for future extensions to the techniques described in this thesis is discussed in chapter 9.

The appendix provides further discussion on improvements to analysis methods for LITGS thermometry, referred to in chapter 4.

2. Optical Internal Combustion Engine

In this chapter a brief introduction to internal combustion (IC) engines is given in section 2.1, covering their principles of operation, thermodynamic efficiency and fuel injection strategies. A summary of relevant engine-related terminology is provided in section 2.2. The optical engine and operating conditions used throughout this work are discussed in section 2.3.

2.1. Internal Combustion Engines

This chapter serves to provide a brief introduction to internal combustion (IC) engines, sufficient for understanding of the development of the optical diagnostic techniques discussed in later chapters. For further in-depth explanations of the field, the reader is referred in the first instance to an excellent textbook [21] and recent review of the field [22].

The operating principle of reciprocating IC engines is based around combustion of a fuel-air mixture to raise the temperature and pressure of gases within a sealed chamber[5] (the cylinder). One wall of the chamber is free to move (the piston) and the high pressure gases do work as they expand and displace this piston. This linear motion of the piston is coupled to the crankshaft via a connecting rod, generating rotational motion which can then be used to drive machinery or generate electricity. In order to provide a useful source of work IC engines must be able to repeat this process by dealing with the exhaust of combustion products and the intake of fresh fuel-air mixture.

[5] Hence the name 'internal combustion'.

2.1.1. Gasoline vs Diesel

There are a variety of designs of IC engine, of which 'gasoline/petrol' and 'diesel' are the most familiar, being found in the vast majority of road vehicles[6]. Gasoline, or more generally 'Spark ignition' (SI), engines typically mix fuel and air into a homogeneous charge before the mixture is compressed and ignited by application of a spark. In contrast, diesel engines use compression ignition (CI) in which fuel is not introduced until the air has already been compressed. The hot compressed gas ignites the fuel immediately after injection without the need for a spark.

The optical diagnostics of this work were developed on a gasoline engine. While it is possible to apply optical diagnostics to both gasoline and diesel engines, in practice it is easier in gasoline engines due to the lower in-cylinder pressures and the ability to use a flat piston crown window for ease of optical access. This chapter will therefore focus on spark ignition.

2.1.2. 4-stroke engines

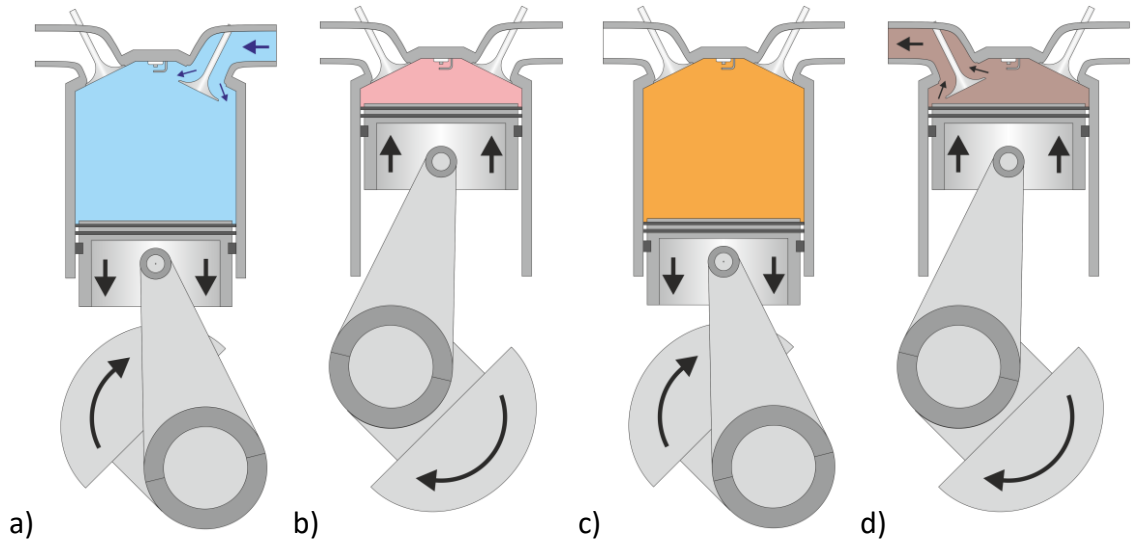

Figure 2-1 4-stroke cycle stages. a) Intake, b) Compression, c) Expansion, d) Exhaust.

The four stages of a four-stroke cycle are depicted in Figure 2-1. The intake stroke (a) draws a fresh mixture of fuel and air into the cylinder through an inlet valve typically at the top of the cylinder. This mixture is then compressed during the compression stroke (b). Just before the end

[6] Mazda's RX line of sports cars are a notable exception due to their use of the Wankel pistonless rotary engine which contains no reciprocating parts.

of the compression stroke a spark ignites the mixture causing a rapid increase in both temperature and pressure. The high pressure does more work on the piston during the expansion stroke (c) than was applied to the gas during the compression stroke, resulting in a net output of work by the engine. The exhaust stroke (d) expels the combustion products, returning the engine to its initial state ready for the following intake stroke.

2.1.3. Otto cycle

The operation of a spark ignition engine is often idealised as a thermodynamic cycle for ease of explanation and derivation of its thermodynamic efficiency, in this case the Otto cycle [Figure 2-2]. The intake (green) and exhaust (blue) strokes are included on the P-V diagram of Figure 2-2 solely for ease of identification of the 4-stroke cycle. The thermodynamic Otto cycle is defined by the upper loop between points 1 to 4.

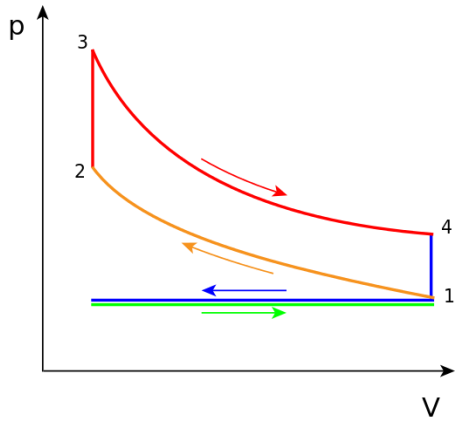

Figure 2-2 Pressure-Volume diagram[7] for the Otto cycle [23] **covering points 1-4, with the addition of the exhaust and intake stroke at constant pressure as required for a 'real' 4-stroke engine cycle.**

The compression stroke in the Otto cycle (1 → 2) is assumed to be isentropic[8]. The ratio of the maximum, V_1, and minimum, V_2, volumes of the compression stroke defines the compression ratio of the engine, r_V:

$$r_V = \frac{V_1}{V_2} \tag{2-1}$$

[7] User: Luc1992, https://commons.wikimedia.org/wiki/File:P-V_Otto_cycle.svg, © CC-BY-SA-4.0

[8] I.e. there is no heat transfer between the gas and the engine walls and the process is reversible.

Ignition occurs at point 2 and is assumed to be rapid such that the pressure associated with the heat input rise occurs at constant volume (2 → 3). The expansion stroke (3 → 4) is again isentropic, followed by the pressure loss and rejection of heat as the exhaust valves open (4 → 1).

The efficiency of the Otto cycle is defined as the ratio of work output to heat input. Treating the fuel-air mixture as an ideal gas such that the ideal gas law ($PV = Nk_BT$) holds and using the fact that PV^γ is a constant for an isentropic process[9], this efficiency, η_{Otto}, may be expressed solely in terms of the engine's compression ratio:

$$\eta_{Otto} = \frac{Work\ output}{Heat\ input} = 1 - \frac{1}{r_V^{\gamma-1}} \tag{2-2}$$

Increasing the compression ratio of an engine therefore results in a higher theoretical efficiency. As compression ratios increase, the maximum pressures and temperatures also increase. This places engineering limitations on achievable compression ratios before engine damage through overheating or auto-ignition (knock) begin to occur. Typical compression ratios for SI engines are of the order of 10 : 1, resulting in theoretical Otto-cycle efficiencies of around 60 %. In practice the variation of γ with temperature, heat transfer between the gases and engine components, finite combustion speed and frictional losses combine to reduce the idealised Otto efficiency of a SI engine by half, around 30 % for a compression ratio of 10 : 1 [21].

SI engines for road vehicle use must have variable power output. By restricting the airflow into the cylinder (throttling) and injecting less fuel to maintain stoichiometry, the power output can be reduced. Restricting the airflow lowers the pressure in the intake manifold, increasing the work required of the piston during the intake stroke. The increase in 'pumping losses' therefore reduces the efficiency of the engine whenever the throttle is partially closed.

[9] Where γ is the ratio of specific heat at constant pressure, c_P, to the specific heat at constant volume, c_V.

2.1.4. 2-stroke engines

It is possible to arrange the design of the engine such that a power stroke is delivered for every rotation of the crankshaft, instead of once every two revolutions. This is known as a 2-stroke engine and combines the four stages of the four-stroke cycle into just two strokes of the piston. For a given power output a two-stroke SI engine will be smaller than a four-stroke, making it a popular choice where size and weight are an issue[10]. Fuel efficiency is however typically lower for 2-stroke engines due to the simultaneous intake and exhaust gas flows leading to partial mixing[11]. This leads to a richer than stoichiometric fuel-air mixture being required to ensure reliable combustion which results in lower fuel efficiency [21]. The optical engine of this work uses a four-stroke cycle, hence 2-stroke operation will not be given further consideration.

2.1.5. Gasoline Direct Injection

Gasoline Direct Injection (GDI) as the name suggests injects fuel into the cylinder[12]. This has seen increased application in production vehicles due to a number of benefits over the older method of Port Fuel Injection (PFI) which injects fuel upstream of the intake ports of a cylinder.

GDI leads to 'charge cooling', where the latent heat for vaporisation of the fuel is supplied by the bulk gas in the cylinder. This reduces the temperature of the fuel-air mixture by typically 30 K and as a result, the volumetric efficiency[13] of the engine is increased by around 5 % [4]. Additionally the reduction in final temperature enables the use of a slightly higher compression ratio without initiating knock. Both of these factors combine to improve the efficiency of the engine.

[10] Such as handheld machinery or light motorcycles.

[11] As well as some loss of fresh charge into the exhaust system.

[12] Typically during the intake stroke to allow time for mixing to form a homogeneous fuel-air mixture.

[13] The volumetric efficiency of an engine describes how effective the intake stroke is at drawing air into the cylinder. More air allows more fuel to be burned per cycle, increasing the maximum power output of the engine. It is defined as the ratio of the mass of air drawn into the cylinder per cycle, to the mass of air required to fill the cylinder at ambient pressure and temperature. By this definition, the volumetric efficiency can be over 100 % for effective intake pressures above 1 atm.

The high level of control over the timing and quantity of injected fuel with GDI also allows for novel injection strategies such as injecting twice per cycle [24]. This allows preparation of an overall lean homogeneous mixture with one 'early' injection during the intake stroke, followed by a second 'late' injection during the compression stroke to provide a stratified charge locally rich around the spark plug for ease of ignition. It is also possible to inject additional fuel during the expansion stroke to undergo additional combustion and raise the temperature of the exhaust gases. This is beneficial during the initial warm-up stage of the engine as it reduces the time taken to heat the catalytic converters of the exhaust system to their operating temperature for effective reduction of emissions.

2.2. Terminology

The field of internal combustion (IC) engines has many well-established acronyms and terminology which will be referred to throughout this thesis. In addition to the comprehensive table of acronyms at the start of this thesis, the most relevant engine acronyms are presented here for convenience of the reader.

TDC 'Top-Dead-Centre'. The highest position of the piston resulting in the smallest in-cylinder volume. There are therefore 2 'TDC' events within a single 4-stroke cycle, at the end of both the compression and exhaust strokes.

CAD 'Crank Angle Degrees'. The two rotations of the crankshaft during a 4-stroke engine cycle are divided into 720 degrees. This allows the timing of engine events to be referred to in relation to a 'Crank Angle' (i.e. angular position) of the crankshaft. This work will follow the convention of [3] in labelling the TDC at the end of the compression stroke as '0 CAD'.

BTDC 'Before-Top-Dead-Centre'. Usually preceded by a value in CAD, BTDC describes an event that occurs before the piston reaches TDC[14].

[14] E.g. the compression stroke begins at 180 CAD BTDC and finishes at TDC.

ATDC ‘After-Top-Dead-Centre’. Usually preceded by a value in CAD, ATDC describes an event that occurs after the piston reaches TDC[15].

EGR ‘Exhaust Gas Residuals’. The finite volume at the end of the exhaust stroke results in some of the combustion products (EGR) remaining in the cylinder to mix with the fresh charge of the next cycle. Not to be confused with ‘Exhaust Gas Recirculation’[16], a technique to deliberately increase the amount of EGR within the cylinder.

GDI ‘Gasoline Direct Injection’. Air is drawn in to the cylinder during the intake stroke and fuel is injected ‘directly’ into the cylinder to form the desired fuel-air mixture.

PFI ‘Port Fuel Injection’. Fuel is injected into the manifold before the intake valve and the fuel-air mixture is then drawn into the cylinder during the intake stroke.

φ ‘Fuel-air equivalence ratio’. The proportion of fuel to air compared to that at stoichiometric conditions[17]. Excess fuel (‘rich’ conditions) will give $\varphi > 1$.

λ ‘Lambda’. The inverse of the fuel-air equivalence ratio (i.e. an air-fuel equivalence ratio). Excess oxygen (‘lean’ conditions) will give $\lambda > 1$.

2.3. Optical Engine

Bore × Stroke	89 × 90.3 mm
Displacement	562 cm^3
Valves per Cylinder	2 intake, 2 exhaust
Compression Ratio	11.1
Fuel Pressure	150 bar
Injector	Bosch Multi-hole Nozzle
Valve Timing (CAD ATDC)	IVO 34, IVC 242, EVO 475, EVC 5

Table 2-1 Optical engine specifications as detailed in [25] (c.f. List of Acronyms).

[15] E.g. the expansion (power) stroke begins at TDC and finishes at 180 CAD ATDC.

[16] Often also referred to as ‘EGR’, though not in this work.

[17] Stoichiometry refers to the exact balance by number of carbon, hydrogen and oxygen atoms in the fuel-air mixture (reactants) to undergo complete combustion to carbon dioxide and water (products).

The optical engine providing the platform for the development of the optical diagnostic techniques is based on a Jaguar AJ133 5.0 L V8 engine. Launched in 2009 to replace the existing 4.2 L V8, the AJ133 provides 30 % more power[18] with a 6 % reduction in specific fuel consumption and with improved emissions to meet the latest Euro 5 standards [26].

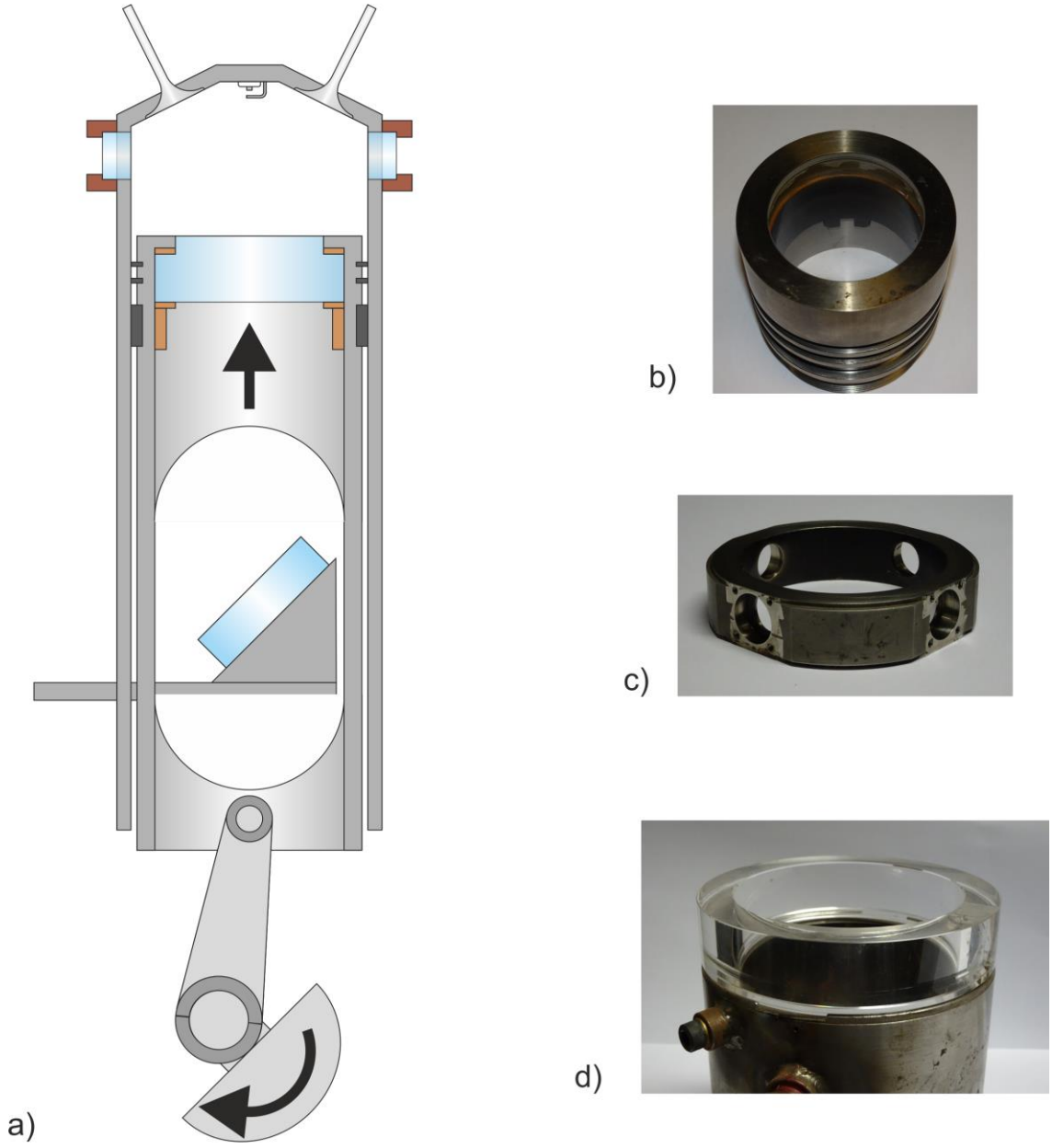

Figure 2-3 a) Cross-section of optical engine layout showing Bowditch piston, piston crown window (b) and optical access annulus (c). b) Optical access piston with window. c) Optical access cylinder section (annulus) with four window ports. d) Quartz annulus resting on water-cooled cylinder section.

[18] 385 hp when naturally aspirated, or 510 hp for the supercharged version.

The optical engine of this work is a single-cylinder engine[19] with an extended 'Bowditch' piston[20], which enables optical access through a window in the reciprocating piston via a stationary 45 degree mirror within the void between the piston supports [Figure 2-3 a), b)]. A window in the side of the 'pent-roof'[21] provides single-sided optical access to the small volume of the cylinder remaining at TDC which also contains the spark plug, fuel injector, inlet valves and exhaust valves [Figure 2-4]. Optical access from the sides of the barrel is either provided by a steel annulus at the top of the barrel with four flat quartz windows of 16 mm clear aperture [Figure 2-3 c)], a quartz annulus at the top of the barrel providing 360° of optical access over a height of 29 mm [Figure 2-3 d)] or a full-length quartz barrel providing 360° of optical access over the entire barrel height. While the fully quartz components provide dramatically increased optical access compared to the steel annulus, they are far less durable[22] and add the complication of curved surfaces to any imaging setup.

In the interests of being able to reliably fire the engine for long enough periods to perform the desired optical diagnostics[23], the steel annulus was selected for use throughout this work. The piston rises past the four side windows of the annulus at around 45 CAD BTDC, hence measurements requiring side optical access may not be performed within 45 CAD either side of TDC.

[19] I.e. one of the 8 cylinders of the AJ133.

[20] The 'Bowditch' piston was proposed by Fred Bowditch in 1961 as an alternative to the existing L-head designs where the valves were mounted in the cylinder walls to permit overhead optical access via a window in the cylinder head. The Bowditch piston allowed for a more 'realistic' overhead valves design, providing a better representation of production engines.

[21] The triangular prism shaped recess within the cylinder head which combined with the barrel and piston crown forms the boundary of the engine cylinder.

[22] This limits the engine operating conditions which may be studied using the full quartz components.

[23] 2 – 5 minutes at a time.

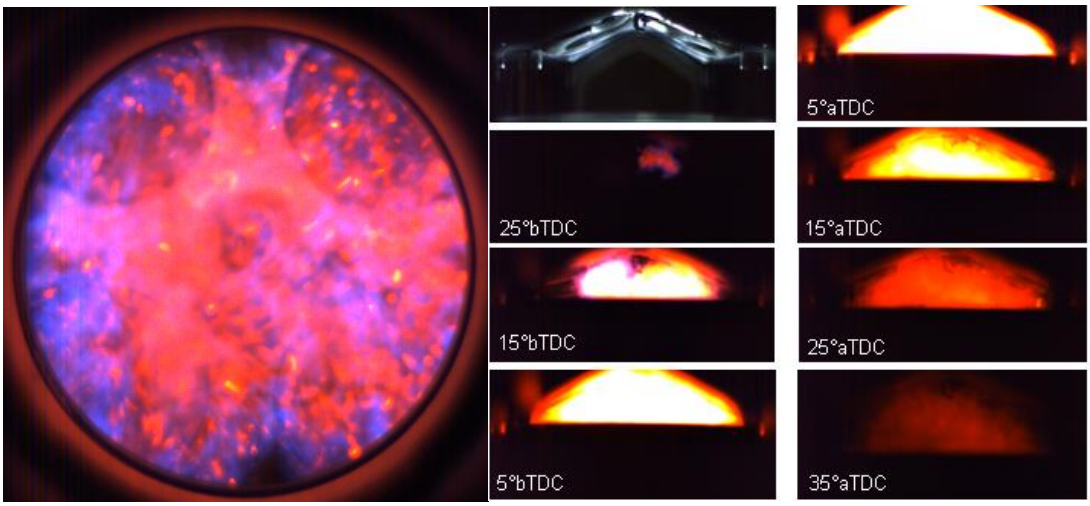

Figure 2-4 (Left) Image of in-cylinder combustion taken from below through the quartz window in the piston crown. The pair of inlet valves are illuminated by the combustion and are visible at the top of the image. (Right) Preliminary combustion imaging of the pent-roof region using the new quartz barrel section [chapter 9]. The spark plug electrodes are visible in the static engine image. [Images taken by B. Scott c.f. acknowledgements].

2.3.1. Operating conditions

Since this work focusses on the development of an optical diagnostic technique, the operating conditions of the engine were typically held constant at the values detailed below.

The air intake of the engine was heated to 313 K to ensure the full evaporation of toluene injected into the airflow before the cylinder under PFI operation. The flow rate was maintained at a low 1.78 ± 0.02 Ls^{-1} in order to avoid high peak pressures within the cylinder at TDC which increase the risk of failure for the quartz components.

Cooling water circulating around the cylinder head and the barrel prevented the engine overheating while running and was maintained at 293 K.

The engine speed was set to 1200 rpm[24]. With 2 crankshaft rotations in a four-stroke engine per cycle, this corresponds to 10 four-stroke cycles per second. The cameras used for recording Laser-Induced Fluorescence (LIF) images, being limited to an acquisition rate of < 1.5 Hz, could be triggered at 1 Hz to capture an image every 10 cycles.

[24] Actually 1185 rpm to avoid a peculiarity with the Surelite pump laser being unable to be triggered at 'exactly' 10 Hz.

The crankshaft of the optical engine is connected to a dynamometer which may be run as an electric motor to drive the crankshaft and cause the piston to reciprocate (referred to as 'motored' operation). Alternatively it may be run as a generator to provide resistance and allow the engine to do work while firing with fuel injection and ignition (referred to as 'fired' operation). Clearly 'fired' operation is the more realistic condition of interest, however 'motored' operation provides a useful, simpler reference condition for development of the diagnostic techniques.

The engine has an injector installed both in the pent-roof of the cylinder for GDI operation and before the inlet valve of the cylinder for PFI operation. Selection of either PFI or GDI operation is controlled by the user via the engine timing and control software and both were used in this work for motored and fired operation.

The standard fuel used in this work was a 2-component blend of 70 % iso-octane and 30 % toluene by volume[25], a '70/30 blend'. '50/50' and '90/10' blends were also used in chapter 6.

[25] The selection of this particular fuel composition is discussed in chapter 6.

3. Literature Review

This chapter presents a review of the literature for thermometry in internal combustion engines. An overview is given of physical (3.1) and optical (3.2) thermometry techniques, which are themselves divided into the categories of linear (3.3) and non-linear (3.4) optical methods. The linear techniques discussed include absorption spectroscopy (3.3.1), Rayleigh scattering (3.3.2), Raman scattering (3.3.3), thermographic phosphors (3.3.4) and Laser-Induced Fluorescence (3.3.5). Nonlinear techniques considered include Coherent Anti-Stokes Raman Spectroscopy (3.4.1), Polarisation Spectroscopy (3.4.2), Degenerate Four Wave Mixing (3.4.3) and Laser-Induced Grating Spectroscopy (3.4.4). This chapter concludes with section 3.5 which details the selection of the techniques for in-situ calibrated 2-dimensional thermometry whose development in this work is discussed in chapters 4 and 5.

3.1. Engine diagnostics

Research and development of engine technology is often the primary aim for cutting-edge diagnostic techniques [22]. As engines become ever more complex, the level of detail required from diagnostic measurements increases. High-speed imaging is one current trend, given its ability to follow the evolution of scalar or vector fields throughout a single engine cycle [27]. However, there is also a requirement for robust sensor technology to enable closed-loop control of engine systems [28].

This chapter will review potential techniques for thermometry of gas mixtures with the aim of selecting techniques with which to perform accurate, time-resolved measurements of 2-dimensional in-cylinder temperature distributions.

Physical probes such as thermocouples are by their very nature an invasive measurement technique and do not accurately report the ‘true’ temperature of the gas which would be observed in the absence of the probe [29]. Corrections must be made for both heat transfer between the thermocouple and the gas and any catalytic effects in reacting flows in an effort to

improve the accuracy of the measurement. These corrections will depend on the dynamics, temperature and composition of the flow [14] yet for complex flows such corrections will not be able to provide an effectively non-invasive measurement.

In IC engine research, thermocouples are typically used for temperature measurements at surfaces e.g. the piston surface [30]. The reciprocating nature of the engine ensures that even disregarding or correcting for their invasive nature, measuring the spatial distribution of gas temperatures within the cylinder, the target of this work, is not practically possible with physical probes. Therefore optical techniques are considered in this work.

3.2. Optical diagnostics

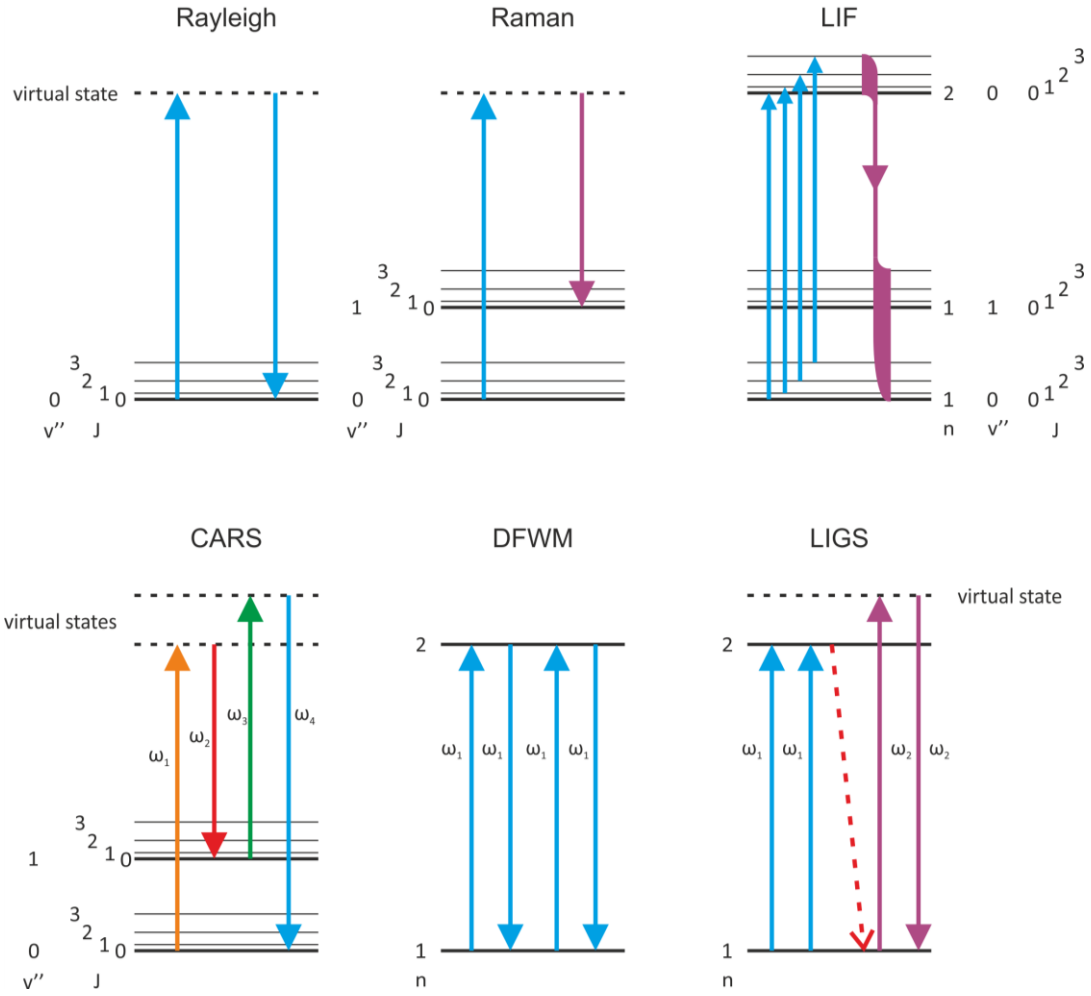

Figure 3-1 Energy level diagrams for optical diagnostic techniques discussed in this chapter showing radiative (solid lines) and non-radiative (dashed lines) transitions. For details of each technique the reader is referred to the relevant section of this chapter: Rayleigh (3.3.2), Raman (3.3.3), LIF (3.3.5), CARS (3.4.1), DFWM (3.4.3) and LIGS (3.4.4).

The field of optical diagnostics, even restricted to those applied to combustion environments, is very wide and has been the subject of a number of excellent reviews. These range from broad overviews of the field [31], [32], [33] to those focusing on a subset of techniques [34], [35], [36] or specific applications [37], [38], [39]. For a complete overview of optical diagnostics for combustion applications the reader is directed to the above texts and the references within. This chapter focuses on a review of only those techniques with potential for thermometry.

Optical diagnostics typically measure gas temperatures in one of two ways. The density of the gas may be measured and combined with an equation of state to derive temperature such as in Rayleigh scattering[26]. Alternatively, the population distribution across energy levels of the molecules is probed and used to infer temperature directly such as in Two-Line Atomic Fluorescence or Four Wave Mixing (FWM) techniques.

When discussing optical diagnostics, a distinction is commonly made between so-called 'linear' and 'non-linear' techniques. This nomenclature arises from the interaction of the electric field of the light with the medium under investigation. 'Linear' techniques can be considered as an interaction between the medium and a single incident photon, such as absorption of a photon by a molecule in absorption spectroscopy. 'Non-linear' techniques require the interaction of multiple photons with the medium simultaneously, as described by the higher order terms of the induced polarisation of a medium, P(ω), for application of an electric field, E(ω),

$$P(\omega) = \varepsilon_0\left(\chi_e{}^{(1)}E(\omega) + \chi_e{}^{(2)}E(\omega)^2 + \chi_e{}^{(3)}E(\omega)^3 + \cdots\right) \tag{3-1}$$

where ε_0 is the permittivity of free space and $\chi_e^{(n)}$ are n^{th} order terms in the expansion of the electric susceptibility of the medium 'χ_e'.

For gases the second order term $\chi_e^{(2)}$ is zero[27], resulting in the lowest order non-linear term being $\chi_e^{(3)}$ which facilitates the mixing of the electric fields of 3 incident photons (E_1 ,E_2 and E_3) to

[26] Or indeed Laser-Induced Thermal Grating Spectroscopy (LITGS) which measures density perturbations in the form of acoustic waves.

[27] This is true for all media which have inversion symmetry [236].

induce a polarisation which radiates a 'signal' photon (E_4). This gives rise to the name 'Four Wave Mixing' (FWM) used to describe the class of non-linear techniques which make use of this $\chi_e^{(3)}$ term. Each higher order $\chi_e^{(n+1)}$ term is many orders of magnitude smaller than the previous $\chi_e^{(n)}$. Non-linear effects are therefore only seen for very high field strengths[28] or when resonantly enhanced and higher-order effects than FWM are not typically observed.

3.3. Linear optical diagnostic techniques

This section reviews the 'linear' optical diagnostic techniques which have potential for thermometry in IC engines. Linear techniques typically involve the absorption or scattering of an incident photon[29]. Information is gained either from the reduction in transmitted intensity or collection of the scattered or emitted light.

3.3.1. Absorption spectroscopy

Absorption spectroscopy investigates properties of a medium by recording the transmitted intensity of a probe beam through the medium in question [40]. These measurements are however limited to integrated measurements along the optical path of the beam. Tomographic reconstruction for 2-dimensional measurements using multiple beams has been applied in SI engines [41] and jet engine exhausts [42]. The number of effective measurement points is related to the number of beams and therefore typically results in poorer spatial resolution than planar techniques such as Planar-LIF (PLIF) for a given field of view.

Each molecule has a characteristic set of transitions which acts as an identifying fingerprint, permitting species detection. The relative absorption strengths of these transitions are affected by the temperature-dependent Boltzmann population of the levels involved and hence can be used for thermometry. In gases the transitions will have their fundamental 'lifetime' or 'natural' linewidths broadened by the pressure-dependent rate of collisions and the temperature-dependent velocity distribution of the molecules.

[28] I.e. high laser pulse intensities.

[29] Though not for passive techniques such as chemiluminescence.

The absorption of light as it passes through the medium will in part be governed by the detuning between the laser frequency (ω_L) and the centre frequency of the transition (ω_0) and will be strongest on-resonance ($\omega_L = \omega_0$). Scanning the probe laser wavelength will record the absorption spectrum of the medium. The width and locations of the transition lineshapes allow for the measurement of various parameters of interest.

Use of the lineshapes for barometry or thermometry relies heavily on the accuracy of theoretical models for the lineshapes in question. HITRAN is a database compiling spectroscopic data for a wide variety of molecular species at a reference temperature of 296 K [43]. The high temperature analogue, HITEMP, is perhaps more relevant to combustion and contains many more transitions for typical combustion products [44] (H_2O, CO_2, CO, NO, OH). As discussed in the Tunable Diode Laser Absorption Spectroscopy (TDLAS) review of 2015 [40] both databases are however, not fully comprehensive or error-free, in particular for the broadening of transitions. Reliable investigations therefore currently require measurement of the absorption spectra of interest under controlled conditions [45].

Reliable tuneable diode laser sources below 300 nm are not available [40]. Elemental spectroscopy, which requires UV wavelengths, must therefore be carried out by taking advantage of nonlinear optical techniques such as harmonic, sum or difference frequency generation [46]. This increases the cost and complexity of the otherwise compact TDLAS system.

Multi-Mode Absorption Spectroscopy (MUMAS)

Typical TLDAS applications have tuning ranges limited to ~ 100 GHz, often limiting composition measurements to the detection of single species. This can be overcome by multiplexing several TDLAS systems at the expense of increased cost and complexity. An alternative approach is to use a multi-mode laser which, when scanned, in effect multiplexes many single mode TLDAS measurements using only a single laser and detector and achieves ~ 250 GHz scanning range [47].

This technique has been successfully applied to temperature, pressure and oxygen number density [48], to methane detection at 25 ppm sensitivity [49], to simultaneous detection of acetylene, nitrous oxide and carbon monoxide [50], and to methane, acetylene and formaldehyde [51]. MUMAS has also been applied to IC engine diagnostics, performing simultaneous measurements of CO_2 and CO number densities in exhaust gases [52]. MUMAS shares the line-of-sight limitation of TDLAS, therefore was not considered for this work.

3.3.2. Rayleigh scattering

Light is elastically scattered from molecules by the electric field inducing an oscillating polarisation of the molecule, which then radiates light in different directions. For molecules and particles whose diameter is much smaller than the wavelength of the incident light this is called Rayleigh scattering. Rayleigh scattering has an intensity proportional to $1/\lambda^4$ making the scattering of shorter wavelengths much more efficient.

For larger particles the Mie scattering dominates[30] [53]. Mie scattering is only weakly dependent on wavelength and predominantly scatters in the forward direction with respect to the incident light[31]. Rayleigh scattering can therefore traditionally only be applied to zero-particulate 'clean' environments such as premixed flames [54]. One option for application to IC engines is to replace the liquid fuel with a gas such as Freon-12 [32] to avoid droplet (Mie) scatter [36].

Elastic scattering does not exchange energy with the molecule, resulting in scattered light with the same wavelength distribution as the incident light. This makes Rayleigh scattering vulnerable to background scatter off surfaces, especially in confined environments like IC engines with time-varying background scatter from moving parts.

[30] As a rough guide, where the diameter is λ/10 or larger. Mie cross sections for such species can be 10 to 20 orders of magnitude larger than for Rayleigh scattering.

[31] The distribution of intensity for Rayleigh scattering is such that the forward- and backward-scattered intensities are of equal magnitude.

[32] Dichlorodifluoromethane (Freon 12) has a high Rayleigh scattering cross-section which produces strong signals and a high density relative to air much like hydrocarbon fuels.

Filtered Rayleigh Scattering offers a potential solution in exchange for a reduction in signal intensity. Scatter from the gas-phase target molecules will be broadened with respect to large particles or stationary surfaces[33]. By selection of a bandpass filter which is both wide enough to block all un-broadened scattered light but narrow enough to transmit the wings of the broadened scattered light, the desired contribution from the gas-phase can be isolated [55]. This technique permits Rayleigh scattering measurements in sooting flames, achieving 10 – 15 % precision for single-shot 2D thermometry [56].

Scatter from hydrocarbons is much larger than air (water, oxygen and nitrogen), so variation in fuel composition in IC engine mixtures will strongly bias resulting temperature[34]. It is possible to mitigate this issue by simultaneous measurement of composition with an independent technique, such that the composition at any point in the Rayleigh scattering image can be corrected for [57].

While there are many limitations preventing its application to some practical combustion systems, the thorough understanding of Rayleigh scattering has led to its use to calibrate a McKenna burner to define a high temperature standard with which to calibrate other, more complex optical diagnostics [58].

3.3.3. Raman scattering

Raman scattering, unlike Rayleigh scattering, is an inelastic scattering process, involving the exchange of energy between the incident photon and the scattering molecule. The ro-vibrational structure of the molecule can also introduce species-specific components shifted down (Stokes) or up (Anti-Stokes) in frequency. With an appropriate dispersive detection system a Raman scattering spectrum may be recorded and used to derive temperature from the relative intensities of the peaks arising from Boltzmann-populated ro-vibrational levels.

[33] Including Doppler and pressure broadening.

[34] Rayleigh scattering is insensitive to the species of scattering particles. While the species cross-section will affect the intensity of scattered light, this effect is indistinguishable from e.g. number density.

As Raman scattering arises from a first-order expansion of the polarizability, the scattering cross-section is approximately 3 orders of magnitude smaller than that of Rayleigh scattering[35] and also shares the $1/\lambda^4$ dependency. The correspondingly weak Raman signals makes the technique vulnerable to interference from Laser-Induced Incandescence (LII) of soot, chemiluminescence from flames and particularly for UV excitation, Laser-Induced Fluorescence (LIF) of other species[36].

Fast gating of the detection system using an electro-optical shutter can remove the longer-timescale interferences such as chemiluminescence and LII [59] but not the short-timescale LIF. Raman scattering preserves the polarisation of the incident light, whereas the internal transitions over the ns-scale fluorescence lifetimes for LIF do not. This can be utilised by recording two images through orthogonal polarisers and inferring the intensity of light with the same polarisation as the excitation pulse [60].

Raman scattering has been applied to measurements of composition in SI combustion engines [61], [62], [63] but is rarely used for thermometry in engines [64] having been supplanted in this specific application by the LIF and Coherent Anti-Stokes Raman Spectroscopy (CARS) techniques[37].

3.3.4. Thermographic phosphors

Thermographic phosphors are widely used for measurements of surface temperatures [65], [66], [30], [55] and can be used for thermometry using two approaches.

The first method records the temporal decay of the emission from the phosphor after excitation with a laser pulse. Phosphor emission is typically approximated by a single-exponential decay over time with a lifetime that decreases as temperature increases [66]. Phosphors are available

[35] Which arises from the zeroth order polarizability.

[36] A drawback to using the shortest possible wavelengths to take advantage of the $1/\lambda^4$ dependency.

[37] Typically LIF is used for 2-dimensional measurements, while CARS performs point-measurements.

that exhibit this decay over several 100 K and depending on the phosphor are suited for thermometry in low (> 200 K) through to high (< 1800 K) temperature environments.

Alternatively, there is often a shift in the emission spectrum with increasing temperature. This allows for time-integrated temperature measurements by taking the ratio of emission intensity in two spectral regions [67].

It is important to select the most appropriate detection method for each phosphor and situation. The lifetime method was found to be both more accurate and more precise[38] than the spectral intensity ratio method for Mg_4FGeO_6:Mn [65]. However its ms – μs range of lifetimes is too slow for application to fast-moving objects or for time-gating removal of background chemiluminescence in flames [67].

Phosphor thermometry is not limited to surface measurements. By seeding the intake air with thermographic phosphor particles, 2-dimensional thermometry within a firing IC engine has achieved precisions of < 5 % [68]. With a suitable choice of phosphor particle size it is even possible to perform Particle Image Velocimetry (PIV), returning measurements of both the temperature distribution and the velocity field within a single experiment [69], [70], [71].

3.3.5. Laser-Induced Fluorescence (LIF)

Laser-Induced Fluorescence utilises the absorption and emission characteristics of the target molecules to perform measurements of composition, temperature, pressure[39] and with appropriate combination of laser wavelengths and target molecules, LIF is species-specific. By illuminating the measurement region with a laser sheet and imaging the resulting fluorescence orthogonally onto a camera system, spatially resolved 2-dimensional measurements may be performed across the plane of the laser sheet. This gives rise to the common acronym ‘PLIF’ for Planar Laser-Induced Fluorescence.

[38] Above 650 K, more precise by over an order of magnitude.

[39] Via the number density or via pressure broadening of the absorption lineshapes.

Compositional LIF measurements

Being a resonant technique, the effective cross-section per molecule for LIF is larger than scattering techniques by as much as 10 orders of magnitude [32]. This high sensitivity has led to LIF being widely applied for quantitative detection of minor species in combustion as has been thoroughly reviewed [72]. PLIF has also seen application for imaging of fuel distributions inside IC engines, for high-speed crank-angle-resolved measurements [73], mapping of exhaust gas recirculation distributions[40] [74] and highly quantitative measurements [75], [76].

It is beyond the scope of this thesis to cover the wide field of LIF diagnostics. Instead the reader is directed to the many excellent reviews on the subject including the initial developments in LIF [77], LIF in combustion gases [78], LIF in flames [79] and LIF in supersonic and multi-phase flows [80], along with the more general reviews referenced in section 3.2. This section will focus on applications of LIF to thermometry, specifically for measurements of gas temperatures within IC engines.

The broad field of LIF may be separated into more focussed areas by the type of species targeted for excitation. For LIF tracers, the theoretical background, practicalities for diagnostics and the application to combustion environments is discussed in the comprehensive review by Schulz and Sick [81].

Two-Line Atomic Fluorescence (TLAF)

TLAF sequentially excites two transitions of different characteristic wavelengths sharing a common upper level in atomic tracer species [Figure 3-2 A)]. As a result of an excitation pulse at $\omega_{a\rightarrow c}$, the common upper level c) is populated to an extent dependent on the thermal population of the pumped lower level a). The subsequent fluorescence occurs on both

[40] This was however, not performed in a firing engine with 'real' exhaust gas. Instead the exhaust gas content was simulated by adding heated air to the cylinder during the intake stroke. Also note Exhaust Gas Recirculation (the deliberate reintroduction of gases to the cylinder) is not the same 'EGR' as Exhaust Gas Residuals (gases left in cylinder due to the non-zero volume at TDC) discussed in this work.

transitions. Emission at $\omega_{b\rightarrow c}$ to level b) can be spectrally separated from the pump scatter and recorded as a measurement of the initial thermal population of level a). In the same way, the thermal population of b) can be measured by an excitation pulse at $\omega_{b\rightarrow c}$ [Figure 3-2 B)]. The relative fluorescence intensities of the two measurements can therefore be used to derive temperature.

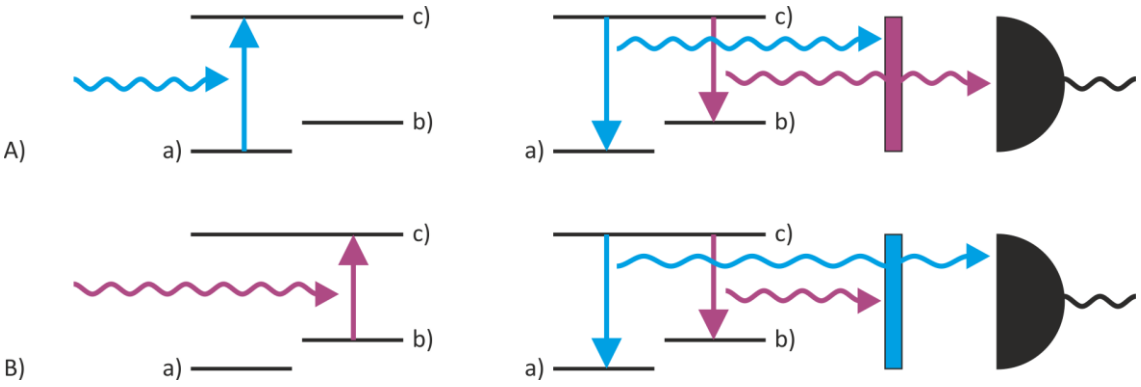

Figure 3-2 TLAF principles considering two transitions (a → c) and (b → c) sharing a common upper level c) for sequential measurement of the thermal populations of level 'a' (A) and 'b' (B). Transfer of population is represented by solid arrows, photon absorption/emission by wavy arrows.

One major advantage of TLAF is that owing to the use of a common upper level, the unknown quenching rate for each transition is identical and cancels during the derivation of temperature [82]. Absorption cross-sections are also many orders of magnitude higher for atomic transitions (of the order of 10^{-10} cm^2 [83]) compared to molecular transitions (of the order of 10^{-19} cm^2 [84], [85]). This permits very low seeding densities or excitation pulse energies for TLAF in comparison to other LIF techniques.

The drawback of TLAF for engine thermometry is that flame temperatures are typically required to break down the tracer compounds, often metal salts, to leave atomic species for excitation. Therefore TLAF is restricted to measurements of post-combustion gases.

The first demonstration of TLAF in-cylinder by Kaminski and Aldén [86], [87] covered a temperature range of 800 K – 2800 K and demonstrated a 14 % single-shot precision of thermometry at 2800 K. Molecular dissociation of $InCl_3$ seeded into the fuel (iso-octane) provided the atomic indium required for TLAF. Unlike LIF which typically requires UV

excitation and hence restricts the base fuel to non-fluorescing species, the 451 nm and 661 nm dye lasers used to excite the indium transitions do not induce fluorescence in the standard hydrocarbon fuel or combustion products.

A recent novel seeding method using Trimethylindium (TMI) in the gas phase instead of the traditional InCl and water solution introduced as droplets to the burner was reported [88] with the aim of minimising the perturbation of the flame chemistry caused by the seeding method. This was coupled with the application of cheap, compact and low-power diode lasers for 2D thermometry in [89] and represents both a reduction in invasiveness and an improvement in accessibility of the TLAF imaging technique.

Despite this recent advance and a reduction in decomposition temperature to 'only' 410 K, atomic tracers remain unavailable for the compression stroke gas temperatures of this work.

Radical (OH, CH, C_2) LIF

Radicals such as OH, CH and C_2 are created during combustion and have seen widespread use, particularly with OH, for thermometry at flame temperatures and imaging of flame fronts. A recent publication by Peterson et al. demonstrated the combination of OH-PLIF and Stereoscopic Particle Image Velocimetry (S-PIV) for 3-Dimensional, time-resolved flame propagation in an IC engine [90], demonstrating the significant capabilities of OH-PLIF as a diagnostic technique.

Much like TLAF however, radical fluorescence cannot be used to observe the gases before combustion and is therefore not suitable for the investigations of this work.

Laser-Induced Exciplex Fluorescence

Laser-Induced Exciplex Fluorescence (LIEF) uses two tracers, a fluorescing molecule 'F' and a quenching molecule 'Q'. By adjusting their relative concentrations, it can be arranged that emission from excited F* dominates in the gas phase, while emission from the exciplex formed by the combination of an excited F* and ground state Q dominates in the liquid phase [91]. This

makes it possible to perform LIF measurements in the liquid and vapour phases simultaneously. This work focusses on the temperature distribution of gases in the compression stroke before combustion, not multi-phase measurements, so LIEF will not be given further consideration.

Molecular tracer LIF

Unlike the sharply defined atomic transitions, more complex organic molecules such as ketones and aromatics have broad absorption and emission spectra where individual rotation-vibration transitions are no longer resolved. The spectral distribution or magnitude of absorption and emission for some of these molecules exhibit temperature dependence and hence may be utilised as a tracer for LIF thermometry. The four most common LIF tracers that have been sufficiently well studied for application to combustion thermometry are acetone [92], [84], [93], [94], 3-pentanone [94], [95], [96], [97], biacetyl, [98] and toluene [96], [5], [99], [100], [101], [97], [102].

The strong absorption of these tracers in the UV at commonly accessible laser wavelengths such as 248 nm, 266 nm and 308 nm, coupled with their stability in the low temperature pre-combustion gases make them promising candidates for investigation in this work.

1-colour total intensity thermometry

The total intensity of fluorescence signal recorded by molecular tracer PLIF measurements is dependent on a multitude of parameters, not only of the molecules and environment of interest but also of the excitation and detection schemes. Derivation of temperature from the spectrally integrated signal is challenging and requires the application of many correction steps to the raw images [103] while being restricted to applications with known, or at least homogeneous, tracer distributions.

The temperature dependence of the spectrally-integrated fluorescence intensity can be more sensitive than the spectral shifts utilised for the two-colour methods described in the following sections. This potentially allows the resolution of smaller changes in temperature such as the

perturbations to the in-cylinder temperature distribution caused by heat transfer to the walls [104].

For IC engines the tracer number density is likely to be inhomogeneous for many conditions of interest. The majority of PLIF thermometry in IC engines is therefore conducted using one of the two methods described below, which take advantage of the spectral dependence of either the absorption or emission of the tracer molecules.

2-line excitation thermometry

2-line excitation PLIF thermometry excites the tracer sequentially with laser pulses at two different wavelengths. As temperature increases, the thermal population of the LIF tracer molecules redistributes amongst the accessible ro-vibrational levels. This causes the absorption spectrum to change shape and typically shift towards longer wavelengths [84]. The relative absorption efficiency of the two pulses therefore changes as a function of temperature. The delay between the two pulses is kept sufficiently short to 'freeze' the gas motion, ensuring that the same molecules are involved in the absorption of both pulses. By taking the ratio of the two fluorescence signals, the technique becomes independent of tracer distribution and can therefore be used in inhomogeneous environments such as a gas burner [105].

First described by Großmann et al. [94], the selection of excitation wavelength for 2-line excitation PLIF has a significant effect on the temperature sensitivity as discussed by Einecke et al. [106] for the 350 K – 600 K range. Modelling of the fluorescence of 3-pentanone over the desired temperature and pressure ranges resulted in an improvement in precision by a factor of 2 to ± 2.1 % in [107], compared to precisions of ± 4 % [106] and ± 5 % [108] in similar work in IC engines. However, the headline precision of 2.1 % is a best-case value achieved at the end of the compression stroke and the precisions in fact varied between 2.1 % – 10 % over the –135 to –24 BTDC range of crank angles investigated.

2-colour detection thermometry

Two-colour detection PLIF (TC-PLIF) thermometry takes the signal ratio principle of 2-line excitation a step further by using a single excitation laser and relying on the temperature dependence of the tracer's emission spectrum. By comparing the ratio of fluorescence intensity emitted over two different spectral windows, a signal ratio is derived which is independent of any parameter which has the same value for both spectral windows including laser intensity profile, absorption cross-section and tracer number density.

TC-PLIF is therefore potentially even more robust than 2-line excitation PLIF due to its independence of laser parameters, removing any need to homogenise or quantify the intensity profile of each pulsed sheet. The trade-off for this robustness comes from the rejection of a large fraction of the fluorescence intensity that falls outside the spectral windows, resulting in much weaker signals for TC-PLIF than 2-line excitation PLIF. The characteristically low signal-to-noise ratios for TC-PLIF data can be observed in the thorough comparison of the 1-colour PLIF and TC-PLIF techniques applied to a motored IC engine [103].

Luong et al. [109] achieved a precision of 5.5 % for single shot TC-PLIF with toluene using a dichroic beamsplitter and Schott-WG series filters to spectrally separate the collected signal. The variation in signal ratio with temperature is significantly affected by the choice of filters as discussed in [110] and in chapter 5. Higher precision could potentially have been achieved had filters with sharper cut-offs been available. A precision of 1.7 % at 295 K to 5.3 % at 550 K was achieved using toluene TC-PLIF in a motored engine observing cold gas entrainment in [111]. This confirms that TC-PLIF is capable of higher precisions than those reported in [109], in particular as the upper precision limit in [111] at 550 K is capable of being reduced to 3.5 % with 10 x 10 pixel spatial averaging at the cost of some loss of spatial resolution.

LIF in fired engines

The challenges of operating PLIF diagnostics in optical engines often lead authors to perform measurements with motored engines (as above) or with simulation of 'fired engine' phenomena

such as using resistively-heated air [74]. Without combustion the in-cylinder conditions are comparatively stable with lower pressures and reduced thermal loading of optical components. 'Real' engines are, of course, fired, so the less common investigations into thermometry under fired operation such as for HCCI engines [112] and SI engines [108] provide valuable insights into phenomena which occur naturally in fired operation.

Particularly impressive fired SI engine results were achieved by Löffler et al. [113] with a full quartz barrel, permitting single-shot temperature and EGR concentration maps to be derived covering the full height of the cylinder. The high quality images presented were in part as a result of the use of a beam homogenizer [114], to minimise spatial variations in the intensity of the two pump sheets.

PLIF Calibration methods

For both 2-line excitation and TC-PLIF, conversion of the signal ratio to temperature requires calibration. This is often calculated from preliminary measurements in comparison with thermocouple data and as such it cannot account for any variation in environment between the calibration and experimental tests. TC-PLIF has been used to record temperature distributions of a seeded gas flow impinging on a cooled metal plate [115]. Care was taken to ensure the calibration and experimental conditions were as equivalent as possible, resulting in accurate measurements of the unsteady thermal boundary layer near the plate's surface.

In contrast, the TC-PLIF measurements of Luong et al. [109] were calibrated using spectroscopic studies in a static cell [85]. The accuracy of the derived temperatures is therefore dependent on the calibration remaining valid for the conditions inside the cylinder of the optical engine. The calibration (conducted in nitrogen at ambient pressure) will not account for any oxygen- or pressure-dependency of the fluorescence spectrum of the toluene-air mixture used for the engine experiments.

Toluene is strongly quenched by oxygen and any reduction in overall fluorescence intensity will leave the signal ratio of TC-PLIF, and therefore the derived temperature, unaffected. However, measurements by Koban et al. [99] for toluene excitation at 248 nm at 1 bar showed that toluene's emission spectrum redshifts with increasing oxygen number density for partial pressures up to 200 mbar. In the engine experiments reported in [109], for any given temperature the fluorescence of the toluene-air mixture will therefore be at longer wavelengths than expected from the calibration, resulting in a bias towards hotter reported temperatures. Indeed, both an isentropic calculation based on the in-cylinder pressure trace and a more sophisticated model which allows for heat transfer [97] report lower theoretical temperatures than the TC-PLIF measurements, particularly at higher pressures closer to TDC which are the conditions furthest from those of the calibration cell.

A more effective calibration approach was employed by Peterson et al. [111], in which the central 5 x 5 mm^2 region of the mean TC-PLIF images was calibrated to the temperatures derived from the pressure trace via an assumption of polytropic compression. Importantly the calibration was performed under identical conditions to the experiment. However, this approach reduces the TC-PLIF technique to an entirely relative measurement of temperature and relies entirely on the accuracy of the conversion of bulk pressure to bulk temperature. This may be reasonably accurate for motored operation given that, ignoring heat loss to the walls, the heating of the gas is solely due to compression. For fired operation where hot exhaust gas residuals will mix with the intake gases, a process that may well vary with different engine operating conditions, this is likely to be subject to greater uncertainty.

In-situ calibration with a simultaneous, independent thermometry technique would provide the most generally applicable calibration for the TC-PLIF signal ratio images. A point thermometry technique such as CARS or LITGS[41] would be able to impart its high accuracy to the TC-PLIF

[41] See section 3.4.1 and 3.4.4

temperatures via the generated calibration curve[42]. The simultaneous nature of the point-reference and TC-PLIF measurements would also allow the calibration to be 'updated' to track any changes in engine conditions, ensuring the accuracy of the calibration would be maintained throughout a set of experiments.

Structured Laser Illumination Planar Imaging (SLIPI)

Structured Laser Illumination Planar Imaging (SLIPI), recently reviewed in [116], offers the capability for a dramatic reduction in secondary scatter and other sources of background intensity from a laser scattering or fluorescence image. The principle is to use three pump sheets instead of one, each with a sinusoidal intensity profile imposed by a grating. Each resulting image represents a combination of the desired signal (direct scatter or fluorescence) with the background from multiple scattering events. Post-processing of the three images can then be used to remove the multiply scattered background.

SLIPI is extremely effective at improving the image quality of highly scattering environments such as TC-PLIF thermometry of GDI fuel sprays [117]. The focus of this work is to improve the accuracy of TC-PLIF measurements via in-situ calibration and will not be performing measurements in the vicinity of the GDI spray[43]. As such, the considerable time investment for application of SLIPI is not appropriate, although SLIPI could be introduced in future work investigating Late Direct Injection or thermometry during the intake stroke.

3.4. Non-linear techniques

This section reviews 'non-linear' optical diagnostic techniques which have potential for thermometry. Non-linear techniques typically involve the interaction of multiple photons to generate a signal photon via an induced third-order polarisation of the medium. The contributions to the signal throughout the interaction constructively interfere and produce a

[42] Precision would remain inherently dependent on the fluctuations in the TC-PLIF signal ratio images.

[43] Start of injection is typically 280 CAD BTDC for this work i.e. during the intake stroke. Fuel injection is therefore completed before the earliest TC-PLIF measurements at 90 CAD BTDC.

coherent signal only for the case where the beam geometries satisfy the phase matching condition $\Delta k = 0$. The coherent nature of the generated signal ensures that it propagates as a laser-like beam which aids in the rejection of background intensity by spatial filtering in comparison to the incoherent emission produced by linear techniques. Information is gained either from scanning or multiplexing the incident frequencies to produce a spectrum or from the temporal behaviour of the signal.

3.4.1. Coherent Anti-Stokes Raman Spectroscopy (CARS)

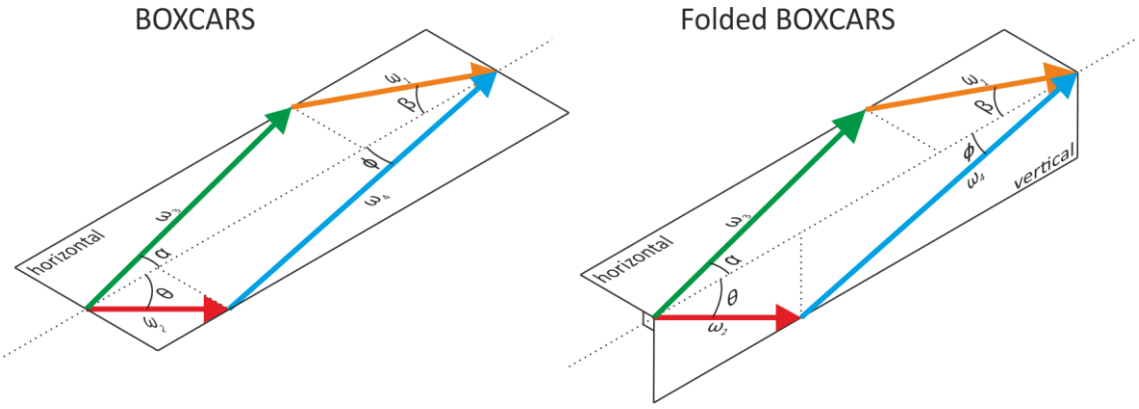

Figure 3-3 BOXCARS and folded BOXCARS geometries for CARS [118]**. Frequencies (ω1-4) and colour scheme corresponds to the transitions detailed in Figure 3-1.**

Coherent Anti-Stokes Raman Spectroscopy (CARS), subject of an excellent recent review [119], is a Four Wave Mixing (FWM) technique combining three incident beams at frequencies $\omega_1, \omega_2, \omega_3$ to generate a fourth at $\omega_4 = \omega_3 + \omega_1 - \omega_2$ where the difference in frequency between two of the incident beams corresponds to a vibrational or rotational 'Raman' transition: $\omega_1 - \omega_2 = \omega_{Raman}$ [Figure 3-1]. While the phase matching condition $\Delta k = 0$ may be satisfied by making all beams collinear, spatial resolution is vastly improved[44] by using the BOXCARS [120] or folded BOXCARS [118] geometries [Figure 3-3].

CARS can be understood conceptually in one of two ways. Firstly, the three beams create a third-order polarisation in the medium, given by equation (3-1), at ω_4 which radiates the signal

[44] Down to 25 µm with appropriate choice of focusing lenses [119].

beam. Alternatively, the application of two beams populates a rotational or vibrational level at their difference frequency $\omega_1 - \omega_2$, followed by scattering off the excited molecules by a third beam at ω_3 resulting in a signal beam at ω_4.

By scanning the frequency of the probe beam, ω_3, or Stokes beam, ω_2, a CARS spectrum is generated which contains peaks in intensity at the frequencies of rotational or vibrational transitions in the target species. The relative intensities of these peaks is related to the thermal (Boltzmann) populations of the various levels involved and can therefore be used to derive temperature by the fitting of a complex theoretical spectrum to the detected spectrum.

Single-shot measurements are possible by the application of a broadband probe laser covering a wide range of frequencies with a single pulse. Modeless lasers may be employed to reduce the noise originating from the broadband source giving high precisions of order 1 % [121], [122].

Vibrational energy levels have larger energy gaps and therefore smaller thermal populations above the ground state than rotational levels, which at room temperatures are insufficient for accurate CARS thermometry. Vibrational CARS has been widely applied to flame thermometry with quoted single-shot accuracies of 2 – 5 % in relation to thermocouple measurements, while rotational CARS is better suited to lower temperature thermometry due to its closer spacing of energy levels resulting in single-shot accuracies of ≤ 10 % [32], [123], [124], [125]. Both techniques are capable of achieving precisions of 3 % in their respective temperature ranges [126].

Vibrational and rotational CARS measurements are limited to major species[45] due to the low effective cross-section and proportionality of CARS to the square of the number density of the target species [119].

CARS is a two-photon technique, i.e. no beam is resonant with a single-photon transition, which means there will be no absorption of the incident or signal beams outside of the interaction

[45] Typically > 1 % by number which precludes CARS of OH, NO and hydrocarbon species in combustion.

region where they overlap. This makes CARS suitable for e.g. sooting flame diagnostics [127], although CARS measurements in sooting environments suffer from interference from Laser-Induced Incandescence (LII).

CARS in engines

CARS has been successfully applied to IC engines for the last two decades[46] [128], [129]. The high precision of CARS thermometry enables the investigation of subtle temperature changes such as the evaporative cooling of direct-injection fuel sprays for a variety of fuel compositions [130], [131], [132].

Single-shot measurements of temperature and number density were performed in an HCCI engine by use of O_2 and N_2 rotational CARS [133]. Owing to the ability to use N_2 as a target species, measurements were also possible after combustion unlike techniques which rely on combustible fuel-based tracers.

ERE-CARS

Electronically resonantly enhanced CARS tunes the pump beam to an electronic transition such that it excites molecules to a 'real' rather than 'virtual' level as in standard CARS [134], [135]. ERE-CARS signal strengths can be more than 3 orders of magnitude stronger than standard CARS [136], enabling an improvement in species detection limits from order of 0.5 – 1 % to ppm levels [137] similar to DFWM.

Femtosecond CARS

The recent availability of femtosecond laser sources has opened up new possibilities for the CARS technique. The very high intensities of fs-pulses improve the signal-to-noise ratio of intensity-dependent processes such as CARS. Additionally, the high (> 1 kHz) repetition rates typical of fs-lasers enable time-resolved temperature and number density measurements at smaller time intervals than is achievable with ns-lasers. Collisions in gases up to 20 bar are

[46] Mostly rotational CARS due to the 300 – 800 K temperatures typical of in-cylinder gas mixtures.

typically on picosecond timescales so ns-CARS requires detailed modelling to account for their effect. A fs-CARS signal is generated quickly enough to be essentially independent of collisions [138]. Picosecond CARS signals may also be considered 'collision free', however picosecond laser sources are inherently less stable than fs-lasers owing to the mode-locking methods used, as opposed to the stable self-mode-locking typical of fs-lasers which take advantage of the optical Kerr effect[47] [139], [140], [141].

Ns-CARS requires temporal overlap of the three incident beams to generate a signal. The coherence in the medium generated by the fs-CARS pump (ω_1) and Stokes (ω_2) beams persists for timescales of the order of 20 ps, enabling the probe beam to be delayed yet still generate a signal [142]. This allows the non-resonant background, present in all ns-CARS measurements, to be eliminated as it is only generated when all three incident pulses are simultaneous[48].

The intensity of the fs-CARS signal decreases with increasing delay of the probe beam as the coherence created between rotational levels by the excitation pulses 'dephases' due to their different characteristic frequencies. The rate of this decrease with probe delay increases with increasing temperature and can therefore be used for thermometry with precisions of between 3 – 8 % over the range 300 – 900 K. However, this requires the probe delay to be scanned over several minutes, removing the both the high repetition rate and temporal resolution advantages of fs-CARS. This problem can be overcome by using group velocity dispersion[49] to stretch the pulse duration to approximately 2 ps. This allows 'probe delay' thermometry to be performed within 2 ps instead of 2 minutes [143].

[47] The optical Kerr effect [236] describes the variation of the refractive index of a medium proportional to the intensity of the light: $n = n_0 + n_2 I$

[48] This non-resonant background and attempts to suppress it with ns-CARS is described in [237].

[49] E.g. by passing the fs probe pulse through a glass rod the shorter-wavelength components of the fs-pulse will be delayed more by the rod's refractive index, arriving at the CARS interaction region later than the longer wavelengths.

1- and 2-dimensional CARS

CARS may be extended from the established point-measurement technique to up to 2-dimensional measurements. For 1-D CARS, the BOXCARS geometry of Figure 3-3 is maintained but laser sheets are crossed instead of beams to generate a linear interaction region [144]. The development of single-shot 2-D CARS imaging is reported in a series of papers from Sandia National Laboratory, Livermore [145]–[149]. A broadband fs-pulse is formed into a sheet to provide both the pump and Stokes photons. A large-diameter (several mm) ps-pulse intersects this sheet at the phase-matching angle to generate CARS signals from each point within the planar intersection region. The signals are then dispersed with a diffraction grating and imaged onto a CCD. This approach works for rotational spectra where the lines are much narrower than their separation[50] as the CARS images generated by each line do not overlap on the CCD after dispersion by the grating.

3.4.2. Polarisation spectroscopy (PS)

Polarisation spectroscopy (PS) uses the birefringence induced by the presence of a strong pump beam to perturb the phase and amplitude of a probe beam, allowing partial transmission of the probe through a polariser orthogonal to the probe's original polarisation. The degree to which the pump beam saturates the transitions and induces birefringence depends on its detuning from each transition's centre frequency. Similarly to absorption spectroscopy, PS can be used to map out an absorption spectrum of the medium. For a detailed explanation of the theory of polarisation spectroscopy the reader is directed to the relevant literature [31], [34]. Polarisation spectroscopy was first reported in [150] and has seen application for thermometry with OH and NH [151], for single-shot thermometry using a broadband laser source [152] and for 2-dimensional flame thermometry [153].

PS can be used with non-fluorescing species (many hydrocarbons) that do not absorb in the visible or UV by targeting the ro-vibrational transitions available in the mid-infra-red [154].

[50] E.g. in nitrogen the S-branch transitions are spaced by 8 cm^{-1} with a linewidth of < 0.1 cm^{-1} [145].

While this feature lends itself to combustion diagnostics, PS signals are very sensitive to any misalignment of the polarisers. Deviations of as little as 0.1° are sufficient to perturb the apparent lineshapes of transitions and hence any derived parameters [155].

The windows of an optical IC engine will experience pressure-induced birefringence which varies both over the engine cycle and through cyclic variations in pressure. As it is not possible to distinguish between the 'window' and 'laser' induced birefringence, PS in IC engines is impractical and hence was not considered for this work.

3.4.3. Degenerate Four Wave Mixing (DFWM)

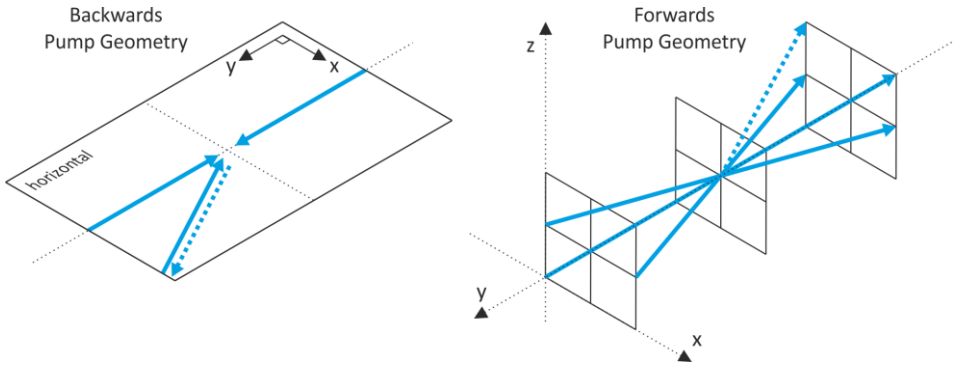

Figure 3-4 'Backward' and 'Forwards' pump geometries for DFWM, signal represented by a dashed arrow.

Degenerate Four Wave Mixing (DFWM) is a nonlinear technique offering the potential for compositional and temperature measurements in combustion environments using just a single laser and generating a coherent signal beam [156], [34].

The mixing of three incident beams of the same wavelength generates a fourth signal beam via the third order electric susceptibility of the medium, equation (3-1). As a resonant technique, DFWM has sufficient sensitivity to target minor combustion species such as flame-generated OH or C_2 [157], [158], [159] or NO detection in an IC engine [160], [161].

There are two typical geometries for DFWM point-measurements [Figure 3-4]. In the 'backwards pump geometry' it is possible to perform Doppler-free measurements if the laser linewidth is narrower than the Doppler width such that only molecules with approximately zero

velocity with respect to the incident beams can interact. In the 'forwards pump geometry' all molecules can interact with all 3 incident beams and therefore typically produces stronger signals than the 'backwards' geometry.

The first model for DFWM in absorbing media was presented by Abrams and Lind [162]. While qualitatively successful in comparison to many experiments [34], the Abrams and Lind model makes many assumptions about the experiment which in general do not hold. These include non-saturating beams, stationary atoms, two-level atoms, all beams have the same linear polarisation, counter-propagating pumps only[51], monochromatic beams, negligible absorption[52], a weak probe beam allowing a perturbation theory approach and a steady-state[53].

A thorough model based on Direct Numerical Integration (DNI) of the FWM polarisation density matrix equations allowed for the modelling of saturating beams [163]. It was found that the optimal pump intensity for both maximising signal strength and minimising the dependence of signal intensity on collision rate is the saturation intensity[54]. Over a series of papers, the limitations of the Abrams and Lind model were overcome, albeit via a computationally expensive numerical solution [164]–[168].

For optimised DFWM signals the issue of a saturated probe beam is one of the most significant limitation of the Abrams and Lind model. This was addressed by a non-perturbative, analytical solution for the treatment of arbitrary pump and probe intensities [169], and can be extended to apply to broadband laser sources for single-shot thermometry[55] [170], [171].

[51] I.e. the 'backward pump geometry' of Figure 3-4.

[52] I.e. an optically thin medium.

[53] I.e. no short laser pulses.

[54] $I_{sat} = \hbar\omega/\sigma\tau\Delta\omega$, where ω is the transition frequency, Δω is the transition linewidth, σ is the cross-section and τ is the fluorescence lifetime of the transition. It turns out that higher intensities reduce the dependence on total collision rate but increase the dependence on the relative rate of dephasing versus quenching collisions, hence an optimal value of I_{sat} as opposed to $I \to \infty$.

[55] Removing the requirement to scan the laser frequency over several minutes to record a DFWM spectrum.

Fluctuations in the intensity distribution between longitudinal modes significantly reduce the practicality of single-shot broadband DFWM[56] [172]. Use of a modeless laser source removes these fluctuations and improves the repeatability of the technique [170], [171], [173].

DFWM forms a periodic spatial variation in the excited state population of the target molecules, a 'population grating'. Any collisions that occur with excited molecules will tend to 'quench' the excitation, returning the molecule to the ground state, depositing the energy as localised heating of the medium and removing that molecule's contribution to the DFWM signal. DFWM therefore performs best at low pressures (< 1 bar) where the collision rate is lower. The heating resulting from collisional quenching can lead to the formation of a thermal grating, which will coherently scatter light along the DFWM signal path and for higher pressures dominates the DFWM signal. This phenomenon leads to the field of Laser-Induced Thermal Grating Spectroscopy (LITGS) discussed in section 3.4.4.

The undesirable LITGS contribution in a DFWM setup may be removed by using orthogonal instead of parallel polarisations of the pump beams[57]. This was initially considered, using diagrammatic perturbation theory, to be detrimental to DFWM signal intensity [174]. A full DNI approach to modelling corrected this finding by demonstrating that the crossed polarisation case has a higher saturation intensity and therefore stronger DFWM signal for saturated intensities than the parallel polarisation case [167].

DFWM imaging

The degeneracy of the frequency of all four beams simplifies the requirements for phase-matching and hence also makes the extension to 1D and 2D measurements conceptually easier than CARS. A cylindrical lens may be used to form sheets from the counter-propagating pump beams and the intersection of a circular cross-section probe defines a planar interaction region.

[56] These fluctuations can lead to a success rate for single-shot spectra being acceptable for temperature derivation as low as 15 % [172].

[57] This prevents the formation of an interference pattern and therefore the thermal grating, see section 3.4.4.

This method was used to perform 2D DFWM measurements of composition [175], [176] and temperature [177] in a flame.

Thermometry with DFWM requires measurement of, if not the entire spectrum, then at least the relative intensities of two lines originating from thermally-populated levels. The 2D-thermometry of [177] was therefore restricted to time averaged measurements by the need to adjust the laser frequency between measurements. Single-shot measurements can instead be performed using a dual-wavelength laser providing light centred at two distinct wavelengths within a single pulse [153], or using a broadband laser[58] [32].

A significant practical difficulty when imaging is that the effect of any non-uniformity of the incident beams is amplified in the signal's intensity by the nonlinear nature of DFWM. A typical approach to correct for this is to compare the DFWM signal to a reference image in uniform medium [178].

3.4.4. Laser-Induced Grating Spectroscopy (LIGS)

Unlike CARS and DFWM, which require a coherent interaction between three beams to generate a signal, Laser-Induced Grating Spectroscopy (LIGS) crosses two beams to generate a spatially periodic perturbation in the density of the medium, the 'grating', that evolves over time. The generation and evolution of the grating is dependent on a range of local gas parameters. The grating can therefore be used as a diagnostic technique by scattering a third beam off the grating to record the evolution of the grating over time.

The theory of LIGS will be discussed in further detail in chapter 4. For now it suffices to say that there are two types of density grating that may be formed, 'thermal' and 'electrostrictive' gratings. The two techniques are closely related and may both be present in a single experiment. For the avoidance of ambiguity, in this work the acronyms of Table 3-1 will be used.

[58] Figure 3.3, Chapter 3, pg 79 of [32].

Technique	Type of grating	Acronym
Laser-Induced Grating Spectroscopy	Unspecified, could refer to thermal, electrostrictive or both.	LIGS
Laser-Induced Thermal Acoustics (Equivalent to LIGS)	Unspecified, could refer to thermal, electrostrictive or both.	LITA
Laser-Induced Thermal Grating Spectroscopy	Thermal	LITGS
Laser-Induced Electrostrictive Grating Spectroscopy	Electrostrictive	LIEGS

Table 3-1 Laser-Induced Grating technique acronyms

For pump beams tuned to an electronic transition in the target molecules, absorption of the pump energy heats the gas locally. This temperature rise perturbs the density forming a 'thermal grating'. For non-resonant pump beams, the electric field of the interference pattern induces a polarisation of the gas molecules which then are displaced by the field, forming an 'electrostrictive grating' [179].

Before use in the gas-phase, LIGS was widely used in studies of relaxation in condensed matter, [180], [181]. The first demonstration of LIGS in the gas phase was by Cummings [182] in which a theoretical model was presented, one of two models now in widespread use for the analysis of LIGS measurements. The initial theoretical treatment was upgraded the following year to include finite beam sizes [183]. The other popular model for LIGS analysis was presented by Paul et al. [1] with associated experimental confirmation [184] alongside a discussion on the relative contributions of DFWM and LITGS in a DFWM experiment [1].

One of the most readily apparent advantages that distinguishes LITGS from similar techniques is that LITGS signals improve with pressure, in direct contrast to DFWM which performs best below atmospheric pressure. Although LITGS can be an unintended side-effect of DFWM measurements and at high pressures will dominate the desired DFWM signal, the reverse is not an issue. A different wavelength source can be used as the LITGS probe or, as DFWM requires all 3 beams to be simultaneous within the coherence time of the pulses, the probe can be delayed by a time exceeding the coherence time to remove DFWM contributions.

Measurements with LIGS

LIGS can be used for measurement of a variety of local gas parameters such as pressure, temperature, velocity and gas composition. The crossed pump beams and probe beam define the interaction region for the measurement, hence high spatial resolutions can be achieved, particularly with focused beams. The lifetime of the grating and therefore the scattered signal is typically between 0.1 – 1 μs, short enough to consider the motion of the gas to be frozen for many applications, giving high temporal resolution.

The lifetime of thermal gratings is highly pressure-dependent. Pressure is most readily determined from the decay rate of the LITGS signal and has been applied to a range of environments including test cells [185], high pressure flames [186] and supersonic flows [187], [188].

Velocimetry with both LITGS and LIEGS has been demonstrated by measuring the Doppler shift of the LIGS signal caused by the motion of the flow both via a fabry-perot etalon [189], and via heterodyne detection with a reference beam [190], [191] and [192].

LIGS thermometry relies on a measurement of the sound speed via the characteristic temporal oscillations in the signal and was first demonstrated by Latzel et al. [186] in premixed methane/air flames. Temperature measurements have since been performed in many environments, including with LITGS in combustion engines [4], with LITGS in high-pressure sooting flames [193] and with LIEGS in air [194].

LITGS signals have been used for tracer number density measurements in three main ways. The relative strengths of thermal and electrostrictive gratings depend on the partial pressure of the tracer versus the total pressure [195] and changes in composition affect both the oscillation frequency [196] and the signal strength [197]. Measurements and discussions of the relative merits of each approach have also been reported [198], [199].

A novel approach for simultaneously measuring both fuel and oxygen number densities was presented in [3]. Toluene number density was determined by the LITGS signal strength, while the strong dependency of the quenching rate on local oxygen number density allowed the fitted quenching rate to be used to derive the oxygen and therefore air partial pressure. The combination results in a time-resolved measurement of fuel-air ratio, a key compositional parameter in the operation of IC engines.

The experimental and analytical requirements to derive pressure, temperature, velocity and composition from LIGS signals are not mutually exclusive. A single LITGS experiment can perform high precision measurements of pressure (4 %), flow velocity (0.2 %) and temperature (0.4 %) simultaneously [187], and indeed many of the studies cited perform measurements of multiple parameters.

LITGS is also highly suited to measurements in challenging combustion environments. A recent development of Infra-red LITGS at 3 μm allows fundamental vibrational modes of water and many hydrocarbons to be excited by the pump beams [200], [201]. Hydrocarbons are plentiful before the flame front and water is a major combustion product, allowing a single LITGS setup to track temperatures throughout the pre- and post-combustion zones of a flame.

Electrostrictive gratings (LIEGS)

The theory and experimental application of electrostrictive gratings have been concisely summarised by Stampanoni-Panariello et al. [202], [203].

The electrostrictive LIEGS signal oscillates at twice the frequency of the equivalent resonant LITGS signal. When the thermal component is stronger in magnitude than the acoustic contribution, as is usually the case with resonant LITGS experiments, the acoustic oscillations modify the reflectivity of the combined grating to reach a minimum once per acoustic period[59].

[59] Defined as the 'grating transit time', i.e. the time taken to propagate from one grating plane to the next at the local speed of sound.

The acoustic contribution dominates the thermal contribution for electrostrictive gratings [204], therefore both the ‘positive’ and ‘negative’ extrema of the standing wave’s oscillation produce a local maxima in the density perturbation as a function of time. Equivalently there are two ‘zeros’ of density perturbation per acoustic period.

Electrostrictive gratings have been successfully applied for measurements of sound-velocity [205] which can be used to derive temperature. Care must be taken to avoid conditions where unintended absorption leads to formation of a thermal grating, in which case the oscillation frequency halves to that of a resonant LITGS grating [206]. Conversely, electrostrictive gratings may also be observed in resonant LITGS experiments if the pump pulses are sufficiently intense [207].

Accuracy and precision

Thermometry with LIEGS has been reported as having a typical precision of 5 % at 1376 K [203], comparable to equivalent CARS measurements. This significantly improves at lower temperatures, such as 0.6 % [208], where the thermal diffusion of the grating is slower leading to longer signals, more oscillation cycles and hence a more precise derivation of frequency.

The single-shot accuracy and uncertainty of electrostrictive grating measurements as a function of pump pulse energy have been carefully evaluated in [209]. Sound speeds were measured to within an accuracy of < 1 % over a range of pulse energies and an optimal precision of 0.5 % was achieved with a high pump pulse energy just below that which causes breakdown of the gas. Given the quadratic dependence of signal magnitude on pump intensity, this agrees with the intuition of maximising the signal-to-noise ratio, while avoiding dramatic perturbations to the medium. The analysis of [209] used fitting to the model of Cummings et al. [183] to determine the speed of sound. As such, their thorough analysis of the causes of inaccuracies at low signal-to-noise ratios and at overly high laser intensities approaching the breakdown energy of the air is unaffected by the issues discussed for FFT and peak-finding analysis in chapter 4.

LITGS measurements under optimal conditions of high pressure (40 bar) and low temperature (300 – 400 K) are capable of accuracies of 0.42 % and single-shot precisions of 0.16 % [185]. For conditions more typical of an optical IC engine[60] the precision has been demonstrated to be 0.4 % [25], enabling the small cyclic variations in temperature of approximately 1.5 % to be resolved.

LITGS measurements in premixed methane/air flames were performed by Latzel et al. [186]. Temperature was derived from the LITGS signals by fitting to the model of Paul et al. [1], modified to account for propagation of the sound waves from the finite volume of the interaction region as described in [183]. Precisions comparable to equivalent CARS measurements (~ 2 %) were achieved for temperature measurement over a range of stoichiometries and pressures between 10 – 40 bar. The high pressures were highly beneficial for LITGS measurements at flame temperatures of ~ 2000 K, helping to counteract the shortening of the LITGS signal by slowing the otherwise the rapid diffusion of the grating density perturbation at high temperatures. Fitting to a theoretical model to recover temperatures proved very effective at 40 bar. At the lower pressure of 10 bar, the breakdown of some assumptions of the model, namely that the formation of the grating is much faster than the timescale of the grating's decay and can be approximated by a single quenching rate, resulted in a slight reduction in the quality of the fit[61].

3.5. Selection of techniques

3.5.1. 2D thermometry

To summarise: Absorption spectroscopy is impractical for planar measurements. An IC engine is by no means a 'clean' environment hence Rayleigh scattering will not be considered. Raman scattering produces weak signals at laser pulse energies low enough to avoid window damage. Without the benefit of PIV, seeding the air intake with thermographic phosphor particles is an

[60] At 50 CAD BTDC under the motored conditions of [25] the pressure is typically around 2 bar.

[61] For further discussion of quenching rates and the improvement in fitting with a two-rate model, see chapter 4.

unnecessary complication and chemiluminescence does not provide a signal for pre-combustion gases. Nonlinear techniques applied to 2-dimensional measurements are complex to perform, do not necessarily provide higher accuracy or precision than their linear counterparts and would require greater optical access than is available in this engine.

Of the LIF techniques, molecular tracer LIF is most applicable to thermometry in the fuel-air mixture before combustion as the independence of the 2-line excitation and 2-colour detection PLIF techniques to compositional inhomogeneity is critical to application to a firing engine where homogeneity cannot be assumed. Molecular tracer PLIF was therefore selected as the 2-dimensional thermometry technique of this work. The selection of TC-PLIF as the specific technique for development in this work is discussed in detail in chapter 5.

3.5.2. In-situ calibration

The reduction in complexity and reduced optical access required by the point-measurement applications of nonlinear optical diagnostics allows the high accuracies and precisions offered by nonlinear techniques to be preferable to their linear rivals. Additionally, the generation of a coherent signal beam by the nonlinear techniques makes it easy to spatially filter scattered light and other incoherent noise sources to provide an improved signal-to-noise ratio.

LITGS thermometry inherently depends on a measurement of an oscillation frequency rather than an intensity. It is therefore less affected by the presence of intensity noise such as that caused by fluctuations in laser intensity, target species number density or window fouling, than techniques which rely on the intensity of a signal such as DFWM or CARS. By deriving temperature from the temporal oscillations of signal intensity, LITGS also removes the requirement for tuneable lasers or broadband/multiple wavelength sources coupled with dispersive optics required for broadband CARS or DFWM.

As LITGS thermometry can provide greater precisions with reduced complexity compared to alternative nonlinear techniques. LITGS was selected for in-situ calibration of the TC-PLIF temperature distributions.

4. Point LITGS

In this chapter the application of LITGS for in-cylinder thermometry of an optical engine will be discussed. The theory of LITGS thermometry is presented in 4.2, firstly with a qualitative description of the key processes and secondly with a summary of the derivation of the LITGS signal expression from [1] highlighting the assumptions required. A review of the literature is presented in 4.3 specific to the areas of discussion in this chapter, namely engine thermometry with LITGS, the influence of weak signals and analysis methods for oscillation frequency extraction. Potential measurements and sources of uncertainty are discussed in 4.4. The merits and issues of three methods for derivation of the oscillation frequency from a LITGS signal are discussed in 4.5. Section 4.6 describes the experimental methods and the results of preliminary investigations into the application of this LITGS system to the optical engine are reported in 4.7.

4.1. Introduction

LITGS was selected in chapter 3 as the measurement technique to provide in-situ calibration of the TC-PLIF images. The accuracy of the TC-PLIF temperature maps of chapter 6 is strongly dependent on the LITGS measurements used for calibration. In order to confirm the production of accurate, precise and reliable reference temperatures, the capabilities of both the experimental and analytical aspects of LITGS are evaluated in this chapter.

LITGS has previously been shown to be capable of performing point-measurements in the optical engine used in this work with a spatial resolution of 1 x 1 x 10 mm and a temporal resolution of < 1 μs, sufficient to 'freeze' the gas motion [4]. The focus of the discussion on LITGS analysis in 4.5 is to determine the performance and robustness of three oscillation frequency recovery methods when applied to signals with low signal-to-noise ratio, characteristic of engine measurements. The experimental section of this chapter, 4.7, will assess detector saturation and the ability of LITGS to resolve small in-cylinder temperature differences using the optimal analytical method selected in 4.5.

4.2. Theory of LITGS

An overview of the LITGS technique has already been given in the literature review of chapter 3. In section 4.2.1 the formation of a LITGS grating and the derivation of temperature from the LITGS signal will be qualitatively described. The theory of thermal gratings from [1] forms the basis of section 4.2.1 and the analysis methods used in this work and is summarised in section 4.2.2.

4.2.1. Qualitative description of LITGS thermometry

LITGS thermometry derives temperature from measurement of the sound speed in a gas. Absorption of laser pulses in the interaction region creates the 'Laser-Induced Grating' and generates acoustic waves which modify the density perturbations in the spatial pattern of the grating over time. The evolution of the 'Laser-Induced Grating' is monitored by Bragg-scattering a probe beam off the grating and recording the scattered intensity as a function of time [34].

The first step in performing a LITGS measurement is to create the grating. Two coherent pump beams are crossed to define the measurement region and interfere to create a sinusoidal spatial variation in intensity [Figure 4-1]. These 'bright' and 'dark' fringes form the parallel planes of the grating at a spacing, Λ, determined by the pump wavelength, λ_{pump}, and the crossing angle of the beams, θ,

$$\Lambda = \frac{\lambda_{pump}}{2\sin\left(\frac{\theta}{2}\right)} \tag{4-1}$$

The wavelength of the pumps is chosen to match an electronic transition of the target molecules. The target species are therefore resonantly excited in the regions of high intensity. Collisions with other molecules occur, for conditions relevant to this work, on picosecond timescales [3] and quench this excitation, depositing the energy into the bulk gas over multiple collisions as kinetic energy (heat). This localised heating perturbs the local temperature and pressure, leading to the formation of two density perturbations.

Firstly the (very small) rise in temperature reduces the local density in regions of high laser intensity. This ‘temperature grating’ decays over time due to thermal diffusion reducing the contrast between the high and low density regions. Secondly, the rapid increase in pressure generates acoustic waves, which constructively interfere for propagation directions orthogonal to the grating planes. The resulting two counter-propagating waves sum to produce a standing wave. This ‘acoustic grating’ decays over time due to viscous damping of the acoustic waves.

The total density modulation is a sum of these two components, where the magnitude of the thermal density grating is modulated in time by the oscillation of the acoustic contribution. This produces a ‘strong’ grating when both components are in phase and a ‘weak’ grating when the two components are out of phase.

The visibility of the combined grating can be probed by Bragg-scattering a third beam at an incident angle, ϕ, given by equation (4-2):

$$\lambda_{probe} = 2\Lambda \sin \phi \tag{4-2}$$

The intensity of the diffracted signal can then be used to measure the oscillations in grating visibility over time [Figure 4-1].

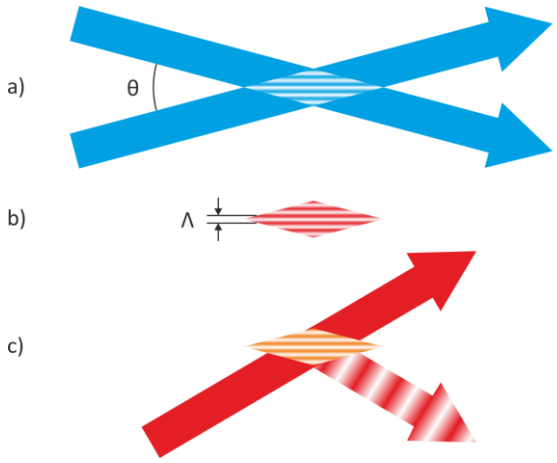

Figure 4-1 a) Pump beams crossing at an angle of θ to produce an interference pattern. b) Thermal and acoustic gratings form with spacing between planes of Λ. c) Probe beam scatters from grating generating a signal beam. a) to c) as drawn in [3].

The frequency, f, of the acoustic standing wave's oscillation and therefore that of the grating's visibility is given in terms of the sound speed, c_s, by equation (4-3):

$$f = \frac{c_s}{\Lambda} \tag{4-3}$$

Therefore by measuring the frequency of the oscillations in diffracted signal intensity, the sound speed can be calculated providing the grating spacing, Λ, is known. While Λ may be determined geometrically from equation (4-1), in practice it may be derived with much higher accuracy from a measurement under known conditions of composition and temperature. Treating the gas as ideal, the isentropic sound speed, c_s, is given by:

$$c_s = \sqrt{\frac{\gamma k_B T}{m}} \tag{4-4}$$

where 'γ' is the ratio of specific heats at constant pressure to constant volume, 'k_B' is Boltzmann's constant, 'T' is temperature and 'm' is the mean molecular mass of the gas.

So given knowledge of the gas composition[62], the temperature in the measurement region, T, can be derived from a measurement of the oscillation frequency, f, of a LITGS signal:

$$T = \frac{m\Lambda^2}{\gamma k_B} f^2 \tag{4-5}$$

4.2.2. Theory from Paul et al.

The theory described in this section is the work of Paul et al. [1]. As with other reviews of LITGS theory [34], [3], the salient points are summarised in this section for the convenience of the reader.

A two-rate quenching model was found in [1] to provide a significantly improved match to experimental results. A single collision will not be 100 % efficient at converting the electronic energy of the excited target molecule into heat. A fraction will instead be stored as ro-vibrational excitation of the colliding 'bulk gas' molecule. This energy will be released over

[62] The effect of gas composition on sound speed is given by the ratio γ/m.

time as the 'bulk gas' molecule undergoes further collisions. The two-rate model combines a 'fast' rate for the initial energy deposition and a 'slow' rate for the subsequent loss of energy over multiple collisions. For clarity, only the single-rate quenching model will be summarised here and the reader is directed to [1] for further details.

As described in section 4.2.1, the two pump pulses are crossed to form an interference pattern with a spacing, Λ, between 'bright' planes given by equation (4-1), leading to a spatially-varying perturbation in the gas density which is designated as the 'grating'. The dimension normal to these planes is labelled as 'x' and the planes are assumed to be of infinite extent such that the problem is reduced to a single spatial dimension. This is a reasonable simplification for the case where the pump beams are much larger than the fringe spacing[63] such that the duration of the LITGS signal is much shorter than the timescale over which acoustic energy escapes the grating.

The evolution of the grating and hence the LITGS signal is determined by the evolution of the gas density, ρ, with time, t. This evolution is governed by a set of hydrodynamic equations,

$$\frac{\partial \rho}{\partial t} + \nabla \cdot (\rho \bar{u}) = 0 \tag{4-6}$$

$$\frac{\partial (\rho \bar{u})}{\partial t} + \nabla \cdot (\rho \bar{u} \bar{u}) + \nabla P = 0 \tag{4-7}$$

$$\frac{\partial (\rho e_{tot})}{\partial t} + \nabla \cdot \left((\rho e_{tot} + P) \bar{u} \right) = \Phi_{heating} \tag{4-8}$$

derived from the fundamental principles of conservation of mass[64] (4-6), conservation of momentum[65] (4-7) and conservation of energy (4-8). In these equations '$\bar{u}$' is the 3D velocity vector, 'P' is pressure, '$\Phi_{heating}$' is a source term for the energy input to the gas and 'e_{tot}' is the total specific energy, defined as:

[63] A typical grating spacing is of the order of 10 µm, and even for focussed beams the spot size is likely to be of the order of 100 µm.

[64] Also known as the continuity equation and is set to zero as no mass is created or lost in this system.

[65] Set to zero because there are no external forces acting on the molecules in LITGS. For LIEGS the force due to electrostriction would have to be represented here.

$$e_{tot} = \left(e + \frac{u^2}{2}\right) \tag{4-9}$$

where ‘e’ is the specific thermal energy.

The heating source term, $\Phi_{heating}$, in equation (4-8) describes the energy input to the gas by collisional quenching of the excited molecules. The population of the upper level of the excited transition per unit volume, N*, can be described by a rate equation:

$$\frac{\partial N^*}{\partial t} = E_P BN2\left(1 + \cos\left(\frac{2\pi x}{\Lambda}\right)\right) g(t, \tau_L) f(x, d) \; - \; (A + Q)N^* \; + \; D\frac{\partial N^*}{\partial x^2} \tag{4-10}$$

where ‘E_P’ is the total laser energy flux per pulse, ‘B’ is the Einstein B-coefficient, ‘N’ is the density of absorbing molecules, ‘g’ is the normalised temporal profile of the pump pulse, ‘τ_L’ is the duration of the pump pulse, ‘f’ is the normalised spatial profile of the pump pulse, ‘d’ is the diameter of the pump pulse, ‘A’ is the Einstein A-coefficient, ‘Q’ is the collisional quenching rate and ‘D’ is the molecular diffusivity for the excited molecule.

Each collisional quenching event will transfer a fraction, ε, of the molecule’s electronic energy into thermal energy. The rate of energy input to the system is therefore given by:

$$\Phi_{heating} = \varepsilon h \nu_0 Q N^* \tag{4-11}$$

where ‘h’ is Planck’s constant and ‘ν_0’ is the frequency of the excited transition.

The hydrodynamic equations (4-6) to (4-8) contain several non-linear terms, such as $\nabla \cdot (\rho \bar{u})$, making analytical solutions difficult. In order to solve these equations for density, it is convenient to linearize the equations. Linearization refers to the process of expanding parameters[66] about an equilibrium point and discarding any terms which are higher order than linear in the perturbation, as illustrated in equation (4-12) for density, ρ:

$$\rho(x, t) = \rho_0 + \Delta\rho(x, t) \tag{4-12}$$

Combination of equations (4-6) through (4-12) results in the dimensionless linearized hydrodynamic equations,

[66] In this case density (ρ), velocity ($\bar{u}$) and pressure (P).

$$\frac{\partial \rho'}{\partial \zeta} + \frac{\partial u'}{\partial \xi} = 0 \tag{4-13}$$

$$\frac{\partial u'}{\partial \zeta} + \frac{1}{\gamma}\frac{\partial P'}{\partial \xi} - \frac{4}{3Re}\frac{\partial^2 u'}{\partial \xi^2} = 0 \tag{4-14}$$

$$\frac{1}{\gamma}\frac{\partial P'}{\partial \zeta} - \frac{\partial \rho'}{\partial \zeta} - \frac{1}{RePr}\left(\frac{\partial^2 P'}{\partial \xi^2} - \frac{\partial^2 \rho'}{\partial \xi^2}\right) = \frac{\gamma - 1}{\gamma}\frac{\varepsilon h \nu_0 Q \Lambda}{c_s}\frac{N^*(\zeta, \xi)}{P_0} \tag{4-15}$$

where 'Re' is the Reynolds number and 'Pr' is the Prandtl number. Equations (4-13), (4-14) and (4-15), are presented using normalised variables of the form $f'(x,t) = \Delta f(x,t)/f_0$. Correspondingly, the distance and time parameters have also been normalised to $\xi = x/\Lambda$ and $= c_0 t/\Lambda$ [67]. Also required in the formulation of equations (4-13) to (4-15) is the linearized ideal gas law $P' = \rho' + T'$ and the equation of state for the enthalpy of an ideal compressible medium $h = c_v T + PV$ where 'h' is enthalpy, 'c_v' is the specific heat at constant volume, 'T' is temperature and 'V' is volume.

The collation of constants into the Reynolds number,

$$Re = \frac{\rho_0 c_s \Lambda}{\mu} \tag{4-16}$$

where 'μ' is the dynamic viscosity and the Prandtl number,

$$Pr = \frac{c_p \mu}{K} \tag{4-17}$$

where 'K' is the thermal conductivity and 'c_p' is the specific heat at constant pressure, is typical of fluid dynamics calculations as they each define characteristics of the flow in question. The Reynolds number corresponds to the ratio of inertial to viscous forces in the flow. A low Reynolds number describes a laminar flow where viscous forces dominate, while high Reynolds number flows are dominated by inertia and are typically turbulent. The Prandtl number corresponds to the ratio of viscous and thermal diffusion rates and over the range of temperatures and pressure in this work is approximately constant at 0.7 [68]. The linearized hydrodynamic equations (4-13) to (4-15) only apply for the case where the fringe spacing, Λ, is

[67] Where c_0 is the isentropic sound speed in the absence of the grating, taken to be ≈ c_s.

[68] For example, the Prandtl number for air varies by only 2 % between 500 – 1000 K and 1 – 10 bar [238].

much greater than the mean free path of the gas molecules. Correspondingly, the derivation of the impulse response function of the grating, W(ζ), defined in equation (4-20), is valid for Reynolds numbers greater than three.

The problem set out in equations (4-13) to (4-15) is both irrotational[69] and has a separable source function[70]. It can therefore be reduced to a single wave equation which may be solved via a combination of Fourier transforms for ξ (space) and Laplace transforms for ζ (time). The solution for the density perturbation,

$$\rho' \propto \cos(2\pi\xi)\, Z(\zeta) \tag{4-18}$$

involves the convolution of the impulse response function of the grating, W(ζ), the temporal profile of the laser pulse, G(ζ), and the temporal profile of the quenching process, M(ζ),

$$Z(\zeta) \propto W(\zeta) * G(\zeta) * M(\zeta) \tag{4-19}$$

where W(ζ) is defined with a constant phase shift, ϕ, as:

$$W(\zeta) = a_1 e^{s_1\zeta} - 2a_2 e^{-b_1\zeta}\cos(b_2\zeta + \phi) \tag{4-20}$$

The constants s_1, b_1, and b_2 defined during the derivation of equation (4-20) are given by:

$$s_1\zeta = -\frac{(2\pi)^2}{RePr}\zeta = -\frac{4\pi^2 K}{\Lambda^2\rho_0 c_P}t \tag{4-21}$$

$$b_1\zeta = -\frac{(2\pi)^2}{RePr}\frac{\left(\gamma - 1 + \frac{4Pr}{3}\right)}{2}\zeta = -\frac{4\pi^2 K}{\Lambda^2\rho_0 c_P}\frac{\left(\gamma - 1 + \frac{4c_p\mu}{3K}\right)}{2}t \tag{4-22}$$

$$b_2\zeta = 2\pi\zeta = 2\pi\frac{c_s}{\Lambda}t \tag{4-23}$$

The impulse response function of the grating 'W(ζ)' justifies the qualitative description in section 4.2.1 of the density perturbation. The first term represents the stationary thermal component of the grating which decays with a time constant of $-s_1 c_s/\Lambda$. The second term represents the acoustic component, a standing wave formed by two counter-propagating acoustic waves which decays over time with a time constant of $b_1 c_s/\Lambda$. For most relevant

[69] The vorticity of an irrotational flow is zero, i.e. $\nabla \times \bar{u} = 0$

[70] The source function can be separated into a product of terms which are solely time- or space-dependent: $N^*(\zeta, \xi) = a(\zeta)b(\xi)$

experimental conditions and gas compositions, b_1 is only slightly smaller than s_1 [71] [3]. The difference is dependent on γ and Pr, and so only has a very weak dependence on pressure and temperature. This results in the acoustic and thermal components of the density perturbation decaying at similar rates.

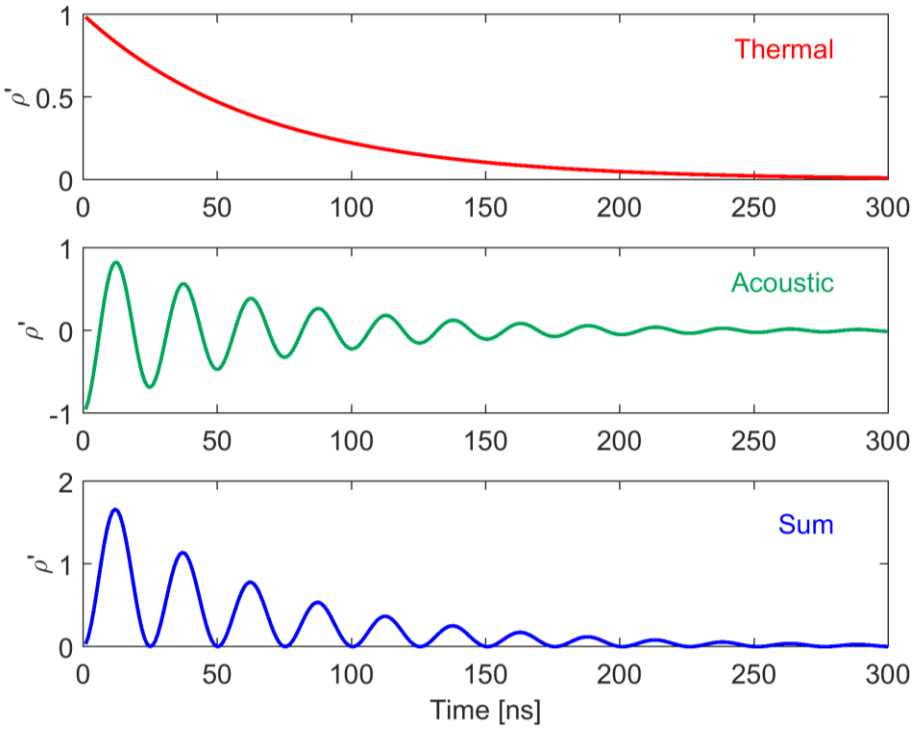

Figure 4-2 Evolution of the LITGS density perturbation 'ρ' [arbitrary units] over time [equation (4-18)] considering the case of an instantaneous excitation pulse and quenching process such that $\boldsymbol{Z(\zeta) \propto W(\zeta)}$. At an antinode of the spatial distribution $\boldsymbol{\cos(2\pi\xi) = 1}$, therefore $\boldsymbol{\rho' \propto W(\zeta)}$.

The scattering efficiency, η, from a density grating of the form of equation (4-18) is defined as the ratio of signal and probe intensities,

$$\frac{I_{signal}}{I_{probe}} = \eta = \left(\frac{\pi \Delta n d}{\lambda}\right)^2 + \left(\frac{\Delta \alpha d}{4}\right)^2 \qquad (4\text{-}24)$$

where 'd' is the pump beam diameter, 'Δn' is the change in refractive index and 'Δα' is the change in absorption coefficient [181].

[71] E.g. $b_1 = 0.675 s_1$ for dry air at standard temperature and pressure. As stated in [1]: "For common gases at moderate pressures we find that this factor varies from 0.67 to 0.8."

In the limit of an optically thin medium[72] $\Delta\alpha$ is negligible and $\partial n/\partial T' \ll \partial n/\partial \rho'$ therefore the change in refractive index is dominated by the density perturbation. The evolution of the LITGS signal is therefore entirely determined by equation (4-18).

4.3. Previous work

A literature review of LITGS has been presented in chapter 3, this section focuses in greater detail on previous work with LITGS in areas that are discussed further in this chapter.

4.3.1. Fourier domain analysis

Fitting in the time-domain is computationally expensive and therefore slow due to the need to convolute the grating response function with the quenching response and finite duration pump pulse functions [1]. By transferring the analysis to the frequency domain via widely available and rapid FFT routines, convolutions can be computed more easily by multiplication[73] which dramatically reduces the time taken to model a LITGS signal [2].

4.3.2. Long pulse probes

The simplest way to implement LITGS is to use a Continuous-Wave (CW) probe, such that the diffracted intensity directly represents the reflectivity of the grating. Typical CW lasers have powers of the order of 1 mW to 1 W. Long-pulse dye lasers can deliver e.g. 0.1 MW for 2 μs, increasing the signal intensity by 5 orders of magnitude [185]. As the probe beam is non-resonant, saturation of transitions in the tracer are not an issue. This approach does however require normalisation for the intensity variation of the probe pulse, hence a need for a time-resolved measurement of the probe pulse in order to determine the time-varying grating reflectivity.

[72] The medium in all typical LITGS experiments may be considered optically thin, at least over the distance of the grating spacing (Λ).

[73] The convolution theorem states that convolution in the time domain is equivalent to multiplication in the frequency domain. $F\{g * h\} = F\{g\} \cdot F\{h\}$ where F{p} is the Fourier transform of p, * is convolution and · is multiplication.

The application of a long-pulse probe laser has also been reported by Balla et al. [194], [190], in which a flashlamp-pumped alexandrite laser is operated in free-running mode. Angle tuning the intra-cavity BBO[74] frequency doubling crystal allows the free-running pulse train to be smoothed into a single approximately flat pulse of up to 1 µs duration with an intensity of 3 kW. While this is weaker than the dye laser used in [185], the much narrower bandwidth compared to the broad output of the dye laser increases the coupling efficiency with the grating and hence signal levels are stronger than the probe power suggests. This laser is however no longer commercially available and required significant modification to avoid mode beating (a severe complication for detection of the oscillations in a LITGS signal), hence the use of a dye laser in the more recent application [185].

4.3.3. Optical engine thermometry

Recent demonstrations of the LITGS system used in this work for IC engine thermometry were reported in [4] and [25]. The high precisions of < 1 % permitted the resolution of the small temperature variations of the order of 1 % associated with the evaporative cooling due to fuel injection of various alcohol-containing fuel blends. Due to the available optical access, crank angles less than 50 CAD either side of top-dead-centre were inaccessible for thermometry using this system in [4]. A modified 'slotted piston' of the same compression ratio prevented the rising piston blocking the LITGS beams and enabled the first LITGS thermometry across an entire compression and expansion stroke of a motored engine [25].

4.3.4. Weak signals

In an ideal world, an optical diagnostic such as LITGS would produce strong signals with high signal-to-noise ratio throughout the desired range of experimental conditions. This is not always achievable, particularly in IC engine experiments where limitations on e.g. gas composition, pressure and optical access are determined by the engine under study, not compatibility with any one optical diagnostic. While LITGS demonstrates excellent performance at high pressures

[74] Beta-phase Barium Borate

(> 1 bar), the low pressures and tracer number densities found early in the compression stroke can result in very weak signals with poor signal-to-noise ratios.

Both the accuracy and precision of LITGS thermometry are reliant on not only the quality of signal produced experimentally, but on the method for recovering the acoustic oscillation frequency from which the temperature is derived. The analysis of weak signals is challenging as displayed by the comparison of atmospheric versus high-pressure resonant LITGS results of Altenhofer et al. [207] where a poor measurement precision of ± 6 % was observed at atmospheric pressure along with a systematic shift in mean LITGS temperatures of + 6 % compared to 10 bar.

Weak signals probe the limitations of commonly used analysis methods, which may not be apparent when applied to stronger signals and will be subject to discussion in section 4.5.

4.3.5. Analysis methods for thermometry

In general, the most precise analysis method for thermometry is fitting to a theoretical model (e.g. Cummings et al. [183] or Paul et al. [1]), resulting in achievable precisions of order 0.1 % [185]. However, fitting routines are computationally expensive and a number of alternative approaches have been utilised for determination of the oscillation frequency and hence temperature.

In the application of electrostrictive gratings by Stampanoni-Panariello et al. [202], the determination of the oscillation frequency of the signal was based on a peak-finding approach, as the separation in time between peaks gives the time period of the acoustic oscillations. This is straightforward in principle and quoted in [203] as typically achieving precisions of 0.5 % for strong, clear signals. However, such an approach becomes less robust for weaker signals with lower signal-to-noise ratios where uncertainty in determining the exact timing of the peak leads to much poorer precisions of 6 % [203].

An alternative approach is to use a Fast Fourier Transform (FFT) routine. This has been used successfully in [3], however, as with most analysis methods, there are several aspects which must be handled with care to avoid systematic errors or reductions in precision and accuracy. For example, the frequency resolution of the power spectra of Altenhofer et al. [210] is extremely coarse and will cause large uncertainties in temperature derivation. This may be compounded by the cropping of the signal to remove the pump pulse scatter which will introduce artefacts into the power spectrum if not treated carefully. Only 10 % precision in the temperature measurements was achieved at room-temperature. However, the raw signals at a high pressure of 9 bar were long enough to show > 10 oscillation peaks and had sufficient signal-to-noise ratio that a potential uncertainty of ~ 1 % could have been obtained if a more sophisticated FFT analysis had been used, such as that discussed in section 4.5.2.

Prony's method for oscillation frequency determination was used by Hart et al. [194]. Prony analysis [211] fits a linear combination of damped complex exponentials to a signal. While the reproduction of the initial rise of a LITGS signal was not captured at all by the fit [194], for sufficiently long signals the fit reproduced the majority of oscillation peaks accurately and the oscillation frequency could be determined. For LITA measurements between 300 – 650 K this resulted in a standard deviation of only 0.5 % from the corresponding thermocouple readings of ± 1 K precision[75]. However the poor fit to the first peak raises questions about the applicability of the Prony analysis for weak signals with only a few peaks.

In summary, peak-finding, FFT analysis and Prony analysis have each been very successfully applied to experimental data to derive LITGS parameters from strong, typically high pressure, signals. However, these more rapid methods of oscillation frequency determination have been sub-optimally applied to weak signals, leading to unnecessary increases in measurement

[75] A more recent study using the experimental data of [194] recommends the 'Auto-Regressive spectrum method' (AR) as a method resulting in improved precision over Prony analysis [211]. AR involves fitting a model in which the value of the function at a given time is predicted based on a linear combination of earlier or later (or both) values of the function and a white noise term. Being more computationally expensive than peak-finding, FFT or Prony's method [239], this work considers it preferential to instead fit to models based on the underlying physics of the signal [1], [183].

uncertainty [210]. Methods for accurate determination of the acoustic oscillation frequency will be discussed in detail in section 4.5.

4.4. Analysis of a LITGS signal

The LITGS signal contains a wealth of information about the local environment of the interaction region. As discussed above in section 4.2.1, the temperature of the medium can be derived from the oscillation frequency of the LITGS signal via derivation of the local speed of sound. While thermometry is the focus of this work, the local value of any parameter that has an impact on the size or shape of a LITGS signal can in theory be recovered (e.g. pressure, absorber (fuel) number density, quencher (oxygen) number density) or, if these are known, the gas dynamic parameters may be found.

4.4.1. Pressure

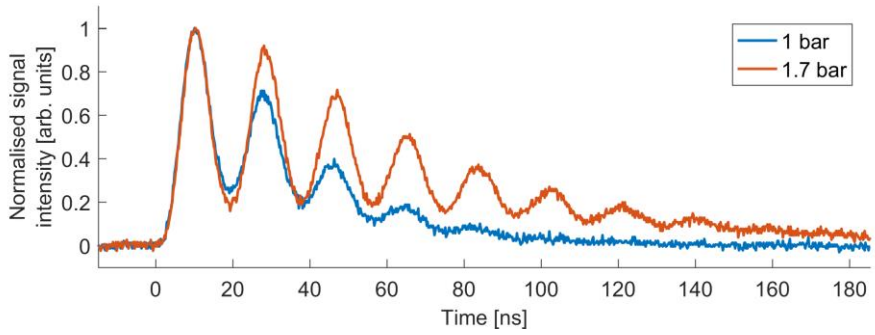

Figure 4-3 Pressurised cell data displaying the effect of pressure on the decay rate of a LITGS signal.

The rate of decay of the grating depends on the rate of diffusion of molecules which acts to equilibrate the initial density perturbation. Considering ideal gases, the diffusion coefficient is proportional to the mean free path[76] and mean velocity[77] of the molecules. The diffusion rate (D) therefore decreases with increasing pressure as $D \propto P^{-1}$ and increases with increasing temperature as $D \propto T^{3/2}$. Provided the temperature is known[78], the time constant of the

[76] Mean free path 'l' is inversely proportional to the gas density 'n', therefore $l \propto n^{-1} \propto T/P$

[77] Mean velocity for an ideal gas 'v' is related to temperature by $v \propto T^{1/2}$

[78] E.g. by deriving the temperature from the oscillations of the same LITGS signal.

underlying exponential decay of a LITGS signal can be used to derive pressure. Even a small change in pressure has a dramatic effect on the duration of a LITGS signal [Figure 4-3].

4.4.2. Tracer number density

The number density of target molecules present in the interaction region will determine the amount of energy absorbed and hence heat deposition, magnitude of the density perturbation and thus signal strength. Integration of the total signal intensity will provide a measure of target molecule number density. As a measurement of an intensity, this will be subject to increased uncertainty due to intensity noise much in the same way as CARS or PLIF.

The FARLIG technique developed in [3] (Fuel/Air Ratio by Laser-Induced thermal Gratings) extends the compositional measurement to also derive the local oxygen number density using the dependence of the quenching timescale Q_1 on oxygen number density. The contrast of the acoustic oscillations is also improved by the presence of oxygen due to the more rapid heat release.

In combination, these two effects can in principle be used to measure oxygen number density in parallel with toluene number density.

4.4.3. Quenching timescales

The timescales for the ‘fast’ and ‘slow’ quenching mechanisms, along with their branching ratio, have a significant effect on the initial rise of the LITGS signal, the relative heights of the first and second peaks and the contrast of the acoustic oscillations. These three parameters may be inferred from the best-fit parameters of a modelled LITGS signal. This can potentially provide a method for measuring oxygen number density in cases such as toluene in air, where the quenching of the toluene molecules is dominated by molecular oxygen.

4.4.4. Sources of uncertainty for thermometry

As with all diagnostic techniques it is important to understand the potential sources of uncertainty associated with using LITGS to perform temperature measurements. Equation (4-5)

offers an initial insight into the main sources of uncertainty for a temperature derived from a LITGS signal and will be separated into 3 terms in the following discussion.

Grating spacing

The conversion factor relating a measured LITGS oscillation frequency to temperature depends on the grating spacing, Λ,

$$T \propto \frac{\Lambda^2}{k_B} \tag{4-25}$$

The determination of the grating spacing from the geometrical alignment alone is prone to significant error. An investigation in [6] estimated a ± 9 % error in temperature assuming the beams could be manually aligned to within 0.3 mm of the targets on the alignment mask. This is unfortunately a best-case scenario given the standard procedure of optimising the alignment of the beams using a live signal after the initial geometrical setup.

In practice, this potentially large source of error does not impact the accuracy of a test cell or engine based setup. In such conditions it is straightforward to perform a calibration measurement at a known gas composition and temperature. The actual grating spacing can be derived from this calibration and applied to all future measurements with the reasonable assumption that the pump alignment will not be altered over the course of the experiments. Small adjustments to the probe beam are commonplace for signal optimisation, however these will not affect the grating formed by the pump beams and thus Λ. The accuracy of the derived value of Λ is therefore limited by the knowledge of the parameters used for the calibration measurement and the accuracy of the frequency recovery technique.

Gas composition

For compositional uncertainties of LITGS thermometry, the reader is directed to [6], [4] and [212] in which there are detailed discussions of the subject. The conclusions of these investigations are summarised below.

At any given temperature, the speed of sound in the interaction region is determined by the mean molecular mass, m, and ratio of specific heats, γ. These values are typically assumed to be fixed during analysis, hence any change in composition will shift the derived temperature proportional to the relative change in γ/m from the assumed value,

$$T_{derived} = \left(\frac{m}{\gamma}\right)_{assumed} \left(\frac{\gamma}{m}\right)_{actual} T_{actual} \quad (4\text{-}26)$$

In a combustion engine, the typical constituents of the gas mixture are air, fuel and exhaust gas residuals (EGR). The error in temperature is relatively insensitive to the exchange of EGR for air [4] as the m/γ ratio for each is essentially the same[79]. Considering a blend of 70 % iso-octane with 30 % toluene as used in this work, 'fuel' molecules have larger masses than molecules in air[80], and a larger value of m/γ by a factor of 5. Uncertainty in the fuel number density therefore dominates the error in derived temperature.

Measurements of the fuel number density for PFI and Early-GDI using QPLIF show a coefficient of variability of 23 % for typical injection conditions in the optical engine used for this work [4]. For the intended 1.97 % fuel concentration to create a stoichiometric mixture, the uncertainty in composition for fuel-rich deviation is therefore restricted to an upper bound of 2.42 % fuel concentration. Fuel-lean deviation is not limited by injection mixing, but instead by fuel content in the pockets of EGR observed in chapter 6. The relevant lower bound therefore corresponds to the minimum number density required to produce a visible signal, typically 10 % of the intended stoichiometric mixture, hence a lower bound of 0.20 %.

Considering the linear dependence of derived temperature on m/γ, in this work the estimated worst-case compositional errors in LITGS derived temperature are therefore – 1.6 % + 5.9 %.

Oscillation frequency recovery

LITGS temperature measurements inherently depend on the acoustic oscillation frequency,

[79] EGR (m = 28.7 gmol^{-1}, γ = 1.38, m/γ = 20.8 gmol^{-1}). Air (m = 29.0 gmol^{-1}, γ = 1.41, m/γ = 20.6 gmol^{-1}) [212].

[80] Fuel (m = 107.6 gmol^{-1}, γ = 1.09, m/γ = 99.2 gmol^{-1}).

$$T \propto f_{acoustic}^2 \tag{4-27}$$

Given the finite duration of a LITGS signal and the combination of a stationary thermal component with an oscillating acoustic component, extraction of the acoustic oscillation frequency is not trivial. Any uncertainty or systematic errors in deriving this frequency will translate into errors in derived temperature, amplified by the quadratic relationship between $f_{acoustic}$ and T. A full investigation into the optimal method for frequency recovery and the associated systematic errors is discussed in section 4.5.

Multiple temperatures

A key assumption made in the use of point-LITGS for thermometry is that the environment being probed has a uniform temperature across the measurement region. The description of point-LITGS as a point measurement is valid on the length scales of the engine cylinder, however the narrow crossing angle of the pump beams, combined with their 1 mm FWHM results in an interaction region on the order of 1 mm x 1 mm x 10 mm in size[81].

This long axial dimension introduces the possibility that the LITGS volume may contain multiple temperature regions. Contributions to the LITGS signal from each region will sum at the detector, resulting in a signal comprised of more than one acoustic oscillation frequency. For strong temperature gradients this can be observed as a beat frequency in the oscillations of a recorded LITGS signal. This effect was investigated in [213], in which a model was written to predict LITGS signals from multiple discrete temperature zones within a single LITGS volume. The technique was validated using measurements in a heated ethylene flow and a Gülder burner. If the standard single-temperature LITGS analysis was applied, the analysis tended to under-estimate the temperature of the interaction region compared to the mean of the two

[81] This would most likely be an upper limit. The actual effective length depends on defining the importance (or not!) of the contributions from the very tips of the 'diamond' crossing region. In these regions only the low-intensity wings of the beams overlap. Given the quadratic dependence of the grating magnitude on local pump intensity, the vast majority of the LITGS signal intensity is generated from the central region of full overlap. The effective axial spatial resolution will therefore be smaller than the tip-to-tip dimension of the 'diamond' intersection region.

temperatures. The signal generated by the hotter region has a shorter lifetime than that from the cooler region. The ‘cooler’ signal therefore has a larger contribution to the overall signal.

Due to the additional complication of the analysis, in what is already a challenging environment for LITGS measurements, the multiple temperature analysis is not used in this work. The effect is instead considered as a potential contribution to uncertainty in the derived temperatures. One advantage of performing simultaneous LITGS and TC-PLIF is the ability to not only use LITGS as a calibration of TC-PLIF, but to use TC-PLIF to determine whether each LITGS shot is measuring a volume with a strong axial temperature gradient.

4.5. Oscillation frequency recovery

The oscillation frequency of a LITGS signal is the critical parameter for thermometry. This frequency can be extracted from a LITGS signal in a number of ways, each with its own advantages. The 3 most appropriate are described below.

4.5.1. Peak separation

Perhaps the simplest method to determining an oscillation frequency is to measure the time between peaks and take the inverse to recover a frequency. This method is very useful as a quick rule-of-thumb for comparison of ‘live’ signals, displayed on an oscilloscope during an experiment. Small temperature differences between signals of the order of 10 K can easily be identified by aligning the first peaks in time and observing the signals drifting out-of-phase for later oscillation peaks.

For quantitative analysis, this method is strongly affected by the choice of peaks to compare, by the procedure used to determine the location in time of each oscillation peak and by the number of available peaks determined by the ratio of acoustic transit time to overall decay time.

Peak choice

For a typical LITGS signal, the separation in time between peaks is not constant for all peak pairs. The separation in time between the first and second peaks is marginally shorter than that of subsequent peaks. For later peaks, the grating has been fully established and, ignoring the exponential decay of the thermal and acoustic components, the time dependency is due to the acoustic oscillations. In contrast, the timing of the first peak is dependent not only on the acoustic oscillation frequency, but also on the timescales of energy deposition and quenching. The effect of finite timescales for grating generation is to delay the time at which the first peak reaches its maximum compared to the timing of an instantaneously generated grating.

It is therefore more accurate to derive the oscillation frequency from the separations of later peaks. This is easiest for long signals, such as those generated in higher pressures and low temperatures (> 1 bar and around 300 K). Such signals provide many visible oscillation cycles which facilitates selection of later peaks. In many practical applications however, either the pressures involved are lower or the temperatures are much higher and only a few peaks may be visible. Disregarding the first, strongest, peak throws away information and forces the peak separation method to rely solely on the weaker and noisier peaks.

Peak location procedure

The derived frequency and therefore temperature is highly sensitive to the location of each peak in time. For a typical peak separation of 20 ns, a shift of just 0.1 ns corresponds to a 1 % change in derived temperature.

For very strong signals finding the location of a peak's maximum is trivial. Weaker signals, such as those generated in the optical engine, have high frequency noise complicating the determination of the maximum. Smoothing procedures which replace each value with a weighted average of itself and its neighbouring values have the potential to shift the peak slightly away from its 'true' location towards any local peaks in noise. For very noisy signals,

the averaging window required to generate a smooth peak is on the same scale as the oscillation itself, leading to a very distorted peak and loss of contrast.

4.5.2. FFT

Origin of MATLAB FFT analysis

MATLAB scripts for FFT analysis of LITGS signals were written prior to this work by Ben Williams [3] and Rob Stevens [2]. These formed the basis of the investigations made by this work in section 4.5.2 into improving the FFT analysis of LITGS signals for application to in-situ calibration of TC-PLIF in chapter 6.

Principles

The Fourier transform of a signals allows its characteristic frequencies to be determined. The power spectrum of a LITGS signal will be comprised of two main features [Figure 4-4]. The underlying decaying exponential will generate a Lorentzian contribution centred at $\nu = 0$ and the acoustic oscillation will generate a second Lorentzian peak centred at the oscillation frequency. The finite duration of the signal and sharp initial rising edge will also introduce higher frequency contributions of smaller magnitude.

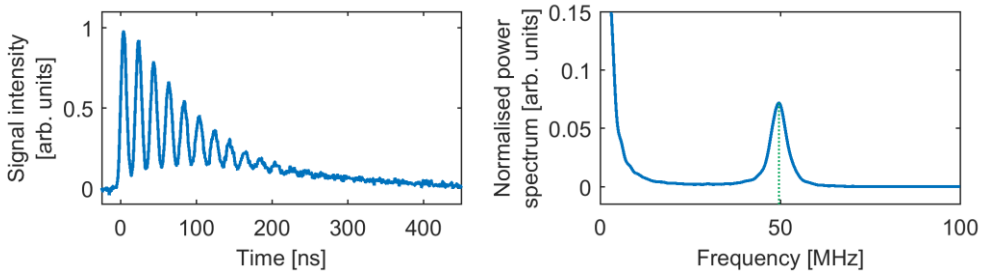

Figure 4-4 Example single-shot experimental LITGS signal (left) and the power spectrum (right) produced by FFT analysis. The location of the characteristic peak in the LITGS power spectrum is marked by the dotted line.

Finding the maximum of this acoustic oscillation peak in the power spectrum is critical to the measurement of the oscillation frequency and therefore temperature.

By taking the Fourier transform of the signal, information from the entire signal is encoded in the power spectrum without the need to define the exact timing of each peak's maximum, hence avoiding the associated sources of error. Fourier transforms have been thoroughly studied and programming environments such as MATLAB offer Fast Fourier Transform (FFT) routines as standard. This allows for very fast processing of experimental data. Using a standard office desktop computer, reading the data, performing the FFT for each signal and recovering the oscillation frequency takes only a few seconds for a 100-shot dataset.

Zero-Pad data vectors

The Discrete Fourier Transform (DFT) approximates the Continuous Fourier Transform (CFT) of a signal. The number of points describing the power spectrum, and therefore its frequency resolution, is determined by the length of the input vector which forms the repeating unit for the infinite-length input to the DFT process. A short initial vector will result in a very coarse power spectrum. To increase the resolution of the DFT output such that it very closely resembles the theoretical CFT output, the input vector is extended with elements of value zero known as 'zero padding'. In this work, the length of the signal vector was padded to lengths of increasing powers of 2 until the improvement in power spectrum resolution was negligible.

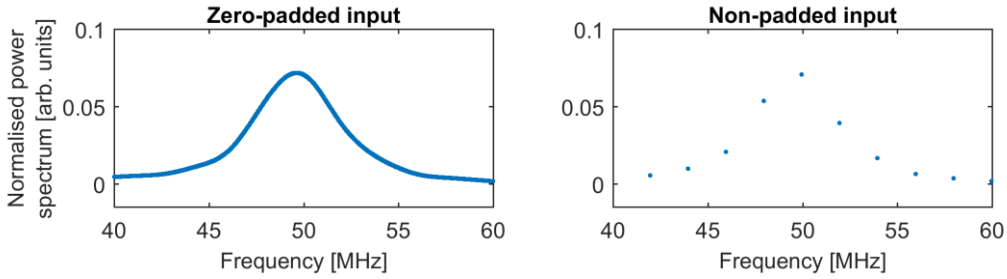

Figure 4-5 Improvement in resolution of power spectrum by zero-padding the input signal vector. N.B. both figures are plotted using the same point markers, the datapoints of the 'Zero-padded' spectrum are simply so close together that the point markers appear as a solid line.

Figure 4-5 displays the LITGS oscillation frequency peak of the power spectrum of Figure 4-4 calculated with and without zero-padding the signal vector before calculating the FFT. The improvement in resolution by applying zero-padding is dramatic, with the number of datapoints defining the LITGS frequency peak increasing by a factor of order 100.

Signal preparation for FFT - Windowing function

One of the principles of taking the Fourier transform of a signal is that the finite-length input signal forms the repeating unit of a signal with infinite length which is the subject of the transform. The start and end values of the input vector must be identical in order to avoid a discontinuity at the boundary between repeated units. Any step change at the boundary introduces spurious frequency content in the FFT output.

Step-changes can be removed by application of a windowing function which multiplies each element of the input vector by a number between 0 and 1. The choice of window, as discussed in [214], can have a dramatic effect on the power spectrum produced. Adding extra structure to the input vector necessarily changes the frequency content, so that each window has a characteristic power spectrum of its own. Doing nothing is not a solution either, this simply corresponds to a 'rectangle window' where every element is multiplied by 1 [Figure 4-6].

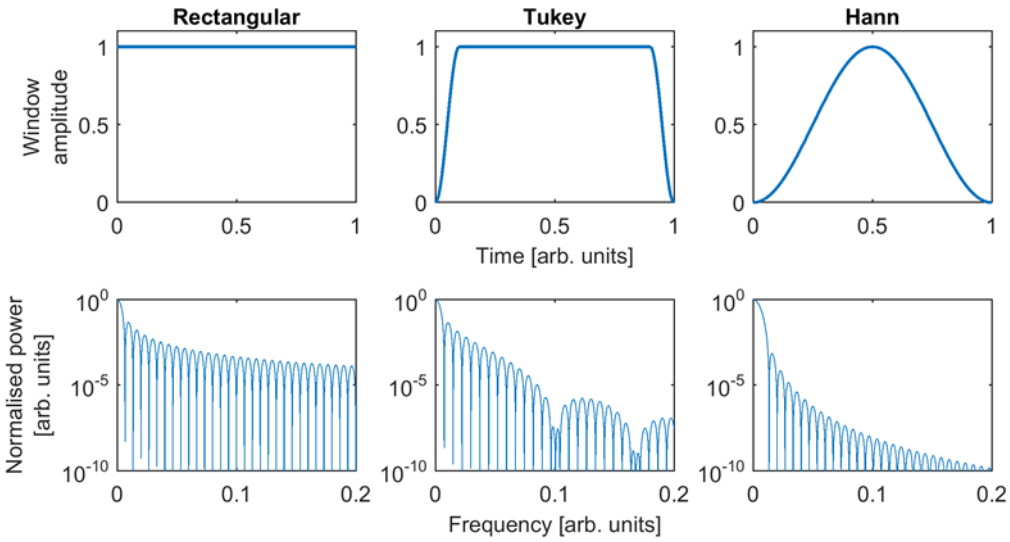

Figure 4-6 Rectangular, Tukey and Hann window power spectra with 'main-lobe' at ν = 0 and side-lobes for ν ≠ 0.

Different windows are optimised for different situations [Figure 4-6]. There is usually a trade-off to be made between heavy smoothing (Hann) which reduces the relative power of the side-

lobe artefacts[82] versus light smoothing (Rectangular or Tukey) which preserves the ability to finely resolve small changes in frequency[83].

For non-transient signals, such as a mixture of sinusoids of different frequencies, a common and effective pre-processing step is to apply a Hann window, $w_H(n)$, to the input vector,

$$w_H(n) = \cos^2\left(\frac{n}{N}\pi\right) \qquad \text{for } n \approx -\frac{N}{2}, \cdots, -1, 0, 1, \cdots, \frac{N}{2} \tag{4-28}$$

for sample 'n' of an input vector with length 'N' [214]. This $\cos^2$ function is smoothly varying with a value of zero at the start and end of the vector and a value of one at the centre. The Hann window has the effect of damping the signal to zero as it approaches each end of the vector, ensuring continuity when used to form a repeating pattern.

A LITGS signal is however very transient in nature. Application of the Hann window to such a signal suppresses the strong peaks near the start of the signal, resulting in a significant loss of information and an amplification of the contribution that weaker, noisier peaks near the centre of the vector make to the resulting power spectrum.

The window selected for use in preparing the LITGS signals for the FFT was the Tukey window, $w_T(n)$, which consists of a rectangular window modified by tapering the edges to zero with a cosine curve and is defined for sample 'n' of an input vector with length 'N' as:

$$w_T(n) = \begin{cases} 1 & 0 \le |n| \le \alpha\frac{N}{2} \\ \frac{1}{2}\left(1 + \cos\left(2\pi\left(\frac{n - \alpha\frac{N}{2}}{(1-\alpha)N}\right)\right)\right) & \alpha\frac{N}{2} \le |n| \le \frac{N}{2} \end{cases} \tag{4-29}$$

where the fraction of the window width composed of the cosine curve is (1 – α) [214].

The purpose of the Tukey window is to retain as much of the un-distorted signal as possible while still dampening the input vector values to zero at the edges. Previous LITGS analysis used

[82] I.e. the relative height of main-lobe to first side-lobe.

[83] I.e. a narrow main-lobe.

the Hann window as a windowing function, resulting in a distorted input to the FFT processing. In this work, the Tukey window was selected and displays a dramatic improvement in signal preservation over the Hann window [Figure 4-7].

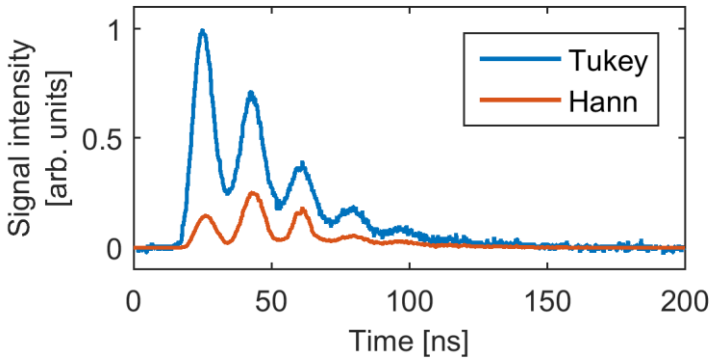

Figure 4-7 Tukey vs Hann windows, as applied to a single-shot experimental LITGS signal[84].

There is a corresponding improvement in the power spectra derived using the Tukey window [Figure 4-8]. The power spectrum of the 'Hann' windowed signal is strongly affected by the periodic troughs of the Hann window's power spectrum [Figure 4-6]. In contrast, the 'Tukey' case is dominated[85] by the two Lorentzian peaks corresponding to the 'thermal' and 'acoustic' contributions to the LITGS signal, as can be seen by comparing experimental to theoretical power spectra [Figure 4-8].

The peak of the power spectrum close to 50 MHz is interpreted as the LITGS oscillation frequency. This peak's location is affected by the Hann windowing, resulting in a shift in derived frequency and therefore temperature [Figure 4-9].

[84] The original signal was an experimental LITGS signal at 1 bar as in Figure 4-3.

[85] For frequencies below 100 MHz, above which the 'window' and noise contributions dominate.

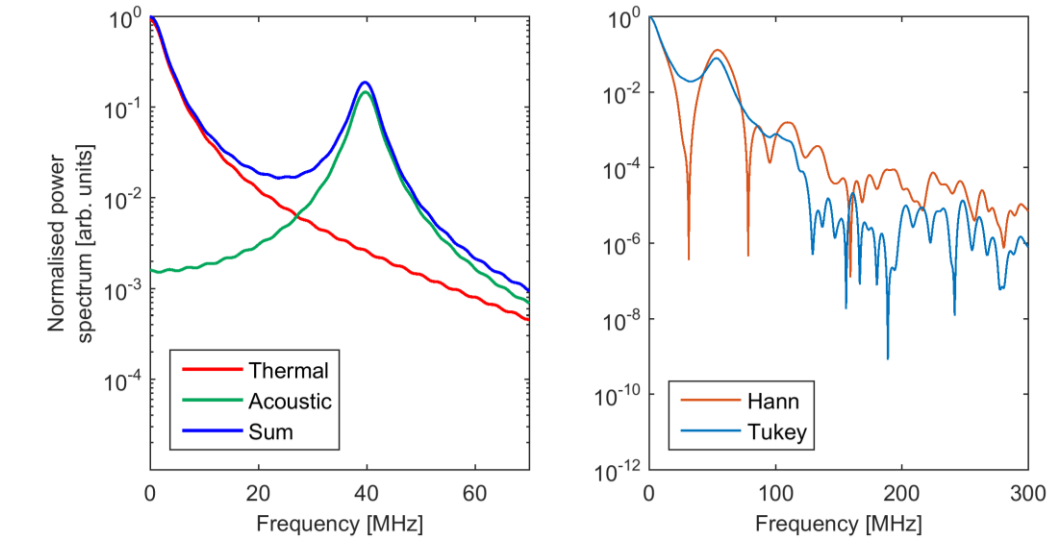

Figure 4-8 Tukey vs Hann windows. Left: 'Tukey' power spectra of theoretical LITGS signal contributions from Figure 4-2. Right: power spectra of the experimental LITGS signal[84] with 'Hann' and 'Tukey' windowing.

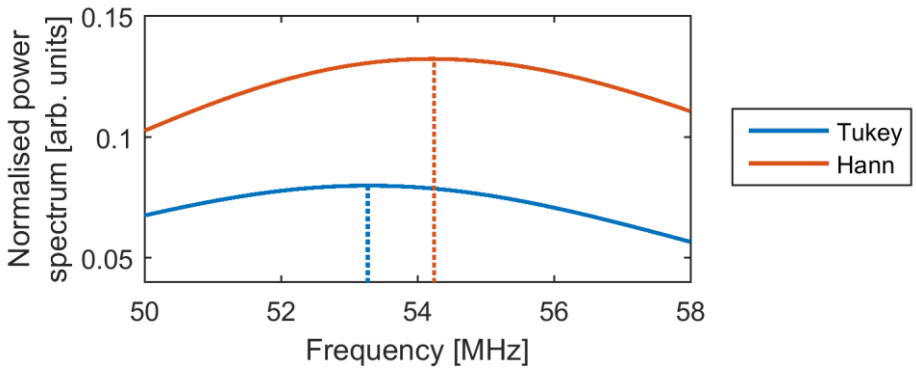

Figure 4-9 Shift in derived frequency owing to the use of a Hann window in comparison to the nominally correct Tukey window result. Magnified plot of the data in Figure 4-8 (Right).

It is therefore crucial to select an appropriate value for α, one which balances noise suppression at each end of the signal vector ($\alpha \rightarrow 0$) with preservation of the shape of the LITGS signal ($\alpha \rightarrow 1$). The value of α used in this work (0.9) lies within the range of values for which the peak position of Figure 4-9 is insensitive to variation of α [Figure 4-10]. The peak position varies by only 0.02 % for variation in α between 0.91 and 0.84, leading to variation in the derived temperature of only 0.04 %. In contrast, a poor selection of α would lead to errors in derived temperature of up to 3.1 % for this experimental signal.

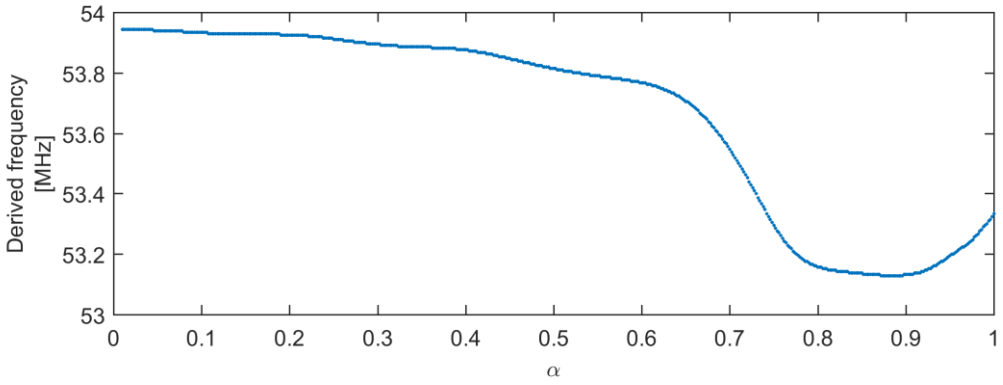

Figure 4-10 Derived oscillation frequency for the 1 bar LITGS signal of Figure 4-3 as a function of the Tukey window parameter 'α', defined in equation (4-29).

Signal strength requirements

Successful use of the FFT method for frequency recovery relies on having a sufficiently strong signal such that the acoustic oscillation frequency peak is well defined in the power spectrum. Key to this condition is that the magnitude of the peak is large enough to dominate both the underlying windowing spectrum and the noise related structure on the power spectrum. Typically this is achieved for signals with four or more identifiable peaks and with noise fluctuations smaller in magnitude than the contrast between peaks as in Figure 4-3 and Figure 4-8.

The FFT analysis runs into issues when the signals are both short (the time constant of the decay of the signal is comparable to the acoustic oscillation period) and noisy (noise fluctuations similar in magnitude to the contrast between peaks). In such cases the contribution of the acoustic oscillation peak is insufficient to dominate 'window' and 'noise' structure in the power spectrum [Figure 4-11]. This hampers identification of the maximum of the acoustic oscillation peak in the power spectrum and prevents meaningful temperature measurement. Application of the FFT routine to a set of such noisy data produces wildly varying peak frequencies because the routine picks out the local maximum from the noise structure in the power spectrum.

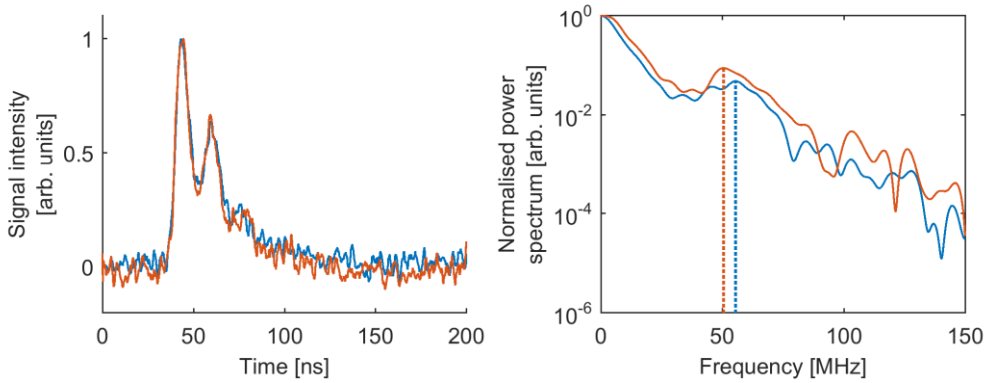

Figure 4-11 Power spectra from a pair of weak LITGS signals taken under nominally identical conditions.

The LITGS signals in Figure 4-11 were taken from a motored optical engine dataset at 90 CAD BTDC. Despite the near identical nature of the signals, the temperature derived from the power spectrum differs by 21 %. The full dataset has a standard deviation of the derived temperature of 13 %. Given that the cyclic variability of the engine for motored operation is around 1 % and the LITGS technique is inherently capable of < 1 % precision for sufficient signal strength even at the just-below-atmospheric pressures found at 90 CAD BDTC, this demonstrates that the FFT routine is not an appropriate method to use for very weak and noisy signals.

Accuracy of FFT temperature derivation

It has been previously assumed that the FFT analysis provides a satisfactory method for recovering the acoustic oscillation frequency of a LITGS signal. This analysis should indeed be successful in application to test cell measurements, where high pressures and stable tracer number densities can be maintained indefinitely, leading to long duration signals dominated by the acoustic oscillations. However, the accuracy of the frequency recovery by FFT cannot be assumed for combustion engine and flame measurements where signals are shorter, often with only a few visible peaks. An investigation into the accuracy of FFT analysis for LITGS in low pressure environments, conducted by Williams [6], found that for conditions with both high temperature and low pressure the ‘standard’ FFT analysis shows a systematic error towards lower derived temperatures. The worst case error in derived temperature, – 16 %, occurred for the extremal low pressure (1 bar), high temperature (650 K) modelled condition [6].

Such a conclusion suggests that FFT analysis is inappropriate for use in the current work or indeed in any environment where pressures are close to atmospheric. Despite this, the speed and simplicity of the FFT approach compared to the full fitting routine merits consideration as to whether it could be adapted for accurate use at low pressure and high temperature. One potential adaptation, the 'subtracted' method written by the author, shows a reduced systematic shift at low temperature and high pressure with a maximum error of – 3.5 % for 650 K at 1 bar. An alternative approach, the 'fitted' FFT method [6], does not show the systematic error at low pressure and high temperature, but is less accurate at low temperature and high pressure with an error of + 1.3 % for 650 K at 4 bar compared to an error of only – 0.36 % for the 'subtracted' method.

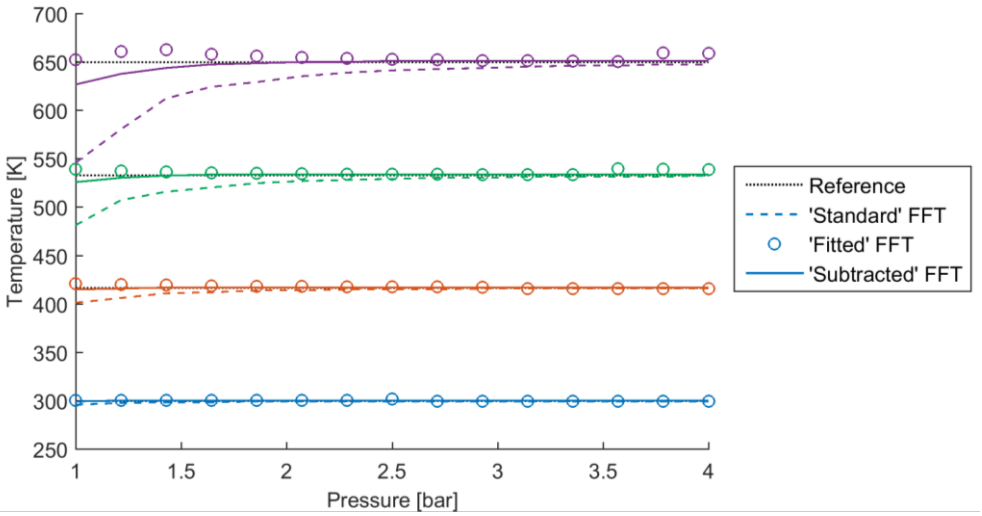

Figure 4-12 Accuracy of FFT temperature derivation by three methods for four reference temperatures (300 K, 417 K, 533 K and 650 K). The LITGS model [2] **was used to generate signals for a range of pressures for analysis by the 'Standard', 'Fitted' and 'Subtracted' FFT methods. The 'Fitted' FFT method is kindly provided by the authors of** [6].

Figure 4-12 shows the temperatures derived by the three different FFT analysis methods ('standard', 'subtracted' and 'fitted') from a reference set of modelled data for 4 different temperatures (300 K, 417 K, 533 K and 650 K) over a range of pressures (1 – 4 bar). An accurate analysis method should derive the reference temperature from the modelled signals for all combinations of pressure and temperature present in Figure 4-12. The systematic error for

the ‘standard’ FFT method is particularly apparent for the 650 K reference temperature, for which the ‘standard’ FFT method derives a temperature of 546 K at 1 bar.

The cause of this systematic shift in derived temperatures and the two potential alternative methods are discussed in the Appendix.

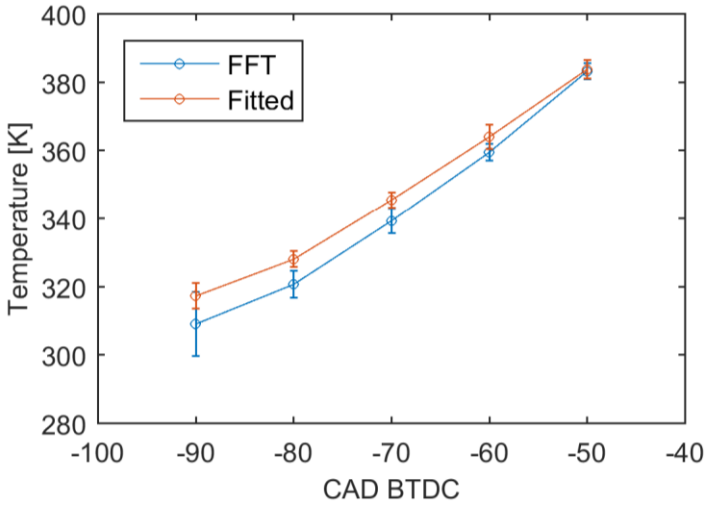

Figure 4-13 FFT vs Fitted derived temperatures for motored compression stroke data. Errorbars correspond to the standard deviation of 20 measurements at each CAD timing.

Experimental confirmation of this predicted difference in derived temperature is presented in Figure 4-13. For the low pressures early in the compression stroke ‘FFT’ temperatures are approximately 10 K cooler than the temperatures derived from the same data by fitting to a theoretical model[86]. This clearly displays the systematic bias to lower temperatures with the FFT analysis. As pressure increases throughout the compression stroke the discrepancy between the two analysis methods decreases until 50 CAD BTDC where the pressure is high enough that the FFT inaccuracy is minimal.

Suitability for engine measurements

Unfortunately, LITGS signals from the optical engine are often unavoidably weak and noisy [Figure 4-11]. Thus the standard FFT routine cannot cope as discussed above.

[86] See section 4.5.3 for a description of the ‘fitting’ approach to LITGS temperature derivation.

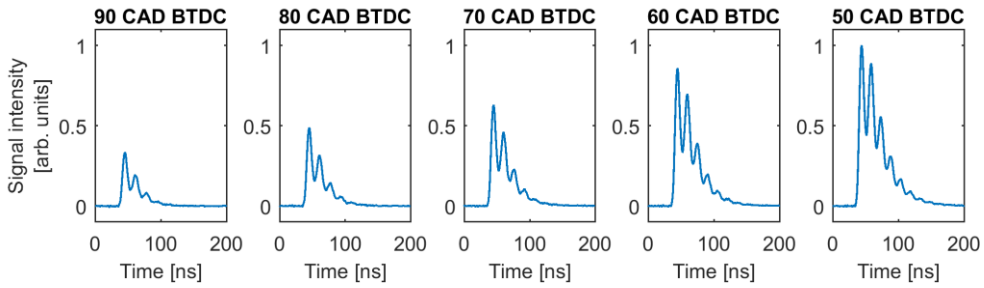

Figure 4-14 Variation in strength of mean LITGS signals as pressure increases during the compression stroke.

Strong signals generated towards the end of the compression stroke at higher pressures and tracer number densities are well suited to FFT analysis [Figure 4-14]. Weaker signals within the same dataset from earlier in the compression stroke can often be unsuitable for FFT analysis. This leads to compression stroke temperature profiles which are well resolved for later CAD values but extremely imprecise and inaccurate for earlier CAD values [Figure 4-15].

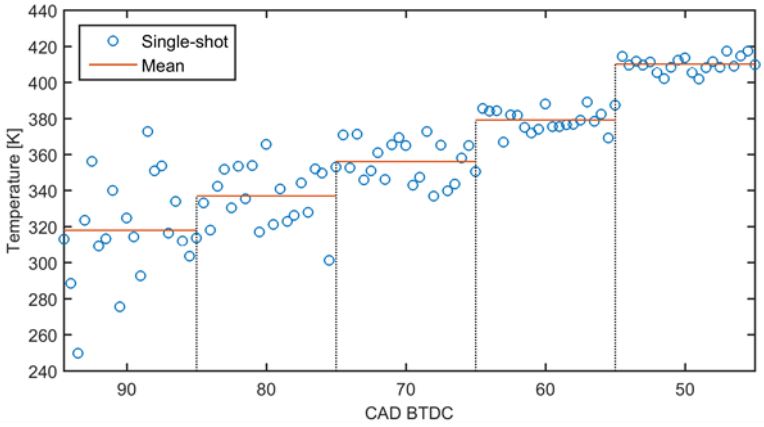

Figure 4-15 Single-shot FFT LITGS temperatures during the compression stroke displaying low precision of derived temperatures between 90 and 70 CAD BTDC.

Increasing the gain of the PMT to increase the signal to noise ratio of these weak signals is not appropriate as it would result in the stronger signals saturating the detector and producing a non-linear response to the incident light intensity. Additionally, as discussed later in chapter 6, varying the gain has other unwanted effects on the temporal response of the PMT.

The necessity of making LITGS temperature measurements reliably throughout the compression stroke motivated an investigation into the use of an existing routine for fitting to the theoretical model of [1] for temperature derivation, discussed below in section 4.5.3.

4.5.3. Fitting

Fitting routines involve the repeated calculation of a theoretical signal and comparison to the input data in an iterative loop. Fitting is therefore a much more computationally expensive method for extracting temperature information from a LITGS signal than the single FFT evaluation required for the FFT analysis routine.

In theory, fitting to a theoretical model could also be used to derive more information about the fluid properties than solely temperature, such as pressure and quenching rates. These investigations are however outside the scope of this work. The desired benefit for this work, in exchange for the extra investment in time and complication, is the potential for extracting temperature information from the weak and noisy signals characteristic of early CAD measurements during the compression stroke of the optical engine.

The LITGS fitting routine used throughout this work is based on the theoretical model of [1], was adapted for application to fitting in the frequency domain by Stevens [2] and applied to measurements of fuel/air ratios by Williams [3]. For a detailed discussion of the fitting routine and model, please refer to the above references. In what follows, the application of the fitting routine to the current experimental data will be discussed along with its suitability for temperature recovery from weak signals.

Fitted parameters

The fitting routine is designed to optimise up to 5 fit parameters from the set of: acoustic wave transit time between grating planes (τ), Reynolds number (Re), 'fast' quenching timescale (Q_1), 'slow' quenching timescale (Q_2) and branching ratio between 'fast' and 'slow' quenching mechanisms (split). 'τ' is the inverse of the acoustic oscillation frequency and is therefore the main parameter of interest for thermometry as it can be used to derive temperature. The Reynolds number is an important parameter in the LITGS signal model discussed in section 4.2.2 and adjustment of 'Re' provides the mechanism for the model to represent the effect of pressure on the signal. 'Q_1', 'Q_2' and their branching ratio 'split' control the energy deposition

to form the grating via the two-rate quenching model referred to in section 4.2.2, for further details the reader is directed to [1]. Throughout the fitting process, the Prandtl number was fixed at 0.7 as its variation over the temperature and pressure range of this work is minimal[87]. It is also important to 'centre' and 'scale' all fit parameters when passing to the optimisation function[88].

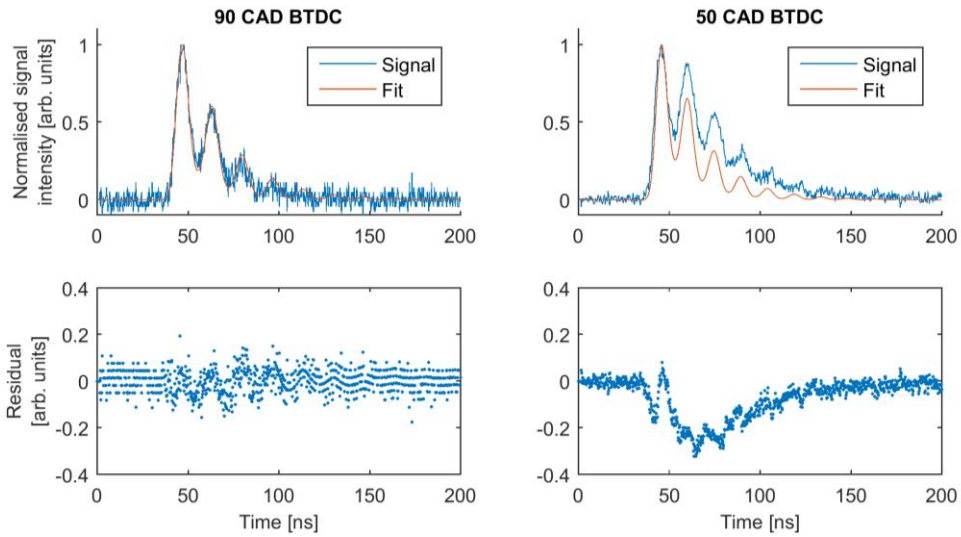

Figure 4-16 Example 1-parameter (τ) fit to LITGS signals at 90 and 50 CAD BTDC with residuals.

The simplest approach is to select appropriate values for all the parameters except the acoustic transit time, τ, then allow the fitting routine to optimise τ which can be readily converted into a derived temperature. Such a simple approach can only reproduce the shape of the recorded LITGS signal accurately for a narrow range of conditions where the other parameters[89] can be considered constant. During a compression stroke, the pressure and density of the gas mixture increases. The Reynolds number, being dependent on density, and the fast quenching timescale, Q_1, being pressure-dependent, are not constant and cannot be treated as such without affecting

[87] For air, the Prandtl number at 0 °C is 0.715, while at 400 °C it is 0.68, a difference of only 4.9 %

[88] It is critical to centre and scale all fit parameters to a range of $-1 < x < 1$ during fitting to ensure that lsqcurvefit.m (standard MATLAB function) varies parameters in appropriately sized increments. Without this scaling, lsqcurvefit.m would take the same sized step for all parameters. As there is a large difference in scale between parameters (Re is O(2) while Q_1 is O(–9)) this has a disastrous effect on converging to a suitable solution for all fit parameters. Only the fit parameter with the scale that matches the step size is optimised, the other parameters are either essentially unaffected by the increment or hit the upper or lower bounds within one iteration.

[89] Re, Q_1, split, Q_2.

the accuracy of the modelled signal. This results in large, systematic residuals for the fit at 50 CAD BTDC as in Figure 4-16, where Re and Q_1 were optimised for 90 CAD BTDC.

The minimum number of fit parameters for an accurate model of the recorded LITGS signal is 3 (τ, Re and Q_1). This single quenching rate model gives a moderately good fit and recovers the correct timing and spacing of the acoustic oscillation peaks but does overestimate the contrast of the acoustic oscillations [Figure 4-17].

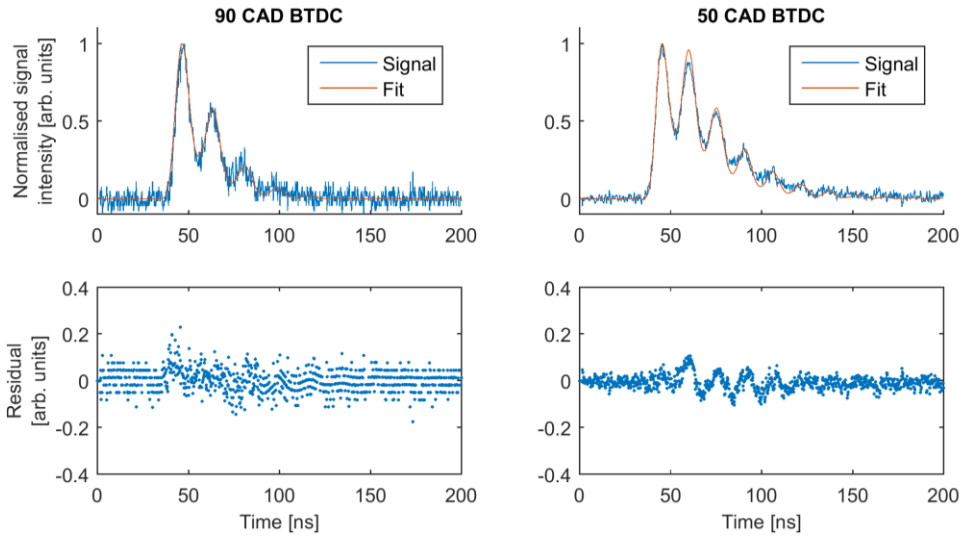

Figure 4-17 Example 3-parameter (τ, Re and Q_1) fit to LITGS signals at 90 and 50 CAD BTDC with residuals.

Inclusion of the slow quenching mechanism (Q_2), along with the branching ratio between the two quenching pathways (split) brings the number of fit parameters up to 5. This is sufficient to give an excellent fit with little to no structure to the residuals [Figure 4-18].

One concern when using the full 5-parameter optimisation is the large number of fit parameters. When combined with the not fully independent nature of the parameters, this can offer multiple solutions to the optimising routine with potentially different combinations of parameter values. If this were to occur and affect the value of τ, there would not be a unique solution for the temperature with a best fit to the data and the fitting routine would be inconsistent. However, the 5-parameter fitting routine is consistent with the 3-parameter derived temperature over a range of temperatures and pressures. In contrast, 1-parameter fitting results in a deviation

toward higher temperatures as pressure increases. This suggests that using the 5-parameter model is appropriate to use throughout the compression stroke.

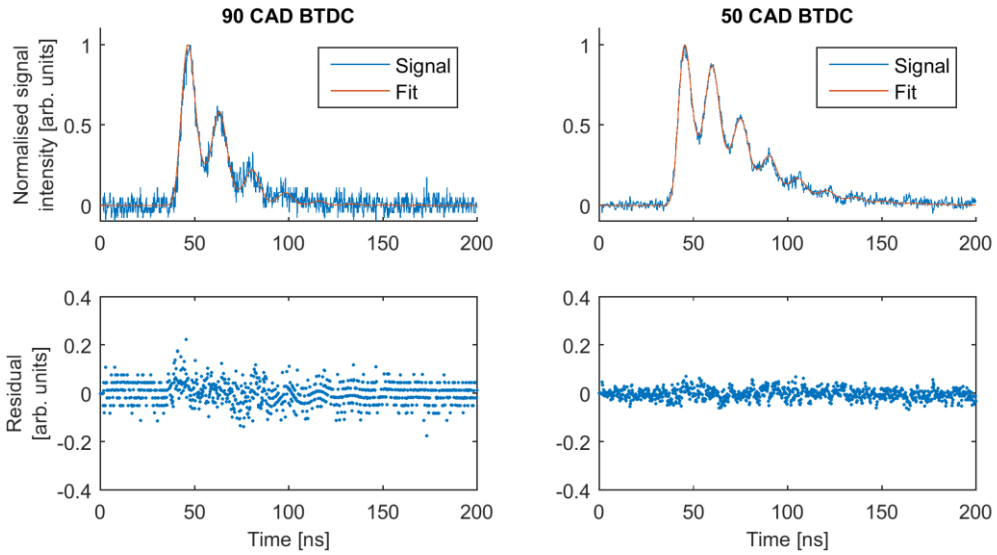

Figure 4-18 Example 5-parameter (τ, Re, Q_1, split and Q_2) fit to LITGS signals at 90 and 50 CAD BTDC with residuals.

Comparison to FFT results

Before the fitting routine can be used to recover temperatures from weak, noisy signals it must first be shown to derive the correct oscillation frequency for strong signals. A straightforward test for the validity of the fitting routine used in this work is whether it produces temperatures consistent with the results of the FFT analysis towards the end of the compression stroke at 50 CAD BTDC. For this late CAD timing, the errors in FFT derived temperature discussed above in section 4.5.2 are minimal due to the strong signals and higher pressures.

As can be seen in Figure 4-19 this is indeed the case. Mean temperatures for the 50 and 60 CAD BTDC measurement timings match to within 0.5 % using identical calibration factors, hence the fitting routine is deriving the same, nominally correct, frequency as the FFT analysis. The inherent resilience of the fitting routine to noisy signals is displayed for the earlier 90 and 80 CAD BTDC measurement timings. Where the FFT analysis is strongly affected by the noise levels and fluctuates wildly in its derived temperature, the fitted temperatures are consistent shot-to-shot with only a marginal decrease in precision compared to the stronger signals.

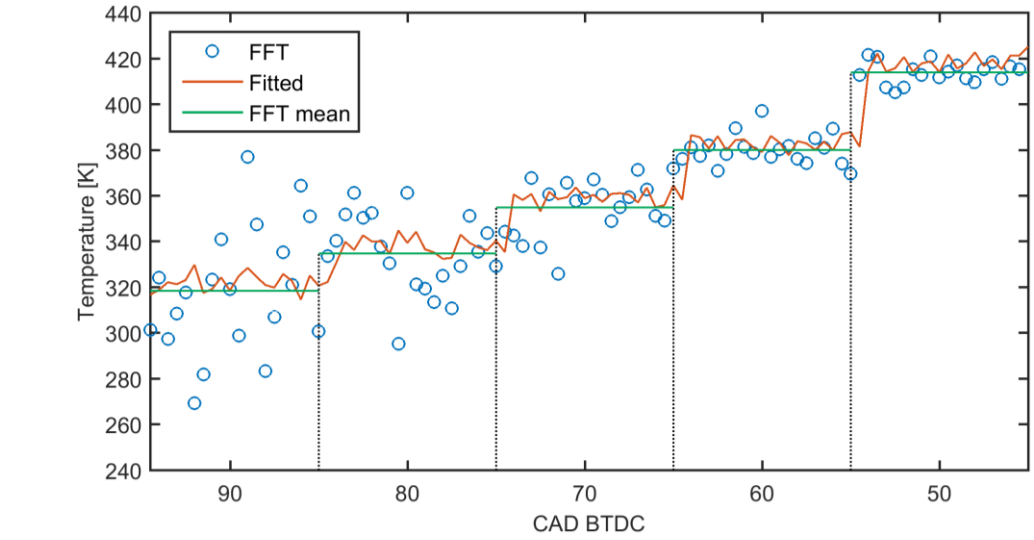

Figure 4-19 Fitted vs FFT-derived single-shot LITGS temperatures. Measurement sets taken at 5 fixed timings during motored operation (90, 80, 70, 60 and 50 CAD BTDC).

For the optical engine investigations of chapter 6, FFT analysis will no longer be considered and fitted LITGS results will be presented throughout due to the large dynamic range of signal strengths produced by the compression stroke measurements.

4.5.4. Suitability for calibration of TC-PLIF

To provide a suitable reference for in-situ calibration of TC-PLIF images, LITGS thermometry must be capable of providing an accurate, precise and robust temperature measurement.

The inherent dependence of LITGS on a measurement of an oscillation frequency rather than an intensity offers some resilience against uncertainty caused by intensity noise. FFT analysis offers a robust and straightforward method for extracting a temperature measurement from LITGS signals of sufficient strength. Challenging practical environments such as an optical engine often produce weaker, noisy LITGS signals. In such cases, application of a fitting routine can reliably recover temperature information from signals too noisy for FFT analysis. LITGS measurements in the engine have been shown to achieve high precisions of 0.1 – 1 % depending on pressure [25]. The accuracy of the LITGS derived temperature is limited by knowledge of

gas composition (γ/m) and its local variation. However, LITGS thermometry has been shown to be robust against the in-cylinder fuel fluctuations present in a fired optical engine[90] [25].

The high precisions achievable with LITGS and the understanding of the largest source of inaccuracy, the local gas composition, make it a suitable technique for in-situ calibration of the TC-PLIF images.

Toluene, as required for the implementation of TC-PLIF discussed in chapter 5, is an appropriate target molecule for LITGS due to its large absorption coefficient at 266 nm and the effective quenching of exited toluene by molecular oxygen allows the electronic excitation produced by the pump pulses to be rapidly transferred to the local environment as heat, generating a grating with good contrast.

4.6. Method

The LITGS system used throughout this work was designed and built for the work of Williams et al. [4] with the aim of reducing the footprint of the system. Typically a LITGS system would fill half a 2 m x 4 m optical table, allowing plenty of free space for development and placement of additional optics or detectors. For application to the confined space of an optical engine bay it was necessary to build a smaller version optimised for engine diagnostics. Freedom to make adjustments to the layout was exchanged for compactness.

4.6.1. Equipment

A flashlamp pumped solid state Nd:YAG laser (Continuum Minilite II) provided the pump pulses for this work. The priority for selection of the pump laser was its compact nature. The Minilite provides 4 mJ per 5 ns pulse at 266 nm with a repetition rate variable over the range 1 – 15 Hz, sufficient to perform point-LITGS experiments within the engine.

[90] Under suitably controlled conditions of plenum injection for PFI or early injection for GDI.

The probe laser for this work is a CW Diode-Pumped Solid State (DPSS) laser (CNI-MLL-III). This provides 300 mW at 671 nm and as with the Minilite the laser is robust, turn-key and compact. The space constraints and simplicity of operation outweigh the signal strength benefits of using a long-pulse probe laser such as [185].

Fast-response photodiodes are readily available and affordable. Typically a 300 mW probe would be sufficient to generate a detectable signal using a photodiode detector in this geometry and in a lab environment. However, in this experiment the optical losses associated with conducting the experiment in a running engine[91], whether motored or fired, are sufficient to degrade the signal. Therefore a photomultiplier tube (PMT) was used to amplify the small photoelectron signal produced by the incident light intensity into a large electrical signal. Additionally, the large active area of the PMT when compared to a fast photodiode was sufficient to capture the entire signal beam without requiring a lens to focus the beam onto the detector surface. This removes the reflection losses of two surfaces from the signal collection path and decreases the amount of scattered light directed onto the detector.

The PMT is sensitive to both the red probe light and the scattered UV pump light. A high-transmission, narrow bandpass filter for 671 nm was used to block scattered light which would otherwise be detected as a prompt small peak before the first LITGS peak.

As will be discussed in chapter 6, varying the PMT gain alters the time response of the detector. It is therefore important to record all measurements within a dataset using a consistent gain value.

4.6.2. Optical Layout

For accessible experiments on a large optical table, the pump and probe wavelengths, along with the desired grating spacing typically specify the crossing angles of the 3 input beams. With the restricted optical access of the optical engine, the critical design factor was to ensure all

[91] E.g. passing through windows which experience fouling while the engine is running or scatter and absorption from gases and particles inside the cylinder.

beams could pass through the 16 mm clear aperture quartz windows in the cylinder wall [4]. The crossing lens (nominal focal length of 300 mm) and pump spacing (12 mm) were chosen to meet this requirement and to ensure the grating spacing (6.2 µm) resulted in an oscillation frequency (56 MHz) low enough to be accurately recorded by the 500 MHz bandwidth oscilloscope. The oscilloscope used for data acquisition in this work has a bandwidth of 2.5 GHz, partly relaxing the restriction on detectable oscillation frequencies.

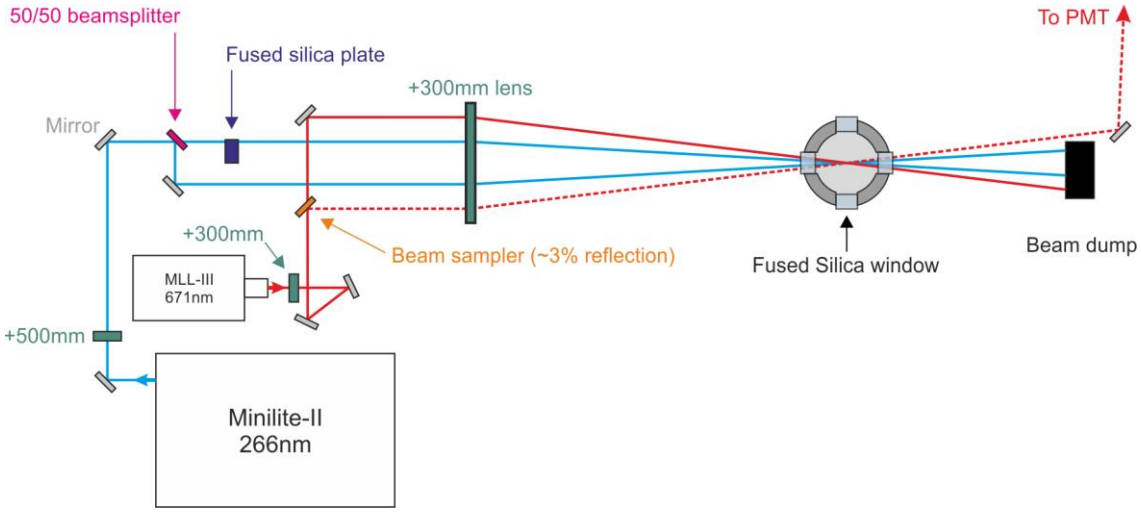

Figure 4-20 Point-LITGS optical layout for engine thermometry showing pump (blue), probe (red) and signal trace (red dashed) beams. Not to scale.

By insertion of spherical lenses into the pump and probe beam paths upstream of the crossing lens, Keplerian telescopes were formed with the crossing lens [Figure 4-20]. This results in collimated pump and probe beams being crossed at the interaction region. The beam widths were matched at a diameter of 1 mm to maximise the spatial overlap of the beams and therefore the magnitude of the scattered LITGS signal. The intersection of comparatively large[92], collimated beams results in a stable interaction region that is resilient to the effects of beam steering.

While the incident angle of the probe beam with respect to the grating planes is specified as the Bragg-scattering angle [equation (4-2)], there is no restriction on the probe beams to lie within the same plane as the two pumps. To aid in the separation of signal, pump and probe beams

[92] A spot size of 1 mm diameter is large compared to e.g. focussed beam geometries of order 100 µm.

after the interaction region it is often advantageous to bring the probe beam out of the (horizontal in this case) plane which increases the separation between the beams at a given distance from the measurement point. The vertical separation of pump and probe reference marks on the masks of Figure 4-21 may therefore be freely chosen.

The LITGS beams lie within a horizontal plane approximately 20 mm below the base of the pent-roof of the cylinder head. The beams cross at the centre of the barrel [Figure 4-20], after which the pump and probe beams are dumped and the LITGS signal is directed to the PMT approximately 5 m away. This long beam path serves to reduce the intensity of unwanted scattered light from the engine (falling as $1/r^2$) while collecting the entirety of the coherent signal beam in an effort to improve the signal-to-noise ratio of the measurement. An iris was used to reduce the aperture of the PMT to match the signal beam diameter, further reducing the potential for scattered light collection.

4.6.3. Alignment procedure

Accurate alignment of the LITGS beams is essential for high quality measurements, in particular matching the beam sizes and obtaining good spatial overlap at the measurement region optimises both the intensity and stability of the signal [215]. The alignment of the LITGS system proceeds as described in detail in [3], but is summarised here for convenience.

The two pump beams, probe beam and signal trace beam are aligned using a pair of masks to ensure the beams propagate through the engine cylinder[93] parallel to each other and with the correct spacing determined in section 4.6.2 [Figure 4-21 a)]. The crossing lens is then positioned such that the two pump beams cross at the desired measurement location and hit the correct reference marks on the rear mask (b). By placing a pinhole at the crossing point, mounted on an XYZ translation stage, observation of the pump beam transmission as the pinhole is translated

[93] Actually, for initial alignment the cylinder barrel is removed as without the crossing lens in place the beams would not pass through the 16 mm clear aperture windows.

allows the location of the intersection point to be determined with considerable accuracy[94] (c). The pinhole and the reference marks on the rear mask now define the correct beam geometry for all beams for production of a LITGS signal. This is important as the dispersion of the crossing lens will result in a different focal length for the UV pump beams compared to the red probe and signal trace beams. The incidence angle of the red beams on the crossing lens must be adjusted to bring all beams into alignment (d). The mask and pinhole are then removed and the signal trace beam is used to correctly position the detector.

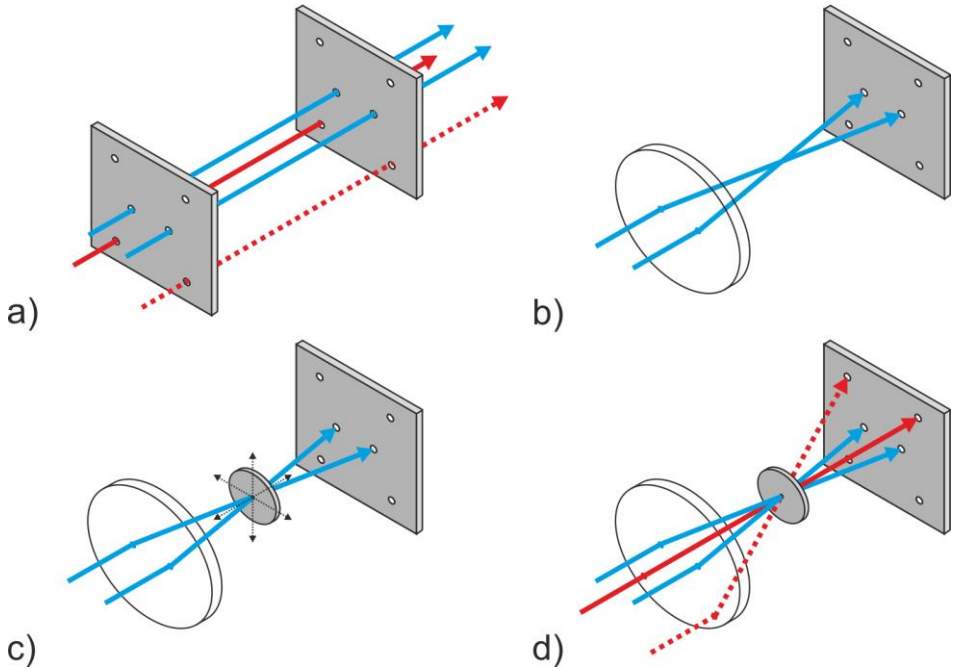

Figure 4-21 LITGS alignment procedure as detailed in the main text for the pump (blue), probe (red) and signal trace (red dashed) beams.

This alignment procedure is typically sufficient to produce a LITGS signal using a test environment of toluene vapour. The alignment is then optimised using a 'live' LITGS signal and very small adjustments to the beam steering mirrors.

4.6.4. Target species selection

As the target species for LITGS simply provides a means of introducing energy into the bulk gas to form the 'grating', with an appropriate choice of pump laser wavelength it can be chosen

[94] When correctly centred on the intersection point, translation of the pinhole transversely to the optical axis will cause both transmitted beams to 'appear' and 'disappear' at the same time.

to be the LIF tracer to simplify simultaneous measurements with LIF and LITGS. The LIF tracer in this work, toluene, is sufficiently well quenched in the fuel-air environment of an optical engine to efficiently deposit energy absorbed from the LITGS beams as heat to form the grating.

4.7. Results, analysis and discussion

The initial developmental work on this LITGS system had already been completed prior to this work [3]. In what follows, the initial testing focusses on the saturation tests and temperature sensitivity validation required in order to apply the LITGS technique to in-situ calibration of TC-PLIF images of the in-cylinder temperature distribution.

4.7.1. Saturation tests

When recording data it is good practice to limit signal strengths to remain within the linear response regime of the detector being used. In the case of LITGS signals recorded using a PMT, either the gain of the PMT or the level of optical attenuation before the detector must be carefully selected to ensure the PMT can accurately record the variations in intensity of the optical signal over the duration of the LITGS signal. If these variables are not correctly set, the current demand on the final dynode stages of the PMT is too great and the effective gain is reduced for the strongest sections of an incident signal. A PMT is considered to be ‘saturated’ when the relationship between the intensity of the incident light and the magnitude of the signal produced is no longer linear.

Temperatures derived from saturated LITGS signals (peak detected voltage greater than 100 mV) in Figure 4-22 are systematically colder than the equivalent unsaturated measurements with a worst-case discrepancy of –1.1 % for a peak PMT signal voltage of 1 V. It is therefore important to remain in the linear regime of the PMT.

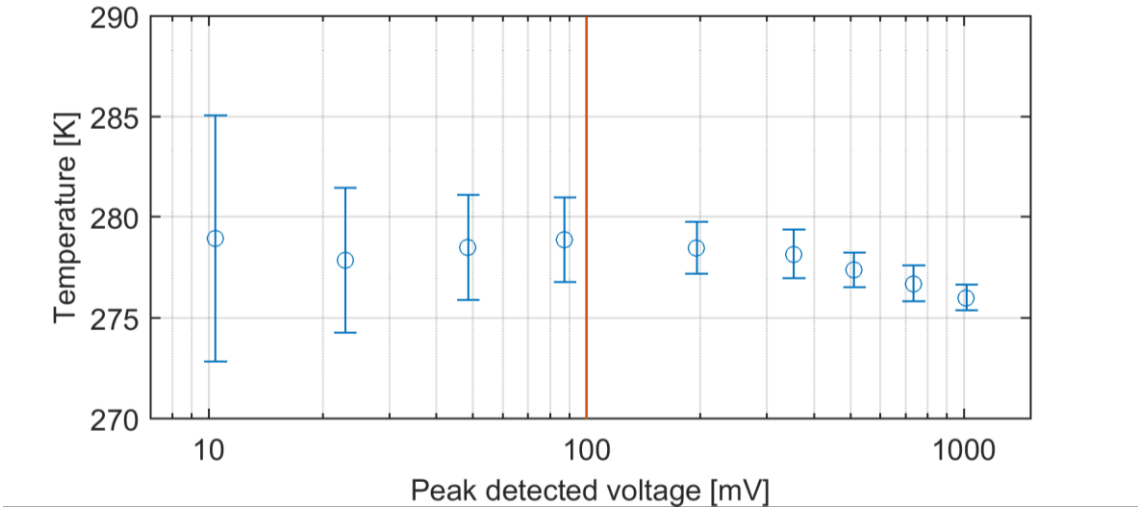

Figure 4-22 Temperatures derived from LITGS signals as a function of incident LITGS signal intensity as recorded by the peak PMT signal voltage. Attenuation of the incident optical signal was achieved using neutral density filters. The PMT was operated at a fixed gain. The 100 mV linearity limit discussed in the text is marked by a red line. Errorbars represent the standard deviation of 100 measurements for each datapoint.

In order to determine a suitable metric for the adjustment of PMT gain and optical attenuation to avoid detector saturation during experiments, the linearity of the PMT response to a LITGS signal was investigated for a range of peak signal voltages produced by the PMT [Figure 4-23].

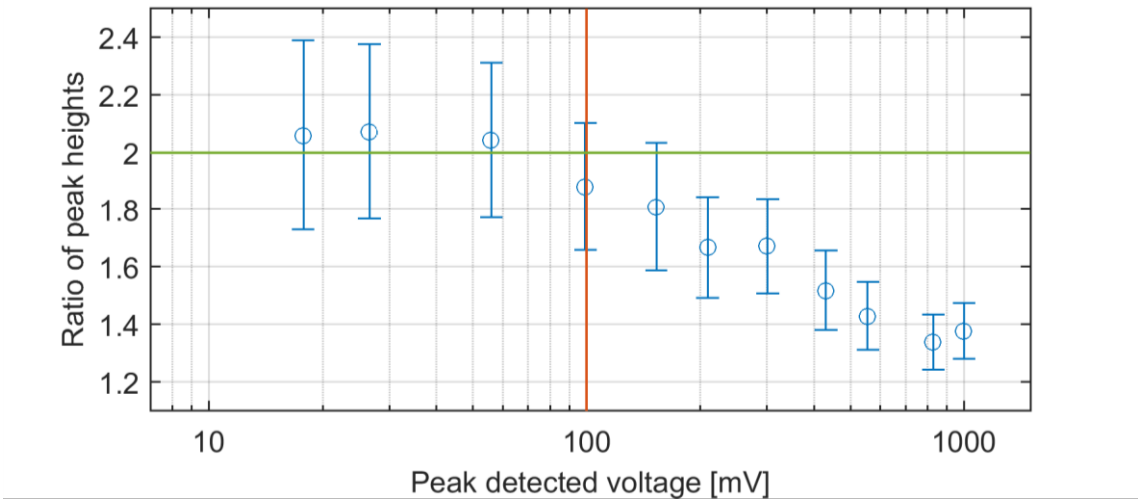

Figure 4-23 Ratio of peak detected signal voltage for an un-attenuated optical LITGS signal and an optical LITGS signal attenuated by 50 %, as a function of peak detected voltage for the un-attenuated optical signal. Variation of the peak detected voltage was achieved by changing the PMT gain. The nominally correct ratio of peak heights for a linear response of the PMT is marked by a green line at a ratio of 2. The 100 mV linearity limit discussed in the text, above which the signals are considered saturated, is marked by a red line at 100 mV. Errorbars correspond to the standard deviation of 100 measurements for each dataset.

For each datapoint of Figure 4-23, two sets of LITGS signals were recorded by the PMT, one set with a neutral density filter of 50 % transmission and one set un-attenuated. Variation of the peak detected voltage for the un-attenuated optical signal between datapoints was achieved by changing the PMT gain. For a linear response, the ratio of mean peak signal voltages between the two sets should be 2, matching the intensity ratio of the incident optical signals. At 100 mV, saturation starts to become apparent as the peak detected voltage of the un-attenuated signal is less than double that of the signal with 50 % attenuation.

It is apparent that the error bars of Figure 4-23 decrease in magnitude for higher peak detected voltages, corresponding to higher PMT gain values. The incident optical signal is consistent for all datasets, hence the fluctuations in the optical signal intensity will have no dependence on gain. Multiplier noise, related to the statistical distribution of the number of secondary electrons emitted from each dynode, also contributes to the fluctuations in the detected signal and its fractional contribution to the overall noise of the signal decreases as the gain is increased to higher values [216].

Clearly the best solution from a PMT linearity point of view is to use signals sufficiently weak to avoid saturation. However, as discussed in section 4.5.2, weak signals with low signal-to-noise ratios present difficulties for the FFT analysis. A limit of 100 mV was set as the strongest acceptable signal output to ensure that even the strongest signals in a dataset were only negligibly affected by saturation. While this made the analysis of the signals significantly more challenging, the penalty of a systematic error in derived temperature was considered an unacceptable price to pay for strong, clean signals.

4.7.2. Engine warm-up measurements

The temperature sensitivity of the LITGS system was verified by recording LITGS measurements at 2 minute intervals during the warm-up phase of the engine. Under motored operation, frictional heating and heat transfer from the compression-heated gases to the cylinder walls acts to raise the temperature of the engine. This heat can then in turn be partially

transferred to the incoming cool fresh charge by conduction from the body of the plenum and the cylinder walls. The engine takes many minutes of running to reach an equilibrium temperature, during which time there is a subtle increase in the temperature of the in-cylinder gases. This offers an opportunity to demonstrate the ability of the LITGS system and analysis to resolve small in-cylinder temperature differences of only a few Kelvin.

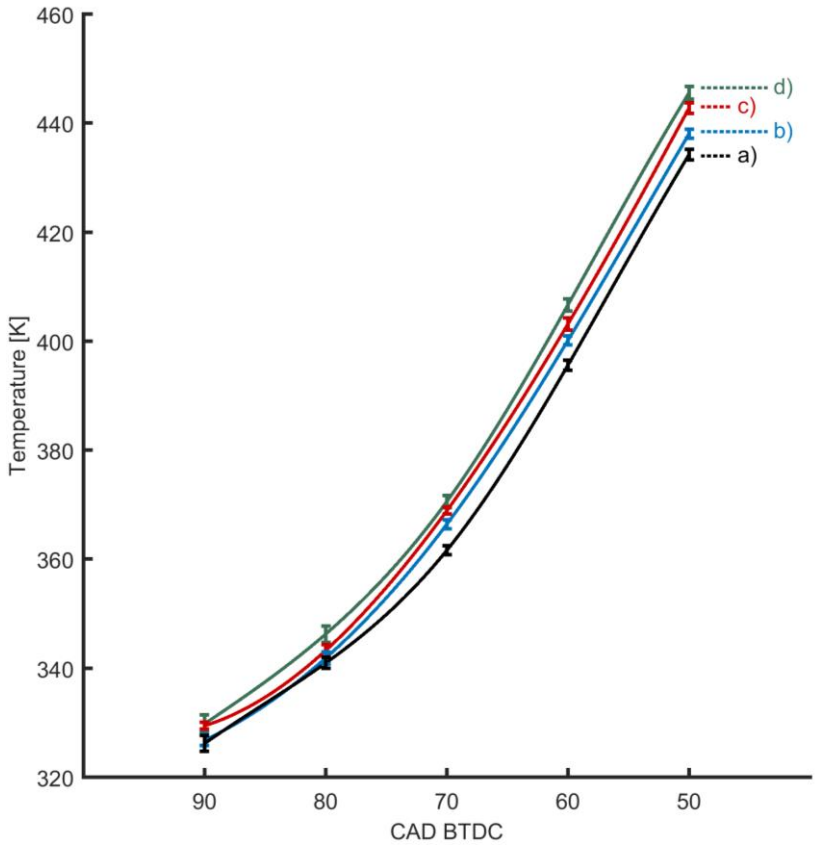

Figure 4-24 Mean LITGS temperature measurements for sequential datasets a) to d) during an 8 - 10 minute period during the warm-up phase of the motored engine. The errorbars represent the standard error of the mean[95] at each CAD timing for each dataset. Spline fits to each dataset have been added as guides to the eye.

For each dataset, 20 LITGS measurements were recorded at each of 5 CAD timings during the motored compression stroke from 90 to 50 CAD BTDC in increments of 10 CAD. The sequential runs a) to d) of Figure 4-24 are each separated in time by approximately 2 minutes and show an increase in the mean temperature at each CAD timing of around 3 K or 1 %.

[95] I.e. each errorbar is $\pm \sigma/\sqrt{N}$ where σ is the standard deviation and N is the number of measurements at the relevant CAD timing for each run, in this case N = 20.

4.7.3. Heated intake air measurements

For a more direct approach to generating variations in temperature, a resistive heater was used to heat the intake air by externally heating the body of the plenum through which the intake air passes. Figure 4-25 displays the temperatures recorded at 90 and 50 CAD BTDC relative to those recorded without heating.

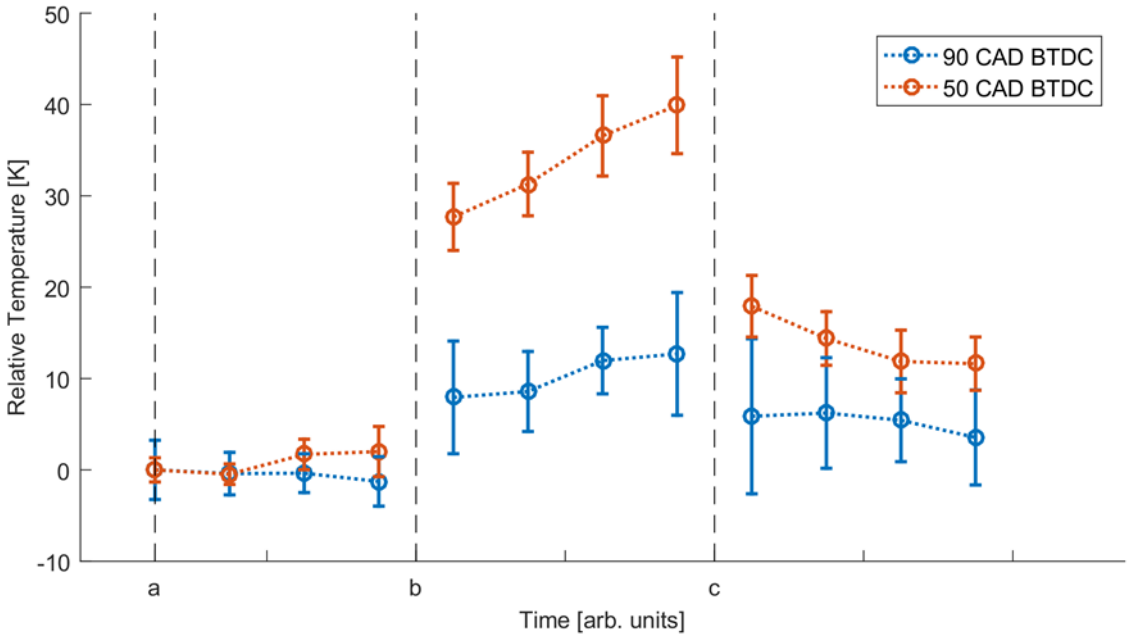

Figure 4-25 LITGS mean temperatures at 90 and 50 CAD BTDC over time. Errorbars correspond to the standard deviation of single-shot temperatures within each dataset. a) Initial unheated condition used as reference for the relative temperature scale. b) Heater switched on. c) Heater switched off.

Figure 4-25 shows constant temperatures derived from the first 4 unheated datasets (a). After the plenum heater is switched on (b), a rapid initial temperature rise is observed, followed by a gradual increase over the following 6 – 8 minutes as the plenum, with a large heat capacity due to its bulk, gradually heats up. A similar effect is observed after the heater is switched off (c) where the plenum cools down by several Kelvin between each dataset. Both the weak signals at 90 CAD BTDC and the stronger signals at 50 CAD BTDC display the same trends over time.

The compression stroke of an engine can be approximated by an adiabatic process, with a corresponding temperature rise dependent on not only the initial temperature, T_1, but also the initial and final pressures, P_1 and P_2,

$$T_2 = T_1 \left(\frac{P_2}{P_1}\right)^{\frac{\gamma-1}{\gamma}} \quad (4\text{-}30)$$

Thus for the same increase in intake air temperature at (b), the temperature increase recorded at 50 CAD BTDC is over twice that recorded earlier in the compression stroke at 90 CAD BTDC owing in part to the different final pressures.

4.7.4. Precision

Based on measurements in a static engine with a known composition of toluene vapour in air, the inherent precision of measurement with this LITGS system is 0.2 % for the strongest signals with 5 – 7 oscillation peaks visible. The actual precision of measurements in a running engine will likely be worse than this, particularly for signals early in the range of compression stroke timings investigated (90 CAD BTDC) where pressure and tracer number density are lower, leading to weak, noisy signals. The value of 0.2 % therefore represents a lower bound for the precision of the LITGS measurements in this work.

Given that the cyclic variability in peak pressure of the motored engine is approximately 1 % and sets of LITGS measurements at each CAD timing produce standard deviations of approximately 1 %, it appears that cyclic variability of the engine provides a significant contribution to the spread of derived temperatures for a given CAD timing. It is therefore likely that the actual precision of the LITGS measurements lies within the range 0.2 – 1.0 %.

4.8. Summary and conclusions

In this chapter, the application of the portable LITGS system developed in [4] to the optical engine was investigated. Approaches to LITGS thermometry in the literature were reviewed and the theory of LITGS grating formation and temperature derivation was summarised.

The potential approaches to analysis of LITGS signals for thermometry were discussed with particular consideration given to assessing the strengths and weaknesses of each technique with regard to signals characteristic of optical engine diagnostics. The ‘peak separation’ method

raises issues with peak selection and location, leading to potential biases in derived temperature. FFT analysis in its current form, while offering rapid derivation of temperatures, was found to be inaccurate in environments with both low pressures and high temperatures and has limitations for application to weak signals. Fitting to a theoretical model is far more computationally expensive than the above two methods but offers higher accuracy and is applicable to weak signals without the dramatic loss of accuracy and precision seen with FFT analysis. All LITGS signals from the optical engine in this work are therefore analysed by fitting to a theoretical model [1], [2], [3]. Preliminary testing of the LITGS system with the optical engine provided experimental data for validation of these conclusions.

Additionally, saturation tests determined the linearity limit of the PMT detector used in this system and motored engine tests validated the LITGS system's capability to track changes in the in-cylinder temperature.

5. Two-Colour PLIF

In this chapter the initial development of a Two-Colour Planar Laser-Induced Fluorescence (TC-PLIF) system is reported. A discussion of the principles of PLIF is presented in 5.2, covering the generation of fluorescence and its application to thermometry. Section 5.3 discusses the motivation for selection of TC-PLIF in this work. Section 5.4 details the experimental methods and data analysis routines. The results of experiments to validate the system and determine its suitability for application to optical engine thermometry are presented in section 5.5.

5.1. Introduction

Molecular tracer PLIF was selected in chapter 3 as the measurement technique to provide 2-dimensional maps of the in-cylinder temperature distributions inside the optical engine. This chapter discusses the development of a TC-PLIF system starting with an explanation of the principles of PLIF thermometry and the selection of TC-PLIF over competing PLIF techniques. The initial selection of tracer species and optimisation of spectral filtering optics are discussed, followed by a description of the equipment, experimental methods and data analysis routines required to capture a pair of fluorescence images and convert the raw images into a temperature map. Finally the results of preliminary experiments to validate the temperature sensitivity of the technique, the image correction process and the capability for time-resolved measurements are reported. The relevant literature for TC-PLIF has already been reviewed in chapter 3, to which the reader is directed for a summary of PLIF techniques as applied to thermometry in combustion.

5.2. Theory of TC-PLIF

In this section a discussion of the principles of PLIF thermometry is presented, forming the basis for the selection of TC-PLIF for development in section 5.3

5.2.1. Qualitative description of PLIF

By forming a pump laser beam into a sheet, tracer molecules in a planar section of the measurement volume can be resonantly excited into a higher electronic energy state. The subsequent spontaneous emission (fluorescence) is incoherently emitted in all directions, a fraction of which can be used to form an image by a lens orthogonal to the laser sheet to provide a spatially-resolved 2D measurement.

The molecular states and processes involved in PLIF are detailed in [Figure 5-1], using toluene as an example of a tracer molecule. The description is based on the discussion in Koban [96] to which the reader is directed for further details. In what follows it is assumed that the laser intensity in PLIF experiments is small enough to make stimulated emission negligible [217].

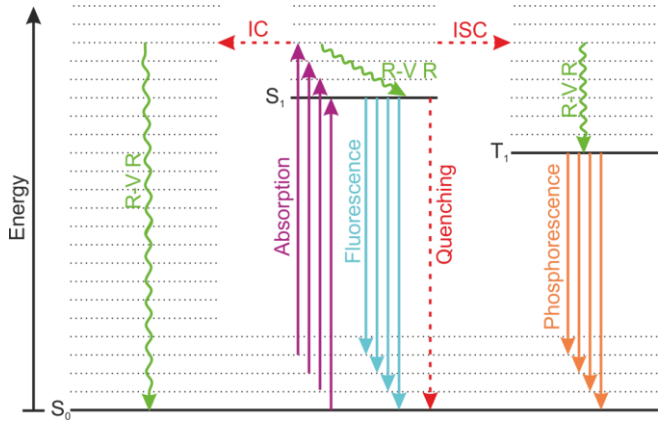

Figure 5-1 Processes involved in PLIF with toluene as a tracer, based on discussion in [96]**. Solid black lines represent electronic states, where S_0 is the ground singlet state, S_1 is the first excited singlet state, T_1 is the first excited triplet state. Dotted black lines represent excited vibrational states, while the closely spaced rotational state lines above each vibrational state line are not shown for simplicity of the diagram. R-VR is ro-vibrational relaxation within the same electronic state, IC is internal conversion between states with the same spin multiplicity, and ISC is inter-system crossing between states with different spin multiplicity.**

A photon from the incident pump beam can be absorbed by the tracer molecule from the ground state S_0, electronically exciting the molecule to the excited state, S_1. This excited electronic state has a nanosecond-scale lifetime [5] before decaying to the ground state via the spontaneous emission of a fluorescence photon. These fluorescence photons comprise the LIF signal. The efficiency of fluorescence emission after excitation with a pump photon is however far from

100 %. For conditions relevant to this work, collisions with other molecules occur on picosecond timescales [3] and can perturb the molecule to either relax into a lower energy ro-vibrational state within S_1, leading to fluorescence at longer wavelengths, or prevent radiative emission entirely e.g. by Internal Conversion [Figure 5-1]. Internal Conversion involves a transfer from S_1 to a highly excited ro-vibrational state in S_0, leading to non-radiative relaxation down the ro-vibrational manifold towards the lower energy, thermally populated levels. Quenching collisions can transfer energy to the colliding species in the form of kinetic energy or excitation, resulting in a transfer from S_1 to S_0 without radiative emission. In contrast, Inter-System Crossing (ISC) does not prevent the emission of photons, however phosphorescence on the spin-forbidden transition from the T_1 triplet state to the S_0 singlet ground state has a ms-scale lifetime compared to the ns-scale lifetime for fluorescence from the excited singlet state. ISC therefore effectively 'quenches' the fluorescence for the purposes of PLIF measurements [96].

The fluorescence quantum yield, FQY, for any given state 'n' is a measure of the efficiency of fluorescent signal generation, defined as the ratio of fluorescent to total decay rates for the state,

$$\varphi_n = \sum_i \frac{A_{ni}}{\sum_i A_{ni} + Q_n} \tag{5-1}$$

where A_{ni} is the rate of spontaneous emission from the excited state 'n' to state 'i' and Q_n is the combined rate of all quenching processes, including internal conversion and inter-system crossing from the excited state 'n' [100].

When referring to molecules, the FQY spectrum '$\phi(\lambda)$' refers to the efficiency of fluorescence emission at any particular wavelength, which when integrated over all emission wavelengths describes the total FQY of the molecule 'ϕ'. The FQY spectrum is therefore the fluorescence analogue to the absorption spectrum of a molecule.

Considering the processes involved in PLIF, an expression for the number of fluorescence photons collected for a given pixel of the PLIF camera after monochromatic excitation may be written:

$$\text{Signal} = N_{photons} * \sigma_{abs} * n_{tracer} * V_{pixel} * \phi * \eta_{collection} \quad (5\text{-}2)$$

Application of the laser sheet results in 'N' photons per m^2 reaching the measurement region imaged by a particular camera pixel. Each tracer molecule has an effective cross-section to 'collide' with a photon resulting in absorption given by the absorption cross-section 'σ'. The number of tracer molecules in the measurement region is given by the tracer number density 'n_{tr}' and the volume imaged onto a particular pixel 'V_p'. For every absorbed photon, the number of fluorescence photons emitted is given by the fluorescence quantum yield 'ϕ'. Finally the efficiency of the collection optics[96] 'η' determines the number of photons successfully reaching the camera pixel 'S', which can be expressed as:

$$S = \frac{E}{h\nu} V_p n_{tr} \sigma \phi \frac{\Omega}{4\pi} \eta_{opt} \quad (5\text{-}3)$$

where 'E' is laser fluence (Jm^{-2}), 'h' is Planck's constant, 'ν' is pump laser frequency, Ω is the solid angle subtended by the collection optics and η_{opt} is the transmission efficiency of the collection optics [107] [218].

The fluorescence signal produced by PLIF measurements therefore contains terms dependent on the laser parameters, tracer number density, absorption cross-section, fluorescence quantum yield (FQY) and collection optics.

5.2.2. Application to thermometry

Thermometry with PLIF using molecular tracers utilizes the temperature-dependence of the absorption and/or emission spectra of the tracer.

Unlike the sharp atomic transitions used in TLAF, the broad and temperature dependent absorption and emission spectra of a molecular tracer arise from the ro-vibrational structure

[96] Including the solid angle subtended by the imaging lens, which will be significantly less than the full 4π.

within each electronic state, which permits many different transitions between S_0 and S_1 with a wide range of energies.

The ro-vibrational levels above each electronic state are thermally populated, therefore at higher temperatures, higher ro-vibrational states of S_1 may be reached by the absorption of a pump photon. The increase in the range of available states leads to a broadening of the absorption spectrum. Additionally, at higher temperatures the reduction in the energy gap between the highest populated S_1 state and the lowest ro-vibrational state of S_1 contributes to a redshift of the absorption spectrum to longer wavelengths[97] [84], [85]. Emission spectra, whose spectral distribution is defined by that of the FQY, as a function of temperature have been less widely studied and may have less generally applicable trends. For example, toluene's emission spectrum red-shifts as temperature increases [5], however no studies of acetone's fluorescence spectrum as a function of temperature were found in the literature review of this work.

A phenomenological model for tracer FQY, such as that developed for toluene by Koban et al. [99], may be used to predict the fluorescence intensity as a function of temperature, pressure and composition[98]. Such an approach is not necessary in this work as the use of an in-situ calibration technique removes the need to model the fluorescence signals of experiments and literature data for measured absorption and emission spectra are sufficient to optimise the design of this PLIF system. The three main approaches to thermometry with molecular tracer PLIF are discussed below.

1-colour total intensity

With sufficient knowledge of the parameters in equation (5-3), including their temperature-, pressure- and spatial- dependence, the integrated intensity of fluorescence provides a measurement of temperature. However, the dependence of the total fluorescence intensity on so

[97] As discussed in [81], the redshift of the absorption spectrum of organic molecules with temperature may be explained by the Sulzer-Wieland mechanism [240].

[98] E.g. concentration of oxygen which strongly quenches excited toluene molecules.

many, often imprecise or unquantifiable, parameters makes it a challenging measurement choice for thermometry.

Of particular concern for many engine applications is the requirement for either quantification of the local tracer number density across the object plane, or a restriction to measurement under homogeneous tracer conditions. The operating conditions of interest to this work involve non-uniform tracer distributions, during GDI operation or as a result of partial mixing with EGR. Without the application of an independent diagnostic technique to measure the tracer distribution for every PLIF measurement, which dramatically increases the cost and complexity of the overall 'thermometry' system, 1-colour PLIF is therefore not suitable.

Two common alternative approaches of time-resolved PLIF thermometry are discussed below. Both take ratios of two PLIF measurements so that many of the terms in the PLIF signal expression, equation (5-3), are identical by definition for both signals and cancel. This leads to perhaps the most significant advantage of the signal ratio detection methods, the independence of any variation in local tracer number density across the measurement region, dramatically reducing the uncertainty of measurements in inhomogeneous tracer environments.

2-line excitation

Two-line excitation LIF relies on the temperature dependence of the tracer's absorption spectrum [106]. By using sequential pulses of different wavelength from two lasers, two regions of the absorption spectrum can be probed. The ratio of the fluorescence signal intensities generated by the two pulses provides a measure of temperature at the excitation region,

$$\frac{S_1}{S_2} = C\frac{I_1(x)\sigma(\lambda_1,T)\phi(\lambda_1,T)}{I_2(x)\sigma(\lambda_2,T)\phi(\lambda_2,T)} \tag{5-4}$$

where S_i is the fluorescence signal in photons per pixel, C is a constant, I_i is the pump laser intensity as a function of position (x), σ is the absorption cross-section as a function of excitation wavelength and temperature (λ_i,T) and ϕ is the FQY as a function of excitation wavelength and temperature (λ_i,T).

The two signals are separated in time by the delay between incident laser pulses and therefore the fraction of emitted signal intensity that reaches the detector is only limited by the collection optics. The collection of all the available fluorescence for two excitation pulses results in 2-line excitation having higher signal-to-noise ratio than 2-colour detection.

The use of two laser pulses for tracer excitation does however result in the signal ratio of equation (5-4) retaining the dependence on laser intensity spatial profile for each pump sheet. This will either reduce the accuracy and precision of the temperature measurement, or require the energy and spatial intensity profile of every shot from both pump lasers to be recorded and used to correct the resulting signal ratios.

The precisions achieved by Rothamer et al. [107] varied between 2.1 % – 10 % over the engine cycle and under the majority of the motored engine conditions studied, the precision of the temperature measurement increased throughout the compression stroke towards top-dead-centre. This trend can be attributed to a combination of two factors. Firstly, the magnitudes of the absorption cross-sections for 3-pentanone at the excitation wavelengths of 277 nm and 308 nm diverge at a faster rate as temperature increases from 300 K to 650 K. This results in higher sensitivities and thus higher precisions for higher temperatures. Secondly, the compression of the gas mixture increases the number density of the tracer, resulting in larger signals and higher signal-to-noise ratios.

2-colour detection

Two-colour detection PLIF relies on the temperature dependence of the tracer's emission spectrum. Filters are used to select two different wavelength-regions of the emitted fluorescence for detection with separate cameras. The ratio of the fluorescence intensities from the two spectral windows provides a measure of temperature at the excitation region,

$$\frac{S_{\Delta\lambda_1}}{S_{\Delta\lambda_2}} = C\,\frac{\phi(\Delta\lambda_1, T)}{\phi(\Delta\lambda_2, T)} \tag{5-5}$$

where S_i is the fluorescence signal in photons per pixel, C is a constant and ϕ is the FQY as a function of wavelengths within a spectral window and temperature ($\Delta\lambda_i$,T).

The tracer can be excited using a single laser pulse, ensuring that the absorption cross-section and any fluctuations in pump intensity are identical for each signal. When taking the ratio of the two signals, these terms in equation (5-3) cancel, producing a measurement independent of not only tracer number density, but also laser intensity profile and absorption cross-section.

For a given tracer, two-colour detection will typically produce weaker signals than two-line excitation due to the deliberate rejection of fluorescence with wavelengths outside the chosen spectral windows. This results in a poorer signal-to-noise ratio for TC-PLIF.

5.3. In-situ calibrated 2-Colour Detection

The motivation for selecting TC-PLIF for development for application to engine thermometry is presented in this section. The merits of in-situ calibration are discussed and an investigation into potential molecular tracers confirms the suitability of TC-PLIF for this work.

Independence of variations in tracer distribution is critical for thermometry in a fired optical engine, hence 1-colour PLIF was immediately discounted. Both TC-PLIF and 2-line excitation are valid choices for thermometry in IC engines [81], [103].

2-line excitation requires measurement of pump laser intensity profiles and modelling of both the absorption cross section and FQY. Imprecision arises if any of these three parameters are not evaluated under exactly the same conditions of the measurement[99]. The potential precision gain from the higher signal-to-noise ratios is at least partly offset by the vulnerability to imprecision arising from these three sources. TC-PLIF simply requires a calibration curve relating signal ratio to temperature and is to a large extent immune to window fouling.

[99] For obvious practical reasons, the detectors recording the intensity profile of each pump sheet must be outside the cylinder. Any window fouling will therefore cause the intensity profile in the measurement region to deviate from that measured outside the cylinder.

Reductions in overall transmission will be likely to affect each spectral window equally, and the single pump laser excitation scheme is the most straightforward of the two ratio techniques.

The challenging environment of a fired optical engine motivates the selection of the technique with the greatest resilience to deviation of in-cylinder conditions[100] from the calibration regimes. Therefore, provided the signal intensities provide sufficient signal-to-noise ratio for analysis, TC-PLIF should be the more robust of the two ratio techniques and is selected for this work, subject to the caveats discussed below.

5.3.1. In-situ calibration

For both ratio techniques discussed above, conversion of signal ratio to temperature requires the measurement of a calibration constant, 'C' in equations (5-4) and (5-5). This is often calculated by making preliminary measurements in comparison with thermocouple data [115] or in the case of engine measurements calibration to the polytropic temperature assuming compression heating of the intake gases. As such it cannot account for any variations between the calibration tests and experimental environment.

The accuracy with which the signal ratio is related to temperature, for both 2-line excitation and TC-PLIF, depends on knowledge of the FQY of the tracer as a function of temperature, pressure, excitation wavelength and mixture composition. Any inaccuracies in these relationships will directly influence the derived temperature. This reliance on theoretical or empirical models of FQY (and absorption cross-section in the case of 2-line excitation) can be removed by performing an empirical calibration of the dependence of signal ratio on temperature.

In principle this empirical calibration can be performed in a test cell under known conditions of temperature, composition and pressure to generate a map between the PLIF signal ratio and each of these parameters. Such a calibration method raises questions about the applicability of

[100] E.g. temperature, pressure, composition, window fouling.

the calibration environment to the conditions inside the measurement environment. For predictable, well-controlled systems such as gas flows used to validate CFD models this may be a highly accurate method. For the more complex and partially unpredictable conditions found inside a firing combustion engine, these relationships may not accurately describe the wide variety of local environments experienced by the tracer.

In-situ calibration of the TC-PLIF signal ratio by an independent thermometry technique such as LITGS guarantees that the calibration conditions, being one and the same as the measurement conditions, are an accurate representation of the tracer's local environment. As engine conditions are varied, the simultaneous independent temperature measurements can be used to update the calibration to ensure the accuracy of the TC-PLIF thermometry is maintained. Strictly, this is the case only for the local region in which the LITGS measurement is performed. For example, the composition may vary across the TC-PLIF measurement plane in such a way that it affects the spectral dependence of the fluorescence and thus biases the temperatures reported by TC-PLIF in a way that is not accounted for by this calibration. The assumption made in the calibration procedure is that the variation of TC-PLIF signal ratio with time (i.e. measurements over a range of CAD timings) may be used to determine a calibration curve which is also applicable to the variation of TC-PLIF signal ratio with location (i.e. local measurements across the TC-PLIF image).

This method of in-situ calibration is therefore not fully comprehensive. Nevertheless, given that parameters such as pressure will not vary hugely across the measurement plane, that any variation that solely affects the total intensity of fluorescence will be corrected for and also that the TC-PLIF data discussed in chapter 6 appears self-consistent, this in-situ calibration method represents an improvement over 'offline' calibration.

5.3.2. Tracer selection

Fluorescence

When selecting a tracer for PLIF measurements, consideration must be given to the predicted signal intensity, temperature sensitivity and compositional effects over the range of relevant experimental conditions. This work focusses on the temperature distributions in the compression stroke before combustion, therefore tracers generated during combustion such as radicals (OH, CH, C_2) and atomic tracers liberated from compounds by the high temperatures of the flame such as metal salts (InCl → In) are not considered here.

Organic molecules can provide strong fluorescent signals and are typically soluble in, as well as having similar boiling points to, gasoline. Acetone and toluene are two of the most popular organic fluorescent tracers and have been sufficiently well-studied to permit temperature measurements based on literature values for their absorption cross-sections and FQY [81].

2-colour detection or 2-line excitation?

While TC-PLIF is attractive for this work due to its inherent independence of laser intensity profile and single pump laser, the tracer must be capable of generating sufficient fluorescence intensity over the relevant range of temperatures, pressures and mixture compositions. If no such tracers were available, it may be determined that 2-line excitation is the optimal 2D thermometry technique for these conditions, despite its increased experimental complexity. In what follows, the properties of toluene and acetone will be compared in order to compare their expected fluorescence intensities for typical optical engine conditions in this work.

Physical properties

Property	Iso-octane	Toluene	Acetone
Molecular weight (g/mol)	114.2	92.1	58.1
Boiling point (°C)	99.2	110.6	56.1
Density at 25 °C (g/cm^3)	0.69	0.87	0.79
Number of carbon atoms	8	7	3

Table 5-1 Physical properties of potential TC-PLIF tracers and their comparison to iso-octane.

For successful TC-PLIF measurements in combustion engines, the fuel must be composed entirely of non-fluorescing species except for the TC-PLIF tracer.

Gasoline is comprised of a wide variety of hydrocarbons each containing between 5 – 12 carbon atoms [219]. Typically the largest fraction is comprised of straight or branched alkanes with a smaller fraction of cyclic alkanes and aromatic hydrocarbons. The evaporation of gasoline proceeds in a step-wise manner, with the lightest species evaporating first and the heavier species remaining longest in the liquid phase. Iso-octane (2,2,4-Trimethylpentane) was used as the base fuel for this work due to its appearance as a major component in standard forecourt gasoline and the fact that it is non-fluorescing.

Acetone is a more volatile species than toluene, with boiling points of 56 °C and 111 °C respectively. When used as a tracer added to a reference fuel mixture, acetone tracks the evaporation of the lighter components of the fuel, toluene co-evaporates with the medium fraction, while a heavier tracer such as tri-methylbenzene (TMB) is required to follow the heavy fraction [76]. Toluene will co-evaporate well with the iso-octane base fuel. Acetone will have much poorer co-evaporation which could result in differences between the spatial distribution of the tracer and base fuel for GDI.

Also, forecourt gasoline has a typical aromatic content of around 30 %. While missing both the lightest and heaviest components of standard gasoline, a blend by volume of 70 % iso-octane with 30 % toluene will serve as a better approximation to standard gasoline than an equivalent mixture of iso-octane with acetone.

Absorption cross-section

The absorption cross section of acetone in the UV displays an overall increase in magnitude and a redshift to longer wavelengths with increasing temperature [84]. However, the effective increase of around 40 % between 300 – 650 K holds only for excitation wavelengths greater than 270 nm. For 266 nm on the short-wavelength edge of the absorption feature, the increase in

magnitude is counteracted by the redshift making the increase far less significant, only of the order of 10 % from the value at 300 K of 4.3 x 10^{-20} cm^2 [84].

The absorption cross-section of toluene increases with temperature when excited at 266 nm, due to a strong peak in the absorption spectrum at around 268 nm at room temperature. As temperature increases from 300 – 650 K, the broadening of the absorption spectrum leads to an increase in the absorption cross-section at 266 nm by almost a factor of 3 from 2 x 10^{-19} cm^2 to 5.5 x 10^{-19} cm^2 [85].

Fluorescence Quantum Yield (FQY)

Acetone has a low FQY of 0.002 [220], which decreases with temperature by approximately 40 % over the 300 – 650 K range relevant to the compression stroke temperatures in this work [84]. Pressure has minimal effect on the FQY of acetone for typical compression stroke pressures of gasoline combustion engines [220].

Toluene has a very high FQY of 0.17 [81], characteristic of aromatic hydrocarbons[101]. The FQY of toluene also has an exponential dependence on temperature, decreasing by a factor of 40 over the 300 – 650 K temperature range [85]. The pressure dependence of toluene is dominated by the effect of oxygen quenching, discussed below.

Oxygen quenching

Quenching by oxygen is a concern in many PLIF experiments as it reduces the fluorescence signal significantly [100]. Usually transitions between singlet and triplet states of a molecule are forbidden under the electric dipole selection rule of $\Delta S = 0$. The ground state of oxygen is, unusually, a triplet state and can permit singlet-to-triplet transitions known as Inter-System Crossing (ISC) of a colliding molecule via a transition state with a very short lifetime. After ISC, the molecule no longer fluoresces and decays to the ground state via ro-vibrational

[101] Benzene has an even higher FQY of 0.22 [81], but being carcinogenic has proved unpopular as a tracer for safety reasons.

relaxation followed by phosphorescence [Figure 5-1]. This reduces the FQY in proportion to the increase in the rate of ISC.

For this transition state partial charge transfer must occur [81], [221]. This may only happen if there is a sufficient energy difference between the singlet and triplet states of the colliding molecule to supply the 0.98 eV to permit an excitation of the oxygen molecule into its singlet state [81]. Ketones, such as acetone, typically have singlet-triplet energy gaps much smaller than this resulting in negligible quenching [81]. Aromatic molecules on the other hand have comparatively large singlet-triplet energy gaps and hence oxygen is very effective at rapidly quenching the exited singlet state and preventing fluorescence [81]. For toluene vapour in air at 1 atm (n_{O_2} = 5.25 x 10^{24} m^{-3}), the presence of oxygen results in a fluorescence emission of 1.5 % of its intensity in nitrogen and reducing to 0.75 % at 2 atm [99].

Oxygen-dependent redshift

For 2-colour thermometry with 248 nm excitation of toluene, oxygen also redshifts the fluorescence, therefore deriving temperature from the emission spectrum requires knowledge of the oxygen number density distribution [99]. As there is no such redshift for excitation of toluene at 266 nm [99], temperature can be derived for any partial pressure of oxygen.

Selection of toluene

Parameter	Toluene	Acetone
σ (x10^{-20} cm^2) at 300 K	20	4.3
σ (x10^{-20} cm^2) at 650 K	55	6.0
FQY at 300 K	0.170	0.002
FQY at 650 K	0.004	0.001
Q_{O2}, Oxygen quenching factor for air (1 bar)	0.0150	1
Q_{O2}, Oxygen quenching factor for air (2 bar)	0.0075	1
σ*FQY*Q_{O2} (x10^{-23} cm^2) at 300 K at 1 bar	51.0	8.6
σ*FQY*Q_{O2} (x10^{-23} cm^2) at 650 K at 1 bar	3.3	7.2
σ*FQY*Q_{O2} (x10^{-23} cm^2) at 300 K at 2 bar	25.5	8.6
σ*FQY*Q_{O2} (x10^{-23} cm^2) at 650 K at 2 bar	1.7	7.2

Table 5-2 Fluorescence parameters at 300 K and 650 K for toluene and acetone.

Toluene is widely considered to be unsuitable for use as a fluorescent tracer in oxygen-containing or high temperature environments due to the strong quenching effect of oxygen and decrease in FQY with temperature.

The calculations in Table 5-2 show, however, that considering the total intensity of fluorescence over the range of temperatures relevant to this work it does in fact outperform ‘oxygen independent’ acetone per molecule by a factor of 6 in air at room temperature and pressure. Although by 650 K and 2 bar acetone outperforms toluene by a factor of 4.

The lower temperature and pressure conditions found earlier in the compression stroke at 90 CAD BTDC is also where the tracer number density is smallest. The action of the tracer number density doubling between 90 CAD BTDC and 50 CAD BTDC acts to mitigate some of the reduction in fluorescence intensity of toluene caused by the increasing temperature and oxygen partial pressure. The corresponding factor of 30 reduction becomes a factor of 15 when tracer number density is accounted for.

For fired operation, there is potential for oxygen-deficient pockets of hot EGR to be present within the cylinder. These would contain only small amounts of toluene, either unburned from crevices or mixed in from the fresh charge. The reduction in local tracer number density could be partially mitigated by the reduction in quenching by oxygen and the corresponding increase in FQY.

Toluene is indeed a poor choice in environments rich in oxygen with very high, of order 1000 K, temperatures. Despite this, over the temperature and pressure range relevant to this work toluene has comparable fluorescence intensities to acetone. In addition, oxygen does not impact the spectral content of toluene fluorescence for excitation at 266 nm. TC-PLIF measurements in environments with spatially varying oxygen number densities may have corresponding variations in local signal-to-noise ratios, but will not experience any systematic biases in derived temperature due to the presence of oxygen.

The choice of technique for this work can therefore be made based on the inherent advantages of the TC-PLIF (toluene) and 2-line excitation (acetone or toluene) methods, unrestricted by tracer limitations. Therefore, as stated above, TC-PLIF was selected for application to in-cylinder thermometry in this work.

5.3.3. TC-PLIF with toluene

As discussed previously, the TC-PLIF signal ratio's temperature dependence is solely due to that of the FQY spectrum of the tracer [equation (5-5)]. For toluene, the peak fluorescence wavelength redshifts (increases) with increasing temperature, as shown in Figure 5-2 [5].

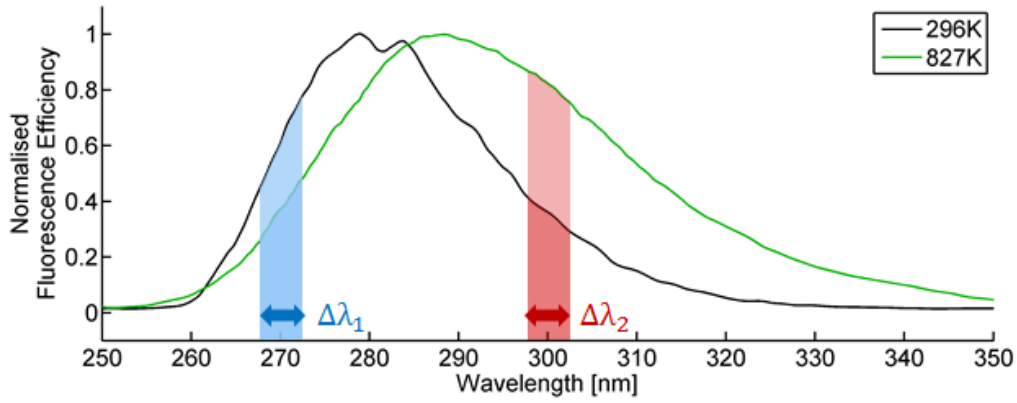

Figure 5-2: Fluorescence quantum yield spectra for toluene at 296 K and 827 K after excitation with 266 nm radiation. Examples of two spectral windows are marked by the blue and red shaded areas. Toluene data used with permission from Faust et al. [5].

For increasing temperature, the normalised intensity of fluorescence at 300 nm increases, while that at 270 nm decreases. The ratio of signals, 'signal ratio', from the two example spectral windows marked in Figure 5-2 therefore provides a measure of temperature.

While the fluorescence spectrum is entirely in the ultraviolet, for convenience the relevant literature and this work refer to the spectral windows according to their central wavelength as 'red' (longer λ) and 'blue' (shorter λ).

5.4. Method

In this section the critical design stage of spectral window selection is discussed, along with a description of the TC-PLIF equipment. The preliminary testing environments are described for 'proof of principle' tests for TC-PLIF in a controlled environment before application to the optical engine. An explanation of the data analysis routine for processing the raw fluorescence images and extracting a 2D temperature map is also presented.

5.4.1. LIF optics selection

The choice of spectral separation optics has a significant effect on the variation in signal ratio per Kelvin and therefore temperature sensitivity. Luong et al [110] found that for different filter choices, a temperature increase of 400 K caused the signal ratios to increase by a factor of between 1.5 and 2.75. Optimisation of the spectral separation optics should allow improvements in single-shot precision over the 6 % quoted previously in [109], as can be seen in [111].

The normalised fluorescence spectra of toluene across a range of temperatures presented in [5] were kindly provided by the authors for use in this work[102]. In combination with the LIF signal equations from [107], the fluorescence signal ratios were modelled for a variety of filter options. While temperature sensitivity is an important quality for filter selection, the intensity of fluorescence collected in each window must also be considered in order to maintain a sufficient signal-to-noise ratio for both cameras.

The longer wavelength 'red' region of toluene's fluorescence spectrum is much more temperature-dependent but also significantly weaker than the 'blue' region, particularly for low temperatures near 300 K. In order to maximise the collected intensity in the 'red' tail of the spectrum, a longpass filter was selected to define the 'red' window. Rejection of visible light from combustion events or room lighting is performed by the short 500 ns gate width of the intensifier of the ICCD cameras. Given the comparatively low intensity of ambient light, these

[102] Two examples of FQY spectra for 296 K and 827 K are displayed in Figure 5-2.

visible sources provide negligible contribution to the total intensity when integrated over only 500 ns.

The ‘blue’ window must collect as much intensity from the ‘blue’ wing of the spectrum as possible, while also blocking any scattered pump light at 266 nm and any light from the ‘red’ wing or longer wavelengths. A bandpass filter was selected as being ideally suited to these requirements.

For this choice of spectral selection optics, the predicted LIF signals were modelled over the expected temperature range for optical engine operation of 300 – 800 K. As is to be expected, the highest temperature sensitivity would be achieved for a very large separation of the ‘red’ and ‘blue’ spectral windows, where the fractional changes in collected intensity at the extreme edges of the spectrum result in a large fractional change in signal ratio. The greatest signal intensity would be collected by a very small separation of the ‘red’ and ‘blue’ spectral windows. Both this cases would be extremely poor choices, producing either negligible temperature sensitivity or negligible collected intensity.

A compromise was chosen by giving approximately equal weighting to signal intensity and temperature sensitivity, and taking into account the commercial availability of suitable optics.

The transmission spectra of the selected optics are shown in Figure 5-3, with details of the individual optics in Table 5-3. A dichroic beamsplitter with transition edge at 310 nm was also selected to minimise the amount of fluorescence rejected by the filters.

Spectral window	Filter type	Centre/edge wavelength	Product code
‘Blue’	Bandpass, 20 nm FWHM	280 nm	BrightLine -FF01-280/10-25
‘Red’	Longpass	305 nm	BrightLine -FF01-300/LP-25
Both	Dichroic beamsplitter	310 nm	BrightLine-FF310-Di01-25x36

Table 5-3 TC-PLIF spectral separation optics specifications.

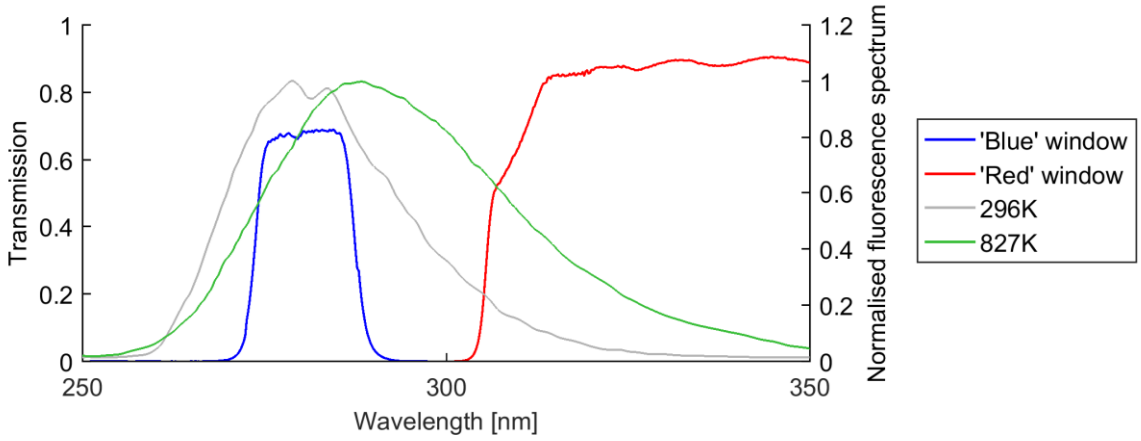

Figure 5-3: Transmission spectra of the combined spectral separation optics compared to the normalised emission spectrum of toluene [5]**. The "Blue" window is defined by the transmission of the Bandpass filter at 280 nm and the reflectivity of the dichroic beamsplitter. The "Red" window is defined by the transmission of the Longpass filter at 305 nm and the transmission of the dichroic beamsplitter.**

5.4.2. Equipment

A flashlamp pumped solid state Nd:YAG laser (Continuum Surelite I-10) was used to provide the pump sheet for this work, with a maximum pulse energy of 30 mJ at 266 nm. Excitation of toluene at 266 nm avoids the oxygen-dependency of the emission spectrum observed for other excitation wavelengths [99].

LIF experiments typically produce very low signal intensities, in part due to the incoherent nature of fluorescence distributing the emission over all 4π steradians of solid angle and are further reduced for TC-PLIF by the requirement of spectral filtering. LIF images are therefore highly susceptible to noise, hence noise reduction and filtering are important issues to consider and will be addressed in section 5.4.3.

The small signal intensities necessitate the use of a detection system with significant gain. In this work Intensified CCD (ICCD) cameras were used to amplify and record the weak fluorescence signals [Table 5-4].

Manufacturer	RS Princeton Instruments	
TC-PLIF spectral window	'Red'	'Blue'
Model	ICCD-576-G/RB	ICCD-512-T
Detector size (pixels)	576 x 384	512 x 512
Pixel size	22.5 µm x 22.5 µm	19 µm x 19 µm
Spatial resolution limit	85 µm (~ 4 pixels)	85 µm (~ 4 pixels)
Spectral response	200 – 900 nm at 50 % drop-off	
Gate time response	5 – 7 ns	
Gate on/off ratio	5 x 10^6 : 1	
Gain	1 – 70 counts per photoelectron	
Response linearity	< 1 % deviation from linearity for upper 95 % of dynamic range. Phosphor nonlinearity produces minor nonlinearity for lower 5 % of dynamic range.	

Table 5-4 'Red' and 'Blue' ICCD camera specifications.

Cooling a CCD dramatically reduces the noise caused by thermally generated electrons in the CCD, for the ICCD-576-G/RB when cooled from room temperature to approximately –20 °C this can be as much as a factor of 6. The heat generated by the Peltier-effect thermoelectric cooler must be carried away by water circulated past the rear of the cooler, introduced via the supplied inlet/outlet ports at a flow rate of 1 – 3 L/min. To avoid condensation forming and freezing on the CCD, dry nitrogen must be used to flush the camera housing at a flow rate of 1 L/min, keeping the water vapour concentration within the camera to below 10 ppm.

The intensifier stage sets the lower limit of spatial resolution achievable with the ICCD camera due to the 85 µm FWHM spot size at the CCD generated by a point-like input. This corresponds to a pixel size of just under 4 pixels, hence the noise filtering image processing stage can filter the images to a 4 x 4 pixel level without any loss of spatial resolution.

One advantage of the large gains available to ICCD (or Electron-Multiplying CCD) cameras is the ability to essentially ignore all forms of electronically generated noise from the CCD's dark current or readout noise when running at very high gain levels [222]. This usually ensures that shot noise from fluctuations in the arrival of incident photons dominates the total noise in an image as it experiences the large gain factor of the intensifier, unlike the CCD related noise. In the spirit of there being 'no such thing as a free lunch', the amplification process does however increase the noise on the signal as it cannot perfectly amplify without adding noise. The overall

noise of an image amplified in this way will be larger by a factor of between 1.3 and 2 compared to the product of the incident shot noise and the gain [223].

Optics layout

A lens tube and camera translation stage system has been designed and built to provide a compact and robust layout for the TC-PLIF optics and ICCDs [Figure 5-4]. A 105 mm f/4.5 Coastal Optics lens is used to collect and image the fluorescence signal. A dichroic beamsplitter transmits 'red window' wavelengths and reflects 'blue window' wavelengths before each path experiences further spectral filtering by the filters detailed in Table 5-3. Relay lenses in each arm transfer images onto each ICCD. Axial translation stages allow each camera to be individually focussed.

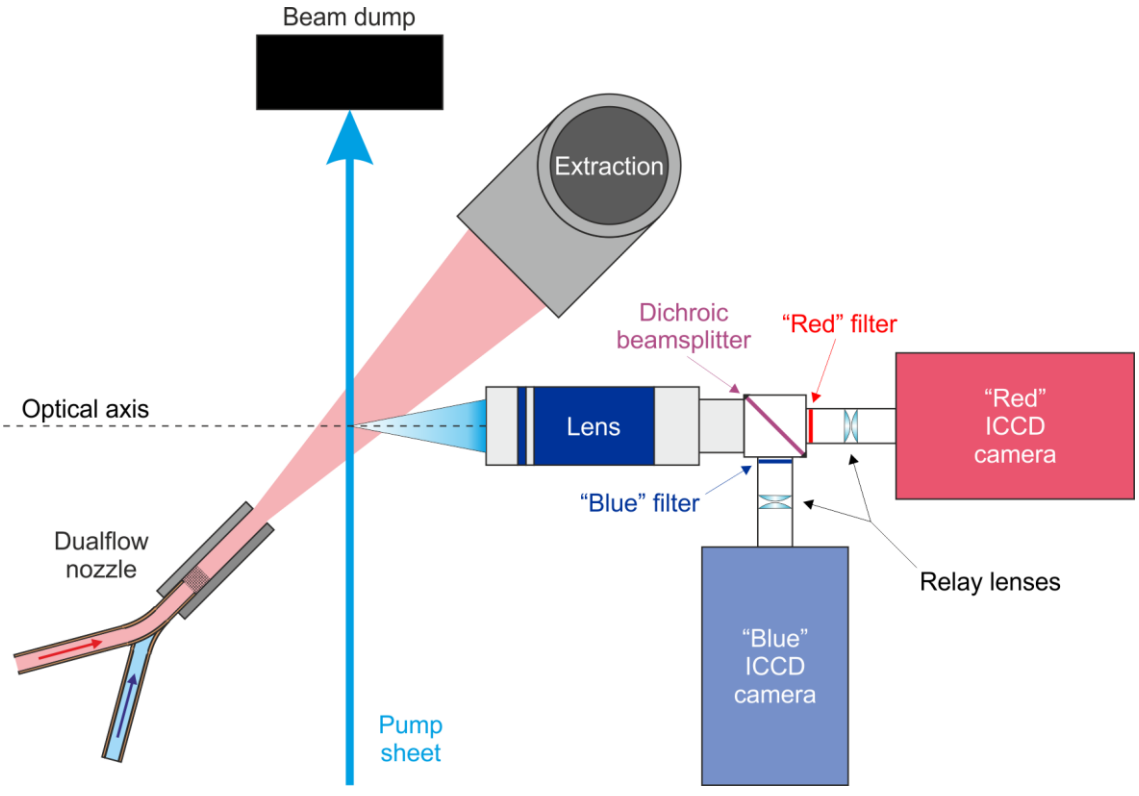

Figure 5-4 Experimental layout for TC-PLIF thermometry displaying the pump sheet, imaging lens, spectral filtering optics, relay lenses and ICCD cameras. Also shown is the Dualflow nozzle and extraction used to provide a stable temperature gradient in a toluene-seeded nitrogen flow.

The inclusion of pairs of 50 mm focal length plano-convex relay lenses transfers the image formed by the UV lens with 1 : 1 magnification onto each ICCD sensor, creating space for the

inclusion of spectral separation optics. A pair of plano-convex lenses is close to the best form solution for minimising spherical aberration. Distortion, which changes sign for reversal of path through an optical element is zero by symmetry, while imaging at 1 : 1 magnification eliminates coma [224]. The spectral filtering of the fluorescence restricts the range of wavelengths transmitted through each relay arm, minimising the effect of chromatic aberration.

Spatial resolution

The spatial resolution of the system is specified by the choice of imaging optics and limited by the best-case 4 x 4 pixel point spread function (PSF) of the ICCD camera due to the intensifier stage. At the imaging conditions specified for the optical engine measurements, the image dimensions correspond to 35 pixels mm^{-1}. The minimum dimension noise-reducing filter applied to the data in this work is a Gaussian filter[103] with a standard deviation of 3 pixels. The FWHM of such a filter is 7 pixels, marginally larger than the best-case PSF of the camera, corresponding to an effective spatial resolution of 200 μm for the TC-PLIF system.

Flow system design

Development of the TC-PLIF system requires both uniform and non-uniform stable temperature distributions to be generated within a toluene-seeded environment. Sealed test cells, while ideal for uniform temperature measurements, suffer from convection effects which act to disturb the intended smooth temperature gradient when regions of the gas are differentially heated.

The selected method for temperature gradient production was a pair of adjacent and parallel nitrogen flows seeded with toluene vapour. One flow could be heated by passing the flow through an in-line resistive gas heater. Ideally this heating would occur independently of the second flow, however heat conduction through the copper sections of the apparatus resulted in partial heating of the nominally unheated flow.

[103] FWHM of a Gaussian centred at x = 0 is given by: $FWHM = 2x = 2\sqrt{2\ln 2}\,\sigma$, using: $1/2 = e^{-x^2/2\sigma^2}$

A pair of 4 mm copper pipes[104] deliver toluene-seeded nitrogen to the entrance aperture of the nozzle [Figure 5-5]. The 8 mm x 4 mm slot which forms the exit aperture is split into 'upper' and 'lower' sections by a 150 µm stainless steel sheet in a horizontal plane. A wire wool diffuser at the exit of each copper pipe encourages each flow to fill the internal volume of the nozzle, such that immediately after the two flows exit the nozzle, they are each 4 mm in diameter, parallel and separated by only 150 µm.

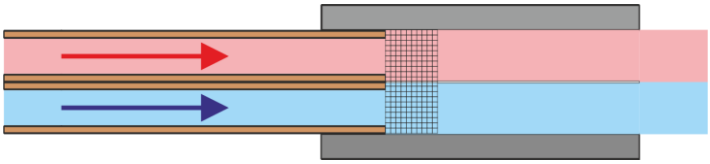

Figure 5-5 Elevation view cross-section of the Dual-flow nozzle. The hot and cold flows pass into the nozzle via diffusers and are kept separate by a 150 µm steel plate until the exit aperture.

The geometrical arrangement of the pump sheet and flow system is depicted in Figure 5-4. The pump sheet is constrained to propagate within a horizontal plane, forming a vertical sheet propagating across the field of view of the TC-PLIF imaging system which is aligned perpendicular to the pump sheet.

The simplest arrangement for TC-PLIF development in isolation would be to have the flow introduced vertically from below the pump sheet. This would negate any complicating effects due to buoyancy when using differentially heated flows, simplify extraction of the gas flow after the measurement region and ensure all directions of interest in the experiment were orthogonal. This system was developed in parallel with the 1D-LITGS work of chapter 7. The flow system was arranged to enable both measurements to be performed simultaneously using the narrow crossing angle of the 1D-LITGS pump sheets to approximate a single pump sheet for TC-PLIF. The 1D-LITGS measurements were restricted to measuring temperatures along a vertical line, requiring the temperature gradient to also be vertical. The pair of flows therefore propagated in the same horizontal plane as the pump sheets, directed at an angle of 45° with respect the optical axes of both the TC-PLIF system and the LITGS beams. This provided the desired vertical

[104] 4 mm outer diameter, 0.6 mm wall thickness, 2.8 mm inner diameter.

temperature gradient, kept the flow plumbing out of the LITGS beam paths and allowed the flow to be extracted to one side of the TC-PLIF collection lens.

5.4.3. LIF analysis

Selection of MATLAB

MATLAB, a software package for matrix-based numerical computing, is a natural environment for the analysis of scientific data due to the tendency for experiments to generate signals (vectors) and images (matrices) that require mathematical manipulation. MATLAB offers a wide array of documented functions for mathematical operations, curve fitting and image processing among others. Of additional interest to this work is the Mathworks file exchange[105], which provides a forum to share community written functions.

The data analysis software throughout this section has been written by the author using either the standard library of functions available in MATLAB or incorporating functions shared via the Mathworks file exchange. In such cases, the author of the relevant function is credited as a footnote in the relevant paragraph.

Image processing overview

The principle behind TC-PLIF is straightforward; record two images in different spectral windows and take their ratio to generate a relative temperature map. In practice a variety of processing steps must be performed before the ratio can be taken. The processing steps are detailed schematically in Figure 5-6 and explained below.

Firstly, the high noise levels of the raw ICCD camera images are reduced by applying spatially averaging filters to the images. Any apparent intensity in the raw images not originating from toluene fluorescence, whether scattered light or electronic noise generated by the camera system, will affect the signal ratio and result in an apparent temperature change. A background

[105] http://uk.mathworks.com/matlabcentral/fileexchange

image is recorded before every test under the same conditions except without tracer. This mean background image is then subtracted from the corresponding TC-PLIF images. Optical aberrations resulting from the sequence of imaging optics may cause minor distortions of the image or result in a non-uniform effective sensitivity across the camera sensor. These issues are dealt with via the distortion and flatfield correction stages.

The two cameras will unavoidably be imaging slightly different regions of the object plane. In part this is due to the coarse manual translation available for alignment in the directions transverse to the optical axis. Mainly, however, it is due to the two ICCD cameras used in this work being different models and having sensors with different aspect ratios. This issue is corrected by the image registration stage. One of the images is considered to be the reference geometry. Transforms are applied to the second image to bring it into alignment with the first, ensuring that each pixel co-ordinate corresponds to the same physical location in the object plane for both images. Once the images have been fully corrected the pixel-wise ratio of the pair can be taken, resulting in a signal ratio image equivalent to a map of relative temperatures.

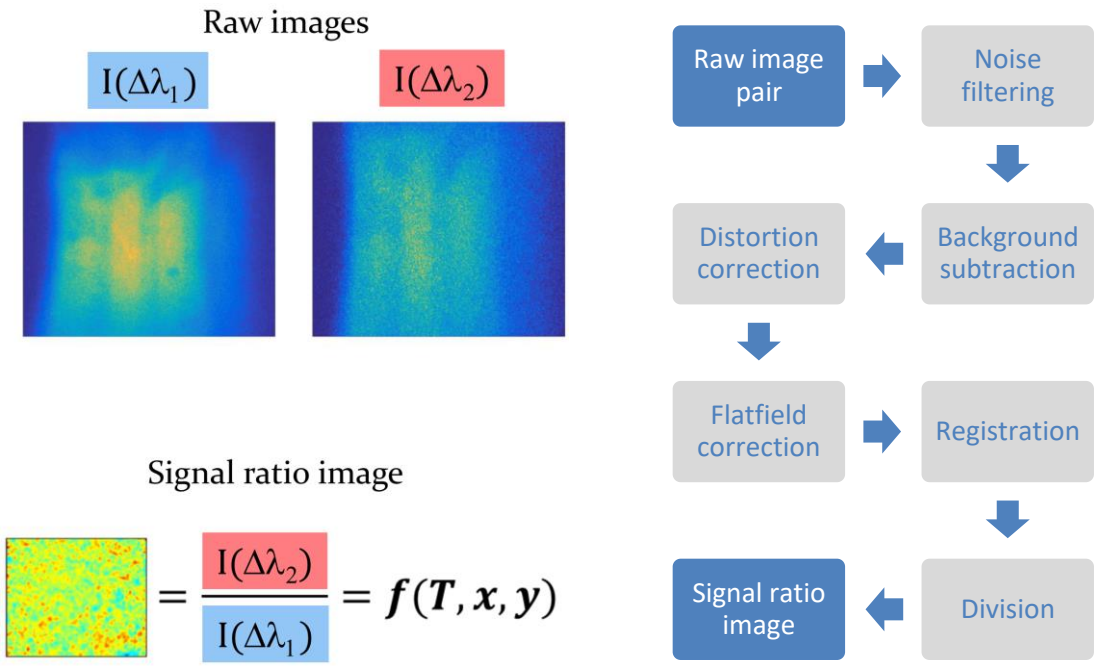

Figure 5-6 Image processing steps for TC-PLIF.

Reference images

In order to calculate the appropriate corrections and transforms to apply to the TC-PLIF raw images, it was necessary to image a structured object in the object plane to provide a grid of reference points for the corrections. For visible applications it is trivial to image a printed grid illuminated by a visible light source. Registration images could be taken using visible light in this setup by replacing the dichroic beamsplitter with a 50/50 visible beamsplitter. This would however align the system correctly for visible light, not the UV fluorescence signal of interest in this work. The effective focal length of the lenses would image the UV fluorescence signal at a different axial location to visible light potentially resulting in out-of-focus TC-PLIF images. Providing a reference structure illuminated with UV light presents a greater practical challenge.

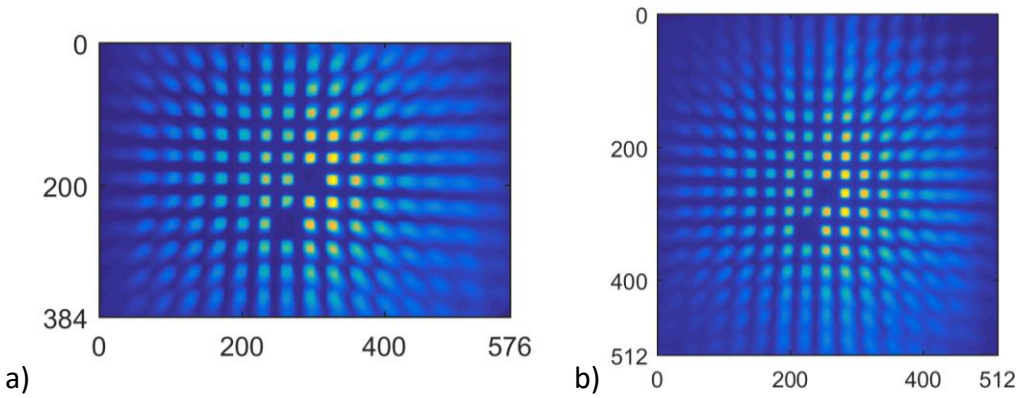

Figure 5-7 Reference images of UV-backlit steel grid from each camera, a) ICCD-576-G/RB ('red' spectral window), b) ICCD-512-T ('blue' spectral window). The pair of 'missing' points in each image act as points of reference to determine the correct relative orientation and position of the images.

A 150 µm thick steel sheet was laser cut to provide a robust sheet with a grid of 0.5 mm x 0.5 mm square holes separated by a centre-to-centre distance of 1 mm. This sheet was fixed inside the cylinder of the engine at the desired location of the TC-PLIF object plane. The UV pump sheet was re-aligned to provide a backlight for the grid by illuminating a static engine filled with a toluene and air mixture. Adjustment of the camera alignment to bring the grid into sharp focus at the correct scale ensured the cameras were optimally aligned in the UV wavelength region of interest. The images from each aligned camera were then recorded to provide the required grid of reference points for calculation of the image processing steps [Figure 5-7].

Noise filtering

TC-PLIF images are highly susceptible to noise due to the low signal intensities, as discussed in chapter 3, which necessitates the use of ICCD cameras. While shot noise, thermal noise and CCD read noise are present, the main contribution is Poisson noise from the Micro-Channel Plate used as the 'intensifier' stage of the camera [107]. It is therefore beneficial to accept some reduction in spatial resolution in exchange for the significant noise reduction achieved by smoothing of the image.

Before the reference images were used to calculate the various image processing steps detailed above, a noise-removal filter was applied to the images. Noise-free reference images with sharply resolved fine detail are beneficial for accurate determination of the required image processing transformations.

Simple weighted average filters are effective at removing high spatial frequency noise, but usually at the expense of smoothing out steep gradients and blurring fine detail in the image. As the edges of each square in the reference grid are marked by sharp transitions from high to low intensities, it is desirable to use a more sophisticated filter capable of preserving the steep gradients present in the reference images. The filter found to be most effective in this work is a nonlinear diffusion filter nldif.m[106], sourced from the MATLAB file exchange [225].

The potential for the nonlinear diffusion filter to introduce systematic bias to the experimental TC-PLIF images has not been investigated. The use of this filter was therefore restricted to the highly structured reference images as the relative intensity of the processed images does not affect the accuracy of the registration process. Instead, the simpler and computationally much faster Gaussian filter was applied to the engine datasets[107]. Each pixel is replaced with a weighted sum of its neighbours, where the distribution of weights as a function of distance from

[106] D'Almeida, F. (2004). Nonlinear diffusion filtering toolbox. Retrieved version last updated 26 Mar 2004. http://uk.mathworks.com/matlabcentral/fileexchange/3710-nonlinear-diffusion-toolbox

[107] A Gaussian filtering function is available in the standard MATLAB library.

the central pixel is a Gaussian. The larger weights at the centre of the filter tend to help preserve edges in an image, although not nearly as effectively as the nonlinear diffusion filter. The degree of smoothing can be chosen by varying the standard deviation of the Gaussian function depending on the desired balance of spatial resolution versus noise reduction. Heavy smoothing removes the majority of noise, highlighting the large scale underlying structure in an image. Light smoothing preserve the smaller scale structure of an image at the expense of granulation [Figure 5-8].

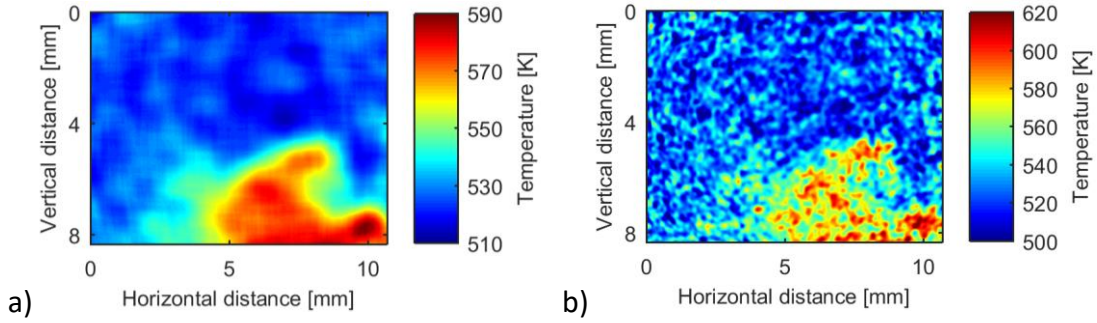

Figure 5-8 TC-PLIF image of an in-cylinder temperature distribution with a) heavy smoothing giving Ø 1 mm spatial resolution, b) light smoothing giving Ø 0.25 mm spatial resolution.

Distortion corrections

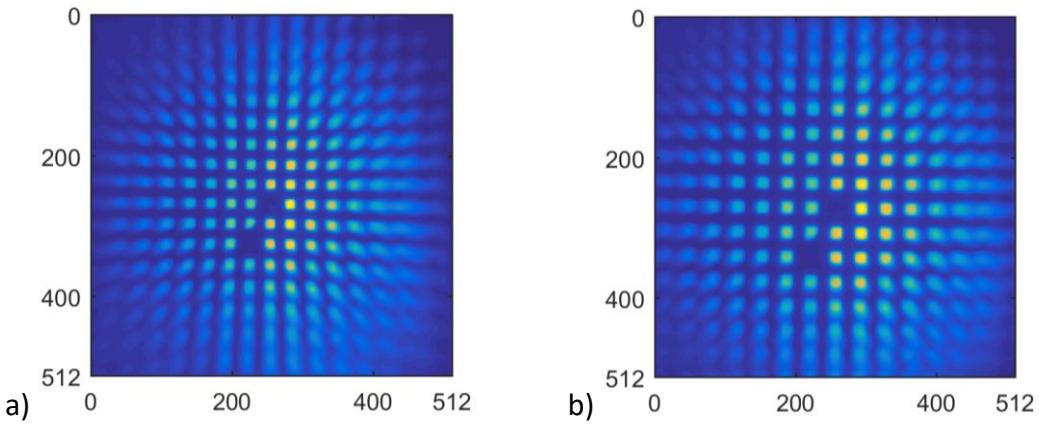

Figure 5-9 Pincushion distortion correction, a) raw image, b) corrected image.

Careful selection of the imaging optics led to pincushion distortion being the main distorting aberration visible in the reference images. This was corrected by applying barrel distortion

using the lensdistort.m[108] function sourced from the MATLAB file exchange [226]. The image from one camera before and after pincushion correction is displayed in Figure 5-9, showing a clear improvement in the orthogonality of the lines of grid points for the corrected image.

Flatfielding

Images recorded by the TC-PLIF system suffer from a reduction in intensity radially away from the centre of the image, as in Figure 5-9 and Figure 5-7. This is an example of vignetting, where light rays originating from a point in the image plane away from the optical axis experience a reduced effective aperture of the lens system compared to on-axis light, leading to lower transmitted intensities. By recording the variation in intensity across an image for uniform illumination, the effective sensitivity of each pixel can be calculated and used to divide out the vignetting effect for all future images, referred to as a 'flatfield' correction [Figure 5-10].

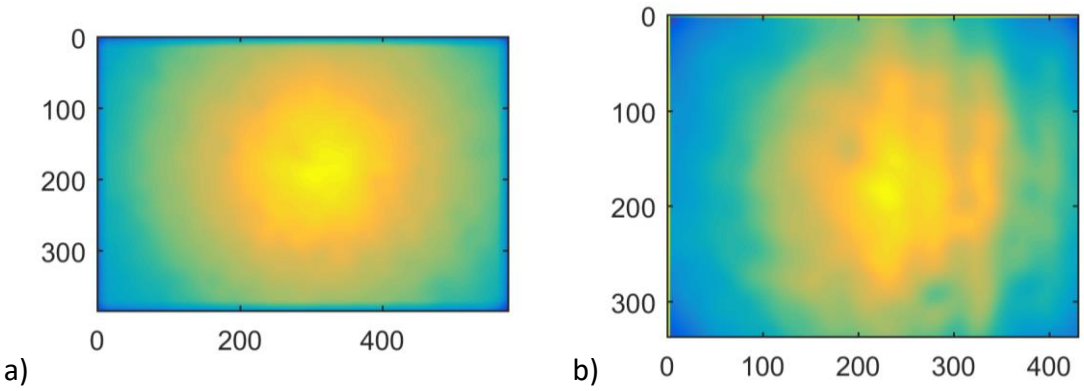

Figure 5-10 a) 'Red' flatfield profile derived from image of uniform illumination. b) 'Blue' flatfield profile derived from fluorescence image at uniform temperature and tracer number density by comparison with a).

With all optical filters in place, the long wavelength 'red' camera can still 'see' visible light, but the filters for the short wavelength 'blue' camera highly attenuate light above 290 nm [Figure 5-3]. This prevents flatfielding both cameras using visible light. The practical solution used was to flatfield the 'red' camera with visible light, then record an image of fluorescence from a quartz cell of toluene vapour in air excited by a UV pump sheet with both cameras. The toluene

[108] Vries, J. de. (2012). http://uk.mathworks.com/matlabcentral/fileexchange/37980-barrel-and-pincushion-lens-distortion-correction. Retrieved version last updated 31 Aug 2012.

number density and the temperature of the gas mixture is considered to be uniform across the cell, leaving the pump sheet intensity as the only spatially varying parameter determining the fluorescent signal. Therefore, while the total intensity will differ between the two cameras due to the choice of spectral windows, the spatial distribution of that intensity should have the same profile for both images. Any deviation in normalised intensity profile between the 'blue' image and the flatfield-corrected 'red' image can then be interpreted as the required flatfield correction for the blue camera [Figure 5-10].

Image registration

Image registration is a procedure which aims to transform a set of images of different scales, locations or orientations such that they match the co-ordinates of a reference image. This enables multiple photographs taken with a handheld camera to be stitched together seamlessly into a single panoramic image, or permits a pixel-wise overlay of multiple images as in this work. The registration stage of the TC-PLIF image processing applies an affine transform to one of the camera images, which can include translating, rotating, scaling and shearing the original image until it aligns with the geometry of the second camera image.

The reference images were registered using a control point method, where the standard MATLAB function fitgeotrans.m[109] infers the affine transformation required to map a set of user-defined control points onto the control points of a reference image. This transform was applied for registration of future TC-PLIF images.

The features chosen to be control points were the centres of each bright square. The co-ordinates were determined by passing each registration image to a 2D peak finding function FastPeakFind.m[110] sourced from the MATLAB file exchange [227]. This function was written to provide peak locations based on local maxima after smoothing with a filter, Gaussian in this

[109] http://uk.mathworks.com/help/images/ref/fitgeotrans.html

[110] Natan, A. (2013). Fast 2D peak finder. http://uk.mathworks.com/matlabcentral/fileexchange/37388-fast-2d-peak-finder. Retrieved version last updated 10 Oct 2013.

work, which matches the expected size of the peaks. As such the function is well suited to robustly locating the reference image peaks which all have nominally the same dimensions.

5.5. Results, analysis and discussion

In this section, initial verification of the TC-PLIF system's thermometry capability using the pair of toluene-seeded nitrogen flows described in section 5.4.2 is reported. Without simultaneous LITGS to provide a reference, calibration of the relationship between signal ratio and absolute temperature could not be performed. For the purposes of this work, the relative temperatures displayed in the signal ratio figures of this section are sufficient to demonstrate the capability of the TC-PLIF system.

5.5.1. Temperature sensitivity

Initial verification of the temperature sensitivity of the signal ratios produced by the TC-PLIF system was performed using a pair of toluene-seeded nitrogen flows. The Dualflow setup described above in section 5.4.2 was used with the nozzle removed. The exposed adjacent copper pipes generate two flows which can be considered separate within a few mm of the nozzle[111]. The upper flow was heated to a range of temperatures using the in-line resistive gas heater, the lower flow was not heated directly. Taking the signal intensity at the centre of each flow as a quasi-point measurement, signal ratios for each flow were calculated.

Two experimental runs were performed at each temperature to demonstrate the repeatability of the technique, giving consistent mean signal ratios within the precision of the measurement for each pair of runs [Figure 5-11 a)]. Runs 1 and 2 (unheated) display the same mean signal ratio for both flows, demonstrating the expected resilience of the TC-PLIF technique to variations in pump laser intensity, tracer number density and optical collection efficiency between the two interrogated regions.

[111] As mixing has not yet caused the flow boundaries, initially physically separated by the thickness of the two pipe walls, to overlap.

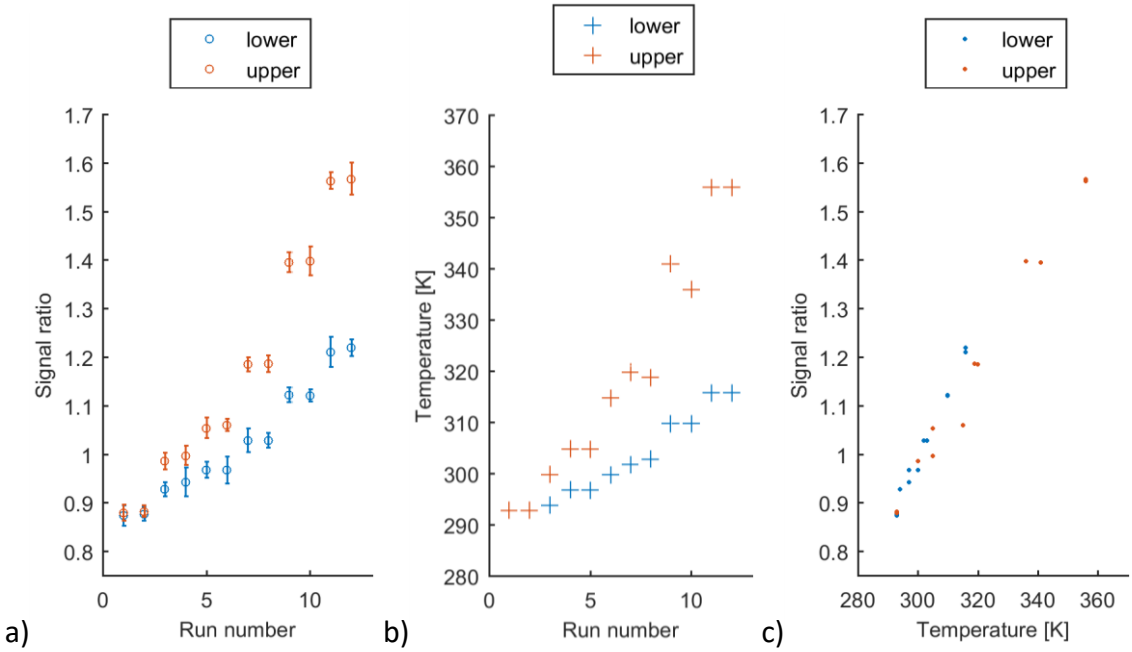

Figure 5-11 Verification of TC-PLIF temperature sensitivity. a) TC-PLIF signal ratios. b) Thermocouple measurements. c) Correlation plot of TC-PLIF signal ratio vs thermocouple temperature.

The variation of signal ratio shows good positive correlation with the flow temperatures measured by a thermocouple placed at the nozzle exit after each run [Figure 5-11 b) and c)]. The thermocouple data will contain systematic errors due to the invasive nature of attempting to measure the temperature of a 4 mm diameter flow with a 1.5 mm diameter physical probe. It was however a temperature reference sufficient for a proof-of-principle.

Due to the high thermal conductivity of copper, heat transfer from the heated upper pipe to the unheated lower pipe was significant, causing the observed increase in signal ratio for the 'unheated' lower flow. Despite this effect, a sufficient temperature difference was maintained to successfully display the ability of the TC-PLIF system to resolve temperature differences of the order of 5 K between points in the same image[112] and between sequential images.

[112] Separated by more than the 200 µm spatial resolution of this TC-PLF system.

5.5.2. Final image corrections

Verification of the ability of the TC-PLIF system to record temperature differences across the entire image was performed with the full Dualflow setup, nozzle in place. The TC-PLIF images were centred on the boundary between the flows in a plane intersecting the flow at 45° to the flow axis. The horizontal distance across this 45° plane in Figure 5-12 is thus both an axial and transverse displacement with respect to the flow. Temperature differences of approximately 0 K (b1), 20 K (b2), 30 K (b3) and 40 K (b4), as measured by a thermocouple, were achieved between the two flows.

Mean signal ratio images with the upper flow heated are presented in Figure 5-12 and show the development of the temperature gradient at the boundary of the two flows. Also visible in the uncorrected images (a) is a strong non-uniform perturbation to the signal ratio map whose spatial distribution, if not magnitude, is independent of temperature.

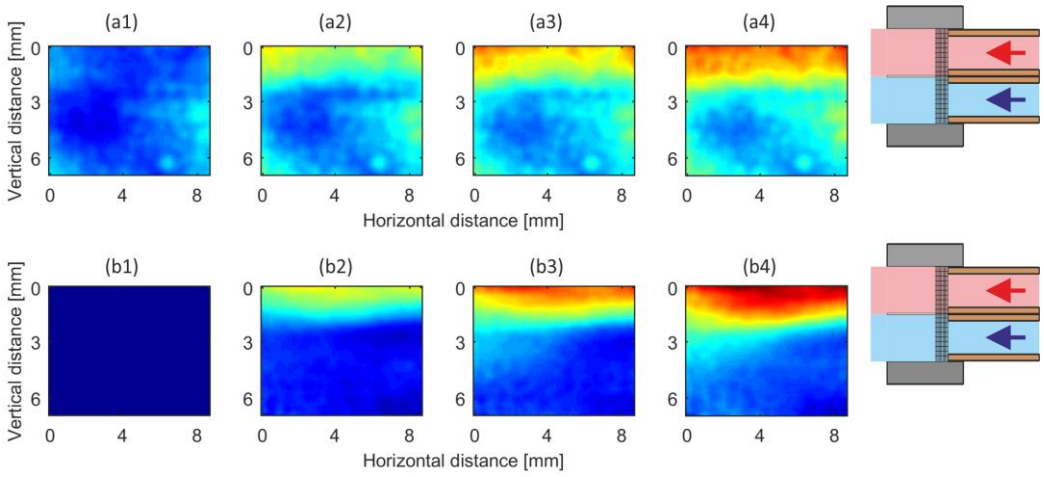

Figure 5-12 Mean TC-PLIF signal ratio images for a pair of adjacent, parallel flows with only the upper flow heated, taken at 45° to the flow axis. a) Uncorrected images. b) Images corrected for the residual flatfield as described in the main text. Horizontal distance = 8 mm is closest to the nozzle.

Considering that image (a1) represents two identically seeded, ambient temperature flows, the signal ratio image should be uniform. However, it is not. The persistence of this distribution throughout the heated datasets (a1 – a4) suggests that the flatfield correction, calculated initially using visible light, is not performing correctly for these UV fluorescence measurements.

The ‘warm’ spot at approximately (x,y) = (7 mm , 6 mm) occurs at the location of a known region of damage in the ‘blue’ camera. A reduction in the apparent signal intensity for the ‘blue’ spectral window would indeed be interpreted by the TC-PLIF analysis as a region of comparatively higher temperature.

A solution to imperfect flatfield correction would be to record TC-PLIF images under similar experimental conditions known to be uniform in temperature. The signal ratio distribution would provide a measure of the relative sensitivities of the ‘red’ and ‘blue’ cameras for each pixel. This could be applied to the main TC-PLIF datasets as a residual flatfield correction.

Image (a1) of Figure 5-12 provides an appropriate uniform temperature reference image for the residual flatfield correction. A copy of this image was normalised to a mean pixel value of 1 in order to perturb the spatial distribution but not the mean signal ratio of the other images. The remaining images [Figure 5-12 (a2 – a4)] were then divided by this normalised reference, to give the fully-corrected images [Figure 5-12 (b2 – b4)].

The first image no longer conveys any useful information as it is forced to be mathematically flat by the correction process described above. An improved measurement of the thermal boundary between the flows is obtained in the remaining images, as the systematic artefacts have been removed.

This improvement permits the observation of subtle features that were obscured in the non-corrected images. The steep temperature gradient observed at x = 8 mm of image (b4), closest to the nozzle aperture, becomes gentler as distance from the nozzle increases towards x = 0 mm. This displays the mixing of the two flows acting to reduce the magnitude of the initial temperature gradient as the flow propagates away from the nozzle.

The equivalent results are displayed in Figure 5-13 for the case where the lower (not upper) flow is heated. The buoyancy effect of the hotter gas is immediately apparent. As distance from the nozzle increases, the lower flow rises to fill a larger fraction of the imaged plane.

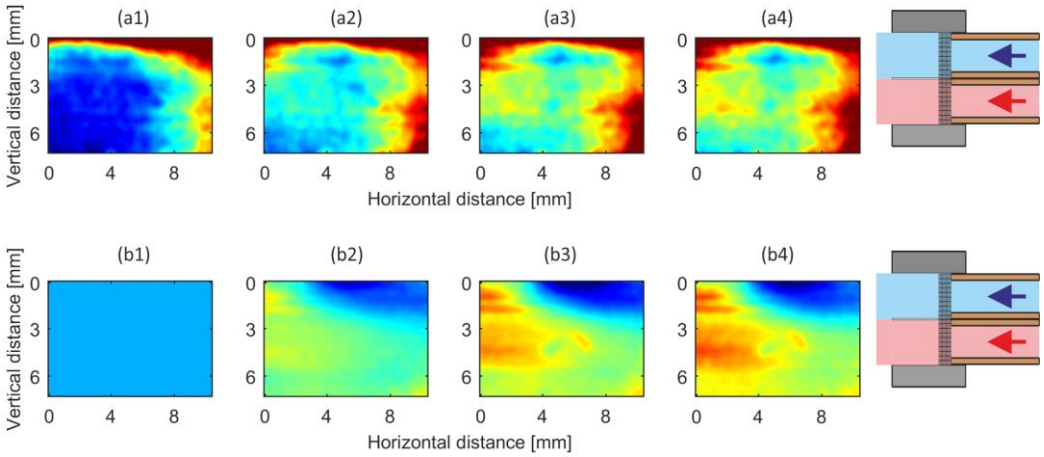

Figure 5-13 Mean TC-PLIF signal ratio images for a pair of adjacent, parallel flows with only the lower flow heated, taken at 45° to the flow axis. a) Uncorrected images. b) Images corrected for the residual flatfield as described in the main text.

Angle-dependence of beamsplitter

Work by Peterson et al [103] identified a systematic error arising from the common use of a dichroic beamsplitter in TC-PLIF systems. Measurements of uniform temperature fields resulted in a horizontal gradient in signal ratio across the image. The culprit was determined to be the fact that the spectral transmission of dichroic filters depends on the incident angle of the light. This effect is well known, indeed there are many commercially available 'tuneable' dichroic filters which make use of exactly this property. Unfortunately for TC-PLIF applications, the fluorescence emitted from the object plane arrives at the beamsplitter from a finite range of angles.

The 45° angle of the beamsplitter about a vertical axis [Figure 5-4] results in light hitting one side of the beamsplitter at an angle closer to the normal than light which hits the other side. As the TC-PLIF analysis treats the spectral transmission of the beamsplitter as spatially uniform, this difference in transmission is interpreted as a temperature shift.

This can be corrected by division of each image by a 'correction image' with a linear horizontal gradient [103]. As the symptom is a systematic non-uniformity in the signal ratio image for measurements of a uniform temperature field, this additional correction is already accounted for in this work by the residual flatfield correction.

5.5.3. Single shot measurements

The measurements in sections 5.5.1 and 5.5.2 demonstrate the capability of the TC-PLIF system for performing time-averaged measurements. In chapter 6, investigations into the in-cylinder temperature distribution of the engine will require single-shot capability. Verification of time-resolved measurements was performed in the same Dualflow setup as before, but with the more challenging environment of a strong extraction system close to the measurement region. This ensured that the flow pattern was very unstable, with the cross-section of the flow which intersected the imaged plane varying in both location and shape from shot to shot.

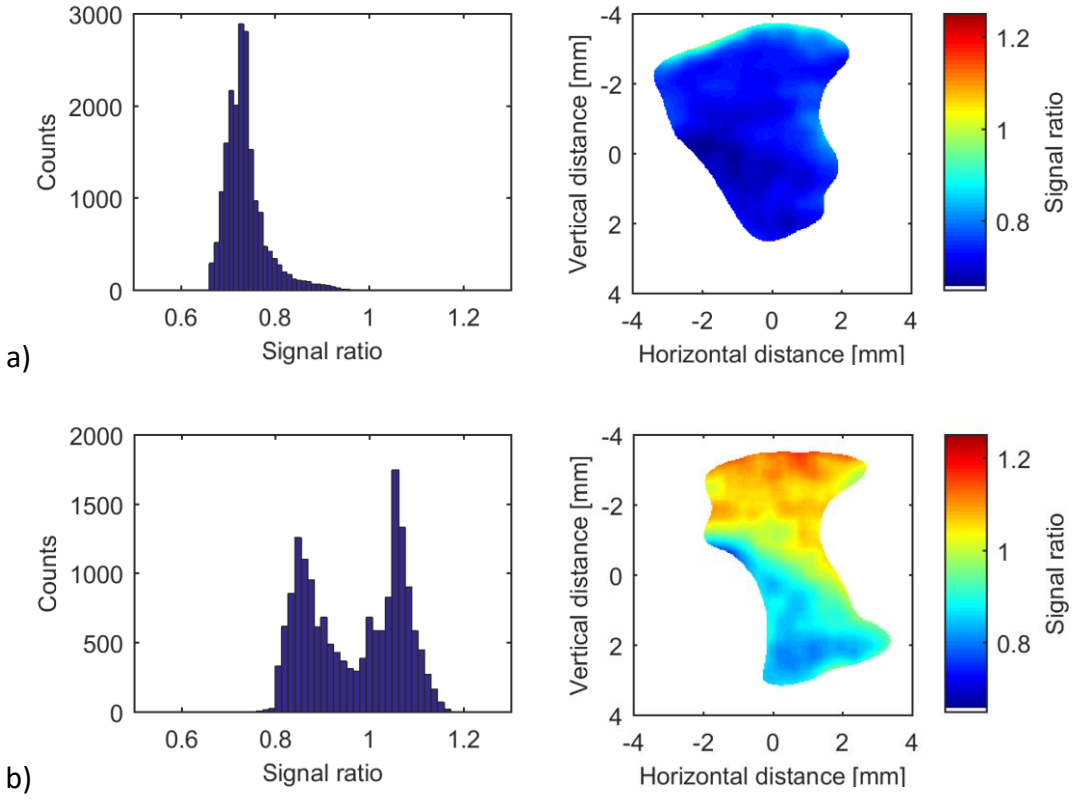

Figure 5-14 Time-resolved signal ratio images (right) masked below 10 % of the maximum signal intensity and histograms of pixel-wise signal ratios (left) of thermal gradients in an unstable flow. a) unheated, b) upper flow heated.

The TC-PLIF system proved to be capable of time-resolved measurements of two zones of temperature with a steep thermal gradient in between. As a guide to the eye, regions of the image with low signal intensity and thus low signal-to-noise ratio were masked in Figure 5-14.

Histograms of the signal ratio for each single-shot image show the transition to a bimodal temperature distribution with heating of the upper flow.

5.6. Summary and conclusions

In this chapter the development of the TC-PLIF thermometry system in a controlled environment was reported. TC-PLIF with toluene was determined to be the technique of choice for 2-dimesional thermometry for this work and subsequently optimal spectral filtering optics were selected. Data analysis routines were written in MATLAB to register the raw images onto a common geometry, perform noise filtering and to correct for image distortions and spatial variations in effective camera sensitivity. This enabled preliminary tests to be performed in the controlled environment of a heated flow seeded with toluene. The temperature sensitivity, repeatability, image quality, spatial resolution and capability for time-resolved measurements of this TC-PLIF system was demonstrated. Following this successful ‘proof-of-principle’ testing, the TC-PLIF system was applied to optical engine thermometry with in-situ calibration by LITGS in chapter 6.

6. Simultaneous LITGS and TC-PLIF

This chapter reports and discusses the development of TC-PLIF for 2-dimensional in-cylinder thermometry with simultaneous LITGS for in-situ calibration. The optical layout is detailed in section 6.2, after which the bulk of this chapter covers the results of the application of the combined technique to the optical engine in section 6.3.

6.1. Introduction

The motivation for using LITGS measurements to provide in-situ calibration for TC-PLIF images has already been discussed in chapters 4 and 5. In summary, TC-PLIF provided single-shot 2-dimensional maps of relative in-cylinder temperatures that were minimally affected by spatial fluctuations in laser intensity, tracer number density or local gas composition[113]. In order to place these temperature maps on an absolute scale, LITGS is used to provide simultaneous in-situ calibration with high accuracy and precision[114] at a single point within the TC-PLIF images.

Section 6.2 describes the optical layout for applying TC-PLIF and LITGS to the optical engine. Preliminary testing of the combined LITGS and TC-PLIF system under motored and fired conditions is reported in sections 6.3.1 and 6.3.2.

Investigations into charge cooling in section 6.3.3 revealed a systematic bias to the temperatures derived by LITGS for some datasets. This restricts measurements with LITGS for some datasets of this chapter to relative measurements of temperature[115]. The bias can be removed for future applications by modification of the detection method, a process confirmed by additional measurements within section 6.3.3.

[113] Specifically oxygen concentration.

[114] Typically in-cylinder LITGS measurements produce accuracies of order 1 % and precisions of < 1 %.

[115] As opposed to absolute measurements of temperature.

Measurements of engine warm-up and temperature inhomogeneities during fired operation are reported in sections 6.3.4 and 6.3.5. The effects of varying the toluene content of the iso-octane/toluene 2-component fuel are discussed in section 6.3.6. Investigations into unphysical artefacts in the TC-PLIF temperature maps are presented in section 6.3.7, along with a discussion on the interpretation of the apparent 'hotspots' observed during fired operation. Finally, the conclusions of this chapter are summarised in section 6.4.

6.2. Optical layout

The TC-PLIF and LITGS systems discussed in chapters 4 and 5 were applied to in-cylinder thermometry of the optical spark-ignition combustion engine detailed in chapter 2.

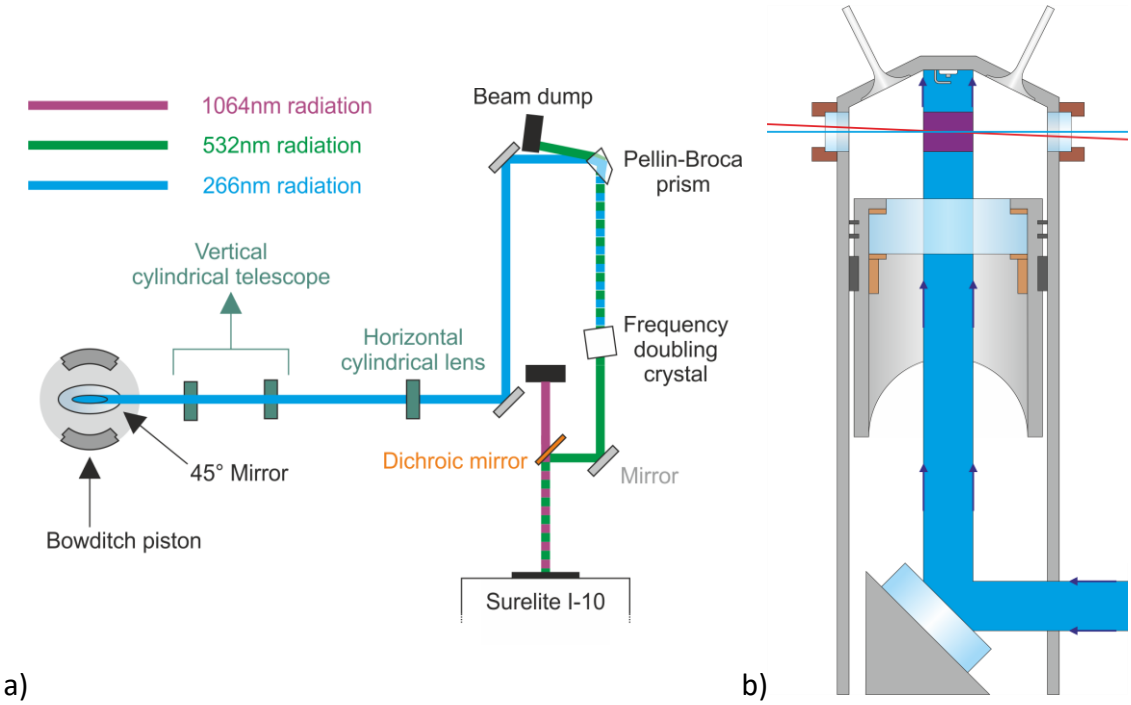

Figure 6-1 a) Layout of TC-PLIF pump sheet optics showing production of the 266 nm (fourth harmonic) for toluene excitation, rejection of 1064 nm and 532 nm radiation, sheet formation and application of 45° mirror within Bowditch piston to introduce pump sheet vertically through piston crown window. b) Geometry of TC-PLIF sheet within cylinder, approximately to scale. Pump sheet intersects LITGS measurement point. TC-PLIF imaged region represented by the central square highlighted in purple.

The 532 nm second harmonic output of the Surelite pump laser was separated from the residual 1064 nm fundamental radiation before being doubled to the 266 nm required for oxygen-independent toluene TC-PLIF in an external frequency doubling crystal. A pair of cylindrical

lenses formed a telescope to increase the diameter of these pump pulses to the desired height of 20 mm. A cylindrical lens of focal length + 1 m focused the pulses in the horizontal direction to form a sheet of thickness 1 mm at the interaction region. A 45° mirror within the Bowditch piston was used to introduce the laser sheet into the cylinder vertically through the piston crown window [Figure 6-1 b)]. The laser sheet therefore illuminates a plane in the centre of the barrel defined by the vertical axis of the cylinder and a line bisecting both the pair of inlet valves and the pair of exhaust valves. The imaging lens and pair of ICCD cameras for the detection of toluene fluorescence are aligned orthogonal to the sheet, looking through the 16 mm window at the top of the cylinder with intake valves on the left and exhaust valves on the right [Figure 6-2].

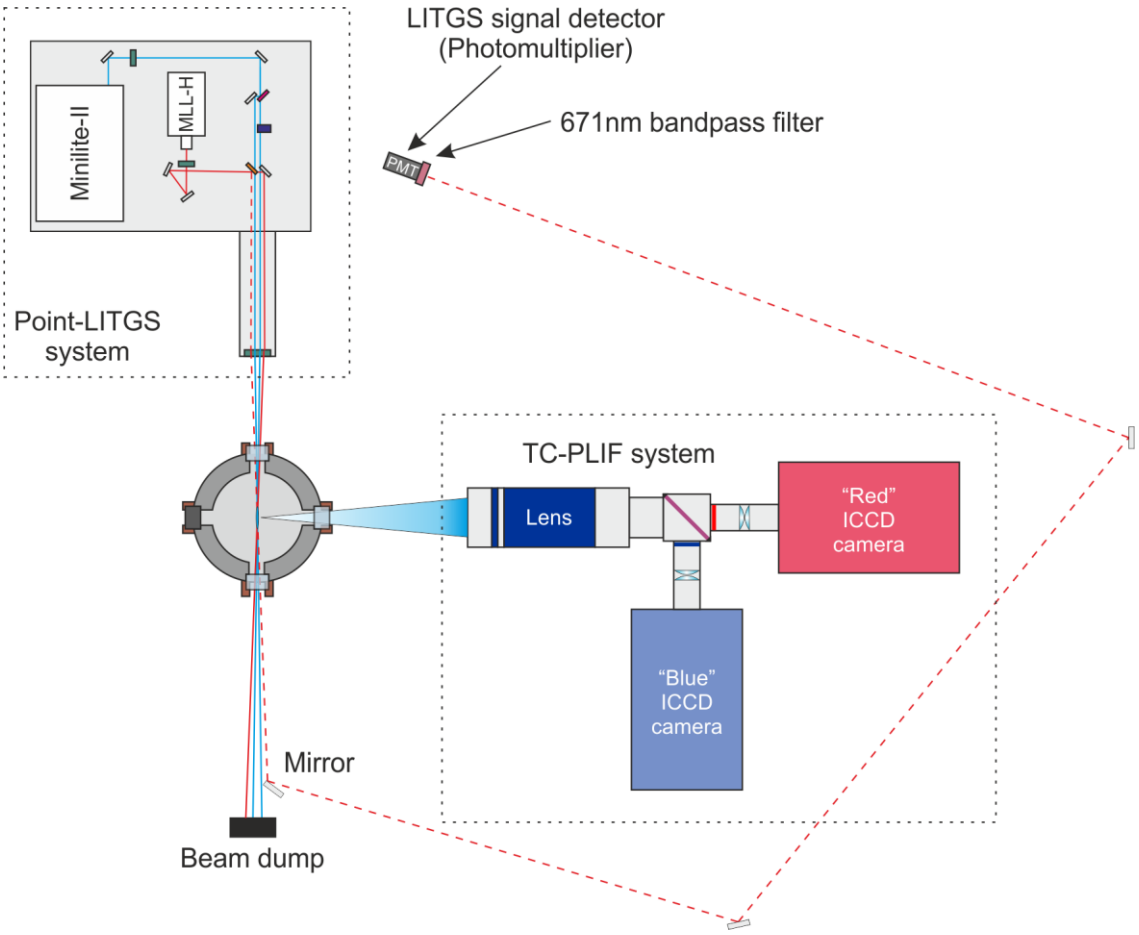

Figure 6-2 Layout of point-LITGS system [chapter 4] and TC-PLIF system [chapter 5] with respect to the optical engine cylinder cross-section. Approximately to scale.

The layout of the LITGS system with respect to the engine has already been described in chapter 4. The LITGS optical axis is aligned through the 16 mm windows at the top of the

cylinder and intersects the central axis of the cylinder [Figure 6-2]. LITGS measurements were therefore performed at a location within the TC-PLIF pump sheet and with the 'longer' axis of the LITGS interaction volume lying within the sheet[116]. The intersection of the LITGS pump beams with the TC-PLIF measurement plane is imaged in Figure 6-3, which displays the location, dimensions and intensity distribution of the intersection region.

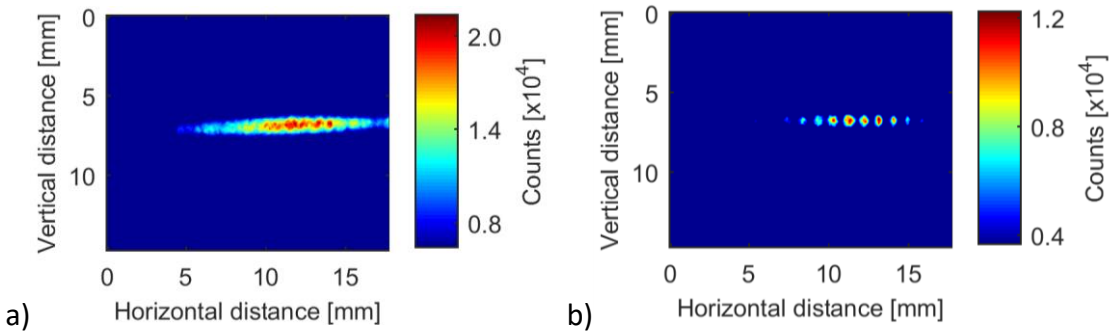

Figure 6-3 Images of the intersection of the LITGS beams with the TC-PLIF measurement plane. These images were taken both unobstructed (a) and with the TC-PLIF reference grid (b).

6.3. Results, analysis and discussion

The investigations of the application of TC-PLIF and LITGS to the optical engine are grouped into those looking at preliminary motored (6.3.1) and fired (6.3.2) tests, charge cooling and systematic biases introduced by the PMT gain (6.3.3), engine warm-up (6.3.4), temperature inhomogeneities (6.3.5), fuel composition (6.3.6) and critical analysis of the technique (6.3.7).

6.3.1. Preliminary results

70/30 iso-octane/toluene

A 70/30 iso-octane/toluene fuel blend was used as the 'standard' fuel composition throughout development of the technique as it represents the aromatic content of forecourt gasoline. Gasoline has, of course, many different components. The selection of a 2-component blend was primarily decided by the TC-PLIF limitation of requiring only one fluorescing component as

[116] This geometry is determined by the available optical access to the cylinder, however it also provides an opportunity to use TC-PLIF to identify the presence of strong thermal gradients within the LITGS volume such as those discussed in chapter 4.

opposed to an accurate representation of a 'real' fuel. 30 % toluene by volume provides sufficient tracer number density during the compression stroke for both techniques to operate effectively. Iso-octane was chosen for the base fuel as it is non-fluorescing and is a major component in forecourt gasoline.

Correlation of TC-PLIF and LITGS motored

The initial verification of the combined TC-PLIF and LITGS technique was performed by recording data at 5 different crank angles (90, 80, 70, 60 and 50 CAD BTDC) during the compression stroke of a motored engine[117]. A 70/30 iso-octane/toluene fuel blend was introduced via Port-Fuel-Injection (PFI) to form a stoichiometric mixture with the intake air, these conditions being nominally the simplest environment of interest in the running engine.

Reference signal ratio values from the TC-PLIF data were obtaining by spatially averaging the TC-PLIF data across the LITGS measurement region, then averaging all 20 images from each of the 50 CAD BTDC and 90 CAD BTDC datasets. These two values were calibrated onto an absolute temperature scale using the mean temperatures derived at 50 CAD BTDC and 90 CAD BTDC from the LITGS measurements. The relationship between signal ratio and temperature determined by this calibration was applied to the individual images in the TC-PLIF dataset. Importantly, the intermediate CAD datasets were not individually corrected to match the temperature of the corresponding LITGS datasets. Instead they show the raw variation in signal ratio over the 5 sets of CAD timings, displayed on a scale of absolute temperature rather than abstract 'signal ratio'.

Figure 6-4 shows the result of comparing the temperatures reported by the two techniques. The TC-PLIF data shows excellent agreement with LITGS for the intermediate, non-directly corrected sets.

[117] 1200 rpm, airflow 1.2 Ls^{-1}, intake air heated to 40 °C.

The distinct step-changes in signal ratio and hence temperature observed between TC-PLIF datasets taken at different CAD are well resolved by TC-PLIF system. This supports the assertion that the temperature sensitivity of the TC-PLIF technique is sufficient to provide a useful diagnostic relevant to a running engine. These datasets supply further evidence against the concept that the TC-PLIF images are insensitive to the changing temperature and are simply being 'corrected' by calibration with LITGS measurements.

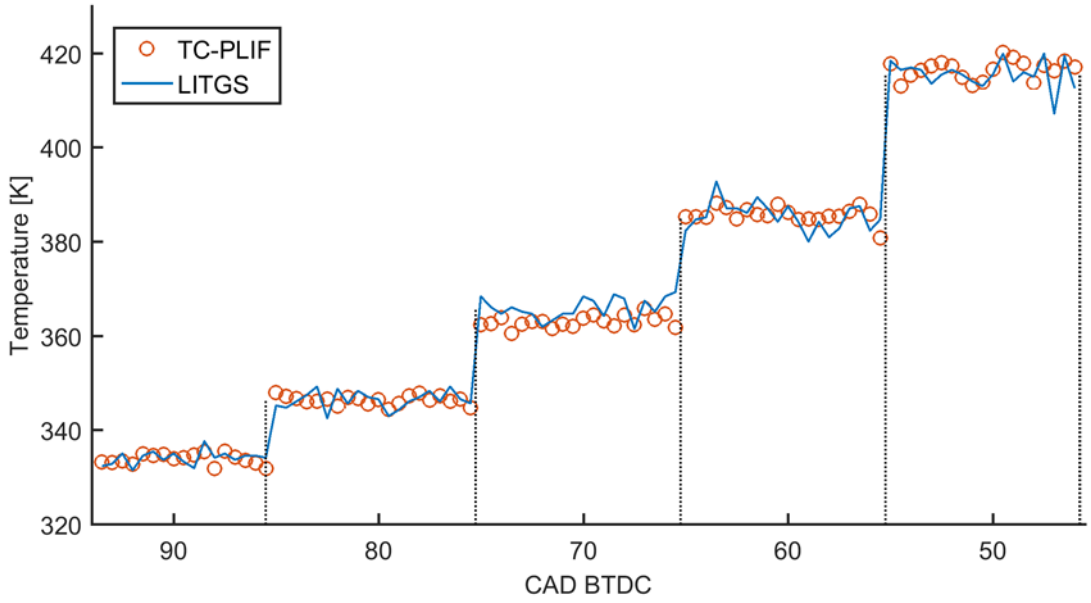

Figure 6-4 Initial correlation check of TC-PLIF and LITGS in motored engine. Sequential sets of 20 single-shot temperatures at each of 5 CAD timings.

Shot-by-shot correlation is not observed as the sensitivity of the TC-PLIF technique is insufficient to follow the minor fluctuations in local in-cylinder temperature between cycles for motored operation. TC-PLIF appears to show comparable variability compared to LITGS. This is most likely an effect of the spatial averaging of TC-PLIF across the LITGS volume which reduces the fluctuations due to noise within the ICCD images and will also suppress any small scale variation in temperature from the mean.

The LITGS measurement, while representing a measurement of the same physical region, does not spatially average the result in the straightforward way of averaging an area of TC-PLIF pixels. Signal contributions from each region of the LITGS interaction volume sum to produce an overall signal. The centre where the overlap between beams is strongest will dominate. As

such, the LITGS measurement will be weighted towards the temperature at the centre of the region and could be more sensitive to small scale fluctuations in temperature.

If the measurement precision of LITGS was the dominant contribution to the observed fluctuations in Figure 6-4, the variability of the LITGS-derived temperatures would decrease for later crank angles due to the improvement in LITGS precision with increasing pressure. As is apparent from Figure 6-4, this is not the case. The expected fluctuations in temperature of 0.6 % based on the variability of the in-cylinder pressure trace are of similar magnitude to the fluctuations in the temperatures derived from the LITGS data of 0.7 %. In combination, these observations suggest that in-cylinder temperature fluctuations are likely to provide a non-negligible contribution to the observed variability of the LITGS results of Figure 6-4.

Calibrated TC-PLIF motored

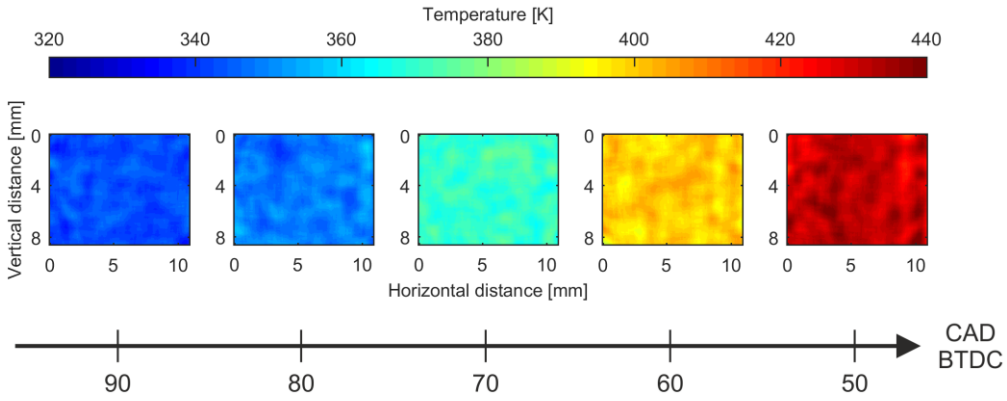

Figure 6-5 Calibrated motored TC-PLIF at a range of CAD timings during the compression stroke.

Upon examination of the single-shot TC-PLIF data, homogeneous temperature distributions are recorded for motored operation with PFI [Figure 6-5]. Direct injection images show an occasional artefact of intense fluorescence which may be from droplets [Figure 6-6 b)] or particularly strong spatial variation in fuel number density [Figure 6-31]. Despite the raw images showing greater variation in intensity, the temperature distributions derived from the motored GDI data are also homogeneous [Figure 6-6 a)].

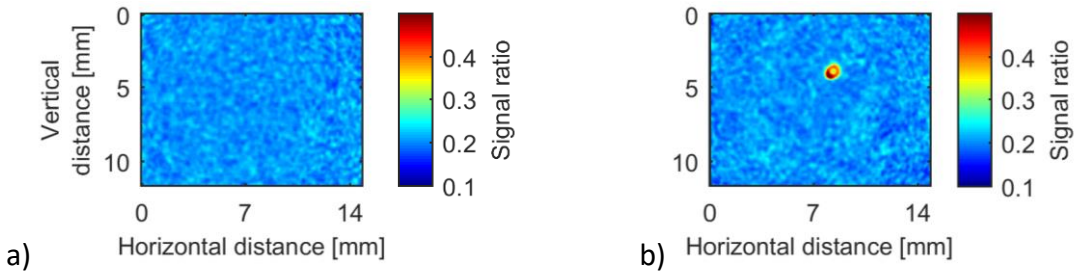

Figure 6-6 TC-PLIF signal ratio (analogous to temperature) maps for GDI operation. a) Homogeneous distribution. b) Droplet fluorescence artefact.

6.3.2. Fired results

The purpose of developing this thermometry technique was not to further characterise the comparatively simple case of a motored engine, but to be able to investigate a wide variety of engine conditions in a firing engine. With this in mind, further experiments continue to contain some motored data as a reference but the focus is on examining and explaining the trends and features discovered during fired operation.

Comparison of motored and fired

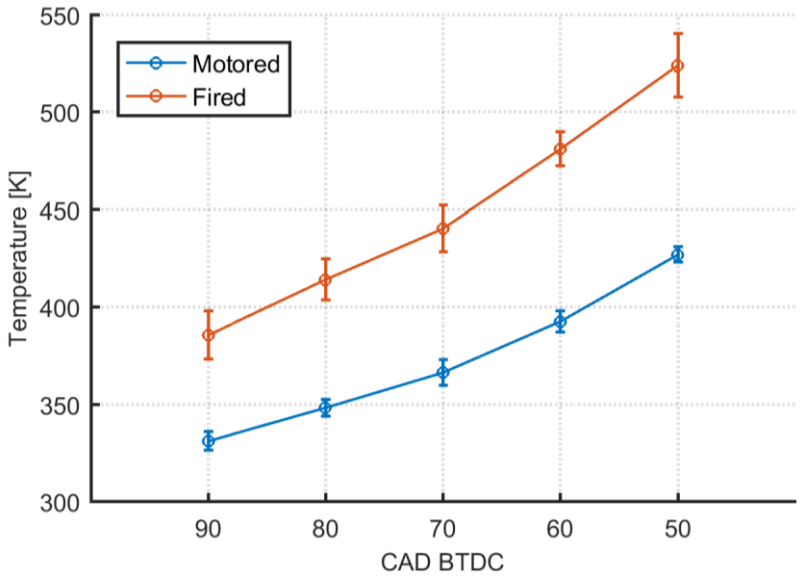

Figure 6-7 Fired vs motored LITGS temperatures between 90 and 50 CAD BTDC. Errorbars correspond to the standard deviation of 20 measurements for each CAD timing.

As expected, firing the engine results in a jump in temperature for all 5 CAD timings between 60 – 100 K. The standard deviation of the data sets at each CAD increased from ~ 1 % to around 2 % corresponding to an increase in variability due to the introduction of combustion.

The shape of the temperature vs CAD curve remained the same as no combustion was occurring during the compression stroke. Despite the complication of hot Exhaust Gas Residuals (EGR) mixing with the fresh air, the temperature rise in this figure is largely due to compression heating of the gas.

Comparison of motored and fired TC-PLIF data shows the appearance of temperature inhomogeneity, in particular for later Crank Angles [Figure 6-8]. These 'hotspots' appear for both PFI and GDI operation and coincide with the increase in variability observed within the fired LITGS data of Figure 6-7 to a standard deviation of 3 % for the 50 CAD BTDC dataset.

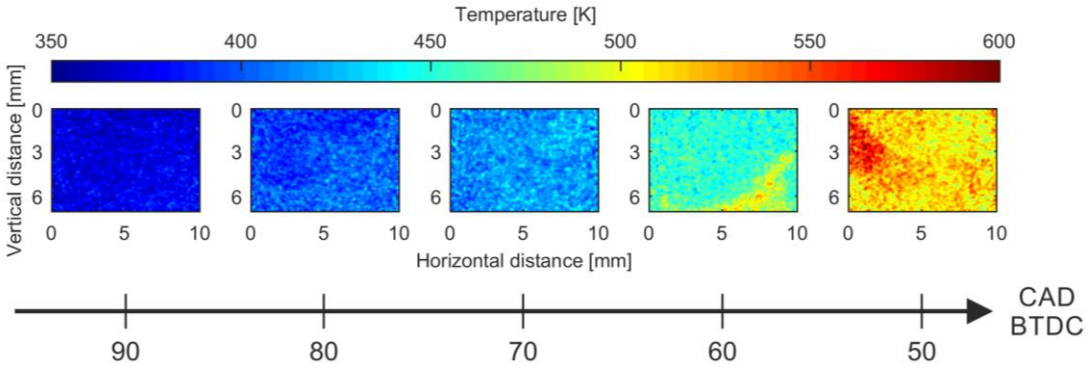

Figure 6-8 Calibrated fired TC-PLIF at a range of CAD timings during the compression stroke.

The appearance of temperature inhomogeneity combined with the higher temperatures and increased cyclic variability of fired operation provide large enough temperature differences to be able to further validate the combined system by observing the shot-by-shot correlation of the temperatures reported by the two techniques.

Fired shot-by-shot correlation

By using the simultaneous LITGS measurements to generate an averaged calibration curve for the TC-PLIF data, then allowing the individual TC-PLIF images to vary independently, we can see shot-by-shot correlation of the temperatures reported by the two techniques [Figure 6-9]. This is particularly noticeable for datasets at 60 and 50 CAD BTDC where the number density of toluene molecules is highest, leading to the strongest signals for both techniques. Pressure is

also highest at these CAD timings, leading to longer LITGS signal durations and therefore higher precision in temperature derivation.

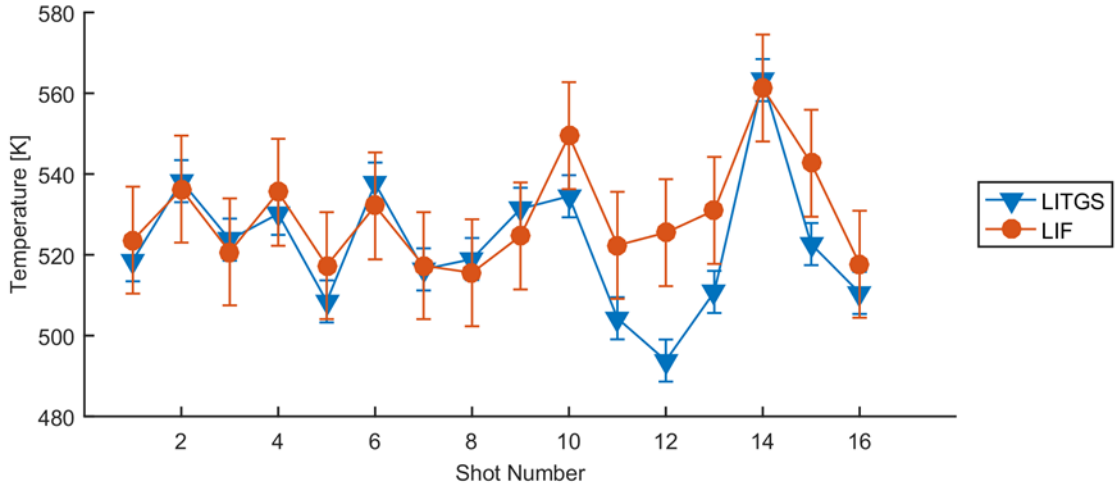

Figure 6-9 Shot-by-shot correlation of LITGS and TC-PLIF temperatures at 50 CAD BTDC for fired operation. TC-PLIF errorbars correspond to the standard deviation of TC-PLIF temperatures across a reference single-shot image for a homogeneous (motored) temperature distribution. LITGS errorbars correspond to the standard deviation of the 16 single-shot temperatures of this dataset. Corresponding TC-PLIF images are presented in Figure 6-11.

This strong correlation confirms that both techniques are independently resolving the cyclic variability of the in-cylinder temperature. One question that remains to be answered however, is whether the TC-PLIF technique is generating a map of local temperature distributions which can be reliably interpreted as having different temperatures at specific locations within the image. Alternatively, is the TC-PLIF data simply tracking the mean bulk temperature as though performing a point (albeit a very large point!) measurement, with variations across any one image being unrelated to temperature?

In order to answer this question, each TC-PLIF image in a fired dataset from 50 CAD BTDC was split into a grid of super-pixels, with each super-pixel representing the mean TC-PLIF temperature across a 50 x 50 pixel area (approximately 1 mm x 1 mm) within the TC-PLIF image. For each image, a correlation map was then generated showing the mean absolute value in Kelvin of the difference between the local TC-PLIF temperature at each super-pixel and the corresponding simultaneous LITGS temperature. Figure 6-10 displays the mean of 100 such correlation maps.

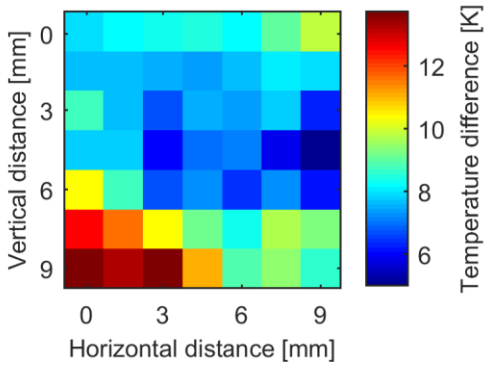

Figure 6-10 Spatial correlation of LITGS temperature versus local TC-PLIF temperatures, averaged over 100 shots.

There is a distinct structure to the correlation map of Figure 6-10, with the smallest difference between the TC-PLIF and LITGS temperatures towards the centre-right of the map. The correlation worsens with distance from this region, with the largest differences in reported temperatures being observed in the lower-left region of the map. From direct measurements during alignment, the LITGS volume is known to be centred over the super-pixel at row 4, column 6. Unsurprisingly, this means the best correlation occurs when comparing the LITGS temperature to the TC-PLIF temperature spatially averaged across the LITGS interaction region, rather than elsewhere in the image.

This map supports the argument the TC-PLIF technique is performing as designed to generate 2D maps showing the variation in local temperature. Also, the correlation shows that both techniques are independently resolving the cyclic variability of local in-cylinder temperatures under fired operation.

Discrepancies between TC-PLIF and LITGS temperatures

Overall, the TC-PLIF and LITGS derived temperatures display excellent correlation in Figure 6-9, in particular shot 14 for which TC-PLIF reports a strong ‘hotspot’ and LITGS also reports a high temperature. Despite this, shots 11-13 display LITGS temperatures cooler than the corresponding TC-PLIF data, with shot 12 showing the largest deviation.

A potential explanation for the LITGS technique reporting cooler temperatures than TC-PLIF would be the presence of multiple temperature zones within the LITGS interaction region. TC-

PLIF would return the mean temperature across the imaged area, while LITGS would return a temperature lower than the mean as discussed in chapter 4. This however is not the case for shots 11-13 as inspection of the relevant TC-PLIF images [Figure 6-11] shows no evidence of multiple distinct temperature zones across the LITGS measurement region.

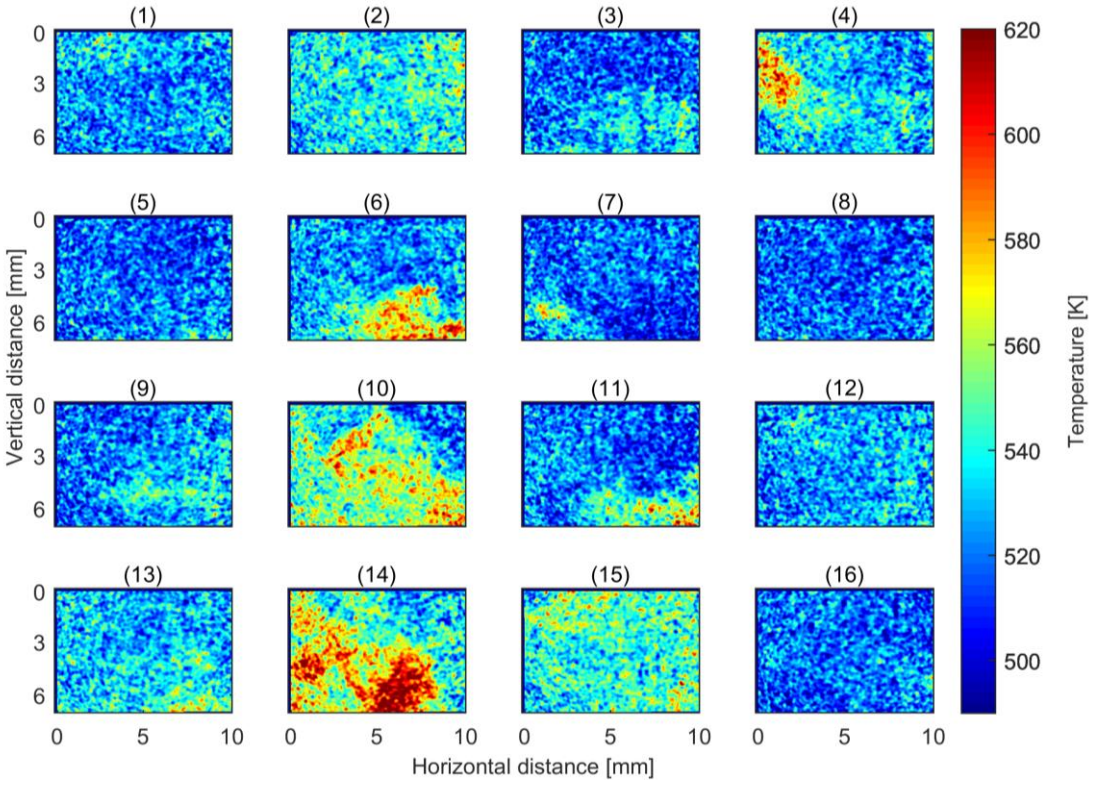

Figure 6-11 TC-PLIF images corresponding to the TC-PLIF temperatures reported in Figure 6-9.

This demonstrates the utility of performing temperature measurements with two techniques simultaneously. Not only can LITGS be used as an in-situ calibration of TC-PLIF data, but the TC-PLIF data can provide information about the local temperature distribution for investigations into the accuracy of LITGS measurements. Currently the cause of the discrepancy between LITGS and TC-PLIF for shots 11-13 is unknown.

6.3.3. Charge cooling

This section discusses a major difference between GDI and PFI operation, the phenomenon of ‘charge cooling’, along with the discovery and mitigation of a systematic bias affecting the temperatures derived from the LITGS measurements.

'Charge cooling' refers to the evaporative cooling effect of injecting liquid fuel directly into the cylinder, leading to a reduction in overall temperature of the order of 30 K [4]. At the low load conditions of this work charge cooling is a more subtle effect, typically resulting in a temperature difference between GDI and PFI of the order of 5 K.

In section 6.3.6 below, the effect of varying the fraction of toluene in the 2-component iso-octane/toluene fuel blend is investigated. Suffice to say, one consequence of increasing the toluene fraction is to increase the signal intensities for both the TC-PLIF and LITGS techniques due to the increased tracer number density. Although the standard fuel blend was 70/30 iso-octane/toluene, much of the discussion that follows uses the higher toluene fraction fuel (50/50 iso-octane/toluene) data. This is in part due to the slight increase in latent heat of vaporisation of the fuel[118] which magnifies the charge cooling effect. Mainly however, it is due to the higher signal-to-noise ratio and hence lower variation of the results of both techniques. This allows the findings to be presented and explained with clarity and without any ambiguity in interpretation caused by noisy data.

A major parameter of interest is injection strategy. Previous work with point-LITGS had demonstrated the ability of LITGS to resolve the effect of charge cooling with direct injection compared to port injection [25].

Measurement of charge cooling with the combined TC-PLIF and LITGS system would demonstrate the ability of the optical diagnostic to resolve temperature differences small enough to be of use to investigate the subtle differences in the absolute temperature distributions between engine conditions.

LITGS

Measurement of the in-cylinder temperatures with LITGS for PFI and GDI under motored operation provides an initial test environment to isolate the potential charge cooling effect.

[118] Toluene's latent heat (38.06 $KJmol^{-1}$) [241] is slightly greater than iso-octane's (35.2 KJ/mol^{-1}) [242].

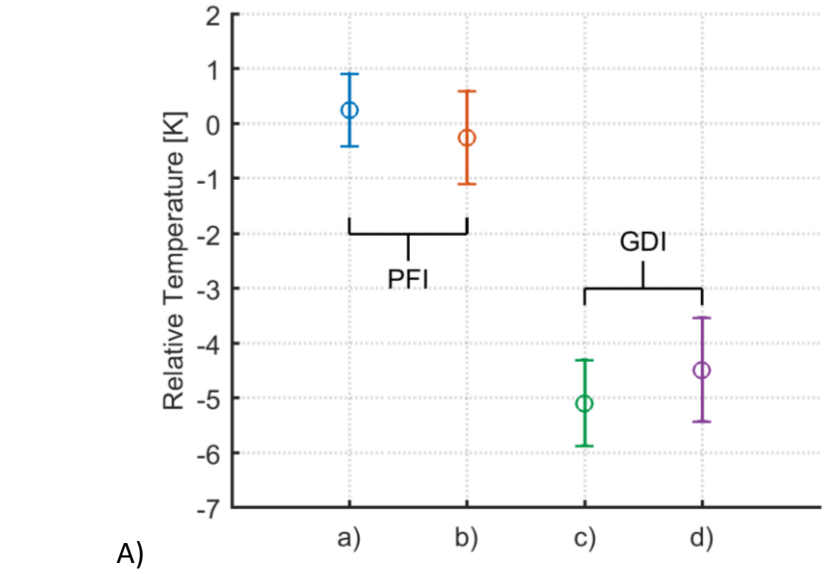

A)

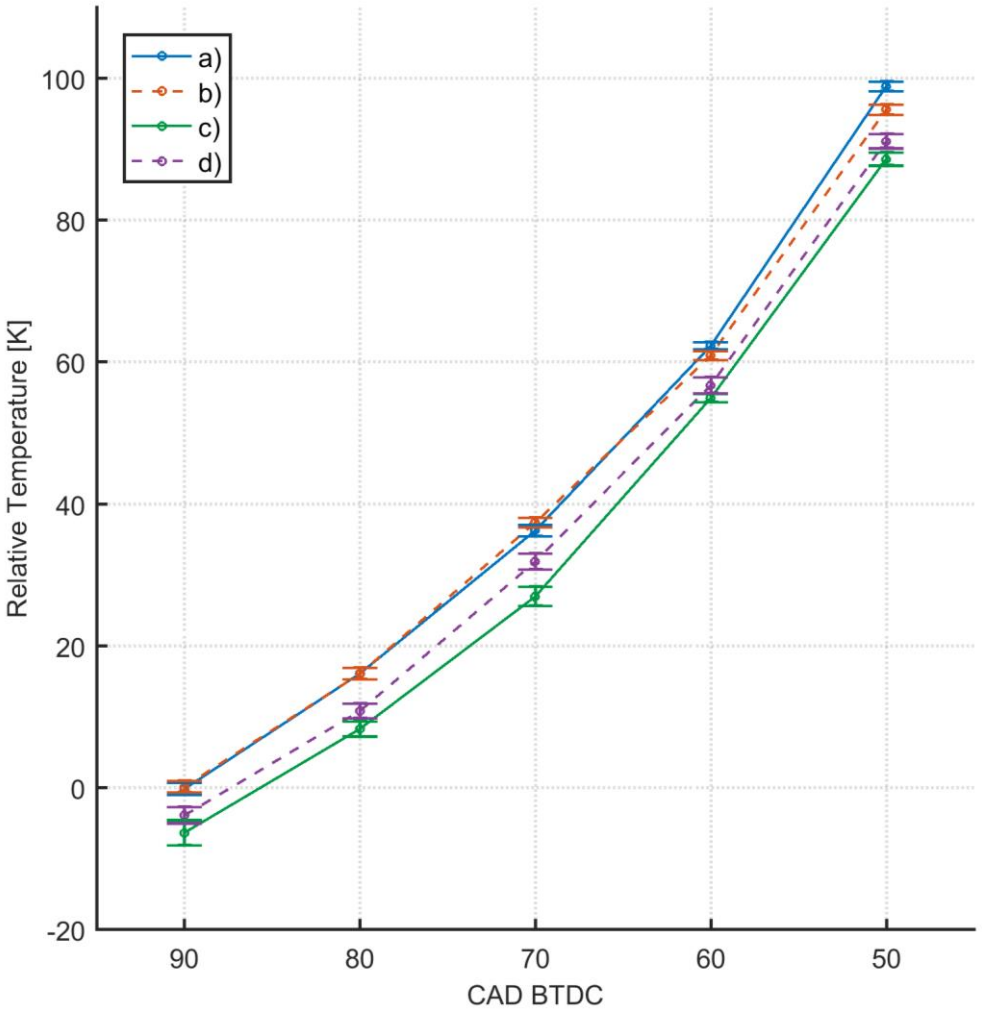

B)

Figure 6-12 A) Motored LITGS temperatures at 90 CAD BTDC with reference to the mean temperature of datasets a) and b). B) Motored LITGS temperatures between 90 and 50 CAD BTDC with reference to the mean temperature at 90 CAD BTDC for datasets a) and b). For the datasets of both A) and B), a) and b) are taken using PFI while c) and d) are taken using GDI. Errorbars in this figure represent the standard error of the mean.

As shown in Figure 6-12 A), the two GDI datasets at 90 CAD BTDC both display lower mean temperatures than the two PFI datasets. This trend continues throughout the compression stroke [Figure 6-12 B)], with mean GDI temperatures consistently 5 – 8 K cooler than those of PFI. These measurements appear to be resolving the charge cooling effect of GDI compared to PFI. However a problem arises if the absolute temperatures from the two experiments are compared.

PMT gain bias to temperature

There exists a mismatch of approximately 20 K between the derived temperatures of the 90 CAD BTDC PFI motored dataset and the first datapoint of the 90 – 50 CAD BTDC PFI motored dataset [Figure 6-13]. These two datapoints should match exactly, within the precision of the measurement, as they represent data acquired under identical engine conditions. The same problem is apparent for GDI operation, as a shift of approximately 20 K between the two measurements of GDI at 90 CAD BTDC.

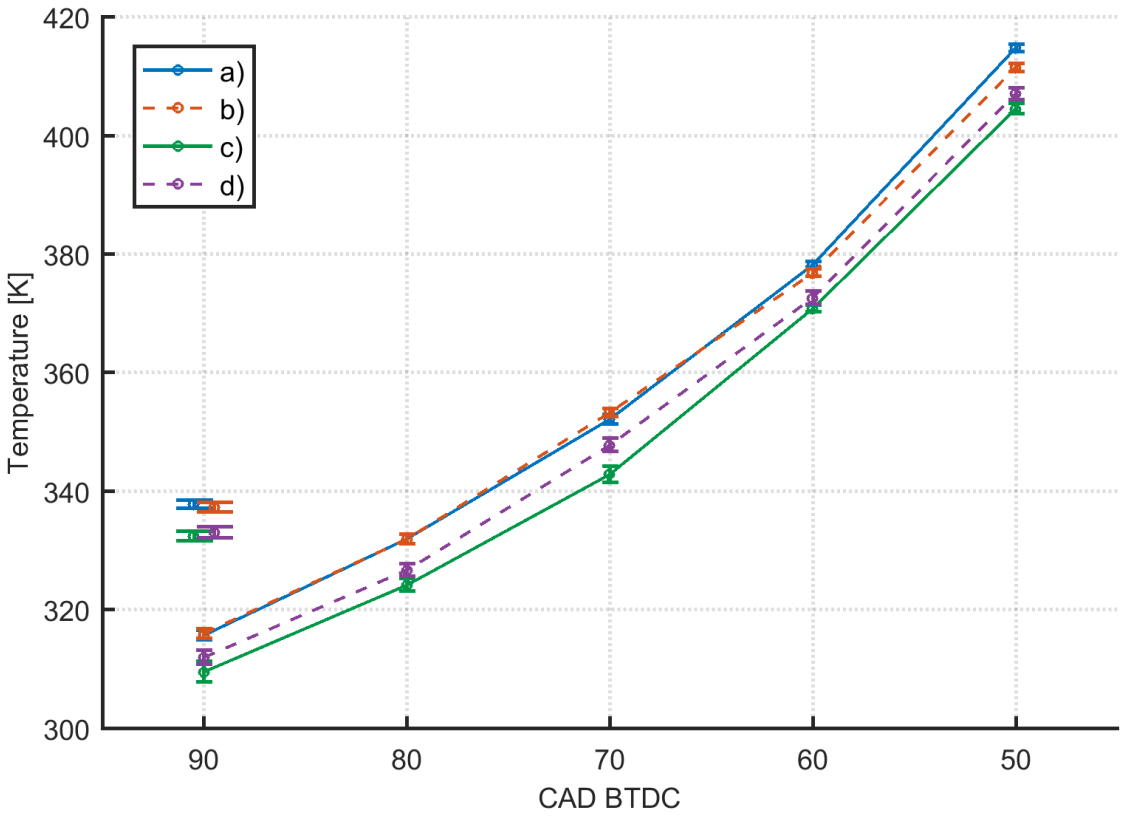

Figure 6-13 Mismatch in derived temperatures for LITGS at 90 CAD BTDC for the motored datasets of Figure 6-12 A) and B). Datasets a) and b) are taken using PFI while c) and d) are taken using GDI. Errorbars in this figure represent the standard error of the mean. Single datapoints at 90 CAD BTDC have been offset by ± 0.5 CAD for clarity.

An investigation into the source of this systematic bias considered both the practical and analytical aspects of the experiment. It was determined that varying the gain of the PMT, a procedure intended to maximise the signal-to-noise ratio of the weak signals from the engine, was responsible for the bias.

As the compression stroke progresses from 90 to 50 CAD BTDC, the volume inside the cylinder halves with corresponding increases in tracer number density, pressure and temperature. This results in a large dynamic range of LITGS signal intensity within the 90 to 50 CAD BTDC datasets. In order to collect the data on an oscilloscope, the gain of the PMT was adjusted to optimise the signal strength of the largest signals (at 50 CAD BTDC) while remaining under the 100 mV limit for the PMT's response to be linear as determined in chapter 4. The oscilloscope scale was then adjusted to make best use of its 8 bits of vertical resolution. The LITGS signals at 90 CAD BTDC were therefore much smaller on the oscilloscope scale, covering perhaps a fifth of the available range.

When recording data solely at 90 CAD BTDC, it was assumed to be beneficial to increase the gain of the PMT to optimise the signal strength, and therefore signal-to-noise ratio, of these much weaker signals. Again, the 100 mV linearity limit was used to determine the optimum PMT gain. This procedure was followed for each type of dataset collected over the course of an experiment. Engine conditions producing similarly sized signals resulted in the PMT gain remaining unchanged. Engine conditions that led to significant changes in signal strength, such as changing the CAD timing of interest or switching from motored to fired operation, resulted in the PMT gain being re-optimised to a new value.

Had varying the PMT gain simply altered the intensity of the signal, no bias in derived temperature would have been introduced. However, the gain setting also affects the time response of the PMT either by delaying the signal output, distorting the shape of the signal or most likely both. A change in the time-response of the PMT with changing gain introduces a different delay between the signal recorded by a photodiode indicating the timing of the pump

pulse and the LITGS signal recorded by the PMT. This has the effect of changing the apparent time behaviour of the LITGS signal which is dependent on quench rates that affect the induced grating evolution.

The LITGS fitting routine generates a modelled signal with reference to the timing of a pump pulse. A shift in time of the recorded LITGS signal with respect to the recorded pump pulse that is not a result of the dynamics of the grating formation cannot be accounted for by the fitting routine. While a delay in the PMT response time of less than 1 ns is on a much smaller timescale than that of the acoustic oscillations, approximately 20 ns, it is on a comparable timescale to the fast quenching rate affecting the grating dynamics and is sufficient to cause a mismatch of the experimental LITGS signal and the modelled LITGS signal generated by the nominally ‘correct’ values of the quenching rates, Reynolds number and acoustic transit time. This mismatch is greatest in magnitude for the steep initial rising edge of the LITGS signal. A better fit to the rising edge of the experimental signal is provided by slowing the quenching rates, which delays the rising edge of the modelled signal to match that of the signal recorded by the PMT. Altering the quenching rates has a more complex impact on the evolution of the signal than simply delaying the formation of the grating, including affecting the contrast of the acoustic oscillations and the duration of the LITGS signal. These effects, which in isolation would reduce the quality of the fit, can in part be compensated for by perturbing the values of the remaining fit parameters from their nominally ‘correct’ values. Unfortunately for a thermometry diagnostic technique, one of the fit parameters biased in this way is the acoustic transit time, from which temperature is derived. Therefore the gain-dependent change in the time response of the PMT leads to the fitting routine altering the temperature from the correct value to compensate for an apparent change in parameters such as quench rates.

The current sets of LITGS data from the engine therefore cannot be interpreted as a self-consistent set of absolute temperature values. Any time the gain of the PMT is changed, the calibration relating the LITGS measurement to an absolute temperature value is lost.

Information recovery

While the comparison of absolute temperatures for some datasets is not possible, it is still possible to recover relative temperature information within a dataset and also between any datasets which share a common PMT gain.

Figure 6-12 a) and b) can therefore each be analysed in isolation as the datasets within each figure have the same PMT gain. Figure 6-13 in contrast is displaying data collected using two different PMT gain settings, leading to the 20 K discrepancy.

One of the major losses in discussing only the relative temperatures of LITGS datasets was the intention to use LITGS to provide an absolute calibration for TC-PLIF measurements. This issue can still be mitigated, in part, for existing datasets by calibrating one of the LITGS datapoints for each ‘new’ value of PMT gain to a LITGS datapoint taken using the ‘original’ value of PMT gain. This requires the assumption that TC-PLIF datasets which show identical signal ratios can be used to identify datasets of different PMT gain which have the same physical temperature. The corresponding ‘new’ LITGS datapoint can then be corrected to the same temperature as the ‘original’ LITGS datapoint. The remaining datapoints in the datasets of interest have known relative temperatures with respect to the first and can therefore all be placed on an absolute temperature scale.

With the absolute values of LITGS temperature measurements restored, the TC-PLIF data can be calibrated as intended. Investigations into the thermal effects of injection strategy, fuel composition and fired operation can continue on those subsets of the initial experimental datasets which meet the conditions for absolute temperature recovery described above.

All LITGS results presented in the remainder of this chapter have absolute temperature values presented with the above discussion in mind and do not mix datasets of different PMT gains.

Future solution

The solution is of course to fix the PMT gain at a constant value for future LITGS experiments. The signal output of the PMT must still be maintained below the 100 mV linearity limit, necessitating some alternative form of control over the signal intensity given the wide range of signal strengths produced during engine experiments. One option is to set a very high fixed gain for the PMT, optimised to record the weakest signals of interest. The problem of intensity control is then reduced to an issue of attenuation.

A filter wheel containing neutral density filters with a variety of optical densities placed in front of the PMT would permit the attenuation to be selected from a discrete range of options for any given run. Solutions with greater potential for fine-tuning the optimisation of the signal include the use of a variable optical density filter or the introduction of an iris in front of the PMT. The smoothly varying aperture size offered by the iris would allow for attenuation from 0 % to 100 %, limited by how small the incremental adjustments to aperture size could be made.

Preliminary optical attenuation tests

Preliminary tests were performed to assess the potential for optimising signal detection using optical attenuation at fixed high PMT gain to replace the variable PMT gain method used previously. For each set of data collected, an iris was used to attenuate the LITGS signal to the highest intensity which retains a linear-response of the PMT.

Figure 6-14 clearly shows the success of the new signal collection method. Derived temperatures at 90 CAD BTDC are consistent between datasets with high optical attenuation (a) and low attenuation (b). This is in contrast to the derived temperatures from datasets with different values for PMT gain [Figure 6-13].

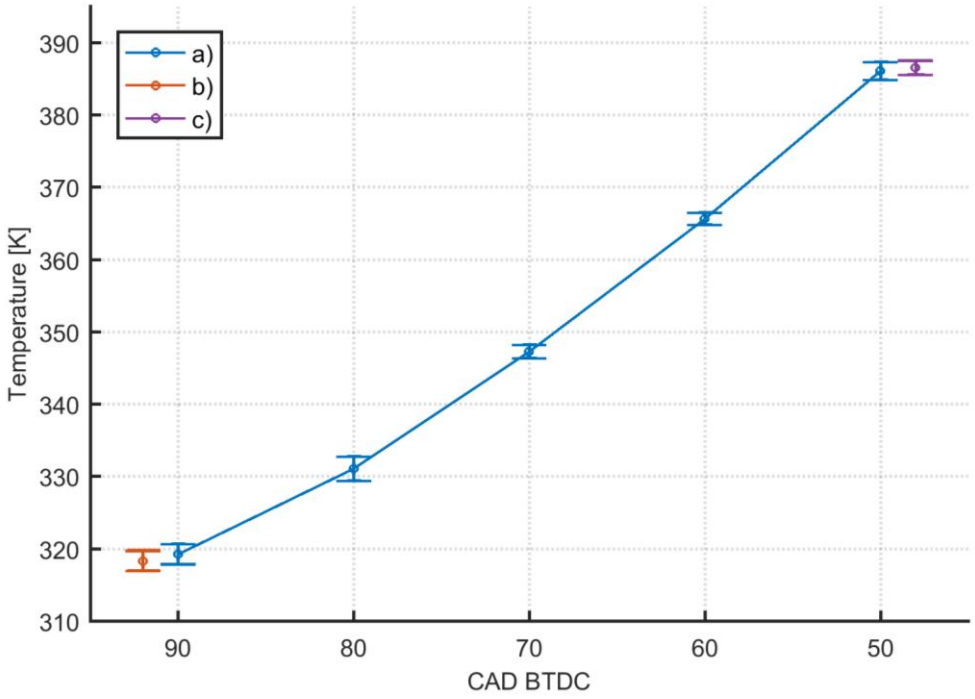

Figure 6-14 Optical attenuation of LITGS signal at fixed high PMT gain produces consistent derived temperatures throughout compression stroke at a) 90 to 50 CAD BTDC, b) 90 CAD BTDC and c) 50 CAD BTDC. Errorbars in this figure represent the standard error of the mean. The datapoints of b) and c) are offset from a) by ± 2 CAD for clarity.

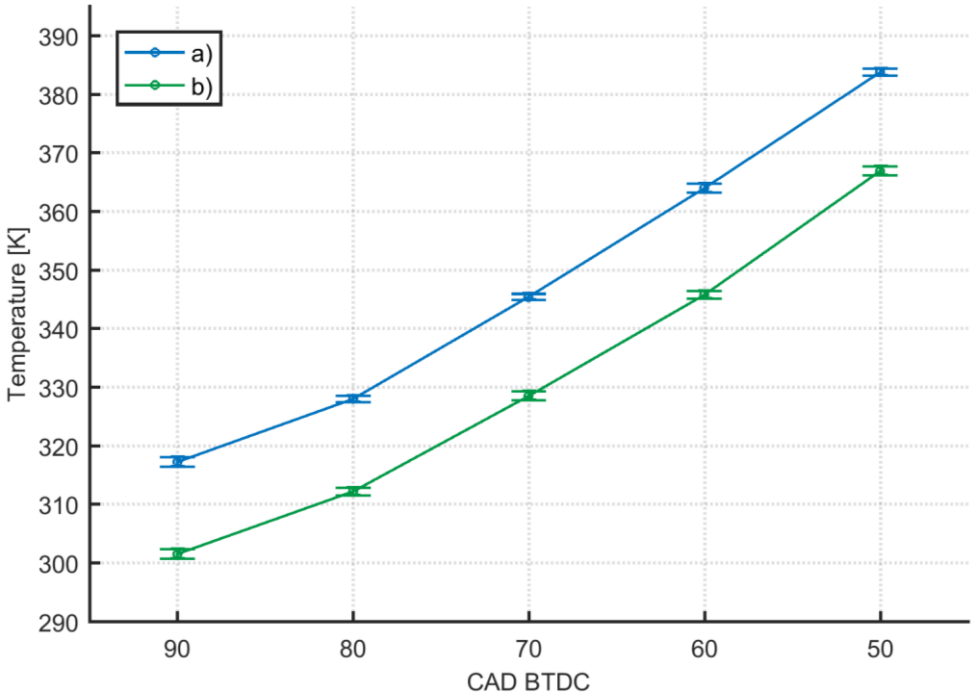

Figure 6-15 Charge cooling between a) PFI and b) GDI operation with new optical attenuation method of LITGS signal control. Errorbars in this figure represent the standard error of the mean.

Figure 6-15 supplies further confirmation regarding the ability of the LITGS system to resolve the charge cooling effect. The temperature decrease for GDI operation is still visible with new optical attenuation method of signal control[119].

Using this new method of signal collection, the LITGS technique can be reliably applied to a wide variety of signal intensities, and therefore engine conditions, without the systematic bias introduced by varying the PMT gain.

TC-PLIF comparison to LITGS

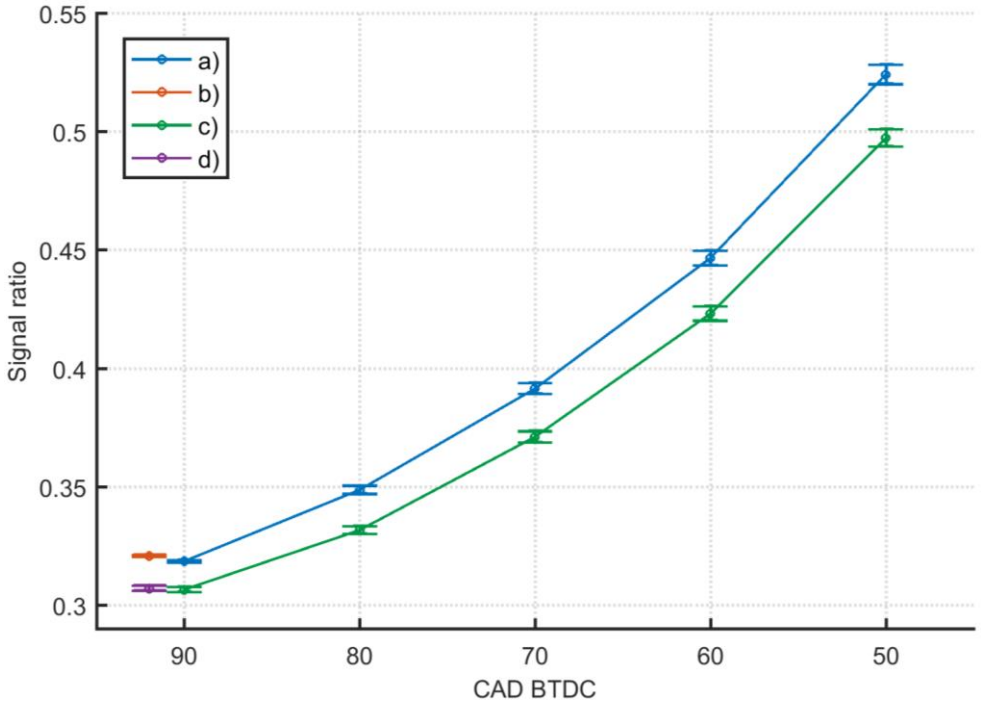

Figure 6-16 Uncalibrated TC-PLIF signal ratios taken simultaneously with the LITGS measurements of Figure 6-13. Datasets a) and b) are taken using PFI while c) and d) are taken using GDI. Errorbars in this figure represent the standard error of the mean. Single datapoints b) and d) are offset by – 2 CAD from 90 CAD BTDC for clarity.

For comparison with LITGS data, uncalibrated TC-PLIF signal ratios for motored operation at 90 CAD BTDC, taken simultaneously with the LITGS datasets of Figure 6-13, were averaged over the LITGS region and presented in Figure 6-16. The TC-PLIF signal ratios, being

[119] This preliminary dataset was taken in a new optical engine, with a new fuel injector and without the ability to fire the engine to accurately determine the stoichiometry of the air-fuel mixture. An overly-rich mixture for the GDI case b) would be consistent with the larger 15 K charge cooling effect in comparison to the 5 K cooling observed in Figure 6-12.

analogous to temperature, show the same trend as the corresponding LITGS data, that GDI operation results in cooler in-cylinder temperatures throughout the compression stroke. Further confirmation that the mismatch of derived LITGS temperatures at 90 CAD BTDC is a systematic bias, not a physical temperature shift between runs, is given by the excellent match of the TC-PLIF signal ratio values at 90 CAD BTDC for both PFI ('a' and 'b') and GDI ('c' and 'd').

Fired operation

Having confirmed the observation of charge cooling for the homogeneous temperature distributions of motored operation, examination of the fired datasets determines whether the cooling effect remains resolvable amongst the inhomogeneous and more variable environment of fired operation.

At 50 CAD BTDC the charge cooling effect remains clear in the LITGS data of Figure 6-17 A). While LITGS is able to resolve the charge cooling effect throughout the compression stroke from 90 to 50 CAD BTDC [Figure 6-17 B)], TC-PLIF is no longer able to consistently resolve the difference in temperatures[120] (without individual calibration of each dataset by the corresponding LITGS measurements) owing to the reduced signal-to-noise ratios compared to motored operation [Figure 6-17 C)].

[120] Although runs a) and c) of Figure 6-17 C) do show a difference in mean temperatures at 60 and 50 BTDC.

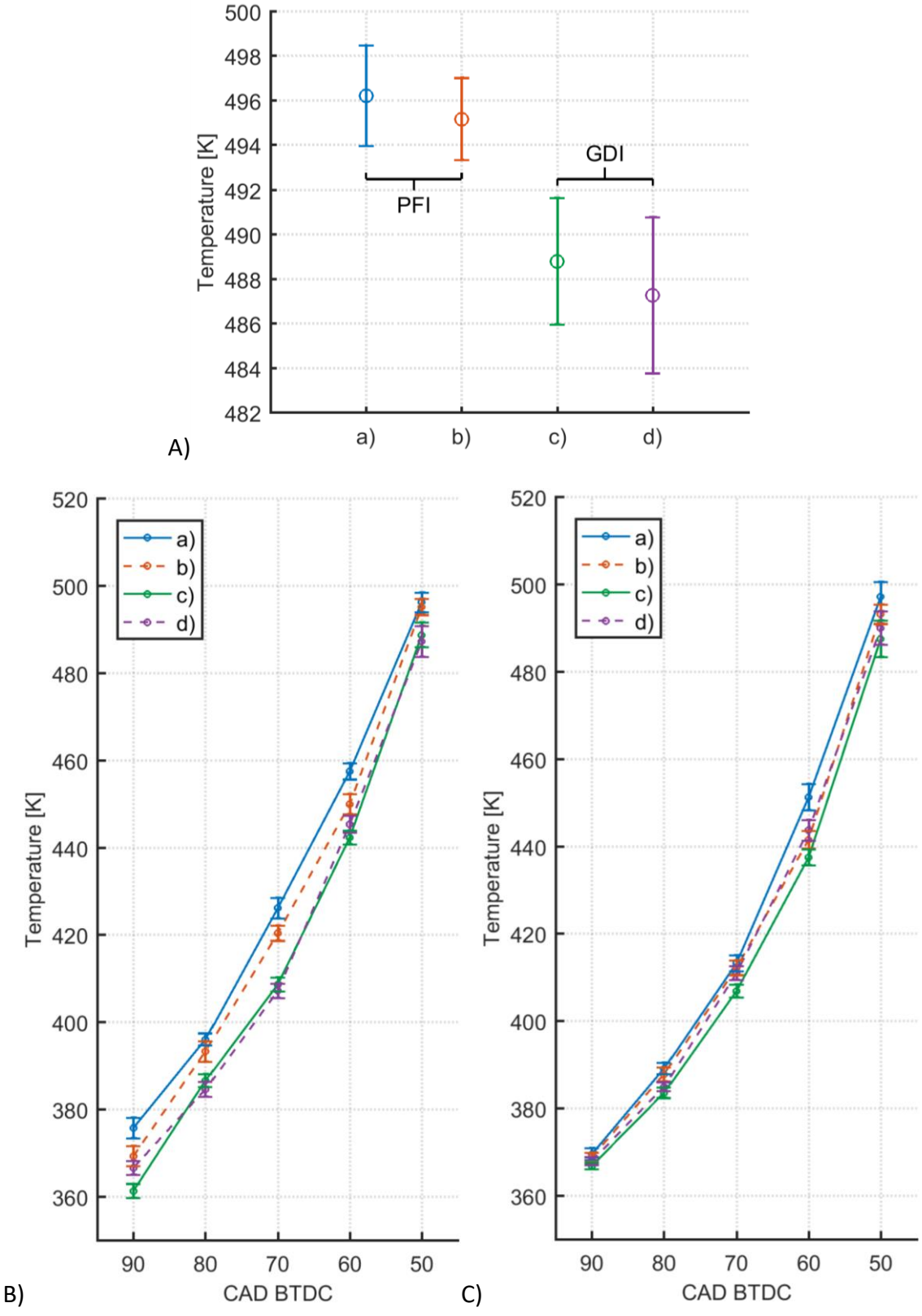

Figure 6-17 Fired LITGS temperatures at 50 CAD BTDC (A) and between 90 and 50 CAD BTDC (B). TC-PLIF temperatures between 90 and 50 CAD BTDC (C) using the same calibration for all 4 datasets to illustrate the capabilities of TC-PLIF without calibration of each individual dataset with LITGS. Datasets a) and b) are taken using PFI while c) and d) are taken using GDI. Errorbars in this figure represent the standard error of the mean. Absolute temperature scale recovered using the re-calibration technique of section 6.3.3. See Figure 6-12 for comparison to motored operation.

6.3.4. Engine warm-up during firing

Figure 6-18 displays the LITGS temperatures recorded over the first two minutes of the engine being fired, averaged into 5 chronological groups of 20 measurements. Before and after firing the engine in short two-minute bursts, for preservation of the optical components, the engine is motored at the same speed and allowed to cool back to its 'motored equilibrium' temperature.

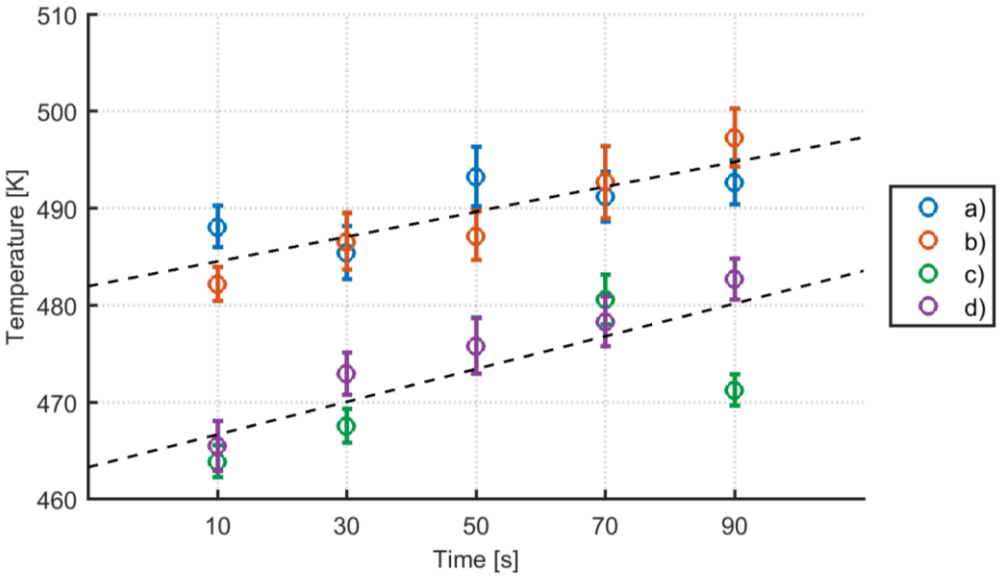

Figure 6-18 LITGS temperatures with PFI ('a' and 'b') and GDI ('c' and 'd') showing warmup of firing engine. Errorbars in this figure represent the standard error of the mean.

A steady trend of increasing temperature with firing duration is observed for both PFI and GDI operation at a rate of approximately 9 $Kmin^{-1}$. This corresponds to the heat produced by the repetitive combustion events gradually raising the temperature of the cylinder head, walls and piston. In turn these hot surfaces transfer heat to the incoming fresh charge, raising the temperature of the pre-combustion mixture being probed by LITGS. The temperature should eventually tend to an equilibrium value for the firing engine. Confirmation of this expectation was not possible due to constraints on the firing duration imposed by a desire to keep the optical access windows in one piece!

6.3.5. Hotspot characteristics

As discussed in section 6.3.2 and displayed in Figure 6-19, TC-PLIF temperature maps of fired operation between 90 and 50 CAD BTDC clearly show the increased prevalence of structure in the temperature distributions or 'hotspots' towards the end of the compression stroke. Hotspots are defined for the purposes of discussion in this work as a local regions of at least 0.5 mm in diameter within a TC-PLIF image whose temperature is greater than the mean temperature of the image by at least 10 %.

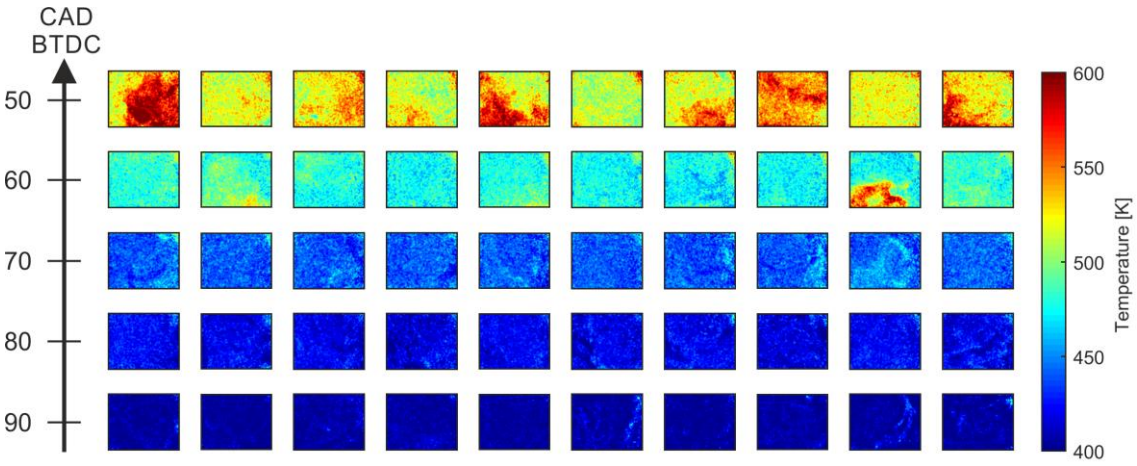

Figure 6-19 Fired TC-PLIF temperature distributions, each covering 9 x 10 mm for GDI operation with a 70/30 blend of iso-octane/toluene. 10 single-shot images are displayed for each of 5 CAD timings.

For each TC-PLIF dataset, the inhomogeneity of the temperature distributions is quantified by calculation of a Coefficient of Variation, 'CoV', image. The CoV images presented in this section each represent the standard deviation of temperatures at each pixel for a 100 image dataset, divided by the mean temperature distribution of the dataset. As such, each CoV image provides a measure of the cyclic variability in temperature of a given dataset, allowing quantitative comparison of TC-PLIF data for various engine operating conditions.

Figure 6-20 displays CoV images for each of the 5 CAD timings of Figure 6-19. Temperature fluctuations across the TC-PLIF images increase both in magnitude and frequency of occurrence for later crank angles, with a spatially-averaged CoV value of 4.7 % at 50 CAD BTDC in comparison to 2.2 – 2.4 % between 90 and 70 CAD BTDC. While compression

heating of the gas will magnify any early temperature inhomogeneity, this is not sufficient to account for the observed increased magnitude of the 50 CAD BTDC hotspots as compared to the inhomogeneity at 90 CAD BTDC.

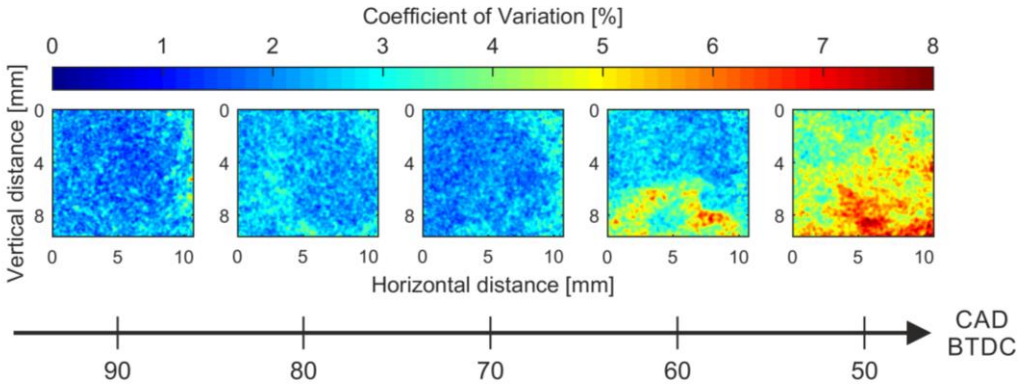

Figure 6-20 Coefficient of Variation images of each CAD timing for the TC-PLIF images of Figure 6-19.

For fired operation at 50 CAD BTDC, the TC-PLIF images for PFI (a) and GDI (b) in Figure 6-21 show highly structured temperature distributions with a large cycle-to-cycle variability. The hotspots are typically 50 – 100 K (10 – 20 %) hotter than the surrounding bulk gas and occur more frequently in the lower half of the images. This results in the mean temperature distributions of Figure 6-22 displaying a temperature difference between the upper and lower halves of the image of a) 7 K (1.3 %) for PFI and b) 9 K (1.7 %) for GDI. Similarly, Figure 6-23 confirms the increase in variability for the lower half of the images with an increase in CoV to a) 3.9 % for PFI and b) 4.1 % for GDI as compared to the upper half CoV of 3 % for both injection strategies.

The spatial distribution and frequency of occurrence of the hotspots does not appear to have a strong dependence on injection strategy, as inferred from the similarity of the mean temperature distributions [Figure 6-22] and CoV images [Figure 6-23]. However, with reference to the colour scale of Figure 6-22 the charge cooling effect of 12 K (2.3 %) for the bulk gas temperatures of GDI b) as compared to PFI a) for Figure 6-22 is clearly visible.

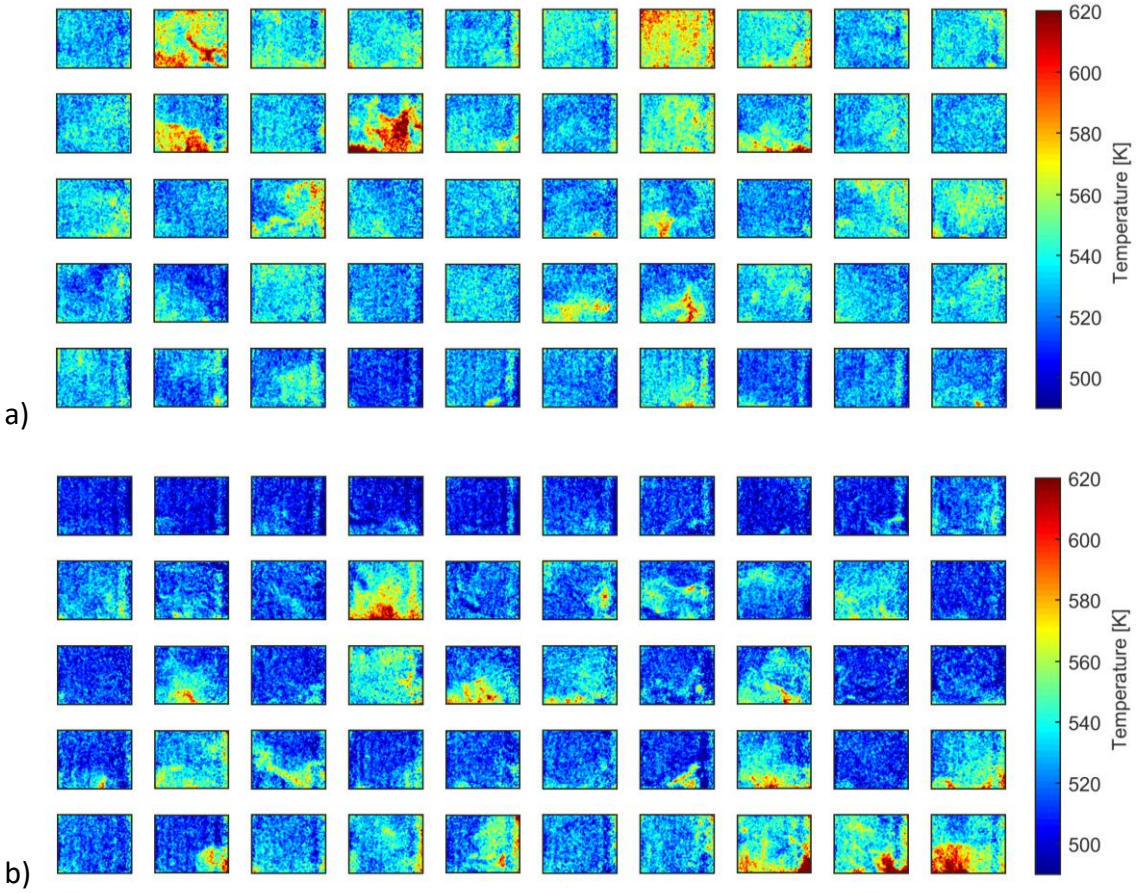

Figure 6-21 Fired TC-PLIF temperature distributions. 50 single-shot images are displayed, each covering 9 x 10 mm at 50 CAD BTDC with a 70/30 blend of iso-octane/toluene for a) PFI and b) GDI operation.

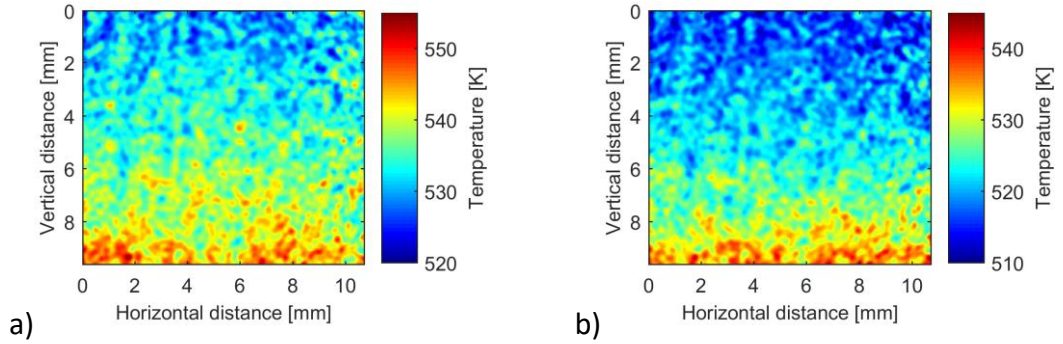

Figure 6-22 Mean temperature distributions of datasets a) and b) displayed in Figure 6-21.

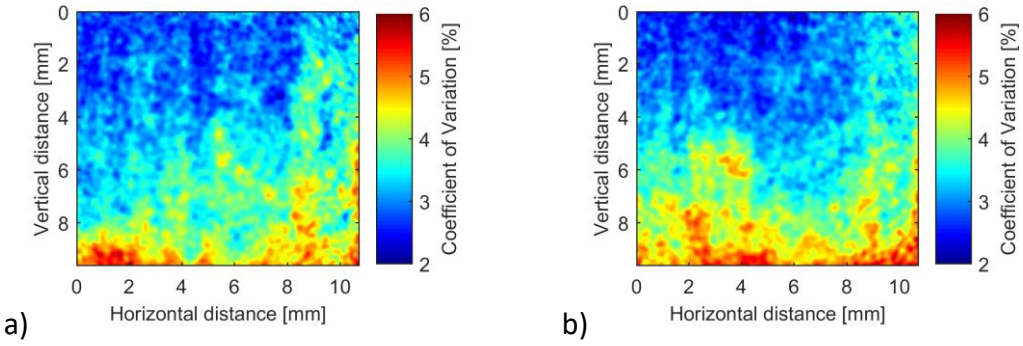

Figure 6-23 Coefficient of variation images of datasets a) and b) displayed in Figure 6-21.

6.3.6. Toluene content

One parameter of significant interest is the effect of varying the fuel composition on the in-cylinder temperature distribution. Development of the TC-PLIF/LITGS diagnostic has been limited to using a blend of iso-octane and toluene for simplicity. In theory multi-component fuels could be investigated, providing the other components did not fluoresce. This precludes the addition of other aromatics or molecules such as ketones found in forecourt gasoline.

For the purposes of the development of the technique it is informative to determine the effect of varying the toluene fraction of the fuel blend. The primary effect is likely to be variation in the signal intensity due to the change in overall toluene number density within the mixture. This will set a lower limit on the toluene content of fuels that can be investigated before the signal-to-noise ratio becomes too poor to derive meaningful results. The investigation may also discover whether varying the aromatic content of the fuel affects the temperature distributions produced.

The standard 70/30 iso-octane/toluene fuel blend was used for the majority of TC-PLIF and LITGS experiments in the optical engine and compared with the increased (50/50) and decreased (90/10) toluene content fuels.

A 90/10 iso-octane/toluene fuel blend results in weaker signals for TC-PLIF and LITGS. For a stoichiometric mixture, under these engine conditions, in practice this represents a lower limit

for the toluene content of the fuel. Lower toluene fractions could be used if other parameters were varied to compensate, such as increasing the airflow which would require a greater volume of fuel to be injected to reach stoichiometry, permitting the minimum effective number density of toluene at the interaction region to be maintained.

Increasing the fractional content of toluene in the fuel to a 50/50 iso-octane/toluene blend gives stronger signals and corresponding improvements in signal-to-noise ratio of the measurements with TC-PLIF and LITGS. However, increasing the aromatic content would further distance the already simplified fuel from being representative of forecourt gasoline. Also, absorption of the UV pump light before the measurement region will reduce the intensity available for 'useful' absorption at the interaction region, so that increasing the toluene number density indefinitely would not necessarily produce ever-stronger signals.

LITGS and TC-PLIF

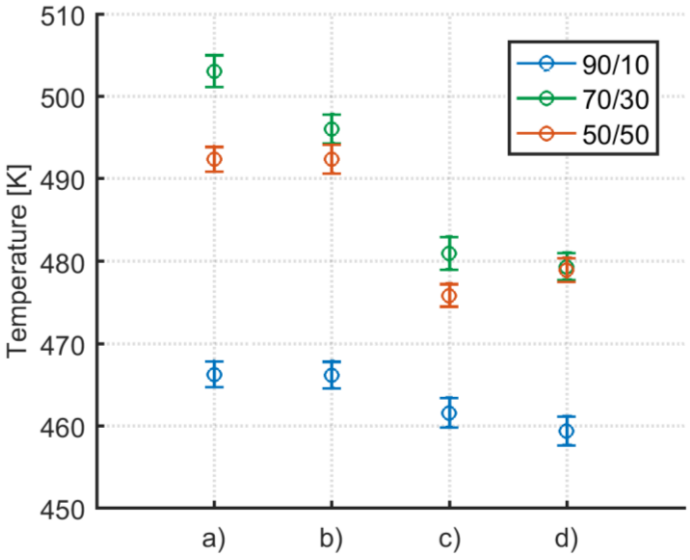

Figure 6-24 Fired LITGS temperatures at 50 CAD BTDC for iso-octane/toluene blends at ratios of 90/10, 70/30 and 50/50. For each fuel blend, datasets a) and b) are taken using PFI while c) and d) are taken using GDI. Errorbars in this figure represent the standard error of the mean of 60 measurements. Absolute temperature scale recovered using the re-calibration technique of section 6.3.3.

At 50 BTDC increasing the toluene content of the fuel from 30 % to 50 % had little effect on the in-cylinder temperatures as measured by LITGS, with both showing charge cooling of

15 – 20 K between PFI (‘a’ and ‘b’) and GDI (‘c’ and ‘d’) operation [Figure 6-24]. The measurements with different fuel blends were performed on sequential days which, given the inherent variability of the optical engine, means the 0 – 10 K reduction in temperatures between the 70/30 and 50/50 datasets should not be attributed to fuel composition.

The reduced toluene (90/10) blend displays reduced charge cooling of only 6 K. While this will in part be due to the 10 % difference in latent heat of vaporisation between iso-octane and toluene, this is not sufficient to account for the reduction in charge cooling by a factor of 3 compared to the 70/30 and 50/50 fuel blends. Additionally, the average LITGS temperatures are 25 K cooler for the 90/10 blend. This suggests that either a difference in engine conditions[121] resulted in a physical temperature difference for the 90/10 datasets, or the fitting routine is not coping with the weak signals produced by the factor of 3 reduction in tracer number density from the standard 70/30 blend.[122] However, further experimental testing would be required to determine the cause of the lower derived temperatures for the 90/10 fuel blend datasets.

TC-PLIF temperature distributions taken simultaneously with the LITGS data of Figure 6-24 are displayed in Figure 6-25, comparing PFI (‘a’, ‘c’, ‘e’) and GDI (‘b’, ’d’, ’f’) operation for iso-octane/toluene fuel blends of 90/10 (‘a’, ‘b’), 70/30 (‘c’, ‘d’) and 50/50 (‘e’, ‘f’).

[121] Whether fuel-specific e.g. a difference in the combustion characteristics of the 90/10 blend, or unintended e.g. increased blow-by past the piston rings reducing the in-cylinder pressures and hence temperatures reached.

[122] The fitting analysis will have a practical lower limit for signal strength, much in the same way as the FFT analysis, and this may be represented by the signals produced by the 90/10 fuel blend.

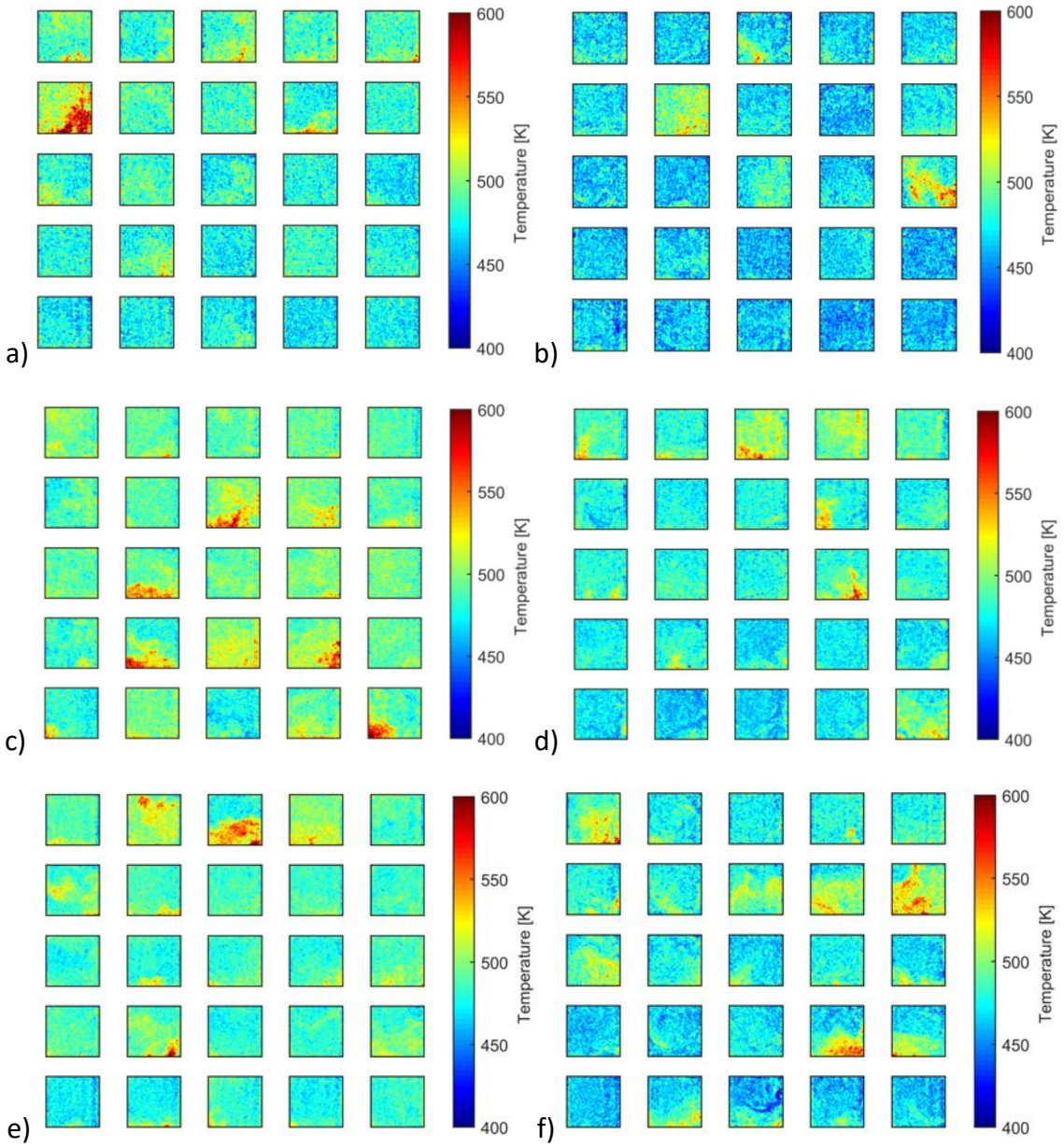

Figure 6-25 Fired TC-PLIF temperature distributions, each covering 9 x 10 mm at 50 CAD BTDC with a 90/10 blend of iso-octane/toluene for a) PFI and b) GDI operation, with a 70/30 blend for c) PFI and d) GDI, and with a 50/50 blend for e) PFI and f) GDI.

On inspection of the corresponding CoV images [Figure 6-26], the spatial distribution of temperature variability within the TC-PLIF images does not show a strong dependence on either fuel injection strategy (PFI or GDI) or toluene content of the fuel (10 %, 30 % or 50 %) for the datasets of Figure 6-25. The lower half of each CoV image [Figure 6-26 a) – f)] displays an increase in CoV of 0.8 % compared to the mean upper half CoV of 3.2 %[123]. This suggests that

[123] Spatially averaged CoV for the upper half of each image, averaged across all 6 datasets.

the hotspots occur with greater frequency within the lower half of the TC-PLIF images, perhaps due to the pattern of fluid motion within the cylinder.

The spatially averaged CoV for the upper half of the 90/10 blend datasets [Figure 6-26 a) and b)] is slightly higher (3.5 %) than the corresponding mean value of the 70/30 and 50/50 datasets (3.1 %). Given that hotspots are less prevalent in this region, this may be a result of the weaker signals and lower signal to noise ratios for the 90/10 blend due to the reduced fractional toluene content of the fuel (10 %).

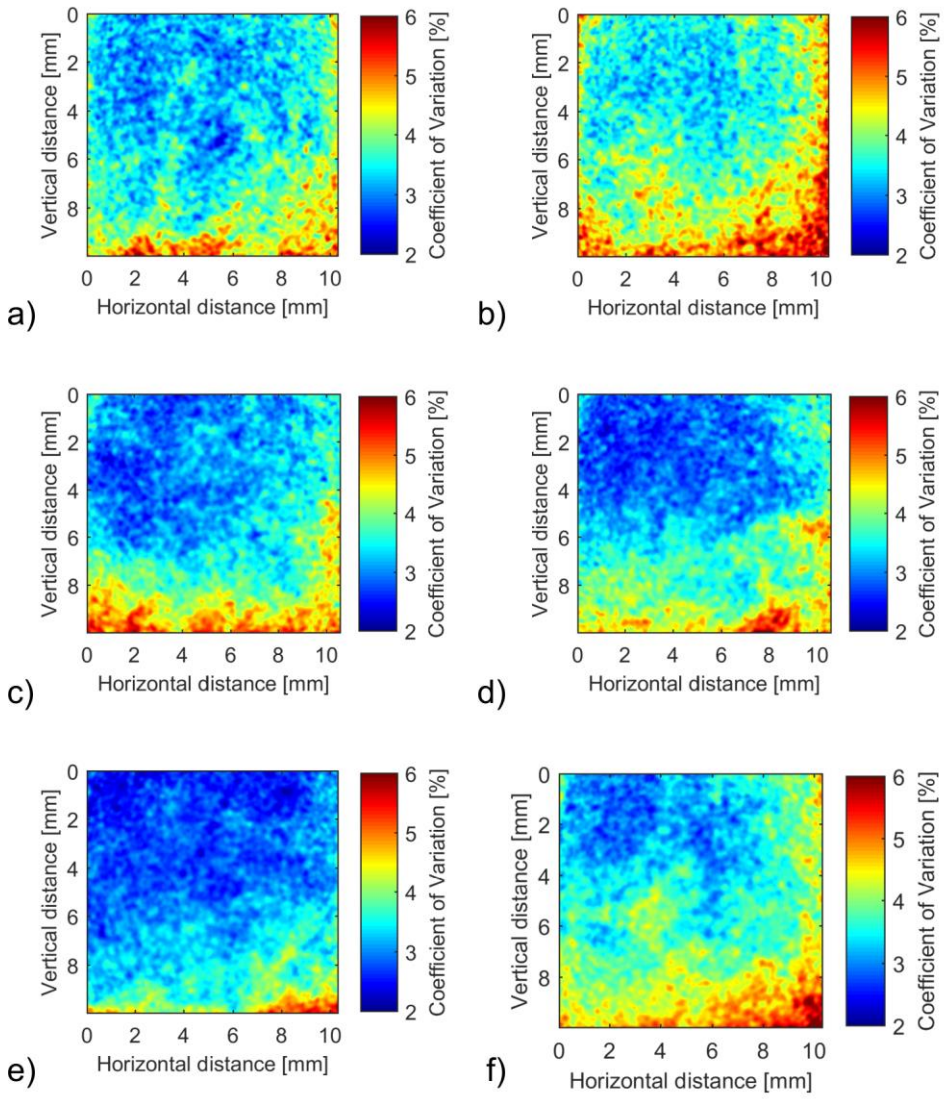

Figure 6-26 Coefficient of variation images of datasets a) to f) displayed in Figure 6-25.

One anomalous dataset using the 50/50 fuel blend for PFI operation displayed a large increase in both the magnitude and frequency of occurrence of hotspots [Figure 6-27 a)]. The spatial distribution of the temperature variability again shows increased CoV values for the lower half of the image [Figure 6-27 b)], however the magnitude of the CoV values is nearly double that of Figure 6-26 (a spatially averaged CoV of 6.6 % compared to 3.6 %). Data from sequential runs under nominally identical conditions [Figure 6-25 e)] and after switching to GDI [Figure 6-25 f)] display hotspot characteristics consistent with the 70/30 and 90/10 fuel blends, hence further investigations would be required to determine the cause of the increased temperature inhomogeneity.

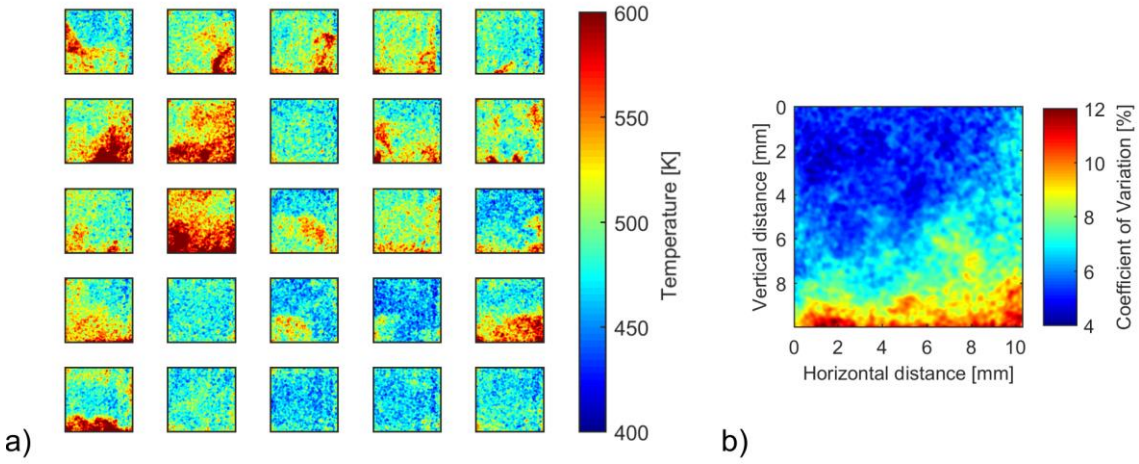

Figure 6-27 a) Anomalous fired PFI TC-PLIF temperature distributions showing increased temperature inhomogeneity, each covering 9 x 10 mm at 50 CAD BTDC with a 50/50 blend of iso-octane/toluene. b) Coefficient of variation image of the dataset displayed in a).

6.3.7. Investigation of TC-PLIF artefacts

TC-PLIF registration artefacts

Two versions of the same 20-image TC-PLIF dataset are presented in Figure 6-28, showing a) the vertical stipe artefacts present on uncorrected TC-PLIF images and b) the corrected images. These stripes are clearly not physical temperature distributions as there is no reason to expect a perfectly vertical, mm-scale banding structure in the temperature distribution of fired or especially motored runs, for every measured cycle. These stripes are most likely to have arisen

from an imperfect alignment and registration of the images from the two ICCD cameras. The optical aberrations present in the TC-PLIF imaging system prevent the MATLAB registration procedure from perfectly overlapping the two images using its available operations of stretching, scaling, rotating and translating, along with a pincushion correction transform.

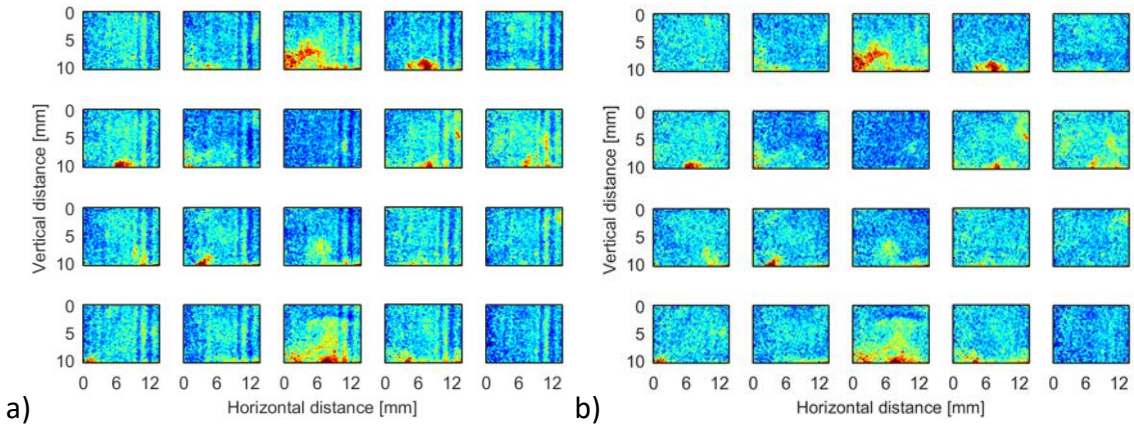

Figure 6-28 a) Vertical stripe artefacts present in TC-PLIF images before correction. b) Corrected images.

This close but imperfect overlap is not a critical issue for slowly varying intensity distributions where the intensities of neighbouring regions of the image are very similar. However, the profile of the pump sheet is very structured. The beam profile of the Surelite is strongly ringed, perhaps due to a defect or damaged spot within the laser head causing a diffraction pattern to modify the otherwise Gaussian intensity distribution [Figure 6-29]. When formed into a sheet using cylindrical lenses, the resulting sheet intensity varies strongly as a function of transverse location across the sheet.

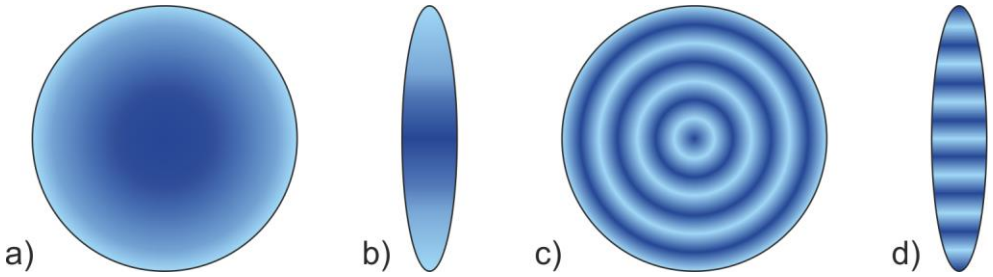

Figure 6-29 Conceptual diagrams of a) a Gaussian beam profile and b) the corresponding sheet intensity profile, compared to c) the Surelite beam profile and d) the sheet intensity profile formed by the Surelite beam.

The raw images from each ICCD therefore have strong vertical stripes of alternating intensity due to the sheet propagation direction being from bottom to top of the image. An imperfect registration of each pair of images results in the division of two slightly mismatched spatial profiles with very strong intensity gradients. This causes vertical stripes to appear in the final 'signal ratio' image wherever the registration error is larger than the spatial scale of the changes in intensity. For the raw 'striped' images in Figure 6-28 a) this error was largest on the right hand side where the stripes are clearly visible. Towards the left hand side of the images the registration is sufficiently accurate to produce no stripes, or at least stripes which are smaller in magnitude than the false colour scale can resolve.

One solution would be to use a smoother beam profile for the pump sheet. The use of a beam homogenizer based on microlens arrays for homogenization of a light sheet generated by a KrF excimer laser has been reported [114]. The un-corrected sheet displayed similar structure to the sheet of this work, with time-stable variations in intensity of up to 50 %. After application of the beam homogenizer, the maximum deviation in intensity from the desired profile was reduced to just 5 %. Insertion of additional optics does however introduce losses and led to a 20 % reduction in intensity of the sheet.

The spatial structure of the pump pulse may also be minimised via propagation within an optical fibre. Use of an optical fibre was not attempted in this work owing to the high risk of damaging the fibre by attempting to focus such an intense pump pulse[124] into the fibre.

In this work, the stripes were removed in post-processing to enable the temperature structures in the data to be seen more clearly. A correction based directly on the laser intensity profile, involving measurement of the laser pulse, is not possible after-the-fact. However, the images can be indirectly corrected for the pump sheet intensity profile if some assumptions about the data are made. The following procedure does introduce some bias to the results but, given its success at removing vertical stripes while preserving the shape of visible temperature structures,

[124] Approximately 20 mJ at 266 nm.

the inaccuracies introduced should not affect the conclusions drawn from these ‘stripe corrected’ results.

Taking each set of shots at a given CAD and engine operating condition, the assumption is made that the average horizontal profile of the set of shots should be flat. All shots in the set are averaged to produce a mean image. This mean image is then averaged column-wise to produce a mean horizontal profile.

Consider a static cell with uniform temperature and fuel distribution. Using perfectly registered cameras, this mean image would be flat/homogenous despite any variations in the transverse intensity profile of the pump sheet, as the pump sheet intensity at any given point in the image would be the same for both cameras. Imperfect registration would result in a slight spatial mismatch in pump intensity for each image, which would translate into a temperature difference in the transverse direction across the pump sheet, giving a structured horizontal profile.

As this mismatch is constant over time, division of each single-shot image by the mean horizontal profile would correct the signal ratio for the slight registration mismatch. This ensures that any vertical structures present in every image of the set are removed. The procedure intentionally has no effect on horizontal structures as these, if present, cannot be attributed to being an artefact of the pump sheet structure.

The main bias introduced to the data by this stripe-correction method is the partial suppression of features that occur frequently and have a strong vertical component. Any ‘stripe’ feature that occurs in the majority of the images, in the same location, across the majority of the height of the image and with similar intensity, contributes strongly to the mean image and hence will be supressed in all of the corrected images. Inspection of the raw images does not identify any obvious vertical structures representing actual temperature variation inside the cylinder. Structures in the data will only be suppressed to the extent that they contribute towards the mean image. Infrequent or variable shape structures, even if intense, will therefore be almost fully preserved.

After application of this correction to the 'striped' data of Figure 6-28 a), the vertical banding has been removed in b) while preserving the structures visible in the uncorrected images.

Fired Hotspots – real or artefacts?

Two main arguments serve to support the interpretation of the TC-PLIF features, referred to above as 'hotspots', as regions of higher temperature and not an artefact.

High on the list of potential suspects for introducing erroneous 'hot' regions into the TC-PLIF data are fluorescing species that could be present in EGR pockets. Any fluorescence from such species in the long-wavelength 'red' spectral window would increase the apparent temperature of the TC-PLIF signal ratio. Toluene, being an aromatic hydrocarbon, can produce Polycyclic Aromatic Hydrocarbons (PAH) within its combustion products. PAH readily absorb the pump light at 266 nm and the fluorescence spectra of several PAH molecules cover the 'red' spectral window of the TC-PLIF system.

The assumption made in interpreting the 'hotspots' as 'hot' is that any PAH or other species are present in negligible quantities in the EGR, if at all, so that any undesirable fluorescence is minimal compared to the intensity of toluene emission. Based on the two arguments detailed below, this is a reasonable assumption.

Correlation of TC-PLIF with LITGS

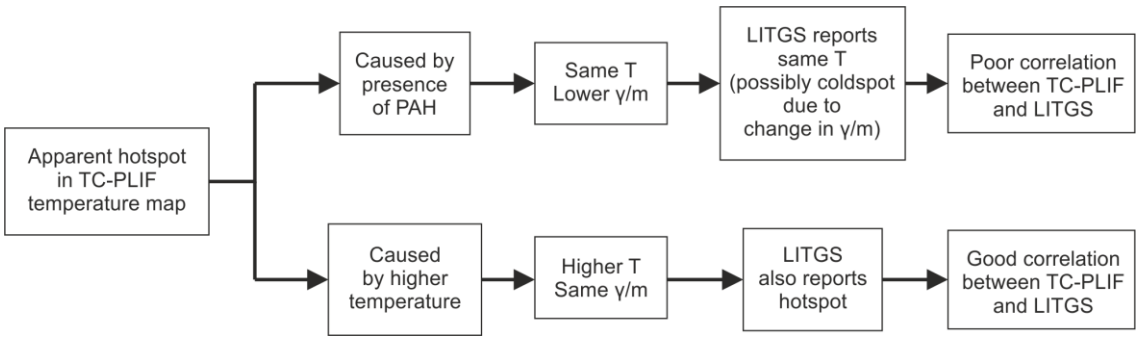

Figure 6-30 Implications of PAH presence versus higher temperatures as proposed causes of the observed 'hotspots' in TC-PLIF temperature maps for fired operation.

The strong correlation between LITGS and local TC-PLIF temperatures supports the fact that the hotspots seen in the TC-PLIF images are actually regions of higher temperature, as opposed to a compositional effect biasing the TC-PLIF measurement [Figure 6-30]. If the hotspot was due to a combustion product (e.g. PAH) rich EGR pocket, this would cause the local mean γ/m to remain the same or reduce. This has the effect of maintaining or reducing the local sound speed and hence the frequency of the LITGS oscillations. As the composition is assumed to be constant in this LITGS analysis, this would be interpreted as the same or a lower LITGS temperature.

Independence of toluene number density

If the hotspots were an artefact associated with fluorescing combustion products of toluene[125], it would be expected that an increase in toluene number density would lead to an increase in fluorescing products and therefore hotspots of greater magnitude or frequency of occurrence. Neither have a strong dependence on the toluene content of the fuel as determined by the investigation in section 6.3.6. This provides support to the conclusion that the hotspots are indeed higher in temperature than the surrounding gas.

GDI fuel distribution TC-PLIF artefacts

Structures similar to 'swirls' of gas, cooler than the surrounding bulk gas, are visible at 60 CAD BTDC and earlier in the compression stroke for GDI but not PFI. These could be artefacts owing to extreme variation in local fuel number density biasing the TC-PLIF images, despite the inherent resilience to such effects.

Figure 6-31 displays an example. It has a characteristic 'hot and cold' nature of the oval region and suggests interpretation as a region with large variation in local fuel number density. If the registration of the ICCD images was less than perfect, this would normally result in very little change in signal ratio for a slowly varying intensity distribution. However, for a strongly

[125] As opposed to a 'real' temperature difference affecting toluene's emission spectrum as intended.

varying intensity distribution, this misalignment would become more apparent. One side of the artefact would show a higher than ideal intensity in the 'red' channel and be assigned a 'hotter' temperature. The opposite side would show a reduced intensity in the 'red' channel and be assigned a correspondingly 'cooler' temperature.

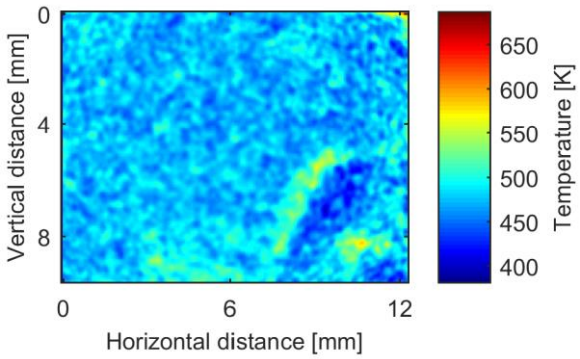

Figure 6-31 GDI 'artefact' in the TC-PLIF temperature distribution for motored operation at 60 CAD BTDC.

This is in contrast to other structures which show temperatures which are e.g. solely 'hotter' than their neighbouring regions [Figure 6-32] and hence do not display the zero-sum style characteristic of fuel number density variation combined with imperfect ICCD alignment.

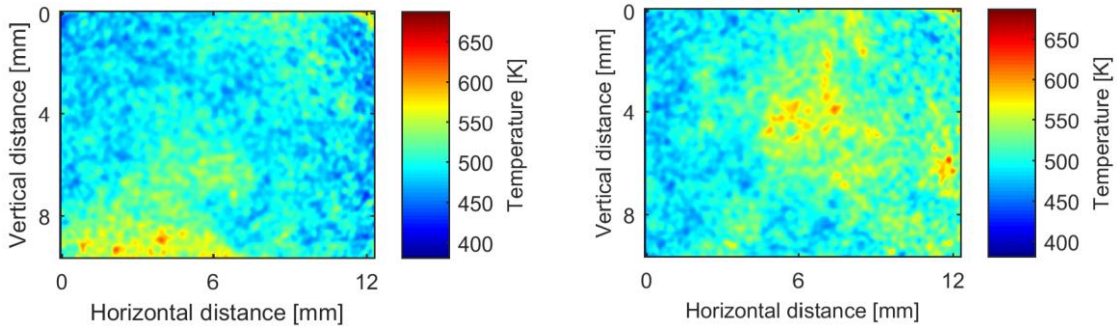

Figure 6-32 GDI 'hotspots' in TC-PLIF temperature distributions for fired operation at 60 CAD BTDC.

An alternative explanation is that colder gases are being drawn out of the crevices during the intake stroke and are mixing during the following compression stroke. As the air-fuel mixture is compressed, some of the gas mixture is forced into the crevices present inside an optical engine barrel[126]. These gases will not undergo combustion and during the next intake stroke may return

[126] Such as beside the piston walls before the 'lowered' piston rings form a seal against the barrel walls.

to the barrel to mix with the fresh charge and any EGR present. This effect could be amplified in GDI operation due to the increased chance of fuel in a liquid state becoming trapped in crevices. Any subsequent evaporation would produce a pocket of cooler gas, providing a source of the 'cooler than bulk gas' region observed in Figure 6-31.

As the TC-PLIF measurement region is centrally located within the cylinder, far from the walls and crevices[127], a strong spatial variation in fuel number density combined with imperfect registration is a more plausible explanation of these artefacts than pockets of cold gas.

6.4. Summary and conclusions

LITGS has been demonstrated to provide in-situ calibration of TC-PLIF temperature maps for in-cylinder temperatures of a firing spark-ignition IC engine.

Adjustment of the PMT gain was found to bias temperatures derived from LITGS. This restricted the analysis of this chapter to using a) LITGS datasets with the same PMT gain or b) LITGS datasets with different PMT gains where TC-PLIF could be used to determine the gain-induced shift. The temperatures recovered from affected datasets still provided the capability to investigate temperature distributions for a variety of engine conditions.

The cause of this bias, variation of the PMT's time-response, has been identified and mitigated for future experiments. An alternative method for avoiding detector saturation involving fixed PMT gain and optical attenuation proved successful at deriving consistent temperatures between different initial optical signal intensities. This method should therefore be applied to future LITGS measurement campaigns.

For motored operation, the TC-PLIF results display homogeneous temperature distributions for both PFI and GDI operation. Correlation of motored LITGS and TC-PLIF temperatures demonstrate that both techniques are independently measuring temperature and can resolve the

[127] The width of the TC-PLIF measurement region is only 1/9 of the cylinder diameter.

changes in temperature of order 10 K due to compression heating between increments of 10 CAD.

LITGS measurements for motored operation show a constant variability of 1 % throughout the compression stroke, instead of reducing with increasing pressure as would be the case if the precision of LITGS was the limiting factor. The cyclic variability of the engine is therefore contributing to the cycle-to-cycle fluctuations in temperature reported by LITGS.

TC-PLIF and LITGS temperatures display excellent shot-by-shot correlation for fired operation, but only if considering TC-PLIF data averaged over the LITGS region, not elsewhere in the image. This confirms the TC-PLIF temperature maps are resolving local temperature variations not just bulk temperature changes and that both TC-PLIF and LITGS can resolve the cyclic variability of this engine for fired operation.

A charge cooling effect of order 5 K between PFI and GDI operation was resolved for both LITGS and TC-PLIF throughout the motored compression stroke between 90 and 50 CAD BTDC. For fired operation, TC-PLIF no longer resolves the temperature difference at 50 BTDC without calibration using LITGS although with its higher precision, LITGS resolved differences in the range of 6 – 20 K between PFI and GDI for the three fuel blends[128]. This extends the previous achievement of measuring charge cooling with LITGS [4] from a point-measurement to 2-dimensions in combination with TC-PLIF.

LITGS measurements during fired operation showed a temperature increase of 9 K min^{-1} as the engine warmed up due to the additional heat generated by combustion.

Strong temperature inhomogeneities were observed for fired operation. These mm-scale ‘hotspots’ were typically approximately 50 K (10 %) hotter than the surrounding bulk gas at 50 CAD BTDC. The frequency of hotspot occurrence increased for later CAD, being most prevalent at the latest CAD timing investigated at 50 CAD BTDC, and could not be attributed to

[128] Iso-octane and toluene in ratios of 90/10, 70/30 and 50/50 by volume.

injection strategy[129] or toluene number density after tests with three fuel blends[128]. The magnitude of the temperature difference between hotspots and the surrounding bulk gas was larger for later CAD, even taking into consideration the compression heating of the in-cylinder gases. Increased variability of in-cylinder temperatures was observed for the lower half of TC-PLIF images at 50 CAD BTDC, compared to the upper half, independent of injection strategy or toluene number density. This suggests the increased frequency of hotspot occurrence within the lower half of the TC-PLIF images could be a result of the pattern of fluid motion within the cylinder.

Unphysical artefacts in the TC-PLIF data were observed, manifesting as vertical stripes in the temperature maps. It was determined that these originated from a combination of the highly structured pump laser sheet and an imperfect registration between the two cameras. A post-processing routine was constructed to remove the artefacts while preserving the underlying structures in the images.

Consideration was given to the possibility that fluorescing compounds in the EGR, most likely PAH, could bias the TC-PLIF temperature maps and be responsible for the apparent hotspots occurring for fired operation. The good correlation between TC-PLIF and LITGS data, combined with the lack of positive correlation between toluene number density[130] and hotspot occurrence suggests that the hotspots discussed in this chapter are indeed regions of higher temperature.

For GDI operation and at earlier CAD timings (90 – 60 CAD BTDC), occasional artefacts were observed in the motored TC-PLIF temperature maps. The zero-sum nature of the artefacts suggests that an imperfect registration between the two cameras, combined with the spatial variations in fuel number density of GDI and lower signal-to-noise ratios of earlier CAD timings are responsible for generating these types of artefacts.

[129] PFI or GDI.

[130] Toluene combustion generates higher concentrations of PAH than iso-octane.

7. 1D LITGS

In this chapter, the extension of LITGS from 'point' to 1-dimensional measurements will be considered. A review of previous work is presented in section 7.2 which focusses solely on the developments in the field of LIGS towards multi-dimensional measurements. Section 7.3 describes the equipment and experimental methods. Investigations into detector performance, compositional effects and 1D thermometry are reported in section 7.4 and summarised in 7.5.

7.1. Introduction

The temperature profile of gaseous flows is a critical parameter in a wide range of fields. Thermal boundary layers and heat transfer between gases and surfaces in IC engines, gas turbines and aircraft components comprise active areas of research. The high precision and accuracy of LITGS, applied to single-shot measurements along a line provides an exciting new diagnostic technique for application to fluid dynamics, combustion and materials research.

The suitability of LITGS for extension to 1-dimensional measurements is discussed in section 7.2 and the recent progress of the field is evaluated. Two detection methods, streak cameras[131] and fibre-coupled photodiode arrays, are presented in section 7.3, along with the seeded flow and temperature control apparatus providing the thermal gradients for validation of the 1D-LITGS technique. Section 7.4 begins with a discussion of the capabilities of the streak camera used in this work. The effect of compositional variation in the flow on the derived temperatures along the line and the invasiveness of the LITGS technique are evaluated and the correction methods applied to the results of this chapter are presented. Quantitative single-shot 1D-LITGS temperature measurements are reported for dual-temperature flows, flows across a heated plate and heated flows across a cooled plate. Finally, the results of this chapter are summarised in section 7.5.

[131] The streak camera system follows on from the work of previous members of this research group, Robert Stevens [2] and Xiaowei Guan.

7.2. Previous work

Aside from the practical complications of extending the LITGS technique for measurements along a line, or even across a plane, the inherent advantages and disadvantages of point-LITGS remain valid. The discussion below will therefore focus on the applicability of LITGS to multi-dimensional measurements and thermometry of flows. For a more general discussion on the relative merits of LITGS and alternative techniques, the reader is referred to the literature review of chapter 3.

LITGS has been applied for thermometry of flows in many environments. The majority of these instances have been point-measurements, where pencil pump and probe beams of diameter ≤ 1 mm are crossed at the measurement region to define a small volume in space. There is however no fundamental restriction of LITGS to point measurements. Hemmerling et al. have demonstrated 2D measurements with LIEGS [228] in which the intensity of the LIEGS signal was recorded by a CCD camera. Given the lack of time resolution of the detector employed, the work focused on the potential of the technique for concentration measurements and particle distribution in sooting flames.

LITGS thermometry requires temporal resolution of the signal with a fast (~ 1 ns response time) detector. Initial progress has been made in extending the interaction region in one dimension to perform measurements of temperature along a line [229]. Cylindrical lenses were used to form the beams into sheets, whose linear, as opposed to point-like, intersection forms the grating. Bragg-scattering a probe sheet off the extended grating provided a spatially as well as temporally varying signal which was imaged onto a streak camera. Thermometry precisions of 0.3 %, with a spatial resolution of 150 μm along a 5 mm line of 1 mm thickness were achieved [229].

While the first 1D-LITGS measurements reported in [229] demonstrate the principles of 1D-LITGS with excellent precision of temperature derivation, the technique was limited to time-

averaged measurements by the short 120 ns timebase of the streak camera[132]. LITGS signals at 1 bar or above are typically 150 – 400 ns in length, such that multiple images were stitched together to recreate the signal [229]. Pressure is derived from the underlying decay of a LITGS signal over time, hence the precision of pressure measurement was also limited to 20 % by the accuracy of the stitching routine. This lack of temporal resolution is a major drawback for non-dynamically stable applications such as internal combustion engines for which single-shot measurements reveal far more information than the time-averaged distribution. The feasibility of the proposed solution of the use of a streak camera with a longer timebase [229] is discussed in section 7.4.1.

Measurements in [229] were performed in a static test cell filled with a mixture of NO_2 and N_2 at 4.8 bar. This confirmed the capability of LITGS to correctly report a 'flat' temperature profile for a homogeneous temperature environment, however no temperature gradients were investigated. It is very challenging to set up a stable temperature gradient in a static cell, therefore an alternative approach is explored in section 7.3.5.

The work presented in the remainder of this chapter builds on initial streak camera tests [230] with the aim of overcoming the lack of temporal resolution in the work of [229]. The streak camera used[133] was capable of an adjustable sweep time up to 560 ns. It was therefore possible to record entire LITGS signals within a single camera frame. Single-shot LITGS signals were recorded in adjacent, parallel hot and cold nitrogen flows seeded with toluene. These displayed only qualitative changes in oscillation frequency at the boundary of the two flows [Figure 7-1] and as will be discussed in section 7.4.1 this streak camera has insufficient time-resolution for accurate 1D-LITGS thermometry.

[132] Hadland Photonics, Imacon 500

[133] Hamamatsu Synchroscan C3681

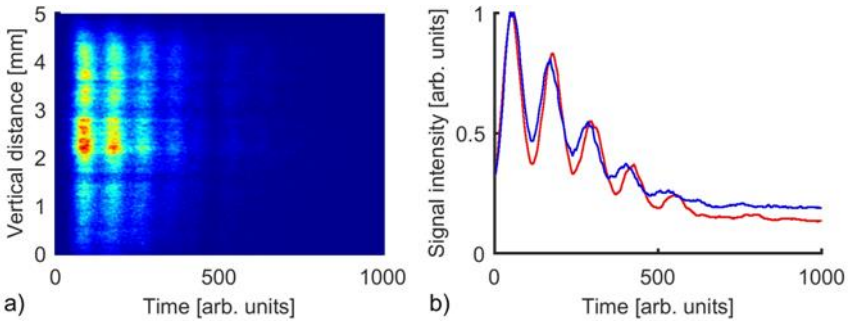

Figure 7-1 Qualitative 1D-LITGS temperature measurements from [230]**. a) Streak camera image. b) example LITGS signals taken from rows of pixels in a) showing a qualitative difference in oscillation frequency.**

As described above, a critical factor to consider for accurate time-resolved detection of LITGS signals is the requirement for a both a long recording duration and a high temporal resolution. To accurately record LITGS signals with pressures up to a few bar typically requires a 500 ns timebase and a temporal resolution of 1 ns or less[134], a ratio of 1 : 500. This 'timescale ratio' is defined as (temporal resolution)/(timebase) and is used in this chapter as a figure of merit for comparison of detection systems.

Electrostrictive gratings have been applied to single-shot imaging of a helium flow in air and soot concentrations in a sooting flame [228] using the DFWM geometry of [176] and integrating the signals over time onto a CCD camera. However, the extreme requirement of a 1 : 500 timescale ratio prevents the use of CCD cameras for 2-dimensional LITGS thermometry.

7.3. Method

In this section the experimental details of the optical layout, seeded flow system, gas heater and temperature controlled plates are presented and the two detection methods are introduced. Firstly a streak camera system, which follows on from the work of previous members of this research group, Stevens [7] and Guan [230], and secondly a fibre-coupled photodiode array.

[134] Estimated based on the accurate reproduction of LITGS signals using DET10A/M photodiodes with a response time of 1 ns.

7.3.1. Beam geometry

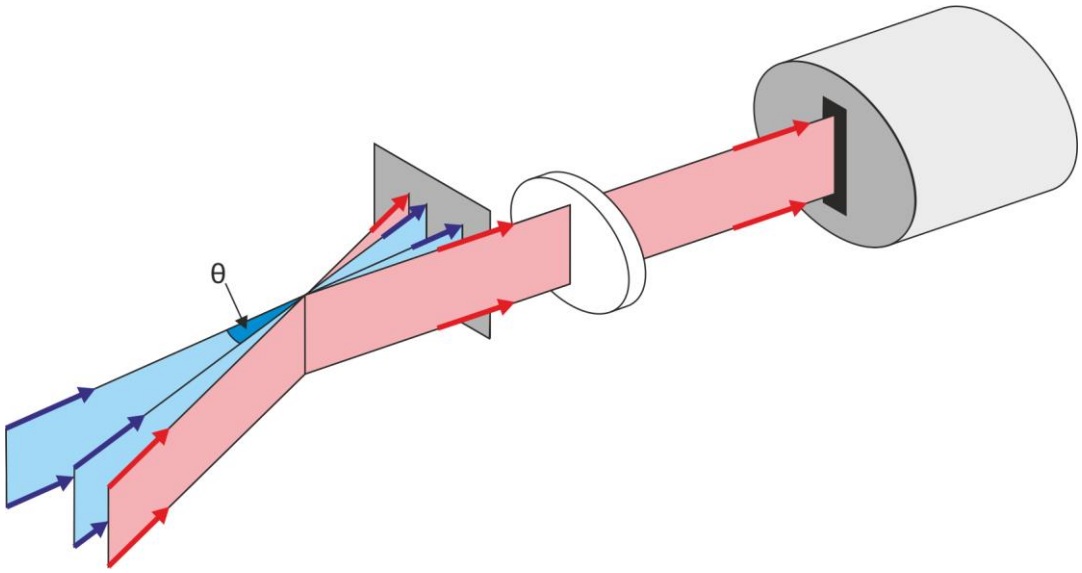

Figure 7-2 1D-LITGS planar beam geometry with crossing angle 'θ', imaging lens and detector with 1D spatial resolution.

The typical beam geometry used in point-LITGS experiments is forward folded BOXCARS as it results in a greater physical separation of the beams after the interaction region, facilitating signal collection and dumping of the pump and probe beams. A major application for 1D-LITGS is the investigation of temperature in flows close to surfaces. As such, an alternative planar geometry, used in this work, minimises the distance between the measurement region and the surface in question without the beams impinging on the surface [Figure 7-2].

7.3.2. Optical Layout

The optical layout for the generation and detection of the 1D-LITGS signal followed the same principles as those discussed in chapter 4 for the point-LITGS experiments [Figure 7-3].

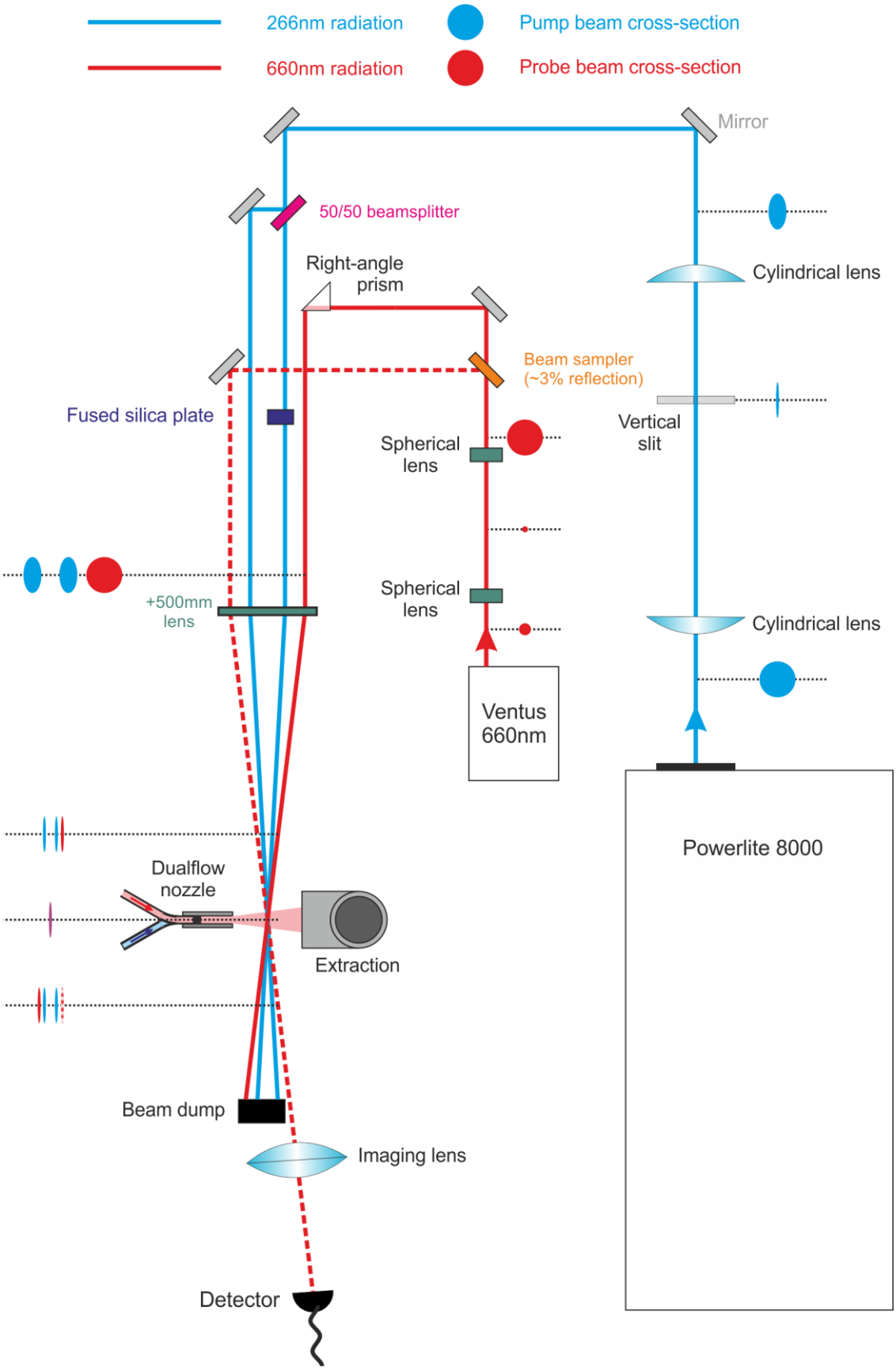

Figure 7-3 Optical layout for the 1D-LITGS experiments detailing pump (266 nm) and probe (660 nm) beam paths. Beam cross-sections are shown for key stages of sheet formation. Not to scale.

A + 500 mm cylindrical lens was used to both cross the three input beams at the interaction region and to produce vertical sheets from the circular cross-sections of the UV pump beams and the red probe beam. A telescope consisting of two spherical convex lenses was added to the probe beam path before the crossing lens, enabling the probe beam diameter to be matched to the 6 mm UV beam height at the crossing lens. A 2 : 1 telescope comprised of quartz cylindrical lenses[135] was employed before the crossing lens to reduce the UV beam width by half. By the principle that all optics conserve or increase the étendue[136] of a beam, reducing the beam size increases its divergence. This had the effect of increasing the thickness of the beam waist produced by the crossing lens at the interaction region to the desired 1 mm.

The UV output of the Powerlite displays a strong 'ringed' structure of the intensity of the beam profile, along with minor inhomogeneity in the underlying intensity distribution. The excess energy available permitted the use of a metal slit placed near the focus of the cylindrical lens telescope to select the most homogenous section of the beam for formation into pump sheets.

The interaction region is defined as the 1 mm x 6 mm vertical line formed by the intersection of the three sheets. The central 1 mm x 4 mm of this line is imaged using a spherical lens system with 1 : 1 magnification, forming an inverted real image of the interaction region and defining the 'image plane'. The detectors are subsequently aligned within this plane to record the LITGS signal at each point along the interaction region.

7.3.3. Laser selection

A flashlamp pumped solid state Nd:YAG laser (Continuum Powerlite 8000) was used to provide the pump beams for this work. The smaller Minilite system used for the point-LITGS measurements in chapters 4 and 6 generated reliable LITGS signals with a pulse energy of 4 mJ at 266 nm over a beam size of approximately 1 mm. The Powerlite is more than capable of

[135] With focal lengths of +500 mm and +250 mm.

[136] Qualitatively, the étendue of a beam is the product of the beam's size and divergence.

providing enough energy per pulse to extend the height of the LITGS measurement region by the desired factor of 4 and still generate a density grating of sufficient magnitude.

The 300 mW CW probe[137] of chapters 4 and 6 is close to the lowest power probe laser required to generate a LITGS signal of sufficient intensity in the optical engine setup. The signal required the high gain of a PMT for reliable detection, as opposed to comparatively cheap photodiodes. Also, the height of the interaction region and hence the required probe cross-section is extended for 1D-LITGS. These factors combine to increase the minimum probe power required. A 750 mW CW probe laser[138] was used in the work of this chapter. In addition to providing more power, the higher beam quality and lower divergence makes initial alignment and sheet formation more straightforward.

If probe power at the LITGS measurement volume were the sole aim, it would be best to use a pulsed probe as in [185] and [229]. Long-pulse lasers such as dye lasers can provide extremely high powers of order 100 kW over the duration of the LITGS grating[139] and therefore much larger detected signals. The disadvantage of pulsed probes is the need to measure the probe pulse in order to normalise the recorded signal for the intensity variation of the probe pulse. This complicates the analysis of the signal, but more significantly requires an additional detector and associated oscilloscope channel. In comparison, the signal generated by a CW laser is a direct representation of LITGS grating visibility. Dye lasers are also bulky, time-consuming to operate and require more maintenance.

[137] CNI-MLL-III DPSS producing 300 mW of CW output at 671 nm.

[138] Laser Quantum Ventus 660 DPSS producing 750 mW of CW output at 660 nm.

[139] A LITGS grating typically lasts between 0.1 – 1 µs. The dye laser of [2] provides 200 mJ in 2 µs = 100 kW.

7.3.4. Detector selection

Streak camera

Streak cameras offer the ability to measure time-dependent signals along a line with very high spatial and temporal resolution. The operating principles of a streak camera are clearly explained in Hamamatsu's guide [231]. In summary, a photocathode [Figure 7-4 c)] converts the incident optical signal into electrons which are accelerated (d) through the camera and a transverse voltage is applied whose magnitude varies with a high-speed 'sweep' (e). The electrons are deflected to an angle dependent on the time they pass the sweep electrodes. The time-dependence of the initial signal is therefore encoded as transverse displacement of the electrons. The electrons are multiplied by a Micro-channel plate (f) before hitting a phosphor screen (g) which in this work was imaged onto an EMCCD camera[140].

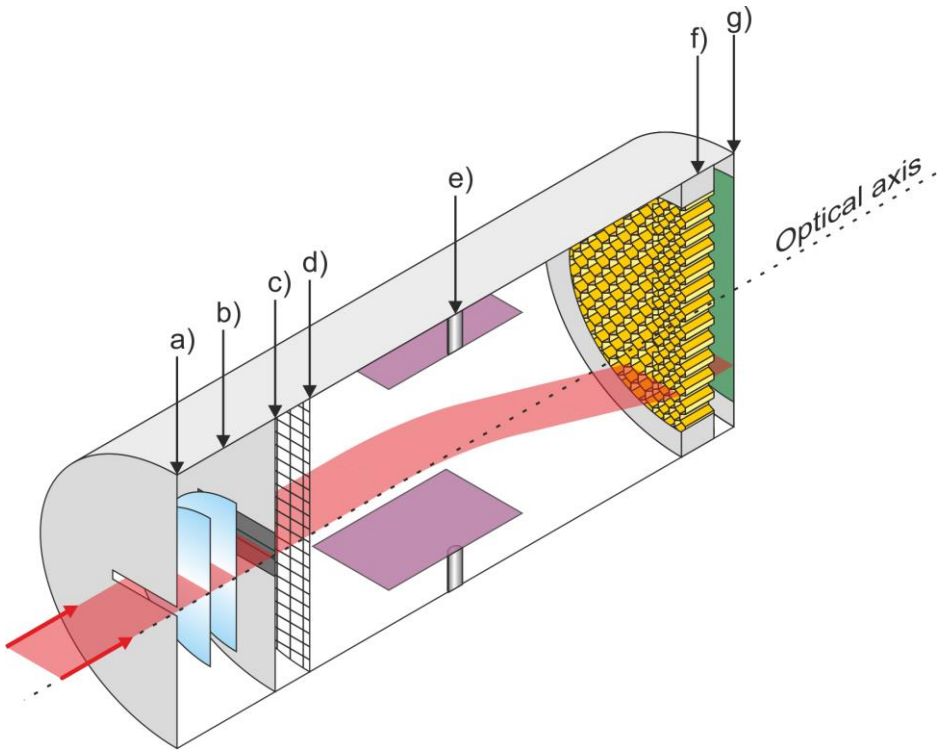

Figure 7-4 Cut-away diagram of streak camera. a) Entrance slit, b) Imaging lenses, c) Photocathode, d) Accelerating voltage grid, e) Sweep voltage, f) Micro-channel plate, g) Phosphor screen.

[140] Andor Luca-R Electron-Multiplying CCD camera

Due to the rapid rate of voltage sweep available and the high spatial resolution of the electron-imaging optics, streak camera systems can provide extremely high (picosecond) temporal resolution for 1-D signals. The spatial resolution of a streak camera will be defined by the imaging optics for both the electron and optical stages and typically provides several hundred measurements along a line.

The telecentric telescope of [229] was formed using two positive spherical lenses for 1 : 1 imaging of the interaction region onto the entrance slit of the streak camera, replacing the imaging lens of Figure 7-3. The sweep time was chosen to produce a timebase of 200 ns to allow a whole LITGS signal at atmospheric pressure to be recorded in a single sweep.

Fibre-coupled photodiode array

Streak cameras are however very bulky and expensive, costing of the order of £100,000. For the purposes of developing a practical 1D optical diagnostic technique with application to many different environments, there is merit in considering a compact and significantly cheaper detection system. Such a system would have the potential for modification into a portable version, which for some applications would be beneficial despite any reduction in spatial or temporal resolution. The fibre-coupled photodiode array detection system (FPDA) discussed in this section is one such possibility.

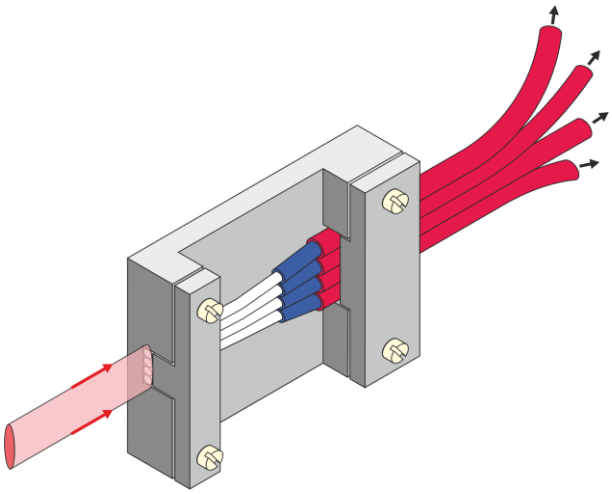

Figure 7-5 Fibre-coupled PhotoDiode Array (FPDA) showing incident signal imaged onto four bare fibre tips. Protective outer jacket (red) and inner sheath (blue) stripped back to expose bare fibres (white) to maximise signal collection (fibre core) fill factor.

By imaging the LITGS signal line onto a linear array of optical fibres, the signal can be transmitted onto a set of independent photodiode detectors [Figure 7-5]. Output signals from the detectors can then be recorded[141], and analysed using the same methods as point-LITGS. This method samples discrete points on the line. Each fibre spatially averages the signals from the section of the line falling within the fibre's aperture. This dramatically reduces the number of sampled points along the line from several hundred with the streak camera to the number of photodiodes.

In exchange, FPDA provides a very robust, compact detection system, which can be installed close to the interaction region e.g. within a test chamber or amongst other diagnostic equipment. The nature of optical fibre transmission means the detectors and oscilloscope can be many metres away, with little degradation of signal quality or need for further imaging optics. Fast photodiodes suitable for the accurate detection of a typical LITGS signal are readily available and affordable[142].

The oscilloscope used for this developmental work was a Teledyne LeCroy Waverunner 625Zi (120 ps rise-time, 2.5 GHz bandwidth, 20 GS/s sample rate). The specifications of this oscilloscope are well above the minimum requirements to accurately record a LITGS signal (1.4 ns rise-time, 250 MHz bandwidth, 1 GS/s sample rate)[143]. The number of available data acquisition channels, 4, determined the maximum number of measurement points along the interaction line achievable in this work. The 4 high-speed reverse-biased photodiodes[144] used in this work have a rise-time of 1 ns and an active area of 1 mm diameter which matches the size of the fibre cores.

[141] E.g. using a multi-channel oscilloscope.

[142] The detectors used in this work (Thorlabs DET10A/M) have a rise-time of 1 ns and cost of order £100.

[143] Based on the Picoscope 6402C being at the limit of faithfully recording a LITGS signal from the optical engine, combined with the rule-of-thumb calculation that 'Bandwidth(GHz) = 0.35/Risetime(10 % – 90 %, ns)'.

[144] Thorlabs DET10A/M, Rise time = 1 ns, Active area = 0.8 mm^2 (Ø 1 mm), Wavelength range = 200 nm – 1100 nm, Dark current = 0.3 nA, Noise-Equivalent Power = 1.2 x 10^{-13} $WHz^{-1/2}$, Junction capacitance = 6 pF, Bias voltage = 10 V.

A single spherical lens was used for 1 : 1 imaging of the interaction region onto the fibre-coupled photodiode array in the 2f – 2f imaging geometry [Figure 7-3]. The 4 optical fibres were stripped of their protective sheaths and held in a custom mount which was designed to securely hold the bare fibre ends in contact in a linear array to minimise the loss of signal between fibre cores. The fibres[145] were chosen to maximise the signal collection over the 4 mm of the imaged interaction region, hence core sizes of 1 mm. The numerical aperture of the fibres, 0.39, was chosen to maximise the collection of incident light from the LITGS signal. Had the numerical aperture been too small, wide-angle light would not undergo total internal reflection within the fibre and would fail to propagate to the detector.

7.3.5. Flow system

The formation of stable temperature gradients played a key role throughout the developmental work of this chapter. Two flow geometries were used to produce dynamically stable temperature distributions in nominally laminar nitrogen flows seeded with toluene vapour. Firstly, a thermal boundary between adjacent, parallel flows was formed by the 'Dualflow' system of chapter 5. Secondly, heat transfer between a flow adjacent to a heated or cooled surface was observed using the 'Hotplate' or 'Coldplate' setup.

Composition

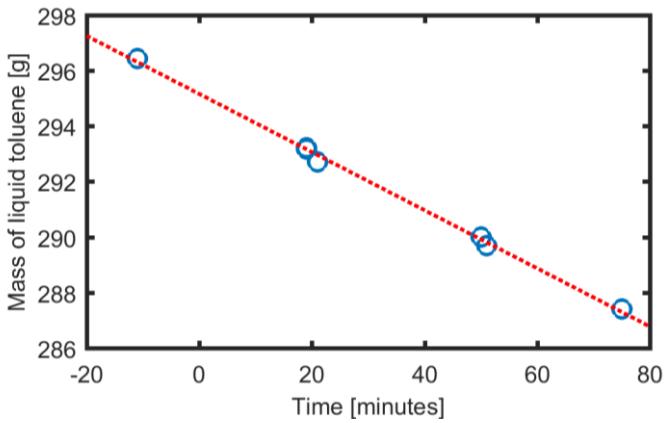

Figure 7-6 Mass loss rate of toluene in seeding jar with linear fitted trendline.

[145] Thorlabs FT1000UMT High OH multimode fibre, NA 0.39

In all cases, the nitrogen flow was metered to a steady 1.2 $Lmin^{-1}$ before being passed over liquid toluene in a seeding jar. The resulting mixture of toluene vapour and nitrogen was passed on to the experiment. The flow exits a nozzle of diameter 4 mm with an estimated flow velocity of 0.6 ms^{-1} and a Reynolds number of 140, corresponding to approximately laminar flow at the exit.

Confirmation of the seeding concentration was obtained by using a mass balance to record the rate of mass loss from the seeding jar. The calculated concentration of toluene molecules by number at the exit of the nozzle of 2.27 % is found to be very consistent over the timescale of typical experiments [Figure 7-6]. Compared to the saturated vapour pressure at lab temperature of 2.7 %, this represents an 84 % seeding efficiency by passing the N_2 flow over liquid toluene.

'Dualflow' apparatus

The Dualflow apparatus has already been described in chapter 5. The nozzle was positioned such that the boundary between the upper heated (292 – 357 K) and lower unheated flow was aligned with the centre of the LITGS measurement line. The nozzle was also mounted on a horizontal translation stage to allow the LITGS measurement to interrogate vertical sections of the flow at distances of 3 – 5 mm from the nozzle aperture. The 3 mm minimum separation of nozzle aperture and LITGS region was set by the requirement to avoid the angled LITGS beams clipping the edges of the nozzle body.

'Hotplate' and 'Coldplate' apparatus

For the 'Hotplate' measurements, near-surface thermal boundary layers were generated using a resistively heated flat aluminium plate[146] [Figure 7-7 a)]. A nozzle with an aperture of 8 mm directed a laminar, room-temperature, toluene-seeded nitrogen flow across the horizontal metal surface of the plate. The plate was positioned such that LITGS measurements were performed along a line normal to the plate surface. The current supplied to the resistive heaters was varied

[146] Plate diameter of 87 mm, thickness of 18 mm.

to produce upper surface temperatures between 293 – 381 K, as measured by a type K thermocouple in contact with the plate surface.

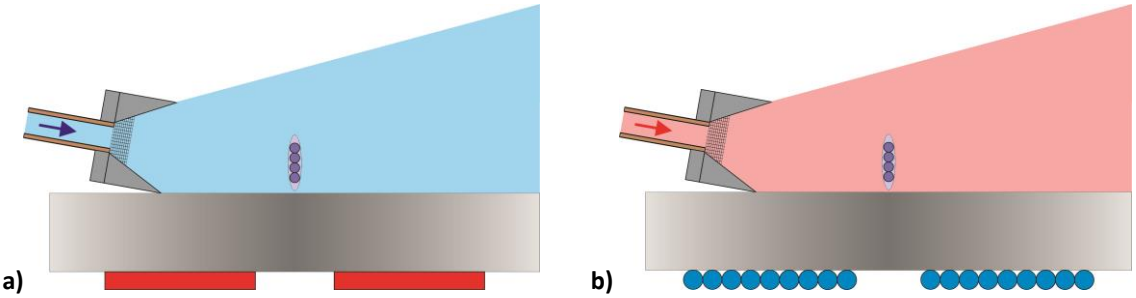

Figure 7-7 a) 'Hotplate' and b) 'Coldplate' apparatus.

For the 'Coldplate' measurements, the resistively heated plate was exchanged for a water-cooled plate of the same dimensions [Figure 7-7 b)], with mains water at 278 K passing through a copper coil fixed to the underside of the aluminium plate. The toluene-seeded flow was heated upstream of the nozzle by insertion of an in-line gas heater which provided control of the initial flow temperature in the range 290 – 350 K.

7.3.6. Data analysis methods

The streak camera output is recorded as a 2D image on an EMCCD camera imaging the phosphor screen. After applying noise filtering to smooth the high spatial frequency noise in the image, each row of pixels in the image is treated as a point-LITGS signal as it represents the variation in time of the intensity from a single location along the measurement line. The analysis may then proceed as for the point-LITGS signals in chapter 4, the only difference being that each pump laser pulse generates several hundred 'signals'.

Each photodiode detector provides a signal indistinguishable from a point-LITGS signal on an independent oscilloscope channel. Analysis for the fibre-coupled photodiode array 1D-LITGS system therefore proceeds as for the point-LITGS technique discussed in chapter 4.

7.4. Results, analysis and discussion

This section begins with an investigation into the capabilities of the streak camera for application to 1D-LITGS thermometry. Compositional variations in the flow and beam heating both have the potential to bias the temperatures derived from LITGS signals. The magnitude of these biases are investigated and the correction scheme applied to results in the remainder of this section is presented. Quantitative single-shot 1D-LITGS temperature measurements are reported across a hot-cold flow boundary ('Dualflow'), and in boundary layers near surfaces ('Hotplate' and 'Coldplate').

7.4.1. Streak camera

Experimental data

In contrast to the previous work with 1D-LITGS in [229], reconstruction of the LITGS signal from multiple images was not necessary due to the sweep time of up to 560 ns being longer than the lifetime of the LITGS signal. The oscillations of the LITGS signal can be seen in the raw data [Figure 7-8]. The strong horizontal banding observed is due to the highly structured transverse intensity profile of the pump sheets[147].

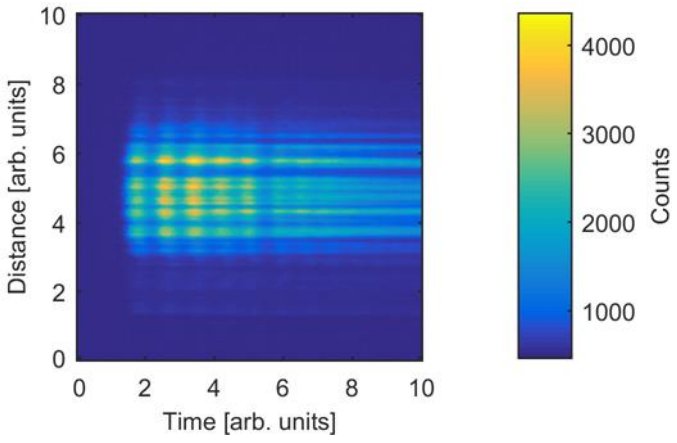

Figure 7-8 Example streak camera image of 1D LITGS signal.

[147] An unexpectedly dark vertical band is also observed, approximately in the centre of the horizontal axis of the image. This corresponds to the reduced sensitivity of pixels in this region caused by previous damage from a high intensity input without the sweep voltage being applied.

Noise filtering

There are many potential noise-filtering routines which could be applied to the streak camera images in an attempt to improve the signal-to-noise ratio. Of these, three were considered:

1) A nonlinear-diffusion filter to reduce noise while maintaining steep gradients.
2) A Gaussian filter to reduce noise with partial maintenance of steep gradients.
3) Pixels binned into AxB super-pixels to match the spatial resolution limit of the streak camera system.

Of the choices, a Gaussian filter was selected for initial noise reduction due to the compromise it offers between options 1 and 3. Nonlinear diffusion filtering performs very well but is computationally expensive and hence time-consuming to run on large datasets. Pixel binning generates step-like changes in the filtered signal intensity, with small flat plateaus separated by discrete jumps. Gaussian filtering provides a much smoother output and avoids the generation of sharp edges which could potentially distort the frequency content of the power spectrum used to derive temperature.

Time response investigation

Preliminary datasets produced by the streak camera system showed significantly distorted LITGS signals compared to the expected signal features of a sharp rise, followed by the combination of an exponentially decaying contribution with a decaying oscillatory contribution. This merited an investigation into the cause of the distortion before applying the streak camera system to the intended measurement campaigns.

By comparison of the responses of the streak camera and a fast-photodiode to LITGS signals and the ns-scale mode-beating structure within a laser pulse, the time-response of this streak camera was found to be too slow (FWHM ~ 5 ns) to accurately record LITGS signals. Applying the ‘standard’ analysis to the streak camera data will assume the temperature dependence of the oscillations is the same as a non-distorted signal. While the oscillation frequency information is still present in some form, the previous development and validation of LITGS was based on

non-distorted signals. As such, the streak camera data cannot be reliably used for LITGS thermometry without extensive testing and validation.

In principle, the actual time response of the streak camera could be measured using the pulse from a picosecond laser as the input signal (effectively a delta function on the timescale of this experiment), however a picosecond laser was not available.

Streak camera summary

1D LITGS thermometry has previously been demonstrated [229] using a streak camera whose time response was sufficiently fast to accurately record the rapid oscillations in the LITGS signal. However, the technique required 'stitching' together of several images and therefore was restricted to time-averaged measurements.

The streak camera investigated in this work is capable of recording an entire LITGS signal in a single image, in theory permitting time-resolved measurements. Accurate recording of the modulation in signal intensity requires a detector rise time of ≤ 1 ns. However, the impulse response function of the streak camera is too slow for accurate recording of LITGS signals[148].

For the 'timescale ratio' figure of merit introduced in section 7.2, a ratio of 1 : 500 for accurate time-resolved LITGS detection is a very demanding requirement and, based on the above investigation, the streak camera used in this work does not satisfy this condition. Commercially available streak cameras[149] can achieve very high temporal resolution (50 ps) but only by using a rapid voltage sweep at the expense of a very short timebase (10 ns). This trade-off between temporal resolution and timebase results in the 'timescale ratio' remaining constant for most sweep rates of a given streak camera.

[148] Using this work's typical grating spacing, composition and temperature, the peak-to-peak timescale of the acoustic oscillations in a LITGS signal is of the order of 20 ns.

[149] The Optronis SC-10 uses a 20 mm detector with 0.1 mm spatial resolution, giving a ratio of 1 : 200. A sweep speed of 25 ns/mm therefore gives a 500 ns timebase and temporal resolution of 2.5 ns. This ratio of 1 : 200 is typical of streak cameras from other manufacturers, the largest ratio available from Hamamatsu's range is 1 : 150.

The majority of streak cameras available on the market have ‘timescale ratios’ of 1 : 200 or less and are therefore incapable of performing this measurement. If higher-spec models could be sourced, with typical streak camera systems costing of the order of £100,000, even if available a higher-spec model would be prohibitively expensive for many applications.

Implications for fibre-coupled photodiode array

The above investigation suggests that rather than being solely a cheaper and simpler alternative to a streak camera detection system, the fibre-coupled photodiode array method is able to perform time-resolved LITGS measurements which a streak camera would be incapable of performing.

The ‘timescale ratio’ of the fast photodiodes used for the fibre-coupled photodiode array can be as high as 1 : 6.4 x 10^7. Photodiodes may be used continuously, giving an effectively infinite timebase. In practice however, the maximum length of a recorded signal is determined by the memory of the data acquisition system[150].

Due to the capability of the fibre-coupled photodiode array for time-resolved measurements and accurate recording of LITGS signals, all results discussed in the remainder of this chapter were obtained using the fibre-coupled photodiode array detection system.

7.4.2. Compositional effects

One of the main sources of uncertainty in a LITGS experiment is the knowledge of the local gas composition. Variation in flow composition has a direct effect on the value of γ/m used to derive temperature from the measurement of sound speed. Errors introduced into LITGS thermometry by uncertainty or variations in mixture composition are discussed in detail in [4]. For the case of this work, entrainment of unseeded air at the edges of the flows will dilute the

[150] The Waverunner 625Zi oscilloscope used in this work is capable of recording 16 million datapoints per vector when operating with 4 channels. If the sample rate was set to the minimum required 1 GHz, this corresponds to a ‘timescale ratio’ of 1 : 1.6 x 10^7. Memory upgrades are also available to increase the recording length by a factor of 4 to 64 Mpts.

toluene seeding density and perturb the local value of γ/m, resulting in a systematic bias to derived temperature if unaccounted for.

Compositional error calculations

The expected variation in derived temperature due to compositional effects can be summarised as follows. The local sound speed, c_s, is the fundamental property determining the oscillation frequency of a LITGS signal and hence the derived temperature (c.f. chapter 4),

$$c_s = \sqrt{\frac{\gamma k_B T}{m}} \tag{7-1}$$

Toluene has a smaller value of γ/m than air[151], therefore any decrease in toluene concentration will increase the mean value of γ/m locally. This increase in γ/m from the assumed value will perturb the sound speed in the same way as an increase in temperature [equation (7-1)].

As the LITGS analysis cannot distinguish between compositional and thermal perturbations to the sound speed, the reduction in toluene concentration causes an increase in the value of the derived temperature.

Effect on derived temperature

The magnitude of the compositional bias to the derived temperature owing to lab air being entrained by the flow is investigated in this section.

Calculation of the systematic error resulting from all possible variations in composition from 0 % to the seeding concentration of 2.27 % produces Figure 7-9. The maximum error (full seeding concentration assumed when the actual concentration tends to zero) would be +6 %. However, this represents a worst-case scenario as the concentration profile can be referenced to ensure that the time-averaged measurement of the flow at room temperature is fixed to room temperature across all 4 measurement points. This will fully correct for the toluene

[151] Toluene has a value of m/γ = 99.2 $gmol^{-1}$. Air has a value of m/γ = 20.6 $gmol^{-1}$.

concentration profile at room temperature. The remaining compositional error will be due to any changes in the mixing of the flow as the temperature varies throughout the experiment.

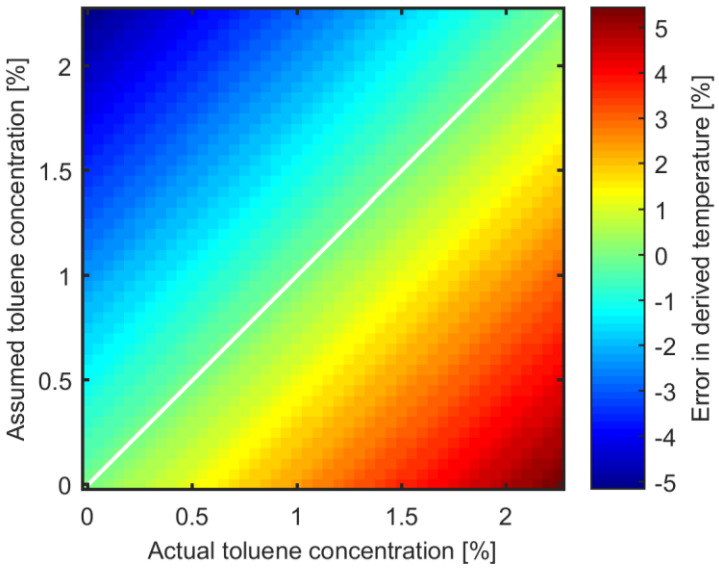

Figure 7-9 Error in derived temperature owing to composition. 0 % error highlighted by a white line.

A more realistic estimate of possible errors is given in Figure 7-10. Variation in concentration from the room temperature profile by ± 50 % results in a worst-case error of + 2.7 % – 1.7 %[152]. Variation of ± 20 % results in a maximum error of 1 % for all assumed concentrations.

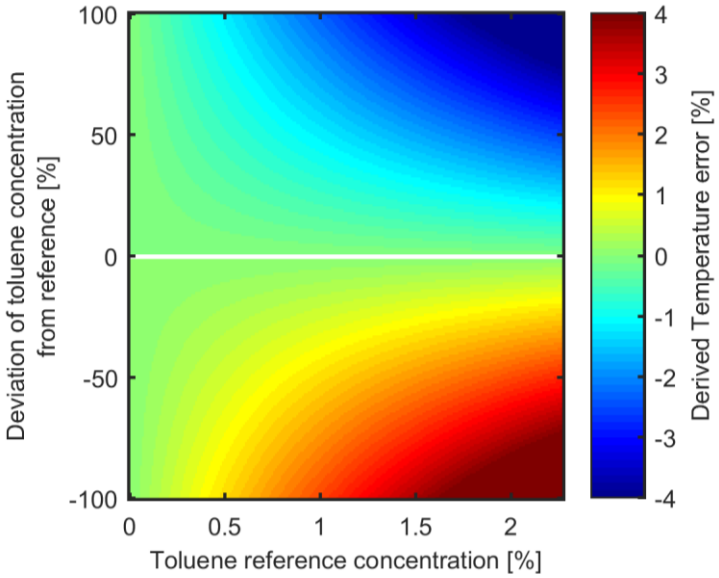

Figure 7-10 Error in derived temperature owing to relative deviation of actual toluene concentration from reference composition, with 0 % error highlighted by a white line.

[152] This is not symmetric, despite the symmetry of Figure 7-10, as the actual concentration cannot exceed the initial seeding concentration, capping the negative worst-case error at – 1.7 %.

For the purposes of minimising the error in derived temperature, the concentration of toluene should be minimised. To ensure errors in derived temperature are below 1 % for compositional shifts up to ± 50 % from the assumed value requires a toluene concentration of < 0.85 %.

Compositional correction

Preliminary testing of a variety of room-temperature flow conditions confirmed that while changes in composition had a significant effect on the derived temperature profile, for any given conditions the influence was consistent over time and did not display any fluctuations as conditions were varied.

Correction method

The calibration constant, C, used to relate the oscillation frequency of a LITGS signal, f, to temperature, T, is dependent on the local composition of the gas mixture, (c.f. equation (4-5)):

$$T = \frac{m\Lambda^2}{\gamma k_B} f^2 = Cf^2 \tag{7-2}$$

Correct selection of the value of this constant is sufficient to account for the direct effect on the oscillation frequency of the changes in γ and m.

The compositional correction method for each of the 1D-LITGS datasets in this chapter is based on determining the local value of this constant for each measurement point from signals recorded at a known temperature.

The procedure for compositional correction of a 1D-LITGS dataset is as follows.

1) Setup flow system as required, ensuring flow conditions are stable over time.
2) Record a set of measurements at a known temperature.
3) For each of the 4 measurement points, fix the mean derived temperature to this known temperature by selecting an appropriate calibration constant.
4) Apply the 4 calibration constants to the remaining measurements in the dataset.

The main advantage of this method is that it provides a calibration referenced to the actual flow conditions of any particular setup given a known temperature. This removes any systematic bias from the derived temperatures caused by consistent differences between the flow and the assumptions made about its compositional profile.

As with all such correction schemes, this method has its disadvantages. While the correction is very consistent for subsequent room-temperature flows, the aim of this correction is to allow investigations into flows where the temperature profile is no longer the same as the calibration conditions. Density changes as a result of temperature will not bias the LITGS measurement as the influence of composition on temperature is through the mean 'm' and 'γ' of the molecules, which are affected by mixture changes but not density changes. Changing the temperature of the flow will however have some effect on the compositional profile, whether due to buoyancy effects or alterations to the mixing behaviour at the flow edges. These changes will not be accounted for by a room-temperature correction.

In what follows, these secondary compositional changes were assumed to have a smaller effect on the derived temperature than the actual effect of temperature variation. This claim is validated with hindsight by comparison of LITGS derived temperatures to thermocouple measurements. The figures are presented under the assumption that the compositional correction is 'perfect'. Any remaining compositional bias will appear as an apparent temperature shift from the 'true' (unknown) value.

For future application to turbulent flows, in which the assumption of stationary mixing conditions no longer holds, this compositional correction procedure would only be able to account for the time-averaged compositional profile. From shot to shot, the variation in mixing would lead to uncorrected local compositional bias to the derived LITGS temperatures. The overall intensity of a LITGS signal is related to the local number density of tracer molecules. For cases in which a local change in tracer number density provided the dominant contribution to the change in 'γ/m' from the time-averaged reference value, there could be some potential in

deriving a relative measurement of tracer number density from the intensity of each LITGS signal and varying the reference value of 'γ/m' accordingly for each shot.

7.4.3. Invasive or non-invasive?

While laser diagnostics are generally less invasive than alternative methods, such as physical probes, they must at some level cause a perturbation in the environment whose properties they are attempting to measure in order to perform the measurement[153]. LITGS is no exception and its most significant perturbative effect is the tracer's absorption of energy from the pump pulses. The formation of the LITGS grating is dependent on the electronic excitation of the tracer molecules being quenched by collisions with the bulk gas and resulting in a non-uniform heating of the medium. This will raise the mean temperature of the gas throughout the grating, referred to as 'beam heating'. By using minimal pulse energies and tracer number densities, the magnitude of this heating can be kept to a minimum. However, ensuring a detectable signal level will set lower limits on both these factors for practical measurements.

Tracer selection

One parameter that can often be freely chosen is the tracer species. The following section will compare the compositional and beam heating effects on derived temperature for toluene and acetone using the 'Dualflow' flow setup.

Toluene

In order to investigate the effects of varying tracer concentration, the initial seeded flow was diluted with nitrogen to reduce the toluene concentration in the flow by a factor of up to 3 from its initial value. Figure 7-11 shows time-averaged temperature measurements in a room temperature flow for 5 different seeding concentrations (specified by the flow rate within the

[153] On the other hand, passive optical techniques such as chemiluminescence can be considered fully non-invasive.

seeded pipe). The total flow rate was maintained at 1.2 L/min by mixing with a non-seeded N_2 flow upstream of the nozzle.

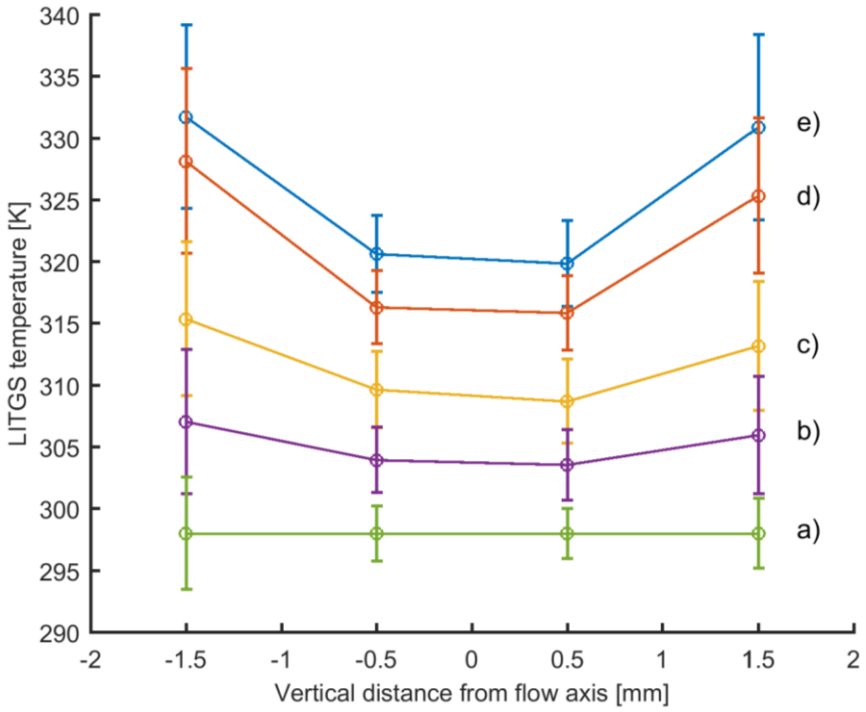

Figure 7-11 Multi-point derived temperatures across the flow for variation of toluene concentration. Toluene-seeded flow rates of a) 0.4 L/min, b) 0.6 L/min, c) 0.8 L/min, d) 1.0 L/min, e) 1.2 L/min. Errorbars represent the standard deviation of 100 temperature measurements at each location.

The two main features of this figure are:

1) Derived temperature increases with increasing seeding concentration.
2) Compared to the flat profile of the lowest concentration measurement [Figure 7-11 a)] (in theory the least affected by both compositional and beam heating effects), derived temperatures in the centre of the flow are lower, while those at the edges are higher.

The derived temperature increases with seeding concentration by approximately 15 K per %. This shows that LITGS is not truly non-invasive for these seeding concentrations due to the strong absorption of 266 nm light.

The variation of composition with height in Figure 7-11 was calibrated using the lowest concentration measurement (a) and applied to all datasets. This calibration method for a single seeding concentration cannot distinguish between variation in oscillation frequency caused by

γ/m or beam heating and so corrects for both effects. The remaining temperature profiles were then corrected for the bulk compositional changes in γ/m between seeding levels. The increase in temperature that remains is likely to be caused by differences in beam heating compared to the calibration measurement.

The derived temperatures at the edges of the flow are higher compared to the flat profile of (a). As described in section 7.4.2, a lean actual mixture when assuming a rich reference mixture results in an erroneously high derived temperature. Entrainment of air into a 'richly' seeded flow causes a greater change to the flow's local mean γ/m than the equivalent scenario with a 'leanly' seeded flow due to the greater compositional difference between the seeded flow and the air. Therefore the edges of the 'rich' flow are 'leaner' than would be expected by extrapolating from the compositional profile of the 'leanest' measurement (a).

As the seeding concentration is constant for any given experiment in this work (sections 7.4.5 to 7.4.7), the variation in beam heating effects will be much smaller than those presented in this demonstration.

Acetone

Toluene is not by any means the only tracer available for LITGS thermometry. While the point-LITGS experiments of chapters 4 and 6 use of toluene was determined by compatibility with the TC-PLIF technique, isolated 1D LITGS experiments are free to choose any appropriate tracer. A common alternative to toluene for LITGS experiments with 266 nm pump beams is acetone. Acetone (58 $gmol^{-1}$) is a much lighter molecule than toluene (92 $gmol^{-1}$) with the potentially beneficial effect of a much closer value of γ/m to air (29 $gmol^{-1}$). Acetone, being a ketone, also absorbs well in the UV. The experiment to vary tracer concentration was repeated using acetone.

As with toluene, the temperature profile shows increased derived temperatures for higher concentrations both across the line as a whole and also at the edges of the flow [Figure 7-12].

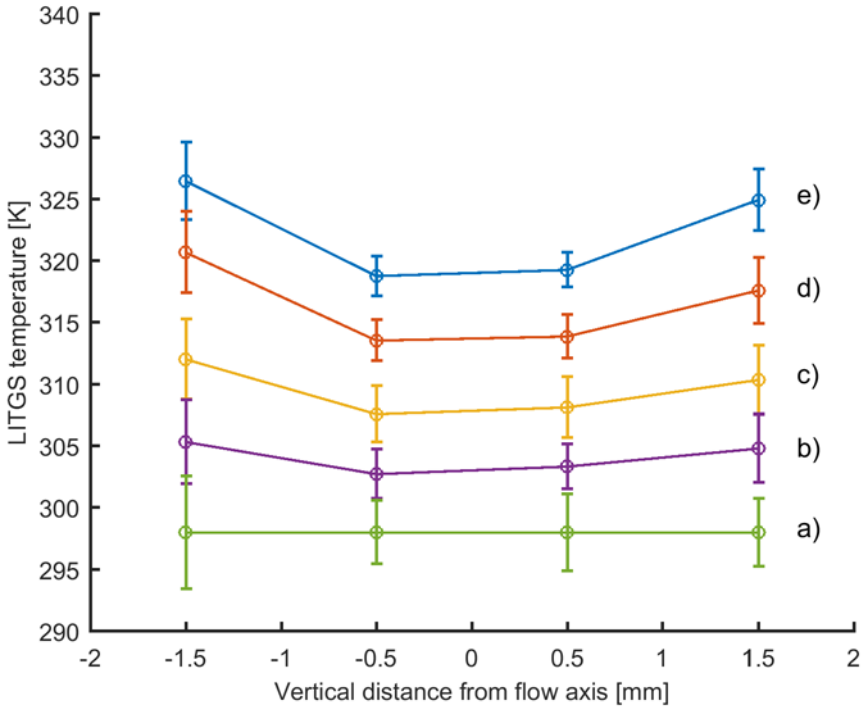

Figure 7-12 Multi-point derived temperatures across the flow for variation of acetone concentration. Acetone-seeded flow rates of a) 0.4 L/min, b) 0.6 L/min, c) 0.8 L/min, d) 1.0 L/min, e) 1.2 L/min. Errorbars represent the standard deviation of 100 temperature measurements at each location.

Acetone would initially seem to be a better choice than toluene for minimising beam heating as the absorption cross-section of acetone at 266 nm is lower than toluene's by two orders of magnitude. However, due to its higher vapour pressure at room temperature[154], the seeding concentration of acetone in this setup is higher by a factor of 4. The net result is that the beam heating effect in this flow arrangement is approximately the same for both toluene and acetone.

The compositional corrections required when using acetone are larger than those of toluene due to the increased seeding concentration of 10.7 % produced by the passive seeding method and required to maintain a detectable signal.

Interestingly the effects of beam heating (frequency up for richer flows) and compositional changes to γ/m (frequency down for richer flows) almost cancel each other out for acetone in this experiment, as can be seen in Figure 7-13 which has not been corrected for γ/m. This shows the importance of understanding the contributions that systematic biases make to temperatures

[154] $Pvap_{acetone}$ = 30 kPa, $Pvap_{toluene}$ = 2.7 kPa.

derived from a LITGS signal, otherwise false conclusions could be drawn such as interpreting acetone as a much less invasive tracer than toluene based on the temperatures derived in Figure 7-13.

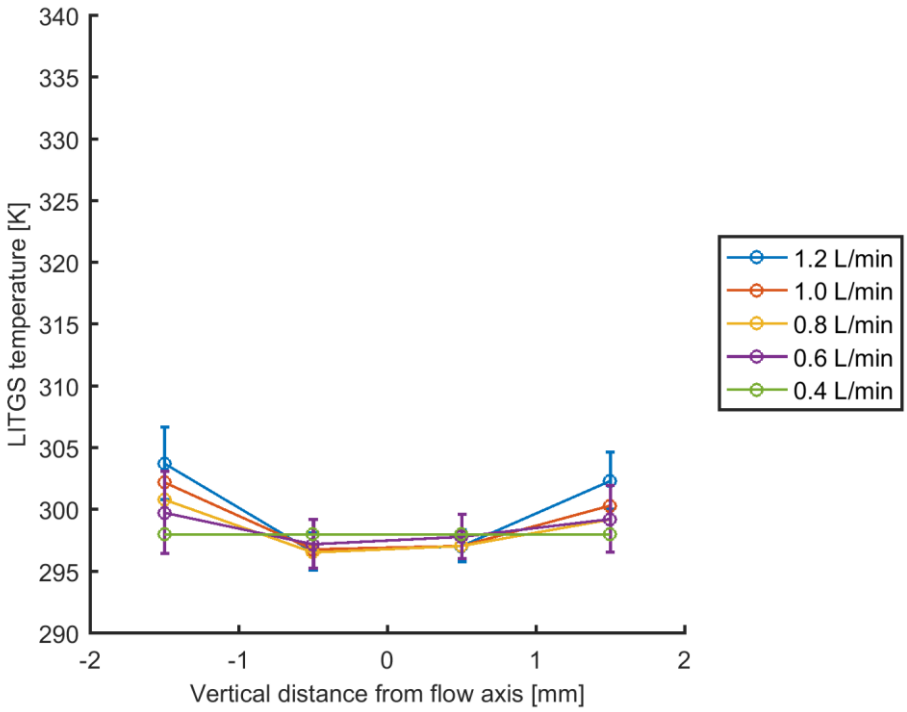

Figure 7-13 Multi-point derived temperatures, uncorrected for bulk changes in γ/m between datasets, across the flow for variation of acetone concentration showing approximate cancellation of beam heating and compositional shift in derived temperature for these conditions. Errorbars represent the standard deviation of 100 temperature measurements at each location.

Comparison of acetone and toluene shows comparable end results for the derived temperature as a function of flow seeding. Using either as a tracer in this experiment does not provide a non-invasive measurement, although the perturbation can be partially compensated for by calibration. At the seeding levels required for comparable signal strengths, toluene experienced less compositional variation in γ/m than acetone. The effects discussed in this section and 7.4.2 can help inform the tracer selection for future experiments.

In this work, measurements were performed primarily with toluene due to an intention for future integration of the 1D-LITGS technique with the existing TC-PLIF thermometry system, which requires toluene as a tracer.

7.4.4. Signal quality

LITGS signals detected using the fibre-coupled photodiode array are very clean at room temperature with sufficient toluene and UV pulses which are below the intensity required to initiate breakdown of the toluene molecules, or to see an electrostrictive grating contribution. The flow systems in this chapter are dynamically stable, hence each shot is representative of the mean flow measurement and the results may be further improved by averaging over many shots. For the remainder of this chapter, the mean temperatures over 100 sequential shots are displayed, with error bars corresponding to the standard deviation of those 100 shots.

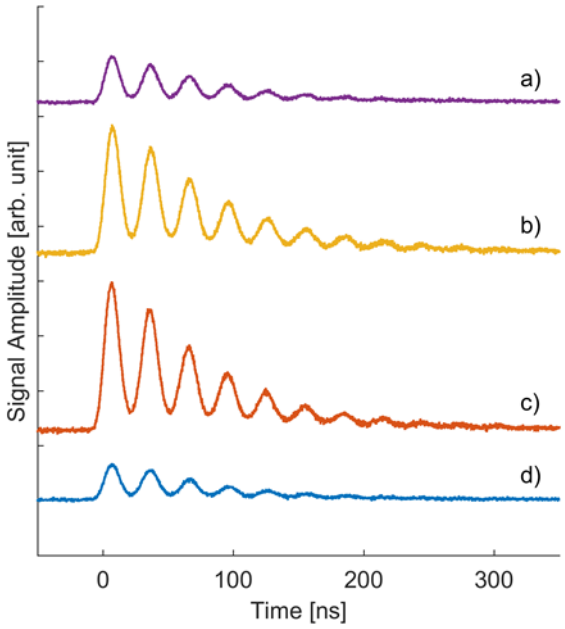

Figure 7-14 Fibre-coupled photodiode array single-shot LITGS signals

Signals from the edges of the sheet (‘a’ and ‘d’) are weaker than at the centre (‘b’ and ‘c’) due to smaller pump and probe intensities as well as possible compositional variation [Figure 7-14]. The pump laser is capable of producing much higher pulse energies, however, the UV energy in the sheet should be limited to avoid breakdown of the toluene molecules and to minimise beam heating. Future tests could consider increasing the pump pulse energy and expanding the UV sheet to give approximately uniform illumination across the 4 mm line of interest.

7.4.5. ‘Dualflow’ results

1D temperature gradient

1D-LITGS measurements were performed across the hot-cold flow boundary generated by the ‘Dualflow’ setup. Derived temperatures are consistent between runs at same flow conditions, within the precision of the measurement. This gives further support to the assumption of compositional stability in the flow for any given set of flow conditions.

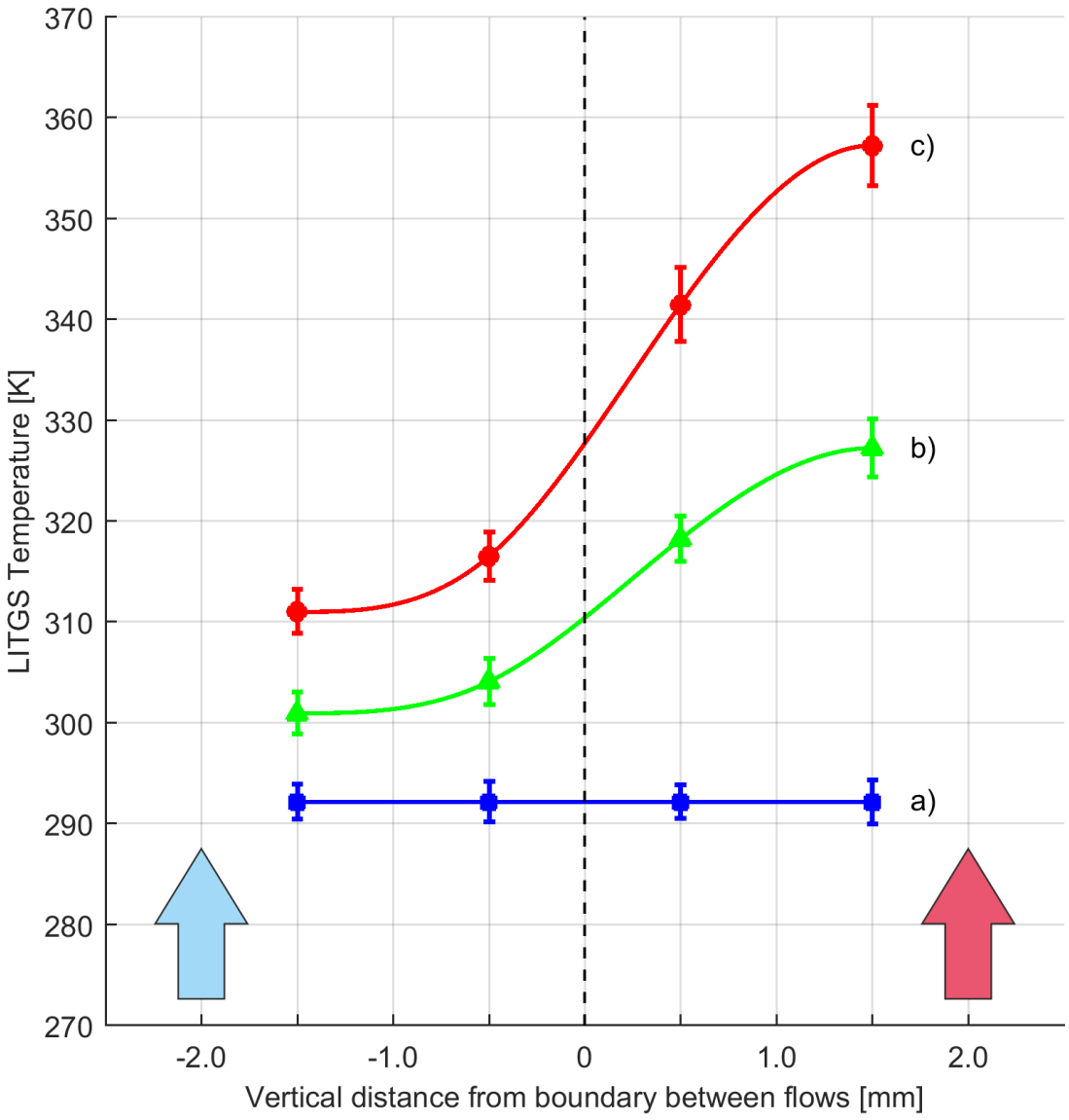

Figure 7-15 Multi-point LITGS temperatures across a horizontal dual-temperature flow for a) unheated flows (used for the compositional reference correction), b) upper flow heated at low power and c) upper flow heated at high power. Errorbars represent the standard deviation of 200 single-shot temperatures. The boundary between the two flows is marked by a dashed line. The arrows at + 2.0 mm and – 2.0 mm mark the location of the axes of the heated (red) and unheated (blue) flows.

The 4 LITGS measurement points were aligned symmetrically across the boundary of the two flows, at an axial distance of 3 mm from the aperture of the ‘Dualflow’ nozzle. The centres of each flow are therefore at transverse distances of –2.0 mm and 2.0 mm in Figure 7-15, with the boundary between flows at 0 mm.

Dataset a) at room temperature formed the basis of the compositional correction procedure for this flow geometry. The error bars of 0.7 % correspond to the standard deviation of 100 shots after compositional correction and represent the measurement precision for the ‘Dualflow’ setup. This can be interpreted as a resolution limit of temperature gradients with this 1 : 1 imaging geometry of 5 Kmm^{-1}. The flow heater raised the temperature of the upper flow to b) 328 K and c) 357 K. Interpolated lines have been added as guides to the eye.

The temperature profiles for the ‘Dualflow’ experiment display the steepest gradient at the boundary between the hot and cold flows. This gradient increases with increased heating of the upper flow as expected, to at least 20 Kmm^{-1} for c).

Quasi-2D temperature map

By sacrificing the time-resolved capability of the 1D-LITGS system and considering only time-averaged measurements, the 2D temperature profile of the flow in the transverse and axial flow directions can be mapped out by sequential 1D measurements at varying distances from the nozzle [Figure 7-16].

At each heating condition for the ‘Dualflow’ setup, 4 sequential 1D measurement sets were taken at 0.0 mm, 0.5 mm, 1.0 mm and 2.0 mm axial distances from the reference point at 3 mm from the nozzle. This generates the 4 x 4 grid of LITGS datapoints displayed as white crosses in Figure 7-16 a) to d).

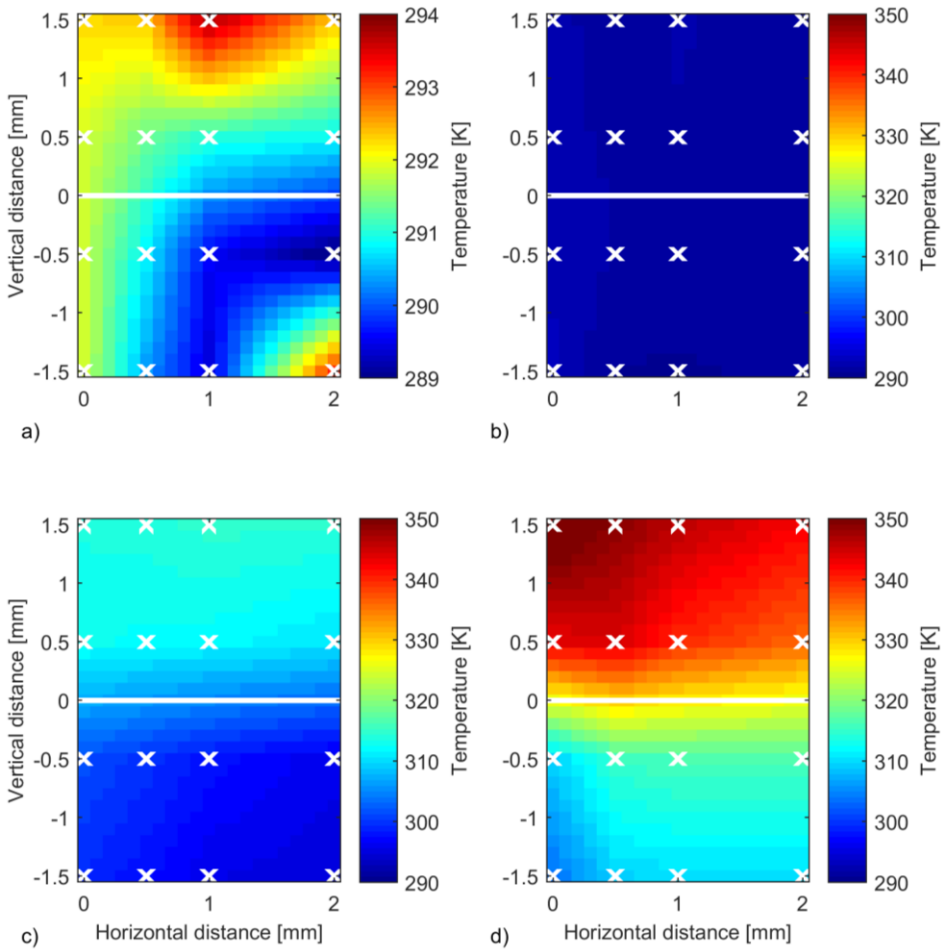

Figure 7-16 Quasi-2D temperature map constructed from interpolation between 4 sets of sequential 100-shot averaged multipoint measurements of the flow's transverse temperature profile, at locations marked by white crosses. a) and b) room temperature, c) partial heating, d) full heating. The boundary between the two flows is marked by a white line.

Across the 16 'real' datapoints of each image, a 21 x 31 grid of linearly interpolated datapoints is displayed with a false colour scale as a guide to the eye for each time-averaged 2D temperature distribution a) to d).

a) The false colour map for the room-temperature measurement has been scaled to show only the min-max range of ± 2.5 K across the pseudo-imaged-plane. This demonstrates that after correction for composition, subsequent room temperature measurements show fluctuations with a standard error[155] of only ± 0.46 % across the plane.

[155] The 'standard error' of the mean is the standard deviation of errors in a set of sample means with respect to the true mean.

b) The same room-temperature measurement as a) with the false colour map rescaled to the min-max values of the combination of all heating conditions [Figure 7-16 b) to d)]. Very little structure is visible across the image, showing the excellent consistency of both the flow setup and the 1D-LITGS measurements over the 5 – 10 minute timescale of the experiment.

c) The upper flow is partially heated by the flow heater, using the same colour scale as b).

d) The upper flow is fully heated by the flow heater, using the same colour scale as b).

As the LITGS measurement region is moved incrementally away from the nozzle aperture, a reduction in the magnitude of the temperature gradient is observed for the fully heated dataset d). This is attributed to mixing across the boundary causing both 'flows' to approach an intermediate temperature.

7.4.6. 'Hotplate' results

The derived temperatures from the 'Hotplate' experiment display the evolution of the thermal boundary layer perpendicular to the plate surface as the plate is heated from room temperature, 293 K, to 381 K [Figure 7-17]. The formation of a steep temperature gradient is observed within 1 – 2 mm of the 'Hotplate' surface, while between 2.5 mm and 3.5 mm the temperature profile is constant to within the high precision of the measurement.

The temperature profiles for the heated plate runs appear to be asymptotically approaching temperatures above the ambient temperature of 293 K. This can be interpreted as conductive heating having a large contribution within 1 – 2 mm of the surface, while radiative heating raises the flow temperature throughout the 4 mm measurement region.

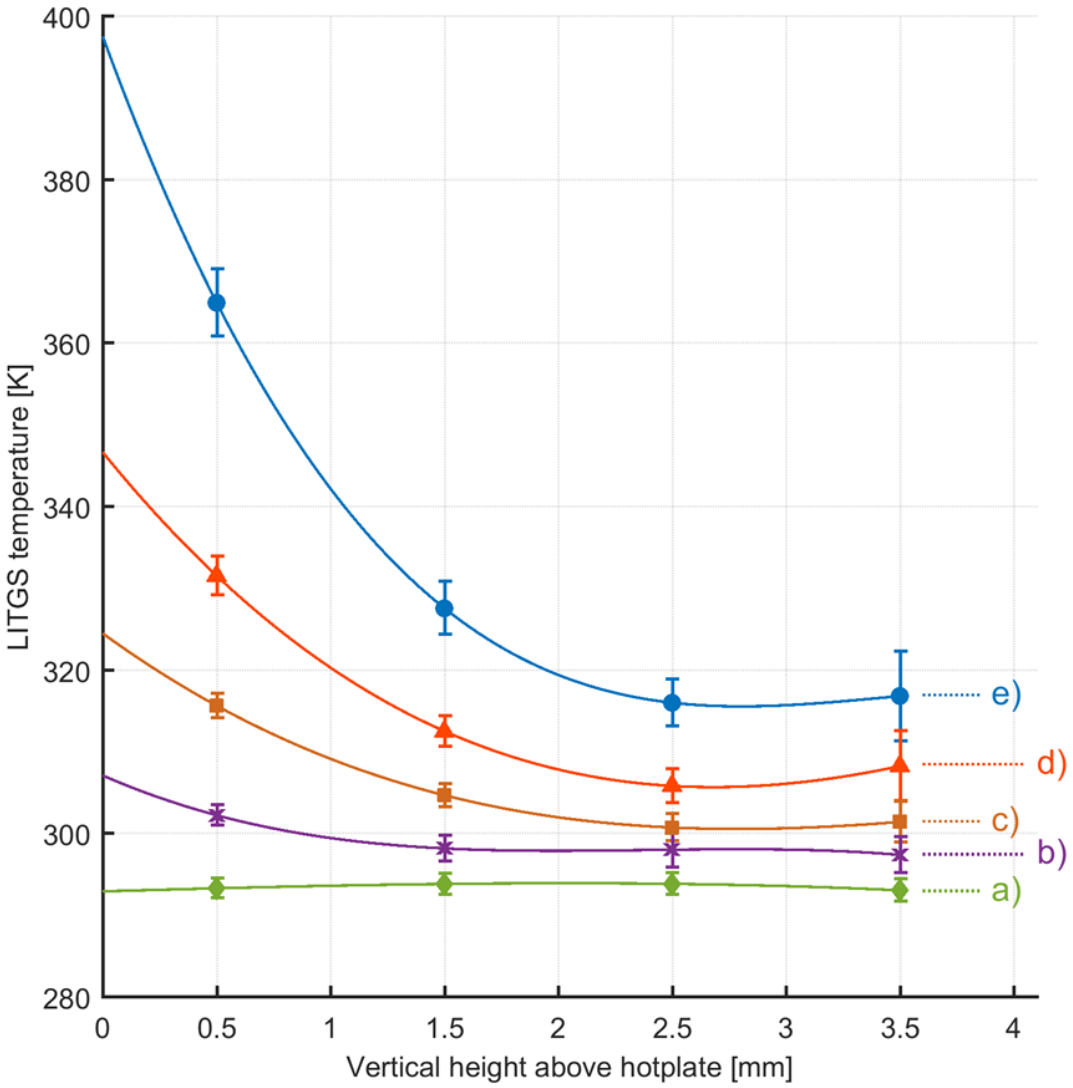

Figure 7-17 LITGS temperatures perpendicular to the 'hotplate' surface at a) 293 K, b) 304 K, c) 318 K, d) 340 K, e) 381 K, as measured by a thermocouple. Fitted spline curves provide a guide to the eye and an extrapolated estimate of surface temperature. Errorbars represent the standard deviation of 100 temperature measurements at each location.

Extrapolation of LITGS temperatures to 0 mm using a cubic spline fit gives surface temperature estimates slightly hotter than the corresponding thermocouple measurement – most significantly for hotter runs. Although this could be because of the fit, it is likely to be an underestimate of the temperature of the surface of the 'Hotplate' by the thermocouple. The thermocouple has a small contact area with the plate, providing imperfect thermal contact. Additionally the connecting wires near the junction will experience some cooling due to contact with the surrounding air. By this logic, 'Coldplate' surface temperatures should be overestimated by the thermocouple measurements, a claim that will be discussed in the following section.

The standard deviation of measurements at the upper edge of the flow, closest to the boundary between the flow and the stationary air, are larger than those closer to the plate's surface, particularly for the strongly heated tests. This may be caused by turbulent mixing at the edges of the heated flow with the ambient air, generating increased shot-to-shot variation in local temperature. Additionally, the reduction in toluene concentration and lower UV energy at the edge of the sheet combine to produce weaker signals in this region.

7.4.7. 'Coldplate' results

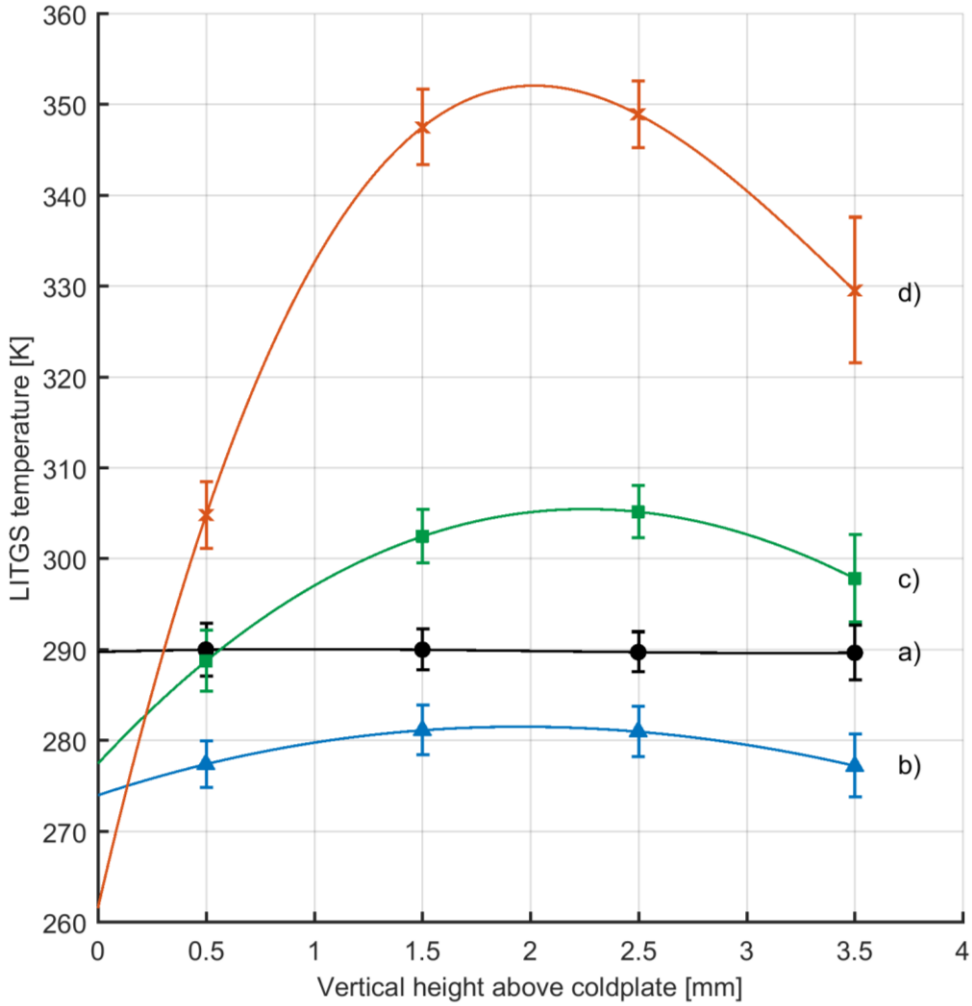

Figure 7-18 LITGS temperatures perpendicular to the 'coldplate' surface for flow temperatures of a) 290 K, b) 289 K, c) 309 K, d) 341 K, as measured by a thermocouple at the nozzle exit. Plate is cooled for all datasets except the ambient dataset (a). Fitted spline curves provide a guide to the eye. Errorbars represent the standard deviation of 100 temperature measurements at each location.

Cooling of the plate via the water-cooling coil appears to affect the entire flow, not just the lower boundary in Figure 7-18 b), approximately 10 K cooler than the flow above a room

temperature plate. The ‘Hotplate’ tests showed a monotonic increase in flow temperature towards the heated plate surface. In contrast, the heated flow present in the ‘Coldplate’ experiment has a maximum local temperature in the centre of the measurement line [Figure 7-18 d)]. This difference in profile shape is due to the heated flow having a boundary with a region of cooler temperature on both sides, as opposed to the ‘Hotplate’ experiment where the room-temperature flow could freely mix with the lab air at the upper boundary without affecting the local temperature.

Examining the flow data for Figure 7-18 d), mixing of the hot flow with room temperature air results in temperatures at 3.5 mm approximately 20 K colder than at the centre of the line. The magnitude of this cooling by mixing is smaller than that at 0.5 mm due to conductive heat loss to the water-cooled plate surface.

Cubic spline extrapolations of the temperature profiles suggest the water-cooled plate temperature is close to 276 K[156]. However, extrapolation is only an estimated prediction of the temperature LITGS would measure adjacent to the surface and is likely to be inaccurate, particularly for the sharp gradient of d).

A larger drop in temperature is observed between the room-temperature plate and water-cooled plate measurements (a) 290 K to b) 276 K, $\Delta T \sim 14$ K) than would be expected from the surface thermocouple measurements (289 K to 283 K, $\Delta T \sim 6$ K). However, this is consistent with the thermocouple having less than ideal thermal contact with the plate and returning some weighted average of the flow and plate temperatures as suggested by the ‘Hotplate’ extrapolation results. If this is the case, the surface is actually colder than the thermocouple-measured 283 K. Measurement of the mains water temperature at 278 K suggests the actual surface temperature could be significantly below 283 K. An improved measurement of the plate temperature would have been obtained with a thermocouple embedded into the body of the plate.

[156] Average of the extrapolation of T_F = 289 K and T_F = 309 K data to 0 mm.

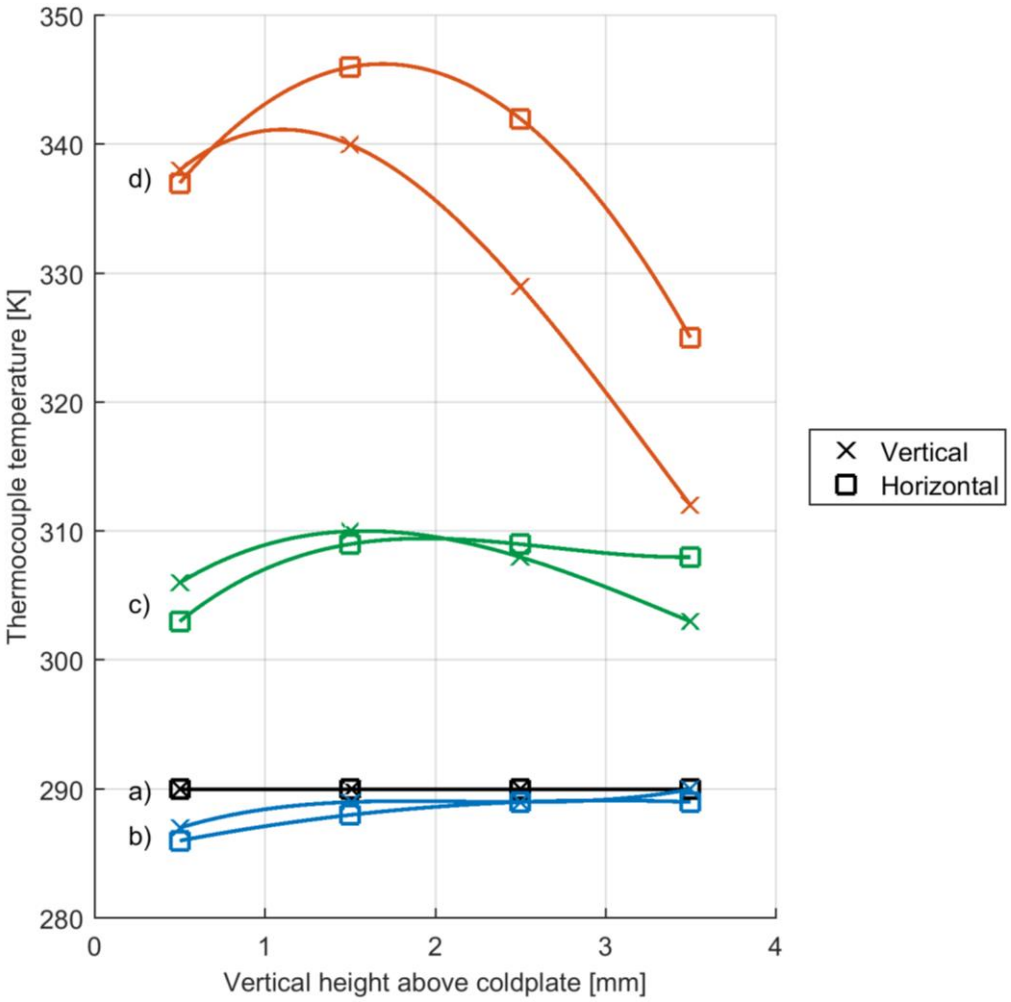

Figure 7-19 Thermocouple temperatures perpendicular to the 'coldplate' surface for different temperatures of the flow as measured by a thermocouple at the nozzle exit, with the thermocouple introduced into the flow along either the vertical or horizontal direction. a) Both plate and flow at ambient temperature, b) plate cooled and flow at ambient temperature, c) plate cooled and flow at 309 K, d) plate cooled and flow at 341 K. Fitted spline curves provide a guide to the eye.

A thermocouple was mounted on a translation stage and introduced into the flow in two orientations after each dataset of Figure 7-18. The orientation of the thermocouple in the flow strongly affects the reported temperature, by as much as 13 K for the strongly heated flow data [Figure 7-19 d)]. This demonstrates the invasive nature of thermocouple measurements, perturbing the flow and reporting a different temperature to that which would exist without the presence of the thermocouple.

7.5. Summary and conclusions

Extension of LITGS to 1D retains the advantages inherent to the point-LITGS technique, enabling subtle temperature gradients to be investigated. In particular the high precision of the technique was demonstrated for single-shot measurements of a nominally stable flow to be 0.7 %, defined as the standard deviation of a set of 100 sequential measurements.

The design and testing of the FPDA system for 1D-LITGS demonstrates its capability to record accurate, single-shot LITGS signals. This overcomes the limitation of streak cameras which are unable to meet the 'timescale ratio' requirement for detection of LITGS signals with high fidelity.

Temperature profiles have been recorded across thermal gradients within flows and within boundary layers of nominally laminar flows across planar surfaces. The spatial resolution of 1 mm was defined by the choice of 1 : 1 magnification for imaging of the LITGS interaction region onto the FPDA. In combination with the high measurement precision of 0.7 %, this corresponds to a thermal gradient resolution of 5 Kmm^{-1}. This resolution may be adjusted at will without altering the beam geometries by altering the magnification of the post-interaction region imaging optics. This approach is subject to the limitation of maintaining sufficient signal intensity collected by each fibre.

Quasi-2D time-averaged temperature maps of an approximately laminar flow from an 8 mm x 4 mm nozzle were generated by sequential 1D measurements. Examination of the temperature map produced for an unheated flow quantified the compositional correction procedure to be accurate to within a standard error of 0.5 % for this steady state flow at room temperature.

Care must be taken to account for compositional variation and the potential for beam heating in the derivation of LITGS temperatures from raw signals. The compositional correction procedure applied throughout this chapter appears to have been effective as it resulted in physically reasonable 'Dualflow', 'Hotplate' and 'Coldplate' results. Not only were reasonable qualitative temperature profiles generated throughout, for measurements of flows across planar surfaces,

reasonable quantitative agreement was achieved with thermocouple measurements of surface temperature, within the potential biases of thermocouple data.

The FPDA provides a very compact detection system. The measurement region must be imaged onto the fibre tips, however the remainder of the detection and acquisition system can be installed elsewhere. Even if the ability to make time-resolved measurements is not critical for an application, the FPDA system offers advantages: it is more robust, simpler to use and at least an order of magnitude cheaper[157] than a streak camera system.

Thermocouples have been demonstrated to be invasive in the types of flow in these measurements. Thermocouples are also inaccurate at reporting surface temperatures if they have poor thermal contact with the surface.

[157] Or two orders of magnitudes cheaper without the cost of a dedicated oscilloscope!

8. Summary

This chapter summarises the achievements of this work with the TC-PLIF, point-LITGS and 1D-LITGS techniques.

8.1. TC-PLIF calibrated in-situ with LITGS

The development of a system for 2-dimensional TC-PLIF thermometry, calibrated in-situ with LITGS, has been completed and the system has been applied to the measurement of in-cylinder temperature distributions during the compression stroke of a firing spark-ignition IC engine. In-situ calibration with a simultaneous, independent thermometry technique provides the most generally applicable calibration for TC-PLIF. Calibration from measurements in a different environment or under different conditions cannot account for any variation in environment between the calibration and experimental tests which is of particular concern for the increased variability of fired operation. LITGS is able to accurately calibrate the TC-PLIF data in-situ, allowing the calibration to track any changes in engine conditions over a series of experiments.

TC-PLIF was selected for 2-D thermometry as the derivation of temperature is independent of the spatial variations in fuel number density found in firing engines, as well as any variations in signal intensity owing to fluctuations in laser intensity profile or changes in window fouling. LITGS was selected for in-situ calibration of the TC-PLIF technique owing to the coherent signal beam and high precisions achievable with minimal complexity for a nonlinear technique.

The limitations of analysis methods for LITGS temperature derivation from weak signals were investigated. While this led to an improvement in the FFT analysis[158], it was determined that fitting to a theoretical model was the more generally optimal analysis method for engine LITGS data. Adjustment of the PMT gain was found to bias temperatures derived from LITGS, an effect which has been mitigated for future experiments and corrected for in this work by use of TC-PLIF to determine the gain-induced shift where present.

[158] Replacement of a Hann windowing function with a Tukey window.

The development of a TC-PLIF system was reported, including the selection of optimal spectral filtering optics, image registration procedure and confirmation of temperature sensitivity for time-resolved measurements. Unphysical artefacts in the TC-PLIF data, relating to imperfect registration, were observed and corrected for by the application of a post-processing routine.

Confirmation of the ability of both TC-PLIF and LITGS to independently resolve the cyclic variations of in-cylinder temperature was provided by the excellent shot-by-shot correlation of temperatures derived by each technique for fired operation. Charge cooling for GDI was resolved for both motored and fired operation and LITGS measurements recorded the gradual mean temperature rise as the optical engine warmed up during fired operation. Temperature inhomogeneities (‘hotspots’) were observed for fired operation, most frequently at later CAD during the compression stroke. In the current work, the formation of these hotspots could not be attributed to injection strategy or toluene number density after tests with three fuel blends and are likely to represent partial mixing of hot EGR with the cooler fresh charge. The system is now ready for application to a range of measurement campaigns investigating the temperature distributions produced by different fuel blends and different engine operating conditions of interest.

8.2. 1D-LITGS

Extension of LITGS to 1D for single-shot thermometry was investigated. It was demonstrated that the FPDA system was capable of recording accurate, single-shot LITGS signals for multi-point measurements, overcoming the limitation of streak cameras which are unable to meet the ‘timescale ratio’ requirement for detection of single-shot LITGS signals with high fidelity. The FPDA system is also more robust, simpler to use and at least an order of magnitude cheaper than a streak camera system. A calibration procedure was described to account for compositional variation and the potential for beam heating in the derivation of multi-point LITGS temperatures. Temperature profiles were subsequently recorded within boundary layers of flows across planar surfaces and in differentially heated flows. The FPDA system is now ready for application to a variety of flow geometries as detailed in chapter 9.

9. Future Prospects

In this chapter, potential improvements and applications of the 1D-LITGS and LITGS-calibrated TC-PLIF techniques are discussed.

9.1. TC-PLIF calibrated in-situ with LITGS

POD analysis

The information readily obtainable from the false colour presentation of TC-PLIF data relies heavily on the colour scale selected, which can both intentionally and unintentionally highlight or suppress certain features of the data. Mean temperature distributions and coefficient of variation images quantify the temperature fluctuations on a cycle-averaged basis but it is difficult to objectively quantify individual hotspot characteristics. What size must a region of different temperature be to qualify as a 'hotspot'? How large must the temperature increase be relative to the bulk gas? Should the hotspots be categorised by shape, or perhaps location in the image? A computational technique requiring little to no decision making on behalf of the researcher offers a solution to these issues.

A promising technique often used to quantify spray measurements [232] but that has also been successfully applied to combustion engines [233] is Proper Orthogonal Decomposition (POD). POD analysis seeks to identify the dominant modes of a set of grayscale/intensity images, in a similar fashion to finding the eigenvalues of a matrix. The first mode will provide the largest contribution to the images in the set. Subsequent modes will define the common structures present in the set of images. Each reconstructed image will be comprised of a sum of the 'modes' determined by the POD analysis, weighted by values that determine which modes contribute to each image. Typically only a few modes are required to reconstruct a good approximation to the original images in a set. The higher order modes represent noise contributions and slight perturbations to the dominant structures. POD analysis works best with larger datasets and would be a reasonable approach to determine the dominant features of the datasets of Figure 6-21, which contain 96 TC-PLIF images at a single CAD timing.

9.1.1. Applications

A wide variety of parameters combine to produce the in-cylinder temperature distribution of a combustion engine. Examples for investigation with LITGS-calibrated TC-PLIF include: variation of the equivalence ratio which would affect the completeness of combustion and the maximum temperatures reached within the cylinder, skip-firing the engine would remove residual gases from the measured compression stroke, while higher airflow would result in increased maximum pressure and higher temperatures. The charge cooling effect of oxygenated fuels has previously been studied with LITGS. Addition of methanol and ethanol to the fuel blend of this work would extend the study from point measurements to 2-dimensional temperature distributions.

A second portable LITGS system has been recently developed and could potentially be applied to the optical engine in tandem with the current LITGS system. This would enable two independent point-LITGS measurements to be performed within one compression stroke, separated either in time or space.

9.1.2. Improvements

New relay lenses

The vertical stripe artefacts discussed chapter 6 were identified as being caused by an imperfect registration between the two cameras and identified due to the strong variation in intensity across the pump sheet magnifying the effect of any misalignment.

As discussed in chapter 5, pairs of plano-convex lenses are the closest solution possible with spherical lenses to a ‘best form’ lens system for the 2f – 2f imaging used in the relay arms. The readily available spherical lenses were selected for the preliminary build of the system. While the performance was sufficient to demonstrate the principle of the technique, the optical aberrations introduced resulted in imperfect registration. Commercially available multi-

component camera lenses, designed using ray-tracing software, have been purchased to replace the pairs of plano-convex relay lenses used for the first iteration of the TC-PLIF system.

Installation of these new relay lenses should give distortion-free images at the two cameras enabling the cameras to be registered with high accuracy. This should ensure that despite the strong spatial variation in pump sheet intensity, the correct TC-PLIF signal ratio is derived for each location.

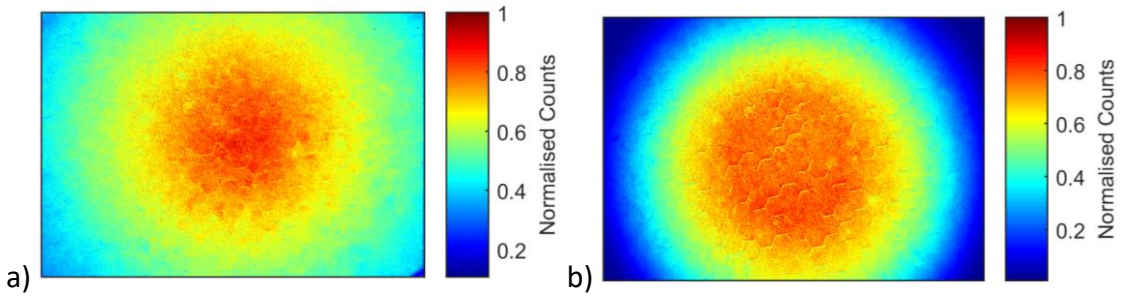

Figure 9-1 Flatfield images taken using the a) 'old' and b) 'new' relay lens systems.

The sacrifice made by installing these new lenses is the reduction in aperture size. The f-number of the relay lenses is f/2.8. While this is smaller[159] than the main imaging lens at f/4.5, it is almost a factor of 3 larger than the previous spherical lens pair. This causes a large increase in vignetting. A comparison of images taken under uniform illumination using the old and new relay lenses is given in Figure 9-1.

LITGS thermal gradient bias

Building on previous work on multiple temperature zones within the LITGS region [213], the hotspot-containing datasets could be used to investigate whether thermal gradients within the LITGS volume[160] are biasing the temperatures derived in this application. A large[161] fired dataset could be divided into homogeneous and structured subsets by comparing the standard deviation of the TC-PLIF temperatures across the LITGS interaction region. Comparison of

[159] A small f-number corresponds to a larger diameter for a given focal length. Therefore a lens with a smaller f-number is capable of collecting more incident light.

[160] E.g. crossing the boundary between a hotspot and the surrounding bulk gas.

[161] > 100 shot.

individual LITGS signals from each set to the mean LITGS signal would reveal any distortion of the LITGS signal due to multiple temperature zones.

New optical engine modifications

The optical engine used in this work has recently undergone renovation to provide increased optical access for future work. The cylinder head and barrel have been reshaped to provide line-of-sight access through both sides of the pent-roof. This opens up the potential for laser diagnostics such as LITGS and CARS[162] to be performed in the critical region at the very top of the cylinder, near the spark plug and fuel injector.

The new steel annulus has increased the clear aperture of its windows looking along the ridge of the pent-roof from 16 mm to 25 mm. This is sufficient to permit line-of-sight optical access at all crank angles as the rising piston never fully obscures these larger windows, in addition to allowing imaging of the region near the spark plug and fuel injector [Figure 9-2].

Figure 9-2 New optical annulus with curved upper surface and larger windows for all-CAD optical access and pent-roof imaging.

The quartz barrel sections have also been updated to allow full imaging of the entire cylinder from both sides[163] [Figure 9-3].

[162] Which require line-of-sight optical access.

[163] As opposed to the single-sided access available in the previous version.

Figure 9-3 New quartz barrel section permitting imaging of the entire pent-roof region from both sides.

9.2. 1D-LITGS

9.2.1. Applications

Calibration of TC-PLIF by 1D-LITGS

Calibration of TC-PLIF by point-LITGS has been discussed in chapter 6. Increasing the number of reference points within each TC-PLIF image from 1 to 4 would improve the precision of the in-situ calibration. It would also offer an opportunity for a much more detailed investigation into any discrepancies between the temperatures reported by each technique, as the profile across 4 points could be compared within a single image, instead of at a single point. This would allow concerns such as the potential TC-PLIF bias of EGR fluorescence to be investigated by examination of an image where the 1D-LITGS line crosses a boundary between ‘EGR’ and ‘bulk gas’ as reported by the TC-PLIF image.

Shock tubes

Work is currently underway in the shock tube facility at the University of Oxford to apply point-LITGS to thermometry in boundary layers and in the stagnation zone of a reflected shock.

Shocks are isolated, single events so the potential increase in recovered information per shot for replacing point-LITGS with 1D-LITGS is a valuable improvement.

Near-surface engine measurements

The heat transfer between the surfaces inside a combustion engine and the in-cylinder gases has important ramifications for the combustion process. In-cylinder temperatures affect the engine's thermodynamic efficiency and, amongst other things, the production of harmful particulates and NO_x which are subject to international legislation. 1D-LITGS could investigate the boundary layers near to critical surfaces within the cylinder with a precision capable of resolving the cyclic variations of the in-cylinder temperature distribution.

Fluid dynamics validation

Application of the current 1D-LITGS FPDA system to a wind tunnel equipped with an iso-thermal plate would provide precise measurements of thermal boundary layer evolution under well-characterised test conditions for comparison to theoretical fluid dynamics models.

Turbine blade cooling strategies

Turbine blades must be cooled in order to withstand the high temperatures and centrifugal stresses during operation. Film cooling transfers cooling air from within the blade to the surface via small holes, forming a layer of air which reduces heat transfer to the blade's surface. Transpiration cooling of turbine blades instead utilises a porous material for the outer surface of the turbine blade in order to provide a more uniform layer of cooling air [234], [235]. The 1D-LITGS FPDA system could provide precise and accurate measurements of the thermal boundary layer in order to evaluate the effectiveness of various cooling strategies.

9.2.2. Improvements

Increased number of measurement points

The major limitation of LITGS measurements using the current fibre-coupled photodiode array is the number of measurement points being only 4. This limit is set, in practice, by the high cost per channel of a high speed acquisition system such as an oscilloscope with high bandwidth and sample rate. Scaling of the system by simply adding more detectors and oscilloscopes is an expensive solution costing of the order of £1000 per channel[164]. This cost could be potentially reduced by the use of a simpler multi-channel DAQ system, without the wide range of functionality provided by an oscilloscope.

An alternative solution would be to construct a multi-fibre delay line to allow two signals, one delayed by for example 500 ns, to be recorded at each detector. This would double the number of measurement points for the same 4 detectors and 4 oscilloscope channels and act as a proof of principle towards scaling up the number of measurements to potentially 10's of points.

Figure 9-4 displays a design of a prototype system using off-the-shelf fibre components for a linear array of 7 fibres[165] using 4 photodiodes. 4 of the fibres transmit the signal directly to each of the 4 photodiodes. The other 3 fibres have an extra length of 100 m each, resulting in a delay of 500 ns before the signals are directed onto 3 of the photodiodes. It is then a simple matter of splitting each recorded signal vector in half in software and analysing each half as an independent LITGS signal.

[164] Assuming the purchase of the cheapest appropriate USB oscilloscope option and a basic laptop.

[165] 7 rather than 8 due to the availability of linear fibre arrays with 7 fibres.

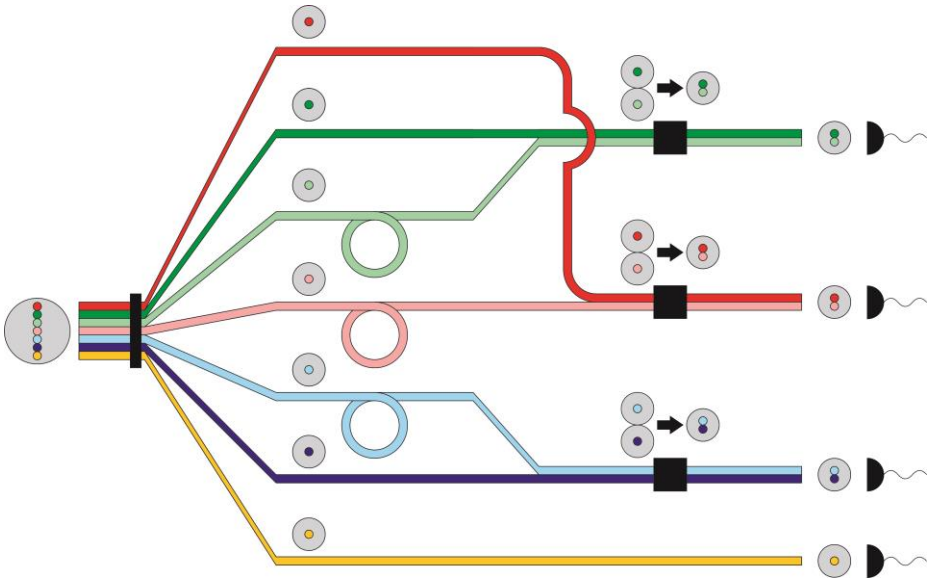

Figure 9-4 Multi-fibre delay line for scaling up the number of measurement points of the 1D-LITGS fibre-coupled photodiode array system.

A significant disadvantage to this setup is the current cost of multiple 100 m lengths of fibre with the associated fibre components. To upgrade a 4-point LITGS system to a 7-point system using off-the-shelf components would be no cheaper than purchasing additional detectors and data acquisition capability[166].

Variable spatial resolution

One aspect of the 1D-LITGS system not explored in this work is the possibility of easily varying the spatial resolution of the technique. By varying the magnification of the imaging optics to enlarge or reduce the image of the interaction region on the fibre tips, the size of the section of the interaction region interrogated by each fibre could be adjusted. As the pump and probe sheets are not altered by this method, any enlargement of the image such that light falls outside the fibre array would result in a reduction in total signal intensity collected by the fibres.

[166] There is some potential for cost-per-channel reduction if some of the off-the-shelf combinations were replaced with single, custom components. However, unless the cost of optical fibres can be significantly reduced for this design, a more cost-effective solution may be the purchase of additional detectors and oscilloscopes, both of which can be used for other purposes when the 1D-LITGS system is not in use.

If there is sufficient signal intensity to sacrifice, this method offers a rapid and simple adjustment of the separation of sampled points over the measured region.

Portable 1D-LITGS

The utility of the technique for real-world applications would be dramatically improved by redesigning the system as a portable 1D-LITGS system, using the same principles as the portable point-LITGS system used to perform measurements in the optical engine of chapter 6. The lasers and optical components would be reselected with compactness in mind to fit on a single breadboard[167], capable of being pre-aligned and subsequently mounted next to the test environment. The compact nature of the FPDA already lends itself to such a design philosophy.

Production of data in the same format as existing point-LITGS experiments, coupled with a low number of measurements 'per shot' renders the data suitable for rapid analysis with a view towards application to real-time temperature measurements in combination with a laptop-based automatic analysis system. This would open up opportunities to investigate real-world test environments currently inaccessible to a complicated optical diagnostic such as LITGS due to size, location or time restrictions.

[167] Unfortunately the Powerlite laser of this chapter is too large and the Minilite laser used for point-LITGS is too weak to provide sufficient UV energy for LITGS across a sheet. A compromise is required.

10.Bibliography

[1] P. H. Paul, R. L. Farrow, and P. M. Danehy, “Gas-phase thermal-grating contributions to four-wave mixing,” vol. 12, no. 3, pp. 384–392, 1995.

[2] R. E. Stevens, “Laser-Induced Grating Techniques for Combustion Diagnostics,” DPhil Thesis, University of Oxford, 2004.

[3] B. A. O. Williams, “Quantitative Laser Diagnostics for Combustion,” DPhil Thesis, University of Oxford, 2009.

[4] B. Williams, M. Edwards, R. Stone, J. Williams, and P. Ewart, “High precision in-cylinder gas thermometry using Laser Induced Gratings: Quantitative measurement of evaporative cooling with gasoline/alcohol blends in a GDI optical engine,” *Combust. Flame*, vol. 161, no. 1, pp. 270–279, 2014.

[5] S. Faust, G. Tea, T. Dreier, and C. Schulz, “Temperature, pressure, and bath gas composition dependence of fluorescence spectra and fluorescence lifetimes of toluene and naphthalene,” *Appl. Phys. B*, vol. 110, no. 1, pp. 81–93, 2013.

[6] L. Lu and B. A. O. Williams, “Pushing the Limits of Optical Thermometry,” 2015.

[7] International Energy Agency, “Key World Energy Statistics 2015.” 2015.

[8] United Nations Framework - Convention on Climate Change, “Paris Agreement.” United Nations Treaty Collection, Paris, 2016.

[9] International Energy Agency, “CO_2 Emissions From Fuel Combustion - Highlights 2015.” 2015.

[10] BP, “BP Statistical Review of World Energy 2016,” no. June, pp. 1–48, 2016.

[11] S. Blundell and K. Blundell, *Concepts in Thermal Physics*. OUP, 2006.

[12] J.-C. Han and L. M. Wright, “Enhanced Internal Cooling of Turbine Blades and Vanes,” *Gas Turbine Handb.*, pp. 321–352, 2007.

[13] K. J. Laidler, “The development of the Arrhenius equation,” *J. Chem. Educ.*, vol. 61, pp. 494–498, 1984.

[14] M. V Heitor and a L. N. Moreira, “Thermocouples and Sample Probes for Combustion Studies,” *Prog. Energy Combust. Sci.*, vol. 19, pp. 259–278, 1993.

[15] A. G. Gaydon, *The Spectroscopy of Flames*. Springer Netherlands, 1974.

[16] Asociación Española de Fabricantes de Automóviles y Camiones, “European Motor Vehicle Parc 2014,” 2014.

[17] Office for National Statistics, “Population and Migration,” 2014. [Online]. Available: http://webarchive.nationalarchives.gov.uk/20160105160709/http://www.ons.gov.uk/ons/guide-method/compendiums/compendium-of-uk-statistics/population-and-migration/index.html. [Accessed: 20-Aug-2016].

[18] European Parliament and Council of the European Union, “REGULATION (EC) No 715/2007 OF THE EUROPEAN PARLIAMENT AND OF THE COUNCIL of 20 June 2007 on type approval of motor vehicles with respect to emissions from light passenger and commercial vehicles (Euro 5 and Euro 6),” *Off. J. Eur. Union*, vol. L171, 2007.

[19] W. Piock, G. Hoffmann, A. Berndorfer, P. Salemi, and B. Fusshoeller, “Strategies Towards Meeting Future Particulate Matter Emission Requirements in Homogeneous

Gasoline Direct Injection Engines," *SAE Int.*, 2011.

[20] B. Bauerle, F. Hoffmann, and F. Behrendt, "Detection of hotspots in the end gas of an internal combustion engine using two-dimensional LIF of formaldehyde," *Twenty-Fifth Symp. Combust. Combust. Inst.*, pp. 135–141, 1994.

[21] R. Stone, *Introduction to Internal Combustion Engines*, 4th ed. Macmillan, 2012.

[22] G. T. Kalghatgi, "Developments in internal combustion engines and implications for combustion science and future transport fuels," *Proc. Combust. Inst.*, vol. 35, no. 1, pp. 101–115, 2015.

[23] Luc1992, "P-V Otto Cycle," *wimkimedia.org © CC-BY-SA-4.0*. [Online]. Available: https://commons.wikimedia.org/wiki/File:P-V_Otto_cycle.svg. [Accessed: 20-Aug-2016].

[24] K. Noma, Y. Iwamoto, and N. Murakami, "Optimized Gasoline Direct Injection Engine for the European Market," *SAE Tech. Pap.*, no. 724, 2016.

[25] P. Ewart, C. Willman, B. A. O. Williams, J. Williams, and C. R. Stone, "High precision in-cylinder thermometry using laser induced grating spectroscopy," *I Mech E*, 2015.

[26] M. Sandford, G. Page, and P. Crawford, "The All New AJV8," *SAE Int.*, p. 9, 2009.

[27] V. Sick, M. C. Drake, and T. D. Fansler, "High-speed imaging for direct-injection gasoline engine research and development," *Exp. Fluids*, vol. 49, no. 4, pp. 937–947, 2010.

[28] N. Docquier and S. Candel, "Combustion control and sensors: A review," *Prog. Energy Combust. Sci.*, vol. 28, no. 2, pp. 107–150, 2002.

[29] R. Luckerath, M. Woyde, W. Meier, W. Stricker, U. Schnell, H. C. Magel, J. Gorres, H. Spliethoff, and H. Maier, "Comparison of Coherent Anti-Stokes Raman-Scattering Thermometry with Thermocouple Measurements and Model Predictions in Both Natural-Gas and Coal-Dust Flames," *Appl. Opt.*, vol. 34, no. 18, pp. 3303–3312, 1995.

[30] T. Husberg, S. Gjirja, I. Denbratt, J. Engström, A. Omrane, and M. Aldén, "Piston temperature measurement by use of thermographic phosphors and thermocouples in a heavy-duty Diesel engine run under partly premixed conditions," *SAE Tech. Pap.*, 2005.

[31] A. Eckbreth, *Laser Diagnostics for Combustion Temperature and Species*, Second Ed. Gordon and Breach Publishers, 1996.

[32] J. B. Jeffries and K. Kohse-Höinghaus, *Applied Combustion Diagnostics*, 1st ed. London: Taylor & Francis, 2002.

[33] C. Schulz, A. Dreizler, V. Ebert, and J. Wolfrum, "Combustion Diagnostics," in *Springer Handbook of Experimental Fluid Mechanics*, C. Tropea, A. L. Yarin, and J. F. Foss, Eds. Berlin, Heidelberg: Springer Berlin Heidelberg, 2007, pp. 1241–1315.

[34] J. Kiefer and P. Ewart, "Laser diagnostics and minor species detection in combustion using resonant four-wave mixing," *Prog. Energy Combust. Sci.*, vol. 37, no. 5, pp. 525–564, Sep. 2011.

[35] V. Sick, "High speed imaging in fundamental and applied combustion research," *Proc. Combust. Inst.*, vol. 34, no. 2, pp. 3509–3530, Sep. 2012.

[36] H. Zhao and N. Ladommatos, "Optical Diagnostics for in-Cylinder Mixture Formation Measurements in IC Engines," *Science*, vol. 24, no. 98, pp. 297–336, 1998.

[37] H. Zhao and N. Ladommatos, *Engine Combustion Instrumentation and Diagnostics*.

SAE International, 2001.

[38] R. K. Hanson, “Applications of quantitative laser sensors to kinetics, propulsion and practical energy systems,” *Proc. Combust. Inst.*, vol. 33, no. 1, pp. 1–40, 2011.

[39] G. J. Nathan, P. a M. Kalt, Z. T. Alwahabi, B. B. Dally, P. R. Medwell, and Q. N. Chan, “Recent advances in the measurement of strongly radiating, turbulent reacting flows,” *Prog. Energy Combust. Sci.*, vol. 38, no. 1, pp. 41–61, 2012.

[40] M. a. Bolshov, Y. a. Kuritsyn, and Y. V. Romanovskii, “Tunable diode laser spectroscopy as a technique for combustion diagnostics,” *Spectrochim. Acta - Part B At. Spectrosc.*, vol. 106, pp. 45–66, 2015.

[41] P. Wright, N. Terzija, J. L. Davidson, S. Garcia-Castillo, C. Garcia-Stewart, S. Pegrum, S. Colbourne, P. Turner, S. D. Crossley, T. Litt, S. Murray, K. B. Ozanyan, and H. McCann, “High-speed chemical species tomography in a multi-cylinder automotive engine,” *Chem. Eng. J.*, vol. 158, no. 1, pp. 2–10, 2010.

[42] L. Ma, X. Li, S. T. Sanders, A. W. Caswell, S. Roy, D. H. Plemmons, and J. R. Gord, “50-kHz-rate 2D imaging of temperature and H 2 O concentration at the exhaust plane of a J85 engine using hyperspectral tomography,” *Opt. Express*, vol. 21, no. 1, pp. 1152–1162, 2013.

[43] L. S. Rothman, I. E. Gordon, Y. Babikov, a. Barbe, D. Chris Benner, P. F. Bernath, M. Birk, L. Bizzocchi, V. Boudon, L. R. Brown, a. Campargue, K. Chance, E. a. Cohen, L. H. Coudert, V. M. Devi, B. J. Drouin, a. Fayt, J. M. Flaud, R. R. Gamache, J. J. Harrison, J. M. Hartmann, C. Hill, J. T. Hodges, D. Jacquemart, a. Jolly, J. Lamouroux, R. J. Le Roy, G. Li, D. a. Long, O. M. Lyulin, C. J. Mackie, S. T. Massie, S. Mikhailenko, H. S. P. Müller, O. V. Naumenko, a. V. Nikitin, J. Orphal, V. Perevalov, a. Perrin, E. R. Polovtseva, C. Richard, M. a H. Smith, E. Starikova, K. Sung, S. Tashkun, J. Tennyson, G. C. Toon, V. G. Tyuterev, and G. Wagner, “The HITRAN2012 molecular spectroscopic database,” *J. Quant. Spectrosc. Radiat. Transf.*, vol. 130, pp. 4–50, 2013.

[44] L. S. Rothman, I. E. Gordon, R. J. Barber, H. Dothe, R. R. Gamache, a. Goldman, V. I. Perevalov, S. a. Tashkun, and J. Tennyson, “HITEMP, the high-temperature molecular spectroscopic database,” *J. Quant. Spectrosc. Radiat. Transf.*, vol. 111, no. 15, pp. 2139–2150, 2010.

[45] C. S. Goldenstein, J. B. Jeffries, and R. K. Hanson, “Diode laser measurements of linestrength and temperature-dependent lineshape parameters of H2O-, CO2-, and N2-perturbed H2O transitions near 2474 and 2482nm,” *J. Quant. Spectrosc. Radiat. Transf.*, vol. 130, pp. 100–111, 2013.

[46] T. N. Anderson, J. K. Magnuson, and R. P. Lucht, “Diode-laser-based sensor for ultraviolet absorption measurements of atomic mercury,” *Appl. Phys. B Lasers Opt.*, vol. 87, no. 2, pp. 341–353, 2007.

[47] Y. Arita and P. Ewart, “Multi-mode absorption spectroscopy,” *Opt. Commun.*, vol. 281, no. 9, pp. 2561–2566, 2008.

[48] Y. Arita, R. Stevens, and P. Ewart, “Multi-mode absorption spectroscopy of oxygen for measurement of concentration, temperature and pressure,” *Appl. Phys. B Lasers Opt.*, vol. 90, no. 2, pp. 205–211, 2008.

[49] Q. Gao, Y. Zhang, J. Yu, S. Wu, Z. Zhang, F. Zheng, X. Lou, and W. Guo, “Tunable multi-mode diode laser absorption spectroscopy for methane detection,” *Sensors Actuators, A Phys.*, vol. 199, pp. 106–110, 2013.

[50] J. H. Northern, a. W. J. Thompson, M. L. Hamilton, and P. Ewart, “Multi-species

detection using multi-mode absorption spectroscopy (MUMAS)," *Appl. Phys. B Lasers Opt.*, vol. 111, no. 4, pp. 627–635, 2013.

[51] P. Ewart, S. O'Hagan, H. Northern, B. Gras, C. Kim, M. Kim, charles Merritt, W. Bewley, C. canedy, I. Vurgaftman, and J. R. Meyer, "Multi-mode Absorption Spectroscopy with Mid-infrared Interband Cascade Lasers for Multi-species Sensing," in *Imaging and Applied Optics 2016*, 2016, p. LT2G.3.

[52] A. Thompson, H. Northern, B. Williams, M. Hamilton, and P. Ewart, "Simultaneous detection of CO_2 and CO in engine exhaust using multi-mode absorption spectroscopy, MUMAS," *Sensors Actuators, B Chem.*, vol. 198, pp. 309–315, 2014.

[53] F. Zhao and H. Hiroyasu, "The Applications of Laser Rayleigh Scattering to Combustion Diagnostics," *Prog. Energy Combust. Sci.*, vol. 19, pp. 447–485, 1993.

[54] B. Zhou, C. Brackmann, Z. Li, M. Aldén, and X. S. Bai, "Simultaneous multi-species and temperature visualization of premixed flames in the distributed reaction zone regime," *Proc. Combust. Inst.*, vol. 35, no. 2, pp. 1409–1416, 2015.

[55] J. Brübach, J. Zetterberg, A. Omrane, Z. S. Li, M. Aldén, and A. Dreizler, "Determination of surface normal temperature gradients using thermographic phosphors and filtered Rayleigh scattering," *Appl. Phys. B Lasers Opt.*, vol. 84, no. 3, pp. 537–541, 2006.

[56] D. Hofmann and A. Leipert, "Temperature field measurements in a sooting flame by filtered rayleigh scattering (FRS)," *Symp. Combust.*, vol. 26, no. 1, pp. 945–950, 1996.

[57] O. Dégardin, B. Renou, and a. M. Boukhalfa, "Simultaneous measurement of temperature and fuel mole fraction using acetone planar induced fluorescence and Rayleigh scattering in stratified flames," *Exp. Fluids*, vol. 40, no. 3, pp. 452–463, Jan. 2006.

[58] G. Sutton, a Levick, G. Edwards, and D. Greenhalgh, "A combustion temperature and species standard for the calibration of laser diagnostic techniques," *Combust. Flame*, vol. 147, no. 1–2, pp. 39–48, Oct. 2006.

[59] H. Ajrouche, A. Lo, P. Vervisch, and A. Cessou, "1D single-shot thermometry in flames by Spontaneous Raman Scattering through a fast electro-optical shutter," *17th Int. Symp. Appl. Laser Tech. to Fluid Mech. Lisbon, Port.*, pp. 1–17, 2014.

[60] G. Magnotti, D. Geyer, and R. S. Barlow, "Interference free spontaneous Raman spectroscopy for measurements in rich hydrocarbon flames," *Proc. Combust. Inst.*, vol. 35, no. 3, pp. 3765–3772, 2015.

[61] P. C. Hinze and P. C. Miles, "Quantitative Measurements of Residual and Fresh Charge Mixing in a Modern SI Engine Using Spontaneous Raman Scattering," *SAE Tech. Pap.*, 1999.

[62] G. Grünefeld, V. Beushausen, P. Andresen, and W. Hentschel, "Spatially resolved Raman scattering for multi-species and temperature analysis in technically applied combustion systems: Spray flame and four-cylinder in-line engine," *Appl. Phys. B Laser Opt.*, vol. 58, no. 4, pp. 333–342, 1994.

[63] M. Knapp, A. Luczak, V. Beushausen, W. Hentschel, P. Manz, and P. Andresen, "Polarization separated spatially resolved single laser shot multispecies analysis in the combustion chamber of a realistic SI engine with a tunable KrF excimer laser," *Symp. Combust.*, vol. 26, no. 2, pp. 2589–2596, 1996.

[64] J. R. Smith, "Temperature and Density Measurements in an Engine by Pulsed Raman Spectroscopy." SAE International , 1980.

[65] N. Fuhrmann, J. Brübach, and A. Dreizler, “Phosphor thermometry: A comparison of the luminescence lifetime and the intensity ratio approach,” *Proc. Combust. Inst.*, Jun. 2012.

[66] J. Brübach, C. Pflitsch, A. Dreizler, and B. Atakan, “On surface temperature measurements with thermographic phosphors: A review,” *Prog. Energy Combust. Sci.*, vol. 39, no. 1, pp. 37–60, 2013.

[67] G. Särner, M. Richter, and M. Aldén, “Two-dimensional thermometry using temperature-induced line shifts of ZnO:Zn and ZnO:Ga fluorescence.,” *Opt. Lett.*, vol. 33, no. 12, pp. 1327–1329, 2008.

[68] R. Hasegawa, I. Sakata, H. Yanagihara, B. Johansson, a. Omrane, and M. Aldén, “Two-dimensional gas-phase temperature measurements using phosphor thermometry,” *Appl. Phys. B Lasers Opt.*, vol. 88, no. 2, pp. 291–296, 2007.

[69] A. Omrane, P. Petersson, M. Aldén, and M. A. Linne, “Simultaneous 2D flow velocity and gas temperature measurements using thermographic phosphors,” *Appl. Phys. B Lasers Opt.*, vol. 92, no. 1, pp. 99–102, 2008.

[70] B. Fond, C. Abram, A. L. Heyes, A. M. Kempf, and F. Beyrau, “Simultaneous temperature, mixture fraction and velocity imaging in turbulent flows using thermographic phosphor tracer particles.,” *Opt. Express*, vol. 20, no. 20, pp. 22118–33, 2012.

[71] C. Abram, B. Fond, A. L. Heyes, and F. Beyrau, “High-speed planar thermometry and velocimetry using thermographic phosphor particles,” *Appl. Phys. B Lasers Opt.*, vol. 111, no. 2, pp. 155–160, 2013.

[72] K. Kohse-Höinghaus, “Laser techniques for the quantitative detection of reactive intermediates in combustion systems,” *Prog. Energy Combust. Sci.*, vol. 20, no. 3, pp. 203–279, 1994.

[73] J. D. Smith and V. Sick, “Crank-angle resolved imaging of biacetyl laser-induced fluorescence in an optical internal combustion engine,” *Appl. Phys. B Lasers Opt.*, vol. 81, no. 5, pp. 579–584, 2005.

[74] C. Morin, V. Modica, and P. Guibert, “Measurement of exhaust gas recirculation rate by laser-induced fluorescence in engine,” *Meas. Sci. Technol.*, vol. 19, no. 10, p. 105105, 2008.

[75] D. Han and R. R. Steeper, “An LIF equivalence ratio imaging technique for multicomponent fuels in an IC engine,” *Proc. Combust. Inst.*, vol. 29, no. 1, pp. 727–734, 2002.

[76] B. Williams, P. Ewart, X. Wang, R. Stone, H. Ma, H. Walmsley, R. Cracknell, R. Stevens, D. Richardson, H. Fu, and S. Wallace, “Quantitative planar laser-induced fluorescence imaging of multi-component fuel/air mixing in a firing gasoline-direct-injection engine: Effects of residual exhaust gas on quantitative PLIF,” *Combust. Flame*, vol. 157, no. 10, pp. 1866–1878, 2010.

[77] R. K. Hanson, “Planar Laser-Induced Fluorescence Imaging,” *J. Quant. Spectrosc. Radtat. Transf.*, vol. 40, no. 3, pp. 343–362, 1988.

[78] R. K. Hanson, J. M. Seitzman, and P. H. Paul, “Planar laser-fluorescence imaging of combustion gases,” *Appl. Phys. B Photophysics Laser Chem.*, vol. 50, no. 6, pp. 441–454, 1990.

[79] J. W. Daily, “Laser induced fluorescence spectroscopy in flames,” *Prog. Energy Combust. Sci.*, vol. 23, no. 2, pp. 133–199, 1997.

[80] F. Grisch and M. Orain, “Role of Planar Laser-Induced Fluorescence in combustion research,” *Aerosp. Lab*, no. 1, pp. 1–11, 2009.

[81] C. Schulz and V. Sick, “Tracer-LIF diagnostics: Quantitative measurement of fuel concentration, temperature and fuel/air ratio in practical combustion systems,” *Prog. Energy Combust. Sci.*, vol. 31, no. 1, pp. 75–121, Jan. 2005.

[82] J. E. Dec and J. O. Keller, “High speed thermometry using two-line atomic fluorescence,” *Symp. Combust.*, vol. 21, no. 1, pp. 1737–1745, 1988.

[83] R. C. Hilborn, “Einstein coefficients, cross sections, f values, dipole moments, and all that,” *Am. J. Phys*, vol. 50, pp. 982–986, 1982.

[84] M. C. Thurber, F. Grisch, B. J. Kirby, M. Votsmeier, and R. K. Hanson, “Measurements and modeling of acetone laser-induced fluorescence with implications for temperature-imaging diagnostics.,” *Appl. Opt.*, vol. 37, no. 21, pp. 4963–78, Jul. 1998.

[85] W. Koban, J. Koch, R. Hanson, and C. Schulz, “Absorption and fluorescence of toluene vapor at elevated temperatures,” *Phys. Chem. Chem. Phys.*, 2004.

[86] C. F. Kaminski, J. Engström, and M. Aldén, “Quasi-instantaneous two-dimensional temperature measurements in a spark ignition engine using 2-line atomic fluorescence,” *Symp. Combust.*, vol. 27, no. 1, pp. 85–93, 1998.

[87] J. Engström, C. F. Kaminski, and M. Aldén, “Experimental Investigations of Flow and Temperature Fields in an SI Engine and Comparison with Numerical Analysis,” no. 724, 1999.

[88] R. Whiddon, B. Zhou, J. Borggren, M. Aldén, and Z. S. Li, “Vapor phase tri-methyl-indium seeding system suitable for high temperature spectroscopy and thermometry,” *Rev. Sci. Instrum.*, vol. 86, no. 9, 2015.

[89] J. Borggren, I. S. Burns, A.-L. Sahlberg, M. Aldén, and Z. Li, “Temperature imaging in low-pressure flames using diode laser two-line atomic fluorescence employing a novel indium seeding technique,” *Appl. Phys. B Lasers Opt.*, vol. 122, no. 3, 2016.

[90] B. Peterson, E. Baum, B. Böhm, and A. Dreizler, “Early flame propagation in a spark-ignition engine measured with quasi 4D-diagnostics,” *Proc. Combust. Inst.*, vol. 35, no. 3, pp. 3829–3837, 2015.

[91] L. A. Melton and J. F. Verdieck, “Vapor / Liquid Visualization in Fuel Sprays,” *Twent. Symp. Combust. Combust. Inst.*, pp. 1283–1290, 1984.

[92] M. C. Thurber and R. K. Hanson, “Pressure and composition dependences of acetone laser-induced fluorescence with excitation at 248, 266, and 308 nm,” *Appl. Phys. B Lasers Opt.*, vol. 69, no. 3, pp. 229–240, 1999.

[93] M. Thurber, “Acetone laser-induced fluorescence for temperature and multiparameter imaging in gaseous flows,” *Stanford Univ.*, no. March, 1999.

[94] J. W. F. Grossmann, P. B. Monkhouse, M. Ridder, V. Sick, “Temperature and pressure dependences of the laser-induced fluorescence of gas phase acetone and 3-pentanone,” *Appl. Phys. B*, vol. 253, no. 62, pp. 249–253, 1996.

[95] J. D. Koch and R. K. Hanson, “Temperature and excitation wavelength dependencies of 3-pentanone absorption and fluorescence for PLIF applications,” *Appl. Phys. B Lasers Opt.*, vol. 76, no. 3, pp. 319–324, 2003.

[96] W. Koban, “Photophysical characterization of toluene and 3-pentanone for quantitative imaging of fuel/air ratio and temperature in combustion systems,” PhD Thesis, Ruperto-Carola University of Heidelberg, Germany, 2005.

[97] W. Koban, J. D. Koch, V. Sick, N. Wermuth, R. K. Hanson, and C. Schulz, “Predicting LIF signal strength for toluene and 3-pentanone under engine-related temperature and pressure conditions,” *Proc. Combust. Inst.*, vol. 30, no. 1, pp. 1545–1553, Jan. 2005.

[98] P. Guibert, V. Modica, and C. Morin, “Influence of pressure, temperature and gas phase composition on biacetyl laser-induced fluorescence,” *Exp. Fluids*, vol. 40, no. 2, pp. 245–256, 2006.

[99] W. Koban, J. Koch, R. Hanson, and C. Schulz, “Oxygen quenching of toluene fluorescence at elevated temperatures,” *Appl. Phys. B*, vol. 80, pp. 777–784, 2005.

[100] J. Koch, “Fuel tracer photophysics for quantitative planar laser-induced fluorescence,” PhD Thesis, Stanford, 2005.

[101] R. Devillers, G. Bruneaux, and C. Schulz, “Investigation of toluene LIF at high pressure and high temperature in an optical engine,” *Appl. Phys. B Lasers Opt.*, pp. 735–739, 2009.

[102] W. Koban, J. D. Koch, R. K. Hanson, and C. Schulz, “Toluene LIF at elevated temperatures: Implications for fuel-air ratio measurements,” *Appl. Phys. B Lasers Opt.*, vol. 80, no. 2, pp. 147–150, 2005.

[103] B. Peterson, E. Baum, B. Böhm, V. Sick, and A. Dreizler, “Evaluation of toluene LIF thermometry detection strategies applied in an internal combustion engine,” *Appl. Phys. B*, vol. 117, pp. 151–175, 2014.

[104] S. A. Kaiser, M. Schild, and C. Schulz, “Thermal stratification in an internal combustion engine due to wall heat transfer measured by laser-induced fluorescence,” *Proc. Combust. Inst.*, Jun. 2012.

[105] M. C. Thurber and R. K. Hanson, “Simultaneous imaging of temperature and mole fraction using acetone planar laser-induced fluorescence,” *Exp. Fluids*, vol. 30, no. 1, pp. 93–101, Jan. 2001.

[106] S. Einecke, C. Schulz, and V. Sick, “Measurement of temperature, fuel concentration and equivalence ratio fields using tracer LIF in IC engine combustion,” *Appl. Phys. B Lasers Opt.*, vol. 71, no. 5, pp. 717–723, Nov. 2000.

[107] D. A. Rothamer, J. A. Snyder, R. K. Hanson, and R. R. Steeper, “Optimization of a tracer-based PLIF diagnostic for simultaneous imaging of EGR and temperature in IC engines,” *Appl. Phys. B*, vol. 99, no. 1–2, pp. 371–384, Nov. 2009.

[108] T. Fujikawa, K. Fukui, Y. Hattori, and K. Akihama, “2-D Temperature Measurements of Unburned Gas Mixture in an Engine by Two-line Excitation LIF Technique,” no. 724, 2006.

[109] M. Luong, R. Zhang, C. Schulz, and V. Sick, “Toluene laser-induced fluorescence for in-cylinder temperature imaging in internal combustion engines,” *Appl. Phys. B*, vol. 91, no. 3–4, pp. 669–675, Apr. 2008.

[110] M. Luong, W. Koban, and C. Schulz, “Novel strategies for imaging temperature distribution using Toluene LIF,” *J. Phys. Conf. Ser.*, vol. 45, pp. 133–139, Jul. 2006.

[111] B. Peterson, E. Baum, B. Böhm, V. Sick, and A. Dreizler, “High-speed PIV and LIF imaging of temperature stratification in an internal combustion engine,” *Proc. Combust. Inst.*, vol. 34, no. 2, pp. 3653–3660, Jul. 2013.

[112] J. Snyder, N. Dronniou, J. Dec, and R. Hanson, “PLIF Measurements of Thermal Stratification in an HCCI Engine under Fired Operation,” *SAE Int. J. Engines*, vol. 4, no. 1, pp. 1669–1688, 2011.

[113] M. Löffler, F. Beyrau, and A. Leipertz, “Acetone laser-induced fluorescence behavior for the simultaneous quantification of temperature and residual gas distribution in fired spark-ignition engines.,” *Appl. Opt.*, vol. 49, no. 1, pp. 37–49, Jan. 2010.

[114] S. Pfadler, F. Beyrau, M. Löffler, and A. Leipertz, “Application of a beam homogenizer to planar laser diagnostics.,” *Opt. Express*, vol. 14, no. 22, pp. 10171–10180, 2006.

[115] M. Cundy, P. Trunk, A. Dreizler, and V. Sick, “Gas-phase toluene LIF temperature imaging near surfaces at 10 kHz,” *Exp. Fluids*, vol. 51, no. 5, pp. 1169–1176, Jun. 2011.

[116] E. Berrocal, “Structured Laser Illumination Planar Imaging : New horizons for the study of spray dynamics , thermometry and droplet sizing,” *18th Int. Symp. Appl. Laser Imaging Tech. to Fluid Mech.*, no. August, 2016.

[117] Y. N. Mishra, S. Polster, E. Kristensson, A. Nada, F. Jouda, and E. Berrocal, “Sprays thermometry using two color LIF and SLIPI,” in *ICLASS 2015 - the 13th international conference on liquid atomization and spray systems*, 2015, pp. 1–8.

[118] J. A. Shirley, J. Hall, and A. C. Eckbreth, “Folded BOXCARS for rotational Raman studies,” vol. 5, no. 9, pp. 380–382, 1980.

[119] S. Roy, J. R. Gord, and A. K. Patnaik, “Recent advances in coherent anti-Stokes Raman scattering spectroscopy: Fundamental developments and applications in reacting flows,” *Prog. Energy Combust. Sci.*, vol. 36, no. 2, pp. 280–306, Apr. 2010.

[120] A. C. Eckbreth, “BOXCARS: Crossed-beam phase-matched CARS generation in gases,” *Appl. Phys. Lett.*, vol. 32, no. 7, pp. 421–423, 1978.

[121] P. Ewart, “A modeless, variable bandwidth, tunable laser,” *Opt. Commun.*, vol. 55, no. 2, pp. 124–126, 1985.

[122] P. Snowdon, S. M. Skippon, and P. Ewart, “Rapid communications,” *Appl. Opt.*, vol. 30, no. 9, pp. 1008–1010, 1991.

[123] M. Aldén, P. E. Bengtsson, H. Edner, S. Kröll, and D. Nilsson, “Rotational CARS: a comparison of different techniques with emphasis on accuracy in temperature determination.,” *Appl. Opt.*, vol. 28, no. 15, pp. 3206–3219, 1989.

[124] D. R. Snelling, R. A. Sawchuk, and T. Parameswaran, “Noise in single-shot broadband coherent anti-Stokes Raman spectroscopy that employs a modeless dye laser.,” *Appl. Opt.*, vol. 33, no. 36, pp. 8295–301, Dec. 1994.

[125] T. Dreier, B. Lange, J. Wolfrum, and M. Zahn, “Determination of temperature and concentration of molecular nitrogen, oxygen and methane with coherent anti-stokes raman scattering,” *Appl. Phys. B Photophysics Laser Chem.*, vol. 45, no. 3, pp. 183–190, 1988.

[126] T. Seeger and A. Leipertz, “Experimental comparison of single-shot broadband vibrational and dual-broadband pure rotational coherent anti-Stokes Raman scattering in hot air.,” *Appl. Opt.*, vol. 35, no. 15, pp. 2665–71, 1996.

[127] O. L. Gülder, D. R. Snelling, and R. A. Sawchuk, “Influence of hydrogen addition to fuel on temperature field and soot formation in diffusion flames,” *Symp. Combust.*, vol. 26, no. 2, pp. 2351–2358, 1996.

[128] P. Bengtsson, L. Martinsson, M. A. N, B. Johansson, B. Lassesson, K. Marforio, and G. Lundholm, “Dual-broadband rotational cars measurements in an IC engine,” *Twenty-Fifth Symp. Combust. Combust. Inst.*, vol. 25, no. 1, pp. 1735–1742, 1994.

[129] C. Brackmann, J. Bood, M. Afzelius, and P.-E. Bengtsson, “Thermometry in internal combustion engines via dual-broadband rotational coherent anti-Stokes Raman

spectroscopy," *Meas. Sci. Technol.*, vol. 15, no. 3, pp. R13–R25, 2004.

[130] F. Beyrau, A. Bräuer, T. Seeger, and A. Leipertz, "Gas-phase temperature measurement in the vaporizing spray of a gasoline direct-injection injector by use of pure rotational coherent anti-Stokes Raman scattering.," *Opt. Lett.*, vol. 29, no. 3, pp. 247–9, Mar. 2004.

[131] A. Birkigt, K. Michels, J. Theobald, T. Seeger, Y. Gao, M. C. Weikl, M. Wensing, and A. Leipertz, "Investigation of compression temperature in highly charged spark-ignition engines," *Int. J. Engine Res.*, vol. 12, no. 3, pp. 282–292, 2011.

[132] S. Hildenbrand, S. Staudacher, D. Brüggemann, F. Beyrau, M. C. Weikl, T. Seeger, and A. Leipertz, "Numerical and experimental study of the vaporization cooling in gasoline direct injection sprays," *Proc. Combust. Inst.*, vol. 31 II, pp. 3067–3073, 2007.

[133] M. C. Weikl, F. Beyrau, and A. Leipertz, "Simultaneous temperature and exhaust-gas recirculation-measurements in a homogeneous charge-compression ignition engine by use of pure rotational coherent anti-Stokes Raman spectroscopy.," *Appl. Opt.*, vol. 45, no. 15, pp. 3646–51, May 2006.

[134] B. Attal-Tretout, P. Berlemont, and J. P. Taran, "Three-colour CARS spectroscopy of the OH radical at triple resonance," *Mol. Phys.*, vol. 70, no. 1, 1990.

[135] S. A. J. Druet, B. Attal, T. K. Gustafson, and J. P. Taran, "Electronic resonance enhancement of coherent anti-Stokes Raman scattering," *Phys. Rev. A*, vol. 18, no. 4, pp. 1529–1557, 1978.

[136] J. P. Kuehner, S. V Naik, W. D. Kulatilaka, N. Chai, N. M. Laurendeau, R. P. Lucht, M. O. Scully, S. Roy, A. K. Patnaik, and J. R. Gord, "Perturbative theory and modeling of electronic-resonance-enhanced coherent anti-Stokes Raman scattering spectroscopy of nitric oxide.," *J. Chem. Phys.*, vol. 128, no. 17, p. 174308, 2008.

[137] W. D. Kulatilaka, N. Chai, S. V Naik, N. M. Laurendeau, R. P. Lucht, J. P. Kuehner, S. Roy, and J. R. Gord, "Measurement of nitric oxide concentrations in flames by using electronic-resonance-enhanced coherent anti-Stokes Raman scattering," *Opt. Lett.*, vol. 31, no. 22, pp. 3357–3359, 2006.

[138] J. R. Gord, T. R. Meyer, and S. Roy, "Applications of ultrafast lasers for optical measurements in combusting flows.," *Annu. Rev. Anal. Chem. (Palo Alto. Calif).*, vol. 1, pp. 663–87, 2008.

[139] D. E. Spence, P. N. Kean, and W. Sibbett, "60-fsec pulse generation from a self-mode-locked Ti : sapphire laser," vol. 16, no. 1, pp. 42–44, 1991.

[140] M. T. Asaki, C. Huang, D. Garvey, J. Zhou, H. C. Kapteyn, and M. M. Murnane, "Generation of 11-fs pulses from a self-mode-locked Ti : sapphire laser," vol. 18, no. 12, pp. 977–979, 1993.

[141] A. I. Ferguson and G. P. A. Malcolm, "Mode-Locked Solid State Lasers," in *Solid State Lasers: New Developments and Applications*, M. Inguscio and R. Wallenstein, Eds. Boston, MA: Springer US, 1993, pp. 29–44.

[142] R. P. Lucht, S. Roy, T. R. Meyer, and J. R. Gord, "Femtosecond coherent anti-Stokes Raman scattering measurement of gas temperatures from frequency-spread dephasing of the Raman coherence," *Appl. Phys. Lett.*, vol. 89, no. 25, pp. 2004–2007, 2006.

[143] S. Roy, W. D. Kulatilaka, D. R. Richardson, R. P. Lucht, and J. R. Gord, "Gas-phase single-shot thermometry at 1 kHz using fs-CARS spectroscopy," *Opt. Lett.*, vol. 34, no. 24, pp. 3857–3859, 2009.

[144] J. Jonuscheit, A. Thumann, M. Schenk, T. Seeger, and A. Leipertz, "One-dimensional

vibrational coherent anti-Stokes Raman-scattering thermometry," *Opt. Lett.*, vol. 21, no. 19, pp. 1532–1534, 1996.

[145] A. Bohlin and C. J. Kliewer, "Communication: Two-dimensional gas-phase coherent anti-Stokes Raman spectroscopy (2D-CARS): Simultaneous planar imaging and multiplex spectroscopy in a single laser shot," *J. Chem. Phys.*, vol. 138, no. 22, 2013.

[146] A. Bohlin and C. J. Kliewer, "Diagnostic imaging in flames with instantaneous planar coherent Raman spectroscopy," *J. Phys. Chem. Lett.*, vol. 5, no. 7, pp. 1243–1248, 2014.

[147] A. Bohlin and C. J. Kliewer, "Single-shot hyperspectral coherent Raman planar imaging in the range 0-4200 cm-1," *Appl. Phys. Lett.*, vol. 105, no. 16, 2014.

[148] A. Bohlin and C. J. Kliewer, "Two-beam ultrabroadband coherent anti-Stokes Raman spectroscopy for high resolution gas-phase multiplex imaging," *Appl. Phys. Lett.*, vol. 104, no. 3, 2014.

[149] A. Bohlin, B. D. Patterson, and C. J. Kliewer, "Communication: Simplified two-beam rotational CARS signal generation demonstrated in 1D," *J. Chem. Phys.*, vol. 138, no. 8, 2013.

[150] C. Wieman and T. W. Hansch, "Doppler-free laser polarization spectroscopy," *Phys. Rev. Lett.*, vol. 36, no. 20, pp. 1170–1173, 1976.

[151] A. Suvernev, A. Dreizler, T. Dreier, and J. Wolfrum, "Polarisation-Spectroscopic Measurement and Spectral Simulation of OH (A2Σ–X2Π) and NH (A3Π–X3Σ) Transitions in Atmospheric Pressure Flames," vol. 427, pp. 421–427, 1995.

[152] M. J. New, P. Ewart, A. Dreizler, and T. Dreier, "Multiplex polarization spectroscopy of OH for flame thermometry," *Appl. Phys. B*, vol. 65, no. 4–5, pp. 633–637, 1997.

[153] K. Nyholm, R. Fritzon, and M. Alden, "Single-pulse two-dimensional temperature imaging in flames by degenerate four-wave mixing and polarization spectroscopy," vol. 43, pp. 37–43, 1994.

[154] S. Roy, R. P. Lucht, and A. McIlroy, "Mid-infrared polarization spectroscopy of carbon dioxide," *Appl. Phys. B Lasers Opt.*, vol. 75, no. 8, pp. 875–882, 2002.

[155] T. A. Reichardt and R. P. Lucht, "Theoretical calculation of line shapes and saturation effects in polarization spectroscopy," *J. Chem. Phys.*, vol. 109, no. 14, pp. 5830–5843, 1998.

[156] R. L. Farrow and D. J. Rakestraw, "Detection of Trace Molecular Species Using Degenerate Four-Wave Mixing," *Science*, vol. 257, no. September, 1992.

[157] P. Ewart and S. V. O. Leary, "Detection of OH in a flame by degenerate four-wave mixing," vol. 11, no. 5, pp. 279–281, 1986.

[158] T. Dreier and D. J. Rakestraw, "Measurement of OH rotational temperatures in a flame using degenerate four-wave mixing.," *Opt. Lett.*, vol. 15, no. 1, pp. 72–74, 1990.

[159] K. Nyholm, M. Kaivola, and C. G. Aminoff, "Detection of C_2 and temperature measurement in a flame by using degenerate four-wave mixing in a forward geometry," *Opt. Commun.*, vol. 107, pp. 406–410, 1993.

[160] A. J. Grant, P. Ewart, and C. R. Stone, "Detection of NO in a spark-ignition research engine using degenerate four-wave mixing," *Appl. Phys. B Lasers Opt.*, vol. 74, no. 1, pp. 105–110, 2002.

[161] R. Stevens, P. Ewart, H. Ma, and C. R. Stone, "Measurement of nitric oxide concentration in a spark-ignition engine using degenerate four-wave mixing," *Combust.*

Flame, vol. 148, no. 4, pp. 223–233, 2007.

[162] R. L. Abrams and R. C. Lind, "Degenerate four-wave mixing in absorbing media.," *Opt. Lett.*, vol. 2, no. 4, p. 94, 1978.

[163] R. P. Lucht, R. L. Farrow, and D. J. Rakestraw, "Saturation Effects in Gas-Phase Degenerate 4-Wave-Mixing Spectroscopy - Nonperturbative Calculations," *J. Opt. Soc. Am. B-Optical Phys.*, vol. 10, no. 9, pp. 1508–1520, 1993.

[164] T. A. Reichardt and R. P. Lucht, "Effect of Doppler broadening on quantitative concentration measurements with degenerate four-wave mixing spectroscopy," *J. Opt. Soc. Am. B (Optical Physics) Publ Opt. Soc. Am. June*, vol. 13, no. 6, pp. 1107–1119, 1996.

[165] P. M. Danehy, E. J. Friedman-Hill, R. P. Lucht, and R. L. Farrow, "The effects of collisional quenching on degenerate four-wave mixing," *Appl. Phys. B Photophysics Laser Chem.*, vol. 57, no. 4, pp. 243–248, 1993.

[166] T. A. Reichardt and R. P. Lucht, "Interaction of closely spaced resonances in degenerate four-wave-mixing spectroscopy," *J. Opt. Soc. Am. B Opt. Phys.*, vol. 14, no. 10, pp. 2449–2458, 1997.

[167] T. A. Reichardt and R. P. Lucht, "Resonant degenerate four-wave mixing spectroscopy of transitions with degenerate energy levels: Saturation and polarization effects," *J. Chem. Phys.*, vol. 111, no. 22, p. 10008, 1999.

[168] T. A. Reichardt, R. P. Lucht, P. M. Danehy, and R. L. Farrow, "Theoretical investigation of the forward phase-matched geometry for degenerate four-wave mixing spectroscopy," *J. Opt. Soc. Am. B*, vol. 15, no. 10, p. 2566, 1998.

[169] R. T. Bratfalean, G. M. Lloyd, and P. Ewart, "Degenerate four-wave mixing for arbitrary pump and probe intensities," *J. Opt. Soc. Am. B*, vol. 16, no. 6, p. 952, 1999.

[170] G. M. Lloyd, I. G. Hughes, R. Bratfalean, and P. Ewart, "Broadband degenerate four-wave mixing of OH for flame thermometry," *Appl. Phys. B (Lasers Opt.*, vol. B67, no. 1, pp. 107–113, 1998.

[171] P. Ewart and P. Snowdon, "Multiplex degenerate four-wave mixing in a flame.," *Opt. Lett.*, vol. 15, no. 23, pp. 1403–5, 1990.

[172] B. Yip, P. M. Danehy, and R. K. Hanson, "Degenerate four-wave mixing temperature measurements in a flame," vol. 17, no. 10, pp. 751–753, 1992.

[173] C. F. Kaminski, I. G. Hughes, G. M. Lloyd, and P. Ewart, "Thermometry of an oxy-acetylene flame using multiplex degenerate four-wave mixing of C_2," *Appl. Phys. B-Lasers Opt.*, vol. 62, no. 1, pp. 39–44, 1996.

[174] S. Williams, R. N. Zare, and L. A. Rahn, "Reduction of degenerate four-wave mixing spectra to relative populations I. Weak-field limit," *J. Chem. Phys.*, vol. 101, no. 1994, pp. 1093–1107, 1994.

[175] P. Ewart, P. Snowdon, and I. Magnusson, "Two-dimensional phase-conjugate imaging of atomic distributions in flames by degenerate four-wave mixing.," *Opt. Lett.*, vol. 14, no. 11, pp. 563–5, 1989.

[176] D. J. Rakestraw, R. L. Farrow, and T. Dreier, "Two-dimensional imaging of OH in flames by degenerate four-wave mixing.," *Opt. Lett.*, vol. 15, no. 12, pp. 709–711, 1990.

[177] P. Ewart and M. Kaczmarek, "Two-dimensional mapping of temperature in a flame by degenerate four-wave mixing in OH," vol. 30, no. 27, pp. 3996–3999, 1991.

[178] P. Ewart, P. G. R. Smith, and R. B. Williams, “Imaging of trace species distributions by degenerate four-wave mixing: diffraction effects, spatial resolution and image referencing,” vol. 36, no. 24, 1997.

[179] K. A. Nelson, D. R. Lutz, M. D. Fayer, and L. Madison, “Laser-induced phonon spectroscopy. Optical generation of ultrasonic waves and investigation of electronic excited-state interactions in solids,” *Phys. Rev. B*, vol. 24, no. 6, p. 3261, 1981.

[180] H. J. Eichler, “Laser-induced Grating Phenomena,” *Opt. Acta Int. J. Opt.*, vol. 24, no. March, pp. 631–642, 1977.

[181] H. J. Eichler, P. Gunter, and D. W. Pohl, *Laser-induced dynamic gratings*. Berlin: Springer-Verlag, 1986.

[182] E. B. Cummings, “Laser-induced thermal acoustics: simple accurate gas measurements.,” *Opt. Lett.*, vol. 19, no. 17, pp. 1361–1363, 1994.

[183] E. B. Cummings, I. A. Leyva, and H. G. Hornung, “Laser-induced thermal acoustics (LITA) signals from finite beams.,” *Appl. Opt.*, vol. 34, no. 18, pp. 3290–302, 1995.

[184] S. Williams, L. A. Rahn, P. H. Paul, J. W. Forsman, and R. N. Zare, “Laser-induced thermal grating effects in flames.,” *Opt. Lett.*, vol. 19, no. 21, pp. 1681–1683, 1994.

[185] R. Stevens and P. Ewart, “Single-shot measurement of temperature and pressure using laser-induced thermal gratings with a long probe pulse,” *Appl. Phys. B Lasers Opt.*, vol. 78, no. 1, pp. 111–117, Jan. 2004.

[186] H. Latzel, A. Dreizler, T. Dreier, J. Heinze, M. Dillmann, W. Stricker, G. M. Lloyd, and P. Ewart, “Thermal grating and broadband degenerate four-wave mixing spectroscopy of OH in high-pressure flames,” *Appl. Phys. B Lasers Opt.*, vol. 67, pp. 667–673, 1998.

[187] R. C. Hart, G. C. Herring, and R. J. Balla, “Pressure measurement in supersonic air flow by differential absorptive laser-induced thermal acoustics.,” *Opt. Lett.*, vol. 32, no. 12, pp. 1689–91, 2007.

[188] F. Förster and B. Weigand, “Characterization of a heterodyne LITA setup for simultaneous flow velocity and speed of sound measurements,” *19th AIAA Int. Sp. Planes Hypersonic Syst. Technol. Conf.*, 2014.

[189] D. J. Walker, R. B. Williams, and P. Ewart, “Thermal grating velocimetry.,” *Opt. Lett.*, vol. 23, no. 16, pp. 1316–1318, 1998.

[190] R. C. Hart, R. J. Balla, and G. C. Herring, “Simultaneous velocimetry and thermometry of air by use of nonresonant heterodyned laser-induced thermal acoustics.,” *Appl. Opt.*, vol. 40, no. 6, pp. 965–968, 2001.

[191] M. Neracher and W. Hubschmid, “Heterodyne-detected electrostrictive laser-induced gratings for gas-flow diagnostics,” *Appl. Phys. B Lasers Opt.*, vol. 79, no. 6, pp. 783–791, 2004.

[192] D. N. Kozlov, “Simultaneous characterization of flow velocity and temperature fields in a gas jet by use of electrostrictive laser-induced gratings,” *Appl. Phys. B Lasers Opt.*, vol. 80, no. 3, pp. 377–387, 2005.

[193] M. S. Brown and W. L. Roberts, “Single-Point Thermometry in High-Pressure, Sooting, Premixed Combustion Environments,” *J. Propuls. Power*, vol. 15, no. 1, pp. 119–127, 1999.

[194] R. C. Hart, R. J. Balla, and G. C. Herring, “Nonresonant referenced laser-induced thermal acoustics thermometry in air.,” *Appl. Opt.*, vol. 38, no. 3, pp. 577–584, 1999.

[195] S. Schlamp and T. Sobota, “Measuring concentrations with laser-induced thermalization and electrostriction gratings,” *Exp. Fluids*, vol. 32, no. 6, pp. 683–688, 2002.

[196] B. Hemmerling, A. Stampanoni-Panariello, P. Radi, A. Kouzov, and D. Kozlov, “Novel non-linear optical techniques for diagnostics: laser-induced gratings and two-colour four-wave mixing.,” *Comptes Rendus L Acad. Des Sci. Ser. Iv Phys. Astrophys.*, vol. 2, no. 7, pp. 1001–1012, 2001.

[197] B. Hemmerling, D. N. Kozlov, O. M. Stel’makh, and B. Attal-Trétout, “Diagnostics of water-containing gas mixtures using thermal laser-induced gratings,” *Chem. Phys.*, vol. 320, no. 2–3, pp. 103–117, 2006.

[198] T. Seeger, J. Kiefer, M. C. Weikl, A. Leipertz, and D. N. Kozlov, “Time-resolved measurement of the local equivalence ratio in a gaseous propane injection process using laser-induced gratings.,” *Opt. Express*, vol. 14, no. 26, pp. 12994–13000, 2006.

[199] T. Seeger, A. Leipertz, D. N. Kozlov, and J. Kiefer, “Local fuel concentration measurements for mixture formation diagnostics using diffraction by laser-induced gratings in comparison to spontaneous Raman scattering,” *J. Raman Spectrosc.*, vol. 39, no. 6, pp. 711–721, 2008.

[200] A.-L. Sahlberg, D. Hot, J. Kiefer, and Z. Li, “Mid-infrared laser-induced thermal grating spectroscopy in flames,” *Proc. Combust. Inst.*, no. July, 2016.

[201] A.-L. Sahlberg, J. Kiefer, M. Alden, and Z. Li, “Mid-infrared pumped laser-induced thermal grating spectroscopy for detection of acetylene in the visible spectral range,” *Appl. Spectrosc.*, vol. 70, no. 6, 2016.

[202] A. Stampanoni-Panariello, D. N. Kozlov, P. P. Radi, and B. Hemmerling, “Gas phase diagnostics by laser-induced gratings I. Theory,” *Appl. Phys. B Lasers Opt.*, vol. 81, no. 1, pp. 101–111, 2005.

[203] A. Stampanoni-Panariello, D. N. Kozlov, P. P. Radi, and B. Hemmerling, “Gas-phase diagnostics by laser-induced gratings II. Experiments,” *Appl. Phys. B Lasers Opt.*, vol. 81, no. 1, pp. 113–129, 2005.

[204] A. Carmen and S. Panariello, “Laser-Induced Gratings in the Gas Phase : Formation Mechanisms and Applications for Diagnostics,” no. 14972, 2003.

[205] W. Hubschmid, R. Bombach, B. Hemmerling, and A. Stampanoni-Panariello, “Sound-velocity measurements in gases by laser-induced electrostrictive gratings,” *Appl. Phys. B Laser Opt.*, vol. 62, no. 1, pp. 103–107, 1996.

[206] A. Stampanoni-Panariello, B. Hemmerling, and W. Hubschmid, “Temperature measurements in gases using laser-induced electrostrictive gratings,” *Appl. Phys. B Lasers Opt.*, vol. 67, no. 1, pp. 125–130, 1998.

[207] T. Sander, P. Altenhöfer, and C. Mundt, “Development of Laser-Induced Grating Spectroscopy for Application in Shock Tunnels,” *J. Thermophys. Heat Transf.*, vol. 28, no. 1, pp. 27–31, 2014.

[208] B. Hemmerling, D. N. Kozlov, and A. Stampanoni-Panariello, “Temperature and flow-velocity measurements by use of laser-induced electrostrictive gratings.,” *Opt. Lett.*, vol. 25, no. 18, pp. 1340–1342, 2000.

[209] S. Schlamp, H. G. Hornung, T. H. Sobota, and E. B. Cummings, “Accuracy and uncertainty of single-shot, nonresonant laser-induced thermal acoustics.,” *Appl. Opt.*, vol. 39, no. 30, pp. 5477–81, 2000.

[210] P. Altenhofer, T. Sander, and C. Mundt, “Preliminary Experiments for Temperature

Measurements in Shock Tunnels Using Laser-Induced Electrostrictive Gratings," no. April, 2011.

[211] S. L. Marple, "Digital spectral analysis with applications," Englewood Cliffs, NJ: Prentice-Hall, 1987.

[212] M. Edwards, "The effect of uncertainty in composition on Laser-Induced Grating thermometry .," MPhil Thesis, University of Oxford, 2011.

[213] N. C. Wijeyasinghe, "Laser-Induced Grating Spectroscopy in Non-Uniform Temperature Fields and Flames," MPhil Thesis, University of Oxford, 2013.

[214] J. Harris, "On the Use of Windows with the Discrete for Harmonic Analysis Fourier Transform," *Proc. IEEE*, vol. 66, no. 1, pp. 51–83, 1978.

[215] J. Kiefer, A.-L. Sahlberg, D. Hot, M. Aldén, and Z. Li, "Misalignment Effects in Laser-Induced Grating Experiments," *Appl. Spectrosc.* , Jun. 2016.

[216] Hamamatsu Photonics K.K. Editorial committee, *Photomultiplier Tubes, Basics and Applications*, 3rd ed. Hamamatsu Photonics K.K. Electron Tube Division, 2007.

[217] J. Crosley and D. R. Luque, "LIFBASE (version 1.5)," vol. 9. SRI International, 1999.

[218] G. Kychakoff, R. D. Howe, and R. K. Hanson, "Quantitative flow visualization technique for measurements in combustion gases.," *Appl. Opt.*, vol. 23, no. 5, pp. 704–712, Mar. 1984.

[219] Elmhurst College, "What is Gasoline?," *Virtual Chemb.*, pp. 1–2, 2003.

[220] J. Heicklen, "The Fluorescence and Phosphorescence of Biacetyl Vapor and Acetone Vapor," *J. Am. Chem. Soc.*, vol. 81, no. 15, pp. 3863–3866, 1959.

[221] R. G. Brown Phillips, D., "Quenching of the first excited singlet state of substituted benzenes by molecular oxygen," *Trans. Farad. Soc. II*, vol. 70, p. 630, 1974.

[222] D. Dussault and P. Hoess, "Noise performance comparison of ICCD with CCD and EMCCD cameras," *Proc. SPIE*, vol. 5563, pp. 195–204, 2004.

[223] D. J. Denvir and E. Conroy, "Electron-multiplying CCD: the new ICCD," *Proc. SPIE*, vol. 4796, no. Cic, pp. 164–174, 2003.

[224] R. S. Longhurst, *Geometrical and Physical Optics*. Longman, 1986.

[225] F. D'Almeida, "Nonlinear diffusion filtering toolbox." MATLAB toolbox, DEE/Federal University of Bahia, Brazil, 2004.

[226] J. de Vries, "Lensdistort.m Barrel and pincushion lens distortion correction." http://uk.mathworks.com/matlabcentral/fileexchange/, 2012.

[227] A. Natan, "FastPeakFind.m Fast 2D peak finder." http://uk.mathworks.com/matlabcentral/fileexchange/, 2013.

[228] B. Hemmerling and A. Stampanoni-Panariello, "Imaging of flames and cold flows in air by diffraction from a laser-induced grating," *Appl. Phys. B Photophysics Laser Chem.*, vol. 57, no. 4, pp. 281–285, 1993.

[229] R. Stevens and P. Ewart, "Simultaneous single-shot measurement of temperature and pressure along a one-dimensional line by use of laser-induced thermal grating spectroscopy.," *Opt. Lett.*, vol. 31, no. 8, pp. 1055–7, Apr. 2006.

[230] X. Guan, "Initial streak camera testing for 1D-LITGS." Unpublished work - University of Oxford, 2012.

[231] Hamamatsu, “Guide to Streak Cameras - Hamamatsu,” *Online*, vol. i, no. 116, pp. 1–6, 2008.

[232] H. Chen, D. L. S. Hung, M. Xu, and J. Zhong, “Analyzing the Cycle-To-Cycle Variations of Pulsing Spray Characteristics By Means of the Proper Orthogonal Decomposition,” *At. Sprays*, vol. 23, no. 7, pp. 623–641, 2013.

[233] H. Chen, D. L. Reuss, and V. Sick, “On the use and interpretation of proper orthogonal decomposition of in-cylinder engine flows,” *Meas. Sci. Technol.*, vol. 23, no. 8, p. 85302, 2012.

[234] J. Polezhaev, “Transpiration cooling for blades of high temperatures gas turbine,” *Energy Convers. Manag.*, vol. 38, no. 10–13, pp. 1123–1133, 1997.

[235] J. Wang, J. Messner, and H. Stetter, “An Experimental Investigation on Transpiration Cooling Part II: Comparison of Cooling Methods and Media,” *Int. J. Rotating Mach.*, vol. 10, no. 5, pp. 355–363, 2004.

[236] C. Davis, *Lasers and electro-optics: Fundamentals and engineering*. Cambridge University Press, 1996.

[237] A. C. Eckbreth and R. J. Hall, “CARS Concentration Sensitivity With and Without Nonresonant Background Suppression,” *Combust. Sci. Technol.*, vol. 25, no. 5–6, pp. 175–192, 1981.

[238] F. Hansen, “Approximations for the Thermodynamic and Transport Properties of High-Temperature Air,” Washington DC, 1958.

[239] F. S. Schlindwein and D. H. Evans, “Autoregressive spectral analysis as an alternative to fast Fourier transform analysis of Doppler ultrasound signals,” *Doppler physics and signal processing*. pp. 74–84, 1992.

[240] P. Sulzer and K. Wieland, “Intensitätsverteilung eines kontinuierlichen Absorptionsspektrums in Abhängikeit von Temperatur und Wellenzahl,” *Helv. Phys. Acta*, vol. 25, pp. 653–676, 1952.

[241] M. V. Roux, M. Temprado, J. S. Chickos, and Y. Nagano, “Critically evaluated thermochemical properties of polycyclic aromatic hydrocarbons,” *J. Phys. Chem. Ref. Data*, vol. 37, no. 4, pp. 1855–1996, 2008.

[242] L. Chen and R. Stone, “Measurement of enthalpies of vaporization of isooctane and ethanol blends and their effects on PM emissions from a GDI engine,” *Energy and Fuels*, vol. 25, no. 3, pp. 1254–1259, 2011.

11.Appendix

11.1. LITGS noise reduction techniques

11.1.1. Uniform smoothing

Often when working with signals with low signal-to-noise ratios it can be beneficial to apply a noise reduction filter. This has the intention of smoothing out the high frequency noise fluctuations in the signal while retaining the lower frequency 'useful' fluctuations in signal intensity. This also applies to LITGS signal analysis, however care must be taken not to sacrifice the accurate representation of the optical signal in order to achieve a cosmetically 'cleaner' signal. If, for example, a moving average filter with a very large window is applied to the signal, the filtered output will both show reduced contrast in the acoustic oscillations and have oscillation peaks shifted in time compared to the original input [Figure 11-1].

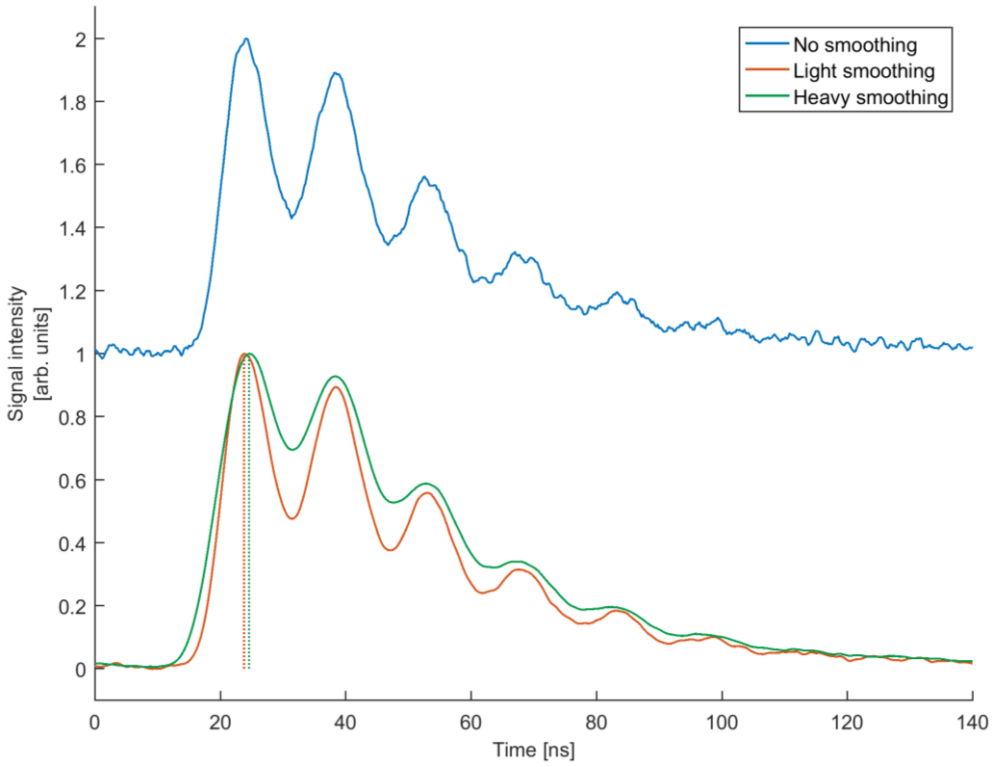

Figure 11-1 Effect of moving average smoothing applied to a LITGS signal with no smoothing, light smoothing (window size of 15 elements i.e. 2.8 ns) and heavy smoothing (window size of 45 elements i.e. 8.8 ns). 'Heavy' smoothing delays the maximum of the first peak by 0.8 ns with respect to 'light' or 'no' smoothing, as highlighted by the vertical lines marking the timings of the maxima of the peaks.

Tests showed that applying heavy smoothing to a signal to remove the high frequency noise can shift the acoustic oscillation peak in the power spectrum enough to bias the derived temperature by several Kelvin. Minimal smoothing was applied to the LITGS data in this work to avoid such biases. Additionally, the nonlinear Wiener filter previously used for smoothing of LITGS signals was replaced with a moving average filter to reduce the distortion of peaks due to the smoothing process.

11.1.2. Selective smoothing

Given the biases introduced by heavy smoothing of the entire LITGS signal, an alternative approach is to apply heavy smoothing solely to the regions of the signal vector after the LITGS signal has disappeared. This could reduce the contribution of the noise to the power spectrum without the information loss associated with applying the heavy smoothing to the LITGS signal itself.

While this does clean up the signal and produce an apparently better resolved acoustic oscillation peak in the power spectrum, it introduces a significant systematic bias to the derived temperature. To smooth the 'noise' sections of the input vector, a threshold time must be defined for where the LITGS signal finishes. Exactly where this cut-off occurs affects the frequency content of the signal. An investigation into the location of the smoothing cut-off determined there was an oscillatory response of the acoustic peak location (and therefore derived temperature) to the length of the smoothed section [Figure 11-2].

The oscillatory nature may be in part due to the edge of the Tukey window suppressing small LITGS peaks hidden in the noisy tail of the signal. As the cut-off location is varied, the Tukey window edge passes through each peak, asymmetrically supressing the peak and distorting the resulting power spectrum. This distortion will be periodic with respect to the location of the cu-off as the edge passes through each hidden LITGS peak.

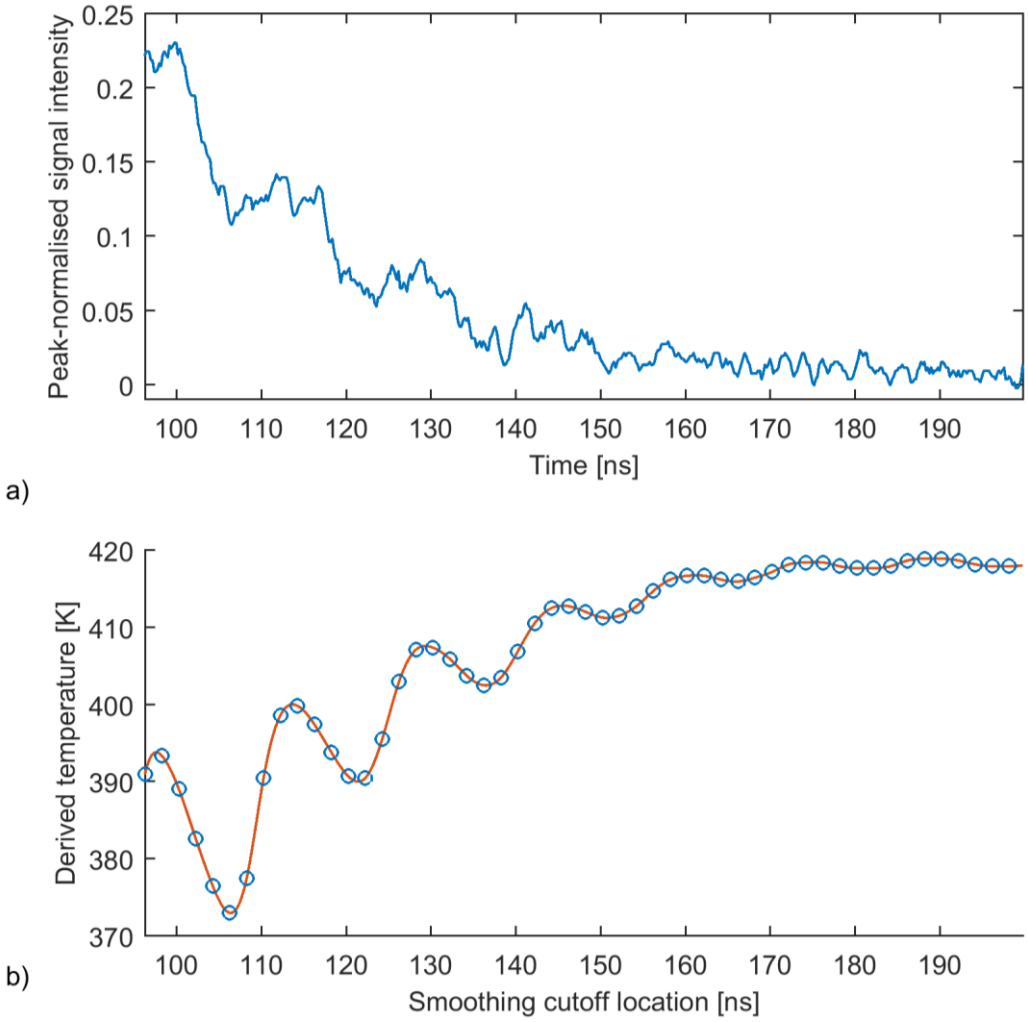

Figure 11-2 Systematic bias to derived LITGS temperature owing to the choice of smoothing cut-off location. a) Final 100 ns of an unsmoothed LITGS signal vector displaying last few visible oscillation peaks before baseline noise from 150 ns onwards. b) Derived temperature as a function of smoothing cut-off location.

Such a large systematic bias, of up to 10 %, in the derived temperature is not suitable for a diagnostic technique intended to be used as a reference calibration for TC-PLIF measurements. As such, selective smoothing of the tail of LITGS signals before FFT analysis should not be applied.

11.2. FFT accuracy at low pressures investigation

11.2.1. Cause of systematic shift

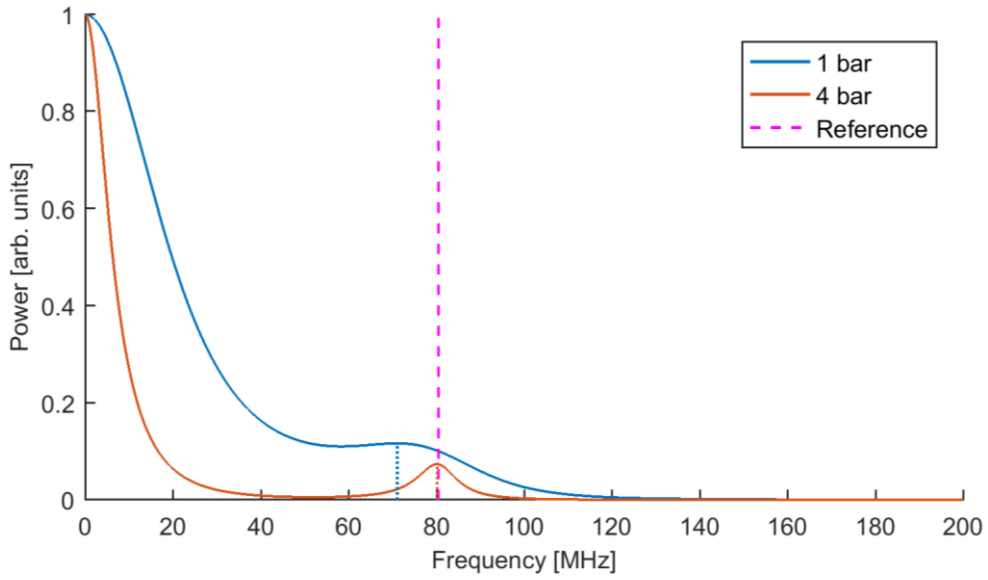

Figure 11-3 Power spectra of modelled LITGS signals at 650 K at low (1 bar) and high (4 bar) pressures using the 'standard' FFT analysis. The 'reference' frequency corresponds to the oscillation frequency for 650 K in this model.

Systematic errors introduced by FFT derivation of the oscillation frequency of a LITGS signal were discussed in chapter 4 section 4.5.2. The cause of these errors is that the FFT produces a power spectrum of the frequency content of the entire signal, not solely the acoustic contribution. At low pressures LITGS signals are short and the acoustic oscillations make up only a small fraction of the characteristics of the signal and are equalled or dominated by the frequency content of the initial sharp rise and exponential decay of the underlying thermal component. This leads to the characteristic twin-peaked power spectrum of a LITGS signal as displayed in Figure 11-3. The acoustic oscillation contribution can be considered to be added to the tail of the large 'DC' peak with a maximum at $\nu = 0$. This results in an asymmetric 'acoustic' peak as the DC peak's contribution is reduced for higher frequencies. This sloping baseline for the acoustic peak raises the left shoulder of the acoustic peak, effectively shifting the peak maximum to lower frequencies. It is this local maximum that the FFT analysis interprets as the acoustic oscillation frequency.

For shorter LITGS signals the DC peak is comparatively large and this peak-shifting effect is more pronounced [Figure 11-3 (1 bar)], resulting in the underestimation of temperatures seen in chapter 4 section 4.5.2. At higher pressures, the signal length and hence the magnitude of the acoustic oscillation peak is increased. The sloping baseline of the DC peak is then a much smaller fraction of the overall magnitude of the peak and results in a much smaller or negligible shift in peak location and derived frequency [Figure 11-3 (4 bar)].

11.2.2. Adaptation of FFT analysis

In this section, an alternative to the standard FFT analysis method is discussed with the aim of adapting the existing FFT analysis to improve its accuracy at low pressures.

Given that the source of the peak-shifting bias is the large DC peak generating an effective non-flat baseline for the acoustic peak in the power spectrum, a more elegant solution would be to remove the DC peak entirely. Experiments with the post-processing removal of the exponentially decaying thermal component from a LITGS signal have historically met with limited success. Subtracting a fitted exponential from the signal or cropping the signal around the acoustic oscillations have proved highly sensitive to the exact nature of the fitted exponential or cropping parameters. Often these processes have introduced more systematic errors than they removed. The key to a successful approach is to provide an objective method for subtracting the underlying thermal component, leaving just the acoustic component oscillating in time about a zero mean.

One approach which has shown promise is the subtraction of a local average from the signal. This is referred to as ‘subtracted’ FFT analysis and was briefly explored in this work. For each point on the LITGS data vector, the average value of its neighbours is computed over a window of datapoints with a width of the approximate peak-to-peak separation. This average is then subtracted from the initial value to return a ‘processed’ datapoint. After application to the entire data vector, what remains is an oscillating signal with peaks (and troughs) corresponding to locations in the initial signal which were higher (or lower) than the average of their neighbours.

This process retains the oscillatory information of the original signal, but produces a zero-mean output such than the DC peak seen in the standard FFT power spectrum of a LITGS signal is removed [Figure 11-4].

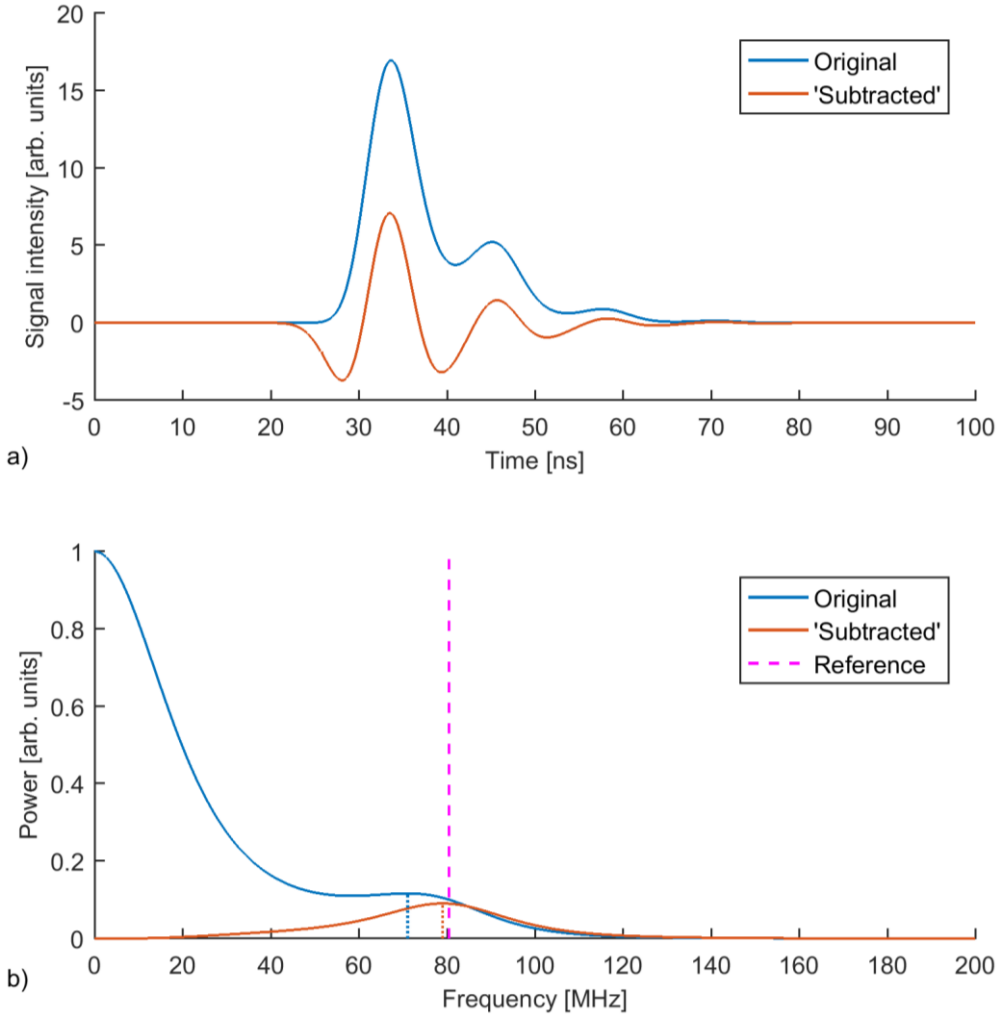

Figure 11-4 'Subtracted' FFT analysis. a) Thermal component subtracted from LITGS signal. b) Power spectrum of 'subtracted' signal has no DC peak, minimising the deviation of peak location from the reference frequency.

This method is not without its own potential drawbacks. It is currently unclear to what extent the oscillations are distorted by this 'moving average' style subtraction. Additionally the initial rise of the signal contributes to the 'processed' signal, much in the same way as the 'standard' FFT analysis, despite its dependence on quenching rate and pressure as well as temperature.

When subjected to the same testing as the 'standard' and 'fitted' FFT analysis methods, the 'subtracted' FFT analysis dramatically improves on the accuracy of the 'standard' FFT analysis

for all temperatures and pressures and performs better than the ‘fitted’ FFT analysis at lower temperatures.

For pressures higher than 1.6 bar or temperatures lower than 420 K, the ‘subtracted’ FFT analysis equals or outperforms the ‘fitted’ FFT analysis with each returning worst case errors of – 0.36 % and + 1.3 % respectively. However, for conditions with both high temperature 475 K < T < 650 K and low pressure 1 bar < P < 1.43 bar, the ‘subtracted’ FFT analysis displays poorer performance than the ‘fitted’ FFT analysis with each returning worst case errors of – 3.5 % and + 2.0 % respectively.

Improvements to FFT accuracy conclusions

The ‘fitted’ FFT analysis and ‘subtracted’ FFT analysis offer different approaches to improving the accuracy of temperature derivation from a LITGS signal. The methods are both rapid compared to the full fitting routine and are complementary in their suitability for different temperature and pressure combinations.

Flame diagnostics in atmospheric pressure flames correspond to very high temperatures and atmospheric (low on this scale) pressures. This is in the regime where the ‘fitted’ FFT analysis offers the higher accuracy of the two methods. Engine environments show strong positive correlation between temperature and pressure due to compression heating. As such, the conditions of simultaneous low pressure and high temperature are less relevant, making ‘subtracted’ FFT analysis the preferred option.

As the ‘subtracted’ FFT method has not been fully developed and has only undergone testing on theoretical ‘clean’ signals, it has not been applied to the LITGS measurements in this work. For future experiments it would be worth the time investment to fully test the adapted FFT method for robustness in deriving temperatures from ‘real’ data.